Doctoral Dissertation
Doctoral Program in Metrology (32.nd cycle)

Quantum enhanced optical measurements

Elena Losero

* * * * * *

Supervisors
Dott. Marco Genovese, Supervisor
Dott. Ivano Ruo-Berchera, Co-supervisor

Doctoral Examination Committee:
To be defined

Politecnico di Torino
October 31, 2019

I hereby declare that, the contents and organisation of this dissertation constitute my own original work and does not compromise in any way the rights of third parties, including those relating to the security of personal data.

Elena Losero

Turin, October 31, 2019

Abstract

Quantum metrology aims at exploiting peculiar quantum mechanics properties in order to enhance the sensitivity of a measurement beyond the possibilities offered in a classical scenario.

In this thesis I discuss three different examples where the use of quantum resources leads to an enhanced sensitivity respect to the classical case. In particular, I focus on optical measurements demonstrating how quantum states of light can offer an improvement respect to the best classical strategies, both theoretically and experimentally. Different quantum states are considered and different quantum properties exploited.

On one side I exploit photon number quantum correlations of multi-mode twin-beam state. I demonstrate how these non-classical correlations can be used both for quantum enhanced mean absorption estimation measurements and image reconstruction. More specifically, I worked with the ghost imaging protocol and some of its possible variations, also proposing a new protocol, optimized for experimental imperfections. In order to pave the way to real applications I also report biological sample reconstructions.

On the other side I consider quantum properties in terms of field quadrature, exploiting them into a peculiar interferometric system consisting in a couple of Michelson Interferometers. In particular I use both single mode vacuum states, presenting reduced uncertainty into one quadrature, and twin-beam like states, presenting quadrature correlation between the two modes. This experiment represents the first feasibility test of quantum enhanced correlated interferometry, paving the way for possible applications to fundamental physical tests.

Summary

Quantum mechanics was formulated in the first half of the last century. The development of this new theory leads to the rising of ground-breaking technologies as for example the laser and the transistor. These technologies could be understood and developed only thanks to quantum mechanics; they are based on bulk effects, where many quantum degrees of freedom are manipulated at once. We usually refer to them as product of a first quantum revolution. According to the European quantum technologies flagship program started in 2018 [1], we are now currently experiencing a second quantum revolution [2]. In fact, more and more technologies (usually named as quantum technologies) are being developed which manipulate individual quantum states to exploit their peculiar quantum properties, such as superposition and entanglement. Quantum communication [3, 4], quantum computation [5], quantum sensors [6] and metrology devices [7–11] are example of promising quantum technologies. This thesis will be mainly focused on the last technology mentioned: quantum metrology. There are different physical systems being investigated for its development, among them photons certainly have an important role [12]. Being optical measurements widespread in all the branches of science, from chemistry and biology to physics and material science, light appears to be a natural choice. According to this observation, we will focus on optical measurements. In general, aim of quantum metrology is to exploit quantum effects to achieve the ultimate quantum limit, i.e. the highest precision allowed by quantum mechanics laws [13, 14]. Typically, in order to increase the signal-to-noise ratio of a noisy measurements the classical approach consists in repeating N independent measurements and then averaging the measurement results. This approach allows to increase the sensitivity as $1/\sqrt{N}$, this scaling is known as standard quantum limit. If limited to classical resources, this limit cannot be beaten. Nonetheless, it is not fundamental, and quantum resources allows reducing the uncertainty below it, ideally down to the so called ultimate quantum limit. In real environments decoherence must be taken into account and necessarily prevents to attain the ultimate quantum limit, however several examples of quantum enhanced measurements, i.e. measurements whose uncertainty is below the "classical" uncertainty, have been so far demonstrated. The first demonstrations were mainly conceived as proof of principle experiments, while nowadays more and more works try to fill the gap to move toward real applications [15].

In this thesis I discuss three examples of quantum enhanced optical measurements,

presenting in each case a theoretical model and the experimental results. The first experiment shows how using quantum states of light it is possible to increase the sensitivity in the estimation of the mean absorption coefficient of a sample. The second experiment consists in exploiting quantum resources for imaging, in particular a reconstruction imaging protocol known as ghost imaging, and some possible variations, are discussed and the performance in terms of signal-to-noise ratio compared to the classical strategies. In both these applications the quantum resource exploited is the non-classical correlation in the photon number between two beams in the so called multi-mode twin-beam state. The last example demonstrates how quantum states of light can enhance the sensitivity in correlated interferometry, i.e. in estimating the phase correlation between two interferometers. While quantum light is currently used in a single interferometer to enhance its sensitivity, being gravitational wave detectors a primary example [16], it is the first time that quantum light is applied to a double interferometric set-up. We perform two different experiments: in the first case squeezed states of light are exploited, in the second case twin-beam like state are used. The first scheme is an extension of the approach currently used in single interferometers, while the second approach has no analogous in conventional interferometry and, according to the theoretical work, could lead to unprecedented sensitivity. In all the cases, in order to pave the way toward real applications, the role of losses and other experimental imperfections is thoroughly discussed. At the same time, the conditions where quantum resources offer a substantial advantage over their classical counter part is highlighted.

Structure of the thesis

This thesis consists in five chapter:

- Ch. 1. In this chapter I give all the theoretical elements which are necessary for the subsequent chapters. In particular, some basic elements of quantum optics are reviewed and the main properties of the quantum states of light used in the subsequent works presented.

- Ch. 2. Here the quantum states of light used in the subsequent works are described under the experimental point view. In particular, the experimental set-ups used for their generation are described and different characterization measurements reported.

- Ch. 3. This chapter is based on the article [17]. Here the advantages of photon-number quantum correlations in multi-mode twin-beam states for mean absorption estimation measurements are discussed. Different absorption estimators are compared from both the theoretical and experimental side. A best quantum advantage of (1.51 ± 0.02) is experimentally demonstrated.

- Ch. 4. This chapter is based on the article [18]. Here the photon-number quantum

correlations in multi-mode twin-beam states are applied to different ghost imaging protocols. In particular I extended to the quantum regime a protocol named differential ghost imaging and I propose an optimization of it, useful in presence of experimental imperfections. In order to pave the way for real application also the imaging of different biological object is considered.

- Ch. 5. This chapter is based on the article [19]. Here the first feasibility test of quantum enhanced correlated interferometry is demonstrated. The advantages of two different quantum states are considered, both theoretically and experimentally. The experimental set-up, consisting in a system of two Michelson interferometers, has been built in Denmark, thanks to a collaboration with the Danish Technical University (DTU). I participated to the set-up realization and the data collection spending four months in the danish laboratories.

Contents

Chapter 1

Elements of quantum optics

In this chapter we introduce, from the theoretical point of view, some elements which are useful for the following chapters. In particular, after revising some basic concepts of quantum optics, we present in details two different examples of quantum states: squeezed vacuum states and twin beam states. In view of the experimental applications we consider in this thesis, we focus on their properties in terms of photon statistics and quadrature of the field.

1.1   Notation and relevant operators

In the quantum optics framework the hamiltonian associated to the electromagnetic field is a quantum mechanical operator. In particular, it corresponds to the sum over all the harmonic oscillators associated to different wave vectors $\mathbf{k}$, each one corresponding to one mode of the field:

$$\hat{H}(t) = \frac{1}{2} \sum_{\mathbf{k}} [\hat{p}_{\mathbf{k}}^2(t) + \omega^2 \hat{q}_{\mathbf{k}}^2(t)] \tag{1.1}$$

where $\hat{p}_{\mathbf{k}}$ and $\hat{q}_{\mathbf{k}}$ are hermitian conjugate operators, obeying to the following commutation rules:

$$[\hat{q}_{\mathbf{k}}, \hat{p}_{\mathbf{k'}}] = i\hbar \delta_{\mathbf{k},\mathbf{k'}}^3 \tag{1.2}$$

$$[\hat{q}_{\mathbf{k}}, \hat{q}_{\mathbf{k'}}] = [\hat{p}_{\mathbf{k}}, \hat{p}_{\mathbf{k'}}] = 0 \tag{1.3}$$

From $\hat{q}_{\mathbf{k}}$ and $\hat{p}_{\mathbf{k}}$ it is possible to define the annihilation and creation operators, $\hat{a}_{\mathbf{k}}$ and $\hat{a}_{\mathbf{k}}^{\dagger}$:

$$\hat{a}_{\mathbf{k}} = \frac{1}{\sqrt{2\hbar\omega}} [\omega \hat{p}_{\mathbf{k}} + i\hat{q}_{\mathbf{k}}] \tag{1.4}$$

$$\hat{a}_{\mathbf{k}}^{\dagger} = \frac{1}{\sqrt{2\hbar\omega}} [\omega \hat{p}_{\mathbf{k}} - i\hat{q}_{\mathbf{k}}] \tag{1.5}$$

1

In terms of $\hat{a}_{\mathbf{k}}$ and $\hat{a}_{\mathbf{k}}^{\dagger}$ the commutation relations in Eq.s 1.2-1.3 become:

$$[\hat{a}_{\mathbf{k}}, \hat{a}_{\mathbf{k}'}^{\dagger}] = \delta_{\mathbf{k},\mathbf{k}'}^{3} \tag{1.6}$$

$$[\hat{a}_{\mathbf{k}}, \hat{a}_{\mathbf{k}'}] = [\hat{a}_{\mathbf{k}}^{\dagger}, \hat{a}_{\mathbf{k}'}^{\dagger}] = 0 \tag{1.7}$$

The operators $\hat{a}_{\mathbf{k}}$ and $\hat{a}_{\mathbf{k}}^{\dagger}$ are not hermitian, therefore they do not correspond to any physically observable quantity. However, combinations of them can be hermitian. Particularly relevant is the number operator, $\hat{n}_{\mathbf{k}}$:

$$\hat{n}_{\mathbf{k}} = \hat{a}_{\mathbf{k}}^{\dagger}\hat{a}_{\mathbf{k}} \tag{1.8}$$

In terms of $\hat{n}_{\mathbf{k}}$ the hamiltonian can be written as:

$$\hat{H} = \sum_{\mathbf{k}} \hbar\omega \left(\hat{n}_{\mathbf{k}} + \frac{1}{2} \right) \tag{1.9}$$

As its name suggests, $\hat{n}_{\mathbf{k}}$ can be interpreted as the number of photons (quanta of energy of the electromagnetic field) in the mode $\mathbf{k}$.

Other important operators are the quadrature operators. Avoiding the repetition of the subscript $\mathbf{k}$, they are defined as:

$$\hat{X} = \frac{\hat{a}^{\dagger} + \hat{a}}{\sqrt{2}}, \ \hat{Y} = \frac{\hat{a}^{\dagger} - \hat{a}}{i\sqrt{2}} \tag{1.10}$$

As conventionally done, we refer to $\hat{X}$ as amplitude quadrature and to $\hat{Y}$ as phase quadrature. Quantum mechanically, they are not commuting variables, in particular, using the commutators in Eq.s 1.6-1.7, we derive:

$$[\hat{X}, \hat{Y}] = i \tag{1.11}$$

The Heisenberg uncertainty relationship for two non commutative operators $\hat{A}$ and $\hat{B}$ is given by [20]:

$$\Delta\hat{A}\Delta\hat{B} \geq \frac{|\langle[\hat{A}, \hat{B}]\rangle|}{2} \tag{1.12}$$

For the quadrature operators therefore it holds:

$$\Delta\hat{X}\Delta\hat{Y} \geq \frac{1}{2} \tag{1.13}$$

Amplitude and quadrature operators can be both seen as particular cases of the more general quadrature operator $\hat{X}_{\phi}$:

$$\hat{X}_{\phi} = \frac{\hat{a}^{\dagger}e^{i\phi} + \hat{a}e^{-i\phi}}{\sqrt{2}} \tag{1.14}$$

which reduces to $\hat{X}$ and $\hat{Y}$ for $\phi = 0$ and $\phi = \pi/2$ respectively. An experimental procedure to measure $\hat{X}_\phi$ is described in Sec. 1.3.1.

Given a state $|\psi\rangle$ and an operator $\hat{A}$, we use the conventional notation:

$$\langle \hat{A} \rangle = \langle \psi | \hat{A} | \psi \rangle \tag{1.15}$$

to indicate the quantum mean value of the operator $\hat{A}$ over the state $|\psi\rangle$.

1.1.1   Beam splitter input-output relations

A beam splitter (BS) is a linear, passive four-port device, with two input ports (a and b in Fig. 1.1) and two output ports (c and d). In this section we treat the BS from the quantum mechanics point of view, deriving the BS input-output relation for the bosons annihilation operators, $\hat{a}, \hat{b}, \hat{c}, \hat{d}$. These relations will be useful several times in the following. In all the treatment the BS is considered as a lossless device.
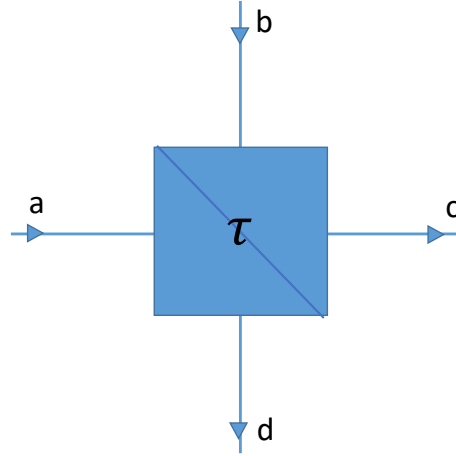
Figure 1.1: Scheme of a lossless beam splitter (BS) of transmittance τ. a and b are the input modes, c and d the output modes. The BS transformations are discussed in the text.

Defining the reflection and transmission coefficients associated to the two output ports as r_c, t_c, r_d, t_d respectively, the output operators are linear combination of the input operators. In particular:

$$\hat{c} = r_c\hat{b} + t_c\hat{a} \tag{1.16}$$

$$\hat{d} = t_d\hat{b} + r_d\hat{a} \tag{1.17}$$

More conveniently, in the matrix form, we can write:

$$\begin{pmatrix} \hat{c} \\ \hat{d} \end{pmatrix} = B \begin{pmatrix} \hat{a} \\ \hat{b} \end{pmatrix}, \text{ where } \quad B = \begin{pmatrix} t_c & r_c \\ r_d & t_d \end{pmatrix} \tag{1.18}$$

Several constraints need to be satisfied:

- B must be unitary, i.e. $B^\dagger = B$, in order to conserve the total probability of finding a photon (the BS is considered as a lossless device).

- The output annihilation operators must satisfy the canonical commutators relations in Eq.s 1.6-1.7, i.e. $[\hat{c}, \hat{c}^\dagger] = [\hat{d}, \hat{d}^\dagger] = 1$, $[\hat{c}, \hat{c}] = [\hat{d}, \hat{d}] = [\hat{c}, \hat{d}] = [\hat{c}, \hat{d}^\dagger] = 0$.

These constraints imply:

$$|r_c| = |r_d|, \ |t_c| = |t_d| \tag{1.19}$$

$$r_c^* t_d + r_d t_c^* = r_c^* t_c + r_d t_\mathrm{d}^* = 0 \tag{1.20}$$

For a balanced BS it holds $|r_c|^2 = |r_d|^2 = |t_c|^2 = |t_d|^2 = 1/2$, and the constraints in Eq. 1.19 can be satisfied in different ways, such as:

$$B = \frac{1}{\sqrt{2}} \begin{pmatrix} 1 & -1 \\ 1 & 1 \end{pmatrix} \tag{1.21}$$

or

$$B = \frac{1}{\sqrt{2}} \begin{pmatrix} 1 & i \\ i & 1 \end{pmatrix} \tag{1.22}$$

or

$$B = \frac{1}{\sqrt{2}} \begin{pmatrix} 1 & -i \\ i & -1 \end{pmatrix} \tag{1.23}$$

In the more general case of a BS of transmittance τ, i.e. $|r_c|^2 = |r_d|^2 = \tau$ and $|t_c|^2 = |t_d|^2 = 1 - \tau$ we can write:

$$B = \begin{pmatrix} \sqrt{\tau} & -i\sqrt{1-\tau} \\ i\sqrt{1-\tau} & -\sqrt{\tau} \end{pmatrix} \tag{1.24}$$

Let us now consider a specific example, consisting in a beam splitted by a BS of transmittance τ. The mode $\hat{a}$ corresponds to the input beam considered, having mean number of photons $\langle \hat{n}_a \rangle$ and variance $\Delta^2 \hat{n}_a$. The mode $\hat{b}$ is empty, i.e. in the vacuum mode. Replacing Eq. 1.24 in 1.18 we can obtain the statistics of the output modes. In particular, we find:

$$\langle \hat{n}_c \rangle = \langle \hat{c}^\dagger \hat{c} \rangle = \tau \langle \hat{n}_a \rangle \tag{1.25}$$

$$\langle \hat{n}_d \rangle = \langle \hat{d}^\dagger \hat{d} \rangle = \tau \langle \hat{n}_a \rangle \tag{1.26}$$

$$\Delta^2 \hat{n}_c = \langle \hat{n}_c^2 \rangle - \langle \hat{n}_c \rangle^2 = \langle \hat{c}^\dagger \hat{c} \hat{c}^\dagger \hat{c} \rangle - \langle \hat{c}^\dagger \hat{c} \rangle^2 = \tau^2 \Delta^2 \hat{n}_a + \tau(1-\tau)\langle \hat{n}_a \rangle \tag{1.27}$$

$$\Delta^2 \hat{n}_d = \langle \hat{d}^\dagger \hat{d} \hat{d}^\dagger \hat{d} \rangle - \langle \hat{d}^\dagger \hat{d} \rangle^2 = (1-\tau)^2 \Delta^2 \hat{n}_a + \tau(1-\tau)\langle \hat{n}_a \rangle \tag{1.28}$$

$$\langle \Delta \hat{n}_c \Delta \hat{n}_d \rangle = \langle \hat{c}^\dagger \hat{c} \hat{d}^\dagger \hat{d} \rangle - \langle \hat{c}^\dagger \hat{c} \rangle \langle \hat{d}^\dagger \hat{d} \rangle = \tau(1-\tau)[\Delta^2 \hat{n}_a - \langle \hat{n}_a \rangle] \tag{1.29}$$

4

1.1.2 Effect of losses

In real experiments the detector efficiency is necessarily limited to $\eta < 1$: this implies that the detected photon statistics differs from the photon statistics of the ideal state. Therefore, in order to properly match theoretical expectations with experimental observations it is necessary to take into account losses. According to [21], the effect of a non-unit quantum efficiency η can be modeled as the evolution of the field after passing through a BS of transmission η. From the unused port the vacuum state enters. Any kind of photon losses (not necessarily at the detection stage, such as losses of the optical components) can be included in η.

Referring to Fig. 1.2 (with output modes dubbed as $\hat{b}_1$ and $\hat{b}_2$ and the input modes as $\hat{a}$ and $\hat{v}$) and using Eq. 1.24, it follows:

$$\hat{b}_1 = \sqrt{\eta}\hat{a} + i\sqrt{1-\eta}\hat{v} \tag{1.30}$$

$$\hat{b}_2 = \sqrt{1-\eta}\hat{v} + i\sqrt{\eta}\hat{a} \tag{1.31}$$

where $\hat{v}$ is the annihilation operator corresponding to the vacuum state, $|0\rangle$.
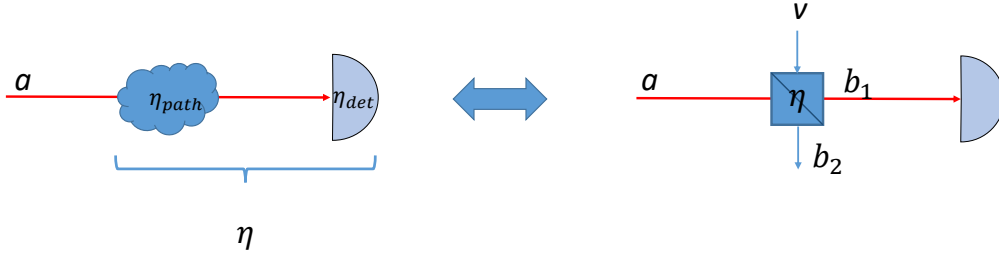
Figure 1.2: Scheme for modelling the effect of losses in the detected photon statistics. The non-ideal system of efficiency η can be modeled as an ideal system where a beam splitter of transmittance η is inserted. In η both the channel efficiency and the detectror efficiency are included.

Said $\langle\hat{n}\rangle$ and $\Delta^2\hat{n}$ the photon statistics of the input state, the number of photons detected in the $\hat{b}_1$ mode, $\langle\hat{N}\rangle$, and its associated variance, $\Delta^2\hat{N}$, are:

$$\langle\hat{N}\rangle = \langle\hat{b}_1^\dagger\hat{b}_1\rangle = \eta\langle\hat{a}_1^\dagger\hat{a}_1\rangle = \eta\langle\hat{n}\rangle \tag{1.32}$$

$$\Delta^2\hat{N} = \langle\hat{b}_1^\dagger\hat{b}_1\hat{b}_1^\dagger\hat{b}_1\rangle - \langle\hat{b}_1^\dagger\hat{b}_1\rangle^2 = \eta^2\Delta^2\hat{n} + \eta(1-\eta)\langle\hat{n}\rangle \tag{1.33}$$

Correlations are also affected from the detection process. In particular, given the covariance between two modes, $\langle\Delta\hat{n}_1\Delta\hat{n}_2\rangle$, and two independent detection processes of efficiencies η_1 and η_2, the detected covariance is:

$$\langle\Delta\hat{N}_1\Delta\hat{N}_2\rangle = \eta_1\eta_2\langle\Delta\hat{n}_1\Delta\hat{n}_2\rangle \tag{1.34}$$

1.1.3 Equivalence interferometer - beam splitter

Since it is extensively used in Ch. 5, let us consider a Michelson interferometer (MI). In its basic form, it is a system formed by a 50-50 BS and two end mirrors, as presented in Fig. 1.3. $\hat{a}$ and $\hat{b}$ are the input modes, while $\hat{c}$ and $\hat{d}$ are the output modes. Being bosons
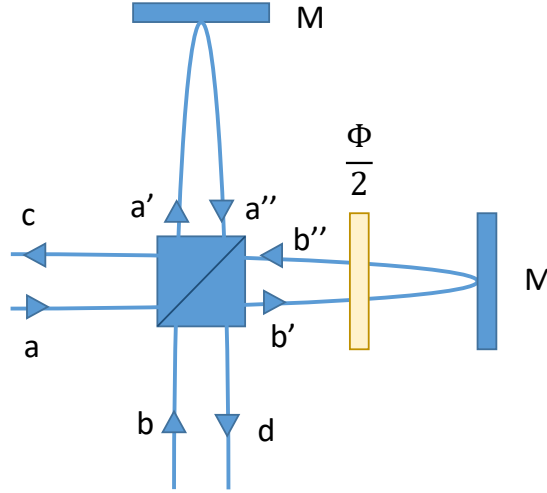
Figure 1.3: Scheme of a simple Michelson interferometer (MI). It is constituted from a beam splitter (BS) and two end mirrors (M). The input beams enter from the *a* and *b* ports respectively, interfere at the BS and then propagate into the two MI arms. After being reflected by the end mirrors they interfer again at the BS, before exiting from the output modes *c* and *d*. The resulting interference depends from the phase difference between the two modes a'' and b'', this is indicated as $\phi/2$ in the figure.

operators, they satisfy the commutation relations in Eq.s 1.6-1.7. The two input modes firstly interfere on the BS, then propagate till the end mirrors and, after being reflected, interfere again at the BS. In the propagation a certain phase ϕ can be accumulated from one mode respect to the other, due for example to a small difference in the arms length. The relations between the input and the output modes can be obtained using the BS relations in Eq. 1.22 and the fact that a reflection at the end mirror corresponds to a factor *i*. Always referring to Fig. 1.3 we have:

$$\hat{a}' = \frac{1}{\sqrt{2}}(\hat{a} + i\hat{b}) \ \text{ and } \ \hat{b}' = \frac{1}{\sqrt{2}}(\hat{b} + i\hat{a}) \tag{1.35}$$

$$\hat{a}'' = i\hat{a}' \ \text{ and } \ \hat{b}'' = ie^{i\phi}\hat{b}' \tag{1.36}$$

$$\hat{c} = \frac{1}{\sqrt{2}}(\hat{a}'' + i\hat{b}'') \ \text{ and } \ \hat{d} = \frac{1}{\sqrt{2}}(\hat{b}'' + i\hat{a}'') \tag{1.37}$$

where $\hat{a}'$ and $\hat{b}'$ are the modes exiting the BS after the first interference and $\hat{a}''$ and $\hat{b}''$ are the modes which interfere at the BS after the reflection at the end mirrors. Writing $\hat{c}$ and $\hat{d}$ in terms of $\hat{a}$ and $\hat{b}$, we obtain:

$$\hat{c} = \cos\left(\frac{\phi}{2}\right)\hat{a} - i\sin\left(\frac{\phi}{2}\right)\hat{b} \tag{1.38}$$

$$\hat{d} = i\sin\left(\frac{\phi}{2}\right)\hat{a} - \cos\left(\frac{\phi}{2}\right)\hat{b} \tag{1.39}$$

Comparing the input-output relations obtained in Eq.s 1.38-1.39 with the BS input-output relations in Eq. 1.24 it can be argued that they are exactly the same with the substitution:

$$\tau = \cos^2\left(\frac{\phi}{2}\right) \tag{1.40}$$

This result demonstrates that a Michelson interferometer of phase ϕ is equivalent to a BS of transmittance $\tau = \cos^2\left(\frac{\phi}{2}\right)$.

1.2   Fock space and Fock states

Fock states, or number states, are defined as the eigenstates of the number operator $\hat{n}_{\mathbf{k}}$. For the sake of simplicity we focus on one mode and remove the subscript $\mathbf{k}$:

$$\hat{n}|n\rangle = n|n\rangle \tag{1.41}$$

where n represents the number of photons in the mode. The action of the creation and annihilation operators on a Fock state is:

$$\hat{a}^{\dagger}|n\rangle = \sqrt{n+1}|n+1\rangle \tag{1.42}$$

$$\hat{a}|n\rangle = \sqrt{n}|n-1\rangle \tag{1.43}$$

From Eq.s 1.42-1.43, the names conventionally used for $\hat{a}$ and $\hat{a}^{\dagger}$ become clear: the creation operator adds a photon on the state, while the annihilation operator removes one photon. The vacuum state is defined as:

$$\hat{a}|0\rangle = 0 \tag{1.44}$$

while the generic excited state can be obtained iteratively applying the creator operator on the vacuum state:

$$|n\rangle = \frac{(\hat{a})^n}{\sqrt{n!}}|0\rangle, \ n = 0,1,2,\dots \tag{1.45}$$

The Fock states can be used as basis in the Hilbert space, in particular they are orthogonal and complete:

$$\langle n | m \rangle = \delta_{n,m} \tag{1.46}$$

$$\sum_{n=0}^{\infty} | n \rangle \langle n | = 1 \tag{1.47}$$

Moreover, two different modes are always independent:

$$\langle n_{\mathbf{k}} | m_{\mathbf{k'}} \rangle = \delta_{n,m} \delta_{\mathbf{k},\mathbf{k'}} \tag{1.48}$$

From their definition, Fock states present a fixed number of photons. For a state $|n\rangle$ it holds:

$$\langle \hat{n} \rangle = \langle n | \hat{n} | n \rangle = n \tag{1.49}$$

$$\Delta^2 \hat{n} = \langle \hat{n}^2 \rangle - \langle \hat{n} \rangle^2 = 0 \tag{1.50}$$

in the presence of losses this photon statistics is affected. Said η the channel efficiency and using the results of Sec. 1.1.2, it holds:

$$\langle \hat{N} \rangle = \eta \langle \hat{n} \rangle = \eta n \tag{1.51}$$

$$\langle \Delta^2 \hat{N} \rangle = \eta^2 \langle \Delta^2 \hat{n} \rangle + \eta(1 - \eta)\langle \hat{n} \rangle = \eta(1 - \eta)\langle \hat{n} \rangle = (1 - \eta)\langle \hat{N} \rangle \tag{1.52}$$

in the presence of high losses ($\eta \ll 1$) the quantum fluctuations of the vacuum are the dominant term. In this case the detected photon statistics tends to a poissonian one, independently from the original statistics.

1.3 Coherent states

The coherent states of the field are the closest to a classical field of definite complex amplitude. Of great practical importance is the fact that a laser produces a great approximation of these states. They are defined as the eigenstates of the annihilation operator $\hat{a}$ (see for example [21]):

$$\hat{a}|\alpha\rangle = \alpha|\alpha\rangle \tag{1.53}$$

Being $\hat{a}$ not hermitian, the eigenvalues are not real, $\alpha = |\alpha|e^{i\phi}$. To express $|\alpha\rangle$ in the Fock basis, we can use Eq. 1.45 and write:

$$\langle n | \alpha \rangle = \frac{\alpha^n}{\sqrt{n!}} \langle 0 | \alpha \rangle \tag{1.54}$$

Therefore,

$$|\alpha\rangle = \sum_n |n\rangle\langle n|\alpha\rangle = \langle 0|\alpha\rangle \sum_n \frac{\alpha^n}{\sqrt{n!}} |n\rangle \tag{1.55}$$

where the coefficient $\langle 0|\alpha\rangle$ can be fixed by $|\langle\alpha|\alpha\rangle|^2 = 1$. This procedure leads to $\langle 0|\alpha\rangle = e^{-|\alpha|^2/2}$. In conclusion a coherent state can be expressed in the Fock basis as:

$$|\alpha\rangle = e^{-|\alpha|^2/2} \sum_n \frac{\alpha^n}{\sqrt{n!}}|n\rangle \tag{1.56}$$

From Eq. 1.56 the photon number distribution can be obtained as:

$$P(n) = |\langle n|\alpha\rangle|^2 = \frac{|\alpha|^{2n}e^{-|\alpha|^2}}{n!} \tag{1.57}$$

It can be concluded that the number of photons follows a poissonian distribution, with mean value $|\alpha|^2$. In particular,

$$\langle\hat{n}\rangle = \langle\alpha|\hat{a}^\dagger\hat{a}|\alpha\rangle = |\alpha|^2 = \langle\Delta^2 n\rangle \tag{1.58}$$

In a coherent state the number of photons is not fixed, but, as emerges from Eq. 1.58, is subject to a certain variance $\Delta^2 n$. The relative uncertainty of the photon number is:

$$\frac{\langle\Delta\hat{n}\rangle}{\langle\hat{n}\rangle} = \frac{1}{\sqrt{n}} \tag{1.59}$$

It follows that it can remarkably high in the presence of small n.

Let us now consider the consequences of splitting a coherent beam on a BS of transmittance τ. According to Eq. 1.29 and using the result in Eq. 1.58, we have:

$$\langle\Delta\hat{n}_1\Delta\hat{n}_2\rangle = 0 \tag{1.60}$$

where $\hat{n}_1$ and $\hat{n}_2$ are the number of photons in the two output modes. This result indicates that the two output beams are uncorrelated.

In the presence of loss, according to Sec. 1.1.2, a coherent state maintains the same statistical properties, simply rescaled by the channel efficiency η:

$$\Delta^2\hat{N} = \eta^2\langle\Delta^2\hat{n}\rangle + \eta(1-\eta)\langle\hat{n}\rangle = \eta^2\langle\hat{n}\rangle + \eta(1-\eta)\langle\hat{n}\rangle = \eta\langle\hat{n}\rangle = \langle\hat{N}\rangle \tag{1.61}$$

Concerning $\langle\hat{X}\rangle$ and $\langle\hat{Y}\rangle$ defined in Eq. 1.10, it follows:

$$\langle\hat{X}\rangle = \langle\alpha|\hat{X}|\alpha\rangle = \frac{\langle\hat{a}\rangle + \langle\hat{a}^\dagger\rangle}{2} = \sqrt{2}\,\mathrm{Re}(\alpha) \tag{1.62}$$

$$\langle\hat{Y}\rangle = \frac{\langle\hat{a}\rangle - \langle\hat{a}^\dagger\rangle}{2} = \sqrt{2}\,\mathrm{Im}(\alpha) \tag{1.63}$$

For their variance it is necessary to calculate the second order momentum:

$$\langle\hat{X}^2\rangle = \frac{\langle\hat{a}^2 + \hat{a}^{\dagger 2} + \hat{a}\hat{a}^\dagger + \hat{a}^\dagger\hat{a}\rangle}{2} = \frac{\alpha^2 + \alpha^{*2} + 2\alpha\alpha^* + 1}{2} = \frac{1 + 4[\mathrm{Re}(\alpha)]^2}{2} \tag{1.64}$$

9

$$\langle \hat{Y}^2 \rangle = \frac{\langle \hat{a}^2 + \hat{a}^{\dagger 2} - \hat{a}\hat{a}^{\dagger} - \hat{a}^{\dagger}\hat{a} \rangle}{2} = -\frac{\alpha^2 + \alpha^{*2} - 2\alpha\alpha^* + 1}{2} = -\frac{1 - 4[\mathrm{Im}(\alpha)]^2}{2} \quad (1.65)$$

From the standard deviation definition, i.e. $\Delta \hat{X} = \sqrt{\langle \hat{X}^2 \rangle - \langle \hat{X} \rangle^2}$, it follows:

$$\Delta \hat{X} = \frac{1}{\sqrt{2}}, \ \Delta \hat{Y} = \frac{1}{\sqrt{2}} \quad (1.66)$$

Considering the product of the standard deviations in the two quadratures we have:

$$\Delta \hat{X} \Delta \hat{Y} = \frac{1}{2} \quad (1.67)$$

thus the coherent states saturate the Heisenberg uncertainty principle in Eq. 1.13. In Fig. 1.4 a vacuum state, $|0\rangle$, and a displaced coherent state $|\alpha\rangle$ are represented in the $(\hat{X}, \hat{Y})$ quadrature space. The coordinates of the center correspond to the quadratures mean values, while the radius is the associated standard deviation, ΔX.
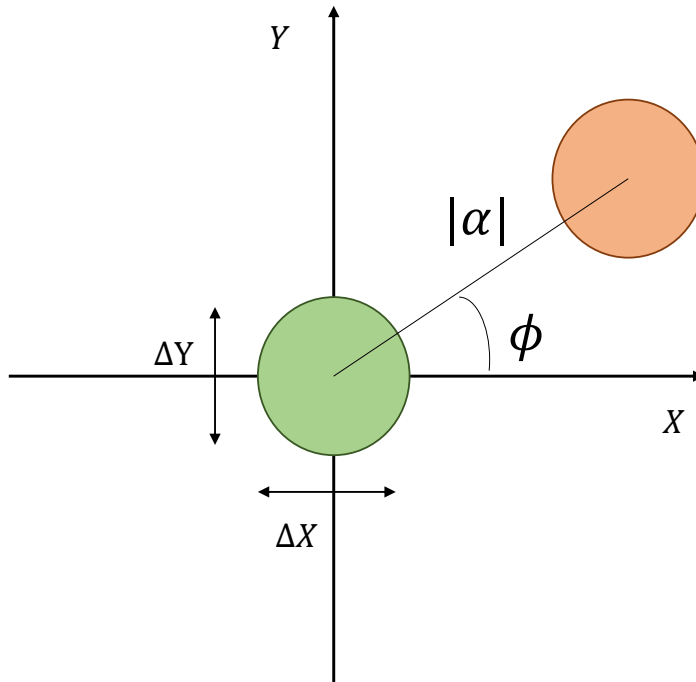
Figure 1.4: Coherent states in the $(\hat{X}, \hat{Y})$ plane. Green ellipse: vacuum state, $|0\rangle$. Orange ellipse: displaced coherent state, $||\alpha|e^{i\phi}\rangle$.

Coherent states are not orthogonal ($\langle \alpha|\beta \rangle \sim 0$ only in the limit $|\alpha - \beta| \gg 1$) and form an over-complete basis [21]. This last property allows us to write every density matrix $\hat{\rho}$ as:

$$\hat{\rho} = \int P(\alpha)|\alpha\rangle\langle\alpha| \mathrm{d}^2\alpha \quad (1.68)$$

$P(\alpha)$ is named as Glauber-Sudarshan function, from the scientist who introduced it in 1963 [21]. The surface element $d^2\alpha = d(\text{Re}\alpha)d(\text{Im}\alpha)$ is usually referred as element of phase space. As we will discuss in Sec. 1.5, it offers a way to distinguish between classical and quantum states.

For the sake of completeness we also mention that an alternative way of defining coherent states is trough the displacement operator $\hat{D}(\alpha)$:

$$|\alpha\rangle = \hat{D}(\alpha)|0\rangle, \ \hat{D}(\alpha) = e^{\alpha\hat{a}^\dagger - \alpha^*\hat{a}}, \alpha = |\alpha|e^{i\phi} \tag{1.69}$$

1.3.1 Balanced homodyne detection

The quadrature operators are defined in Eq. 1.10. These operators are hermitian, thus meaning that they correspond to physical observables. In this section we describe a scheme, named asbalanced homodyne detection, which allows to have experimental access to these quantities.

Aim of the homodyne detection scheme is to measure the two quadratures $\hat{X}$ and $\hat{Y}$ of the state $|\psi\rangle$, or any other pair of quadratures related to them by a phase rotation. In Fig. 1.5 the homodyne detection scheme is reported. The state $|\psi\rangle$ interfers on a 50-50
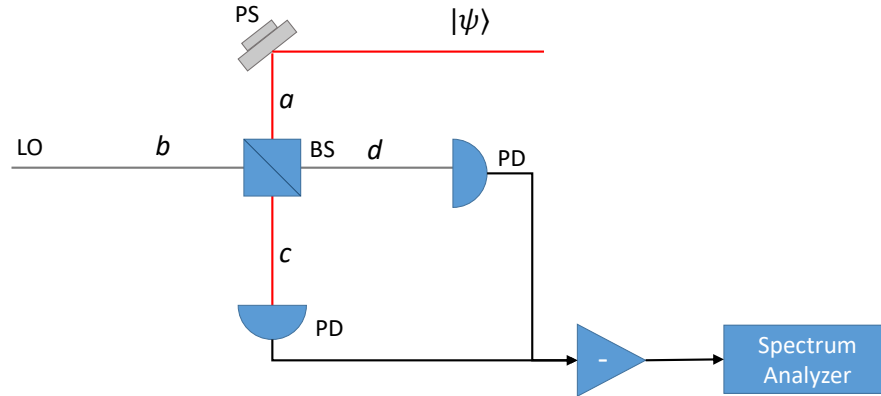
Figure 1.5: Scheme of an homodyne detection scheme. This measurement allows to experimentally measure the quadrature of the field, $\hat{X}_\theta$, from the difference of two photon currents. LO: local oscillator, PS: phase shifter, PD: photo-diode, BS: beam splitter.

BS with a state $|\beta\rangle$, named as local oscillator. The name *balanced* homodyne detection comes from using a balanced BS, while *homodyne* refers to the fact that both $|\psi\rangle$ and $|\beta\rangle$ have same frequency (otherwise the measurement is defined as heterodyne). The state $|\beta\rangle$ is assumed to be in a coherent state of adjustable phase θ, i.e. $|\beta\rangle = |\beta_0 e^{i\theta}\rangle$.

Referring to the BS quantum description presented in Sec. 1.1.1 we name $\hat{a}$ and $\hat{b}$ the

input ports and, according to Eq. 1.22, it follows:

$$\hat{c} = \frac{1}{\sqrt{2}}(\hat{a} + i\hat{b}) \tag{1.70}$$

$$\hat{d} = \frac{1}{\sqrt{2}}(\hat{b} + i\hat{a}) \tag{1.71}$$

Let us now consider the following quantity, combination of the output operators:

$$\hat{I}_- = k(\hat{c}^\dagger \hat{c} - \hat{d}^\dagger \hat{d}) =$$

$$= \frac{k}{2}(\hat{a}^\dagger \hat{a} + \hat{b}^\dagger \hat{b} + i\hat{a}^\dagger \hat{b} - \hat{b}^\dagger \hat{a} - \hat{b}^\dagger \hat{b} - \hat{a}^\dagger \hat{a} - i\hat{b}^\dagger \hat{a} - \hat{a}^\dagger \hat{b}) =$$

$$= ik(\hat{a}^\dagger \hat{b} - \hat{b}^\dagger \hat{a}), \tag{1.72}$$

where k is a proportionality factor, depending on the detectors properties. Since $|\beta\rangle$ is assumed to be in a strong coherent state, its quantum nature is negligible and we can write:

$$\hat{I}_- = ik(\beta_0 \hat{a}^\dagger e^{i\theta} - \beta_0 \hat{a} e^{-i\theta}) \tag{1.73}$$

In particular, for $\theta = -\pi/2$:

$$\hat{I}_- = \sqrt{2}k\beta_0 \frac{\hat{a}^\dagger + \hat{a}}{2} = \sqrt{2}k\beta_0 \hat{X} \tag{1.74}$$

while, for $\theta = 0$:

$$\hat{I}_- = -\sqrt{2}k\beta_0 \frac{\hat{a}^\dagger - \hat{a}}{\sqrt{2}i} = -\sqrt{2}k\beta_0 \hat{Y} \tag{1.75}$$

Eq.s 1.74-1.75 show that, measuring the output currents difference, $\langle \hat{I}_- \rangle$, allows to measure both $\langle \hat{X} \rangle$ and $\langle \hat{Y} \rangle$. More generally, by varying the local oscillator phase, any quadrature $\langle \hat{X}_\phi \rangle$ can be measured:

$$\hat{I}_- = \sqrt{2}k\beta_0 \frac{\hat{a}^\dagger e^{i\left(\theta + \frac{\pi}{2}\right)} + \hat{a} e^{-i\left(\theta + \frac{\pi}{2}\right)}}{\sqrt{2}} = \sqrt{2}k\beta_0 \hat{X}_\phi, \quad \phi = \theta + \frac{\pi}{2} \tag{1.76}$$

1.4   Thermal states

Thermal light is another relevant example of classical light since it describes the state of light associated to a black body radiation. Given a black-body at temperature T and a single radiation mode ω inside the cavity, the density operator associated to it can be written as:

$$\hat{\rho}_{th} = \sum_n^\infty P(n)|n\rangle\langle n| \tag{1.77}$$

where $P(n)$ is the probability of having n photons in the radiation mode considered. From statistical physics it is known that for a canonical ensemble the probability for a system at temperature T to have energy $E = E(n) = \hbar\omega\left(n + \frac{1}{2}\right)$ is:

$$P(n) \propto e^{-\frac{\hbar\omega\left(n+\frac{1}{2}\right)}{K_B T}} \tag{1.78}$$

where K_B is the Boltzmann constant and the proportionality coefficient can be obtained by imposing $\sum_n^\infty P(n) = 1$. Using this procedure it follows:

$$P(n) = e^{-\frac{n\hbar\omega}{K_B T}}\left(1 - e^{-\frac{\hbar\omega}{K_B T}}\right) \tag{1.79}$$

known as Bose-Einstein distribution. For the mean photon number in the mode it results:

$$\langle \hat{n} \rangle = \text{Tr}(\hat{\rho}_{th}\hat{n}) = \sum_{n=0}^\infty nP(n) = \frac{1}{e^{\hbar\omega/K_B T} - 1} \tag{1.80}$$

It is possible to rewrite Eq. 1.79 in terms of $\langle \hat{n} \rangle$ as:

$$P(n) = \frac{1}{\langle \hat{n} \rangle + 1}\left(\frac{\langle \hat{n} \rangle}{\langle \hat{n} \rangle + 1}\right)^n \tag{1.81}$$

and to calculate $\Delta^2 n$:

$$\Delta^2 n = \sum_{n=0}^\infty (n - \langle \hat{n} \rangle)^2 P(n) = \langle \hat{n} \rangle(1 + \langle \hat{n} \rangle) \tag{1.82}$$

Comparing Eq. 1.58 and Eq. 1.82 it emerges that, for the same average number of photons in the mode, a thermal state has larger photon number fluctuations than a coherent state. In particular, being $\Delta^2 n > \langle \hat{n} \rangle$ we refer to this statistics as a super-poissonian statistics.

Let us now consider the consequences of splitting a thermal beam, having mean photon number $\langle n \rangle$, on a BS of transmittance τ. According to Eq. 1.29 and using the result in Eq. 1.82, we have:

$$\langle \Delta \hat{n}_1 \Delta \hat{n}_2 \rangle = \tau(1 - \tau)\langle \hat{n} \rangle \tag{1.83}$$

where $\hat{n}_1$ and $\hat{n}_2$ are the number of photons in the two output modes. We conclude that the two output beams present correlation. This result is particularly relevant for the experimental application described in Ch. 4.

In the presence of losses, according to Sec. 1.1.2, a thermal state maintains the same statistical properties, simply rescaled by the channel efficiency η:

$$\Delta^2 \hat{N} = \eta^2 \langle \Delta^2 \hat{n} \rangle + \eta(1 - \eta)\langle \hat{n} \rangle = \eta^2 \langle \hat{n} \rangle + \eta^2 \langle \hat{n} \rangle^2 + \eta\langle \hat{n} \rangle - \eta^2 \langle \hat{n} \rangle = \tag{1.84}$$

$$= \eta\langle \hat{n} \rangle(1 + \eta\langle \hat{n} \rangle) = \langle \hat{N} \rangle(1 + \langle \hat{N} \rangle) \tag{1.85}$$

13

The black-body radiation is intrinsically multi-mode (i.e. M equally-populated radiation modes ω_M are present at the same time). Considering this fact, the variance on $\langle \hat{n} \rangle$ is:

$$\Delta^2 \hat{n} = \langle \hat{n} \rangle + \frac{\langle \hat{n} \rangle^2}{M} = \langle \hat{n} \rangle \left(1 + \frac{\langle \hat{n} \rangle}{M} \right) \tag{1.86}$$

It follows that, for number of photons per spatio-temporal mode, $\mu = \langle n \rangle / M$, sufficiently low, the thermal distribution converges to a poissonian distribution.

1.5   Classical vs non classical states

In Sec.s 1.3-1.4 we described the coherent and thermal states of light, referring to them as "classical" states. In this section we deeper discuss this point, and we formally introduce some parameters of non-classicality.

According to Eq. 1.68, every density matrix $\hat{\rho}$ can be written as combination of coherent states, opportunely weighted by the function $P(\alpha)$. This representation is usually known as P-representation of the state $\hat{\rho}$, and suggests that the state of the electromagnetic field can be regarded as a mixture of coherent states.

Being $\hat{\rho}$ hermitian, $P(\alpha)$ must be real. Moreover, from $\text{Tr}(\hat{\rho}) = 1$, it follows that $P(\alpha)$ must be normalized to unity, i.e. $\int P(\alpha)d\alpha = 1$. Both these properties are in accordance with the intuitive idea of $P(\alpha)$ as a probability function in the coherent states space. However, the interpretation of $P(\alpha)$ is more complicated in general. Firstly because coherent states are not orthogonal thus preventing the interpretation of probabilities of mutually exclusive states. Secondarily because there are no constraints that limit $P(\alpha)$ to have all the properties of a well defined probability density function.

According to [21], we define a classical state of light as a state for which $P(\alpha)$ is a true probability density function, in particular it must be:

- $0 \leq P(\alpha) \leq 1$

- $P(\alpha)$ not more singular than a delta function.

Since a coherent state $|\alpha\rangle$ is analogous to a classical field of complex amplitude α, if $P(\alpha)$ is a true probability density function, it follows that $\hat{\rho}$ in Eq. 1.68 corresponds to an ensemble of classical fields with probability density $P(\alpha)$. Such a state has therefore a "classical" analogous, exactly as it happens for coherent states.

There are states of light where $P(\alpha)$ assumes negative values, or is more singular than a delta function. For these states there is no classical analogous and they are referred as quantum states of light. In these cases the results obtained in the semi-classical theory of photodetection framework do not reproduce the experimental results, and a full quantum treatment is necessary.

For the states of light presented so far, we have:

- Coherent state. $\hat{\rho} = |\alpha'\rangle\langle\alpha'| = \int \delta^2(\alpha - \alpha')|\alpha\rangle\langle\alpha|\mathrm{d}^2\alpha$, where $P(\alpha)$ can be identified as $P(\alpha) = \delta^2(\alpha - \alpha')$. It is exactly a delta function, thus satisfying all the conditions for being a true probability density function.

- thermal light. For each mode of the field it holds: $P(\alpha) = \frac{1}{\pi\langle n\rangle}e^{-|\alpha|^2/\langle n\rangle}$, where $\langle n\rangle$ is the mean number of photons in the mode. This is a Gaussian distribution in the complex variable α, and is therefore a well defined density probability function.

- Fock state. $\hat{\rho} = |n\rangle\langle n| = \int P(\alpha)|\alpha\rangle\langle\alpha|\mathrm{d}^2\alpha$. It can be derived (see for example [21]) that $P(\alpha) = \frac{e^{|\alpha|^2}}{n!}\frac{\partial^{2n}}{\partial\alpha^{*n}\partial\alpha^n}\delta^2(\alpha)$. In this case $P(\alpha)$ is the 2n'th derivative of a delta function and therefore it is more singular than any classical probability density function. Fock states are purely quantum states, without any classical analogous. The only exception is for the vacuum state, $n = 0$, for which $P(\alpha) = \delta^2(\alpha)$. This is in agreement with the fact that the vacuum state can be seen as both a coherent state or a Fock state.

Using the P-representation and the coherent states definition in Eq. 1.53, we can write:

$$\langle(\hat{a}^\dagger)^m(\hat{a})^n\rangle = \mathrm{Tr}(\hat{\rho}(\hat{a}^\dagger)^m(\hat{a})^n) = \int P(\alpha)(\alpha^*)^m(\alpha)^n\mathrm{d}^2\alpha \tag{1.87}$$

For the variance of the photon numbers, this leads to:

$$\Delta^2 n = \langle\hat{n}\rangle + \int \mathrm{d}^2\alpha P(\alpha)(|\alpha|^2 - \langle|\alpha|^2\rangle)^2 \tag{1.88}$$

An interesting property emerges from Eq. 1.88: for classical states of light $P(\alpha)$ is positive and therefore $\Delta^2\hat{n} \geq \langle\hat{n}\rangle$. Therefore, classical states necessarily have a poissonian or super-poissonian photon statistics. On the contrary, quantum states of light have not this limitation, and $\Delta^2\hat{n}$ can go below $\langle\hat{n}\rangle$.

1.5.1 Fano Factor

A first parameter of non-classicality is the Fano factor. It is defined as [22]:

$$F = \frac{\Delta^2\hat{n}}{\langle n\rangle} \tag{1.89}$$

$F \geq 1$ for F classical states of light; coherent states saturate this limit. On the contrary, there are quantum states of light presenting $0 \leq F < 1$. Fock states have $F = 0$. As discussed in Sec. 1.1.2, photon statistics are degraded with losses. This produce a discrepancy between the Fano factor of the unperturbed state and the detected Fano factor. Using Eq.s 1.33-1.32 we obtain:

$$F_{det} = \frac{\Delta^2\hat{N}}{\langle\hat{N}\rangle} = \eta\frac{\Delta\hat{n}}{\langle\hat{n}\rangle} + 1 - \eta = \eta F + 1 - \eta \tag{1.90}$$

where $\hat{N}$ is the number of detected photons and η the efficiecy of the system. It follows that, in the presence of losses, the lower bound for the detected Fano factor is $F_{min} = 1 - \eta$.

1.5.2 Noise reduction factor

The analogous of the Fano Factor when considering bipartite states is named noise reduction factor (NRF), and it is defined as:

$$\sigma = \frac{\Delta^2(\hat{n}_1 - \hat{n}_2)}{\langle \hat{n}_1 + \hat{n}_2 \rangle} = \frac{\Delta^2 \hat{n}_1 + \Delta^2 \hat{n}_2 - 2\langle \Delta \hat{n}_1 \Delta \hat{n}_2 \rangle}{\langle \hat{n}_1 + \hat{n}_2 \rangle} \tag{1.91}$$

If two independent coherent states are considered, as the ones obtained splitting a coherent state on a balanced BS (Eq. 1.60), according to Eq. 1.58, it follows:

$$\sigma^{(coh)} = \frac{\langle \hat{n}_1 \rangle + \langle \hat{n}_2 \rangle}{\langle \hat{n}_1 + \hat{n}_2 \rangle} = 1 \tag{1.92}$$

This result can be generalized to any classical bipartite state. As a remarkable example, given a beam incident on a balanced BS and considering the two output beams, it results $\sigma = 1$, irrespective of the statistics of the incident beam. This result can be obtained simply considering Eq.s 1.25-1.29 for $\tau = 1/2$.

On the contrary, quantum states of light can present a higher level of correlation, leading to $0 \leq \sigma < 1$. As it will be discussed in Sec. 1.6.1, a particular bipartite quantum state, known as twin-beam state, leads to $\sigma = 0$.

Experimentally, losses are present and, similarly to what is discussed for the Fano Factor, degrade the value of σ experimentally measured. Using the results in Sec. 1.1.2, and assuming same efficiency in the two channels, i.e. $\eta_1 = \eta_2 = \eta$, we obtain:

$$\sigma_{det} = \frac{\Delta^2(N_1 - N_2)}{\langle N_1 + N_2 \rangle} =$$

$$= \frac{\eta^2(\Delta^2 n_1 + \Delta^2 n_2 - 2\langle \Delta n_1 \Delta n_2 \rangle) + \eta(1-\eta)\langle n_1 + n_2 \rangle}{\eta \langle n_1 + n_2 \rangle} = \eta\sigma + 1 - \eta \tag{1.93}$$

Therefore, the lower bound in the presence of losses is $\sigma_{det} = 1 - \eta$.

1.5.3 The shot-noise-limit

When restricted to classical states of light we are necessarily limited by the so called shot-noise. This noise emerges from the quantum nature of light and corresponds to the unavoidable fluctuation in the number of photons. In particular, in Eq. 1.88, we

demonstrate that classical states of light present poissonian or super-poissonian photon statistics, i.e. $\Delta^2 \hat{n} \geq \langle \hat{n} \rangle$. The best we can classically obtain is:

$$\frac{\Delta \hat{n}}{\langle \hat{n} \rangle} \geq \frac{1}{\sqrt{\langle \hat{n} \rangle}} \propto \frac{1}{\sqrt{P}} \tag{1.94}$$

where P is the optical power of the beam. We usually refer to this limit as shot-noise limit. Note that this source of noise becomes negligible in presence of high $\langle \hat{n} \rangle$, but can be dominant in the opposite regime.

There are relevant practical situations where it is not possible to arbitrarily increase $\langle \hat{n} \rangle$. This constraint can be due to several reasons, such as:

- Limitations inthe available optical output power.

- Detector damage threshold.

- Emergence of technical issues in the apparatus at increasing the optical power. This is for example the case of gravitational wave detectors. E.g. in [23] it is stated that, for a further increased laser power, thermally induced optical waveform distortion due to light absorption and the excitation of parasitic instabilities represent an issue difficult to deal with.

- Potential damage or alteration of the sample. This issue is particularly relevant while considering biological samples. For example in [24] it has been demonstrated that Escherichia coli and Listeria Bacteria are damaged by optical tweezers. In [8] and [25] the most common light-induced damages on cells are reviewed, and the use of the lowest possible optical dose is recommended.

However, the limit in Eq. 1.94 is not fundamental, in the sense that it is not imposed by quantum mechanics laws. In particular, it can be beaten if considering quantum states of light having sub-poissonian statistics, quadrature squeezing or quantum correlation. This idea is at the basis of the quantum enhanced optical measurements and, more in general, of quantum metrology. Aim of quantum metrology is to use quantum properties of nature to overcome the classical limits, thus leading to enhanced sensitivities. Interesting reviews on this topic can be found in [13, 14].

1.6 Sub Poissonian quantum states of light

In this section we introduce two quantum states of light that have been used in the experiments I worked on during my PhD. We do not report all the calculations, but we discuss the main results and properties. A more exhaustive description of these states can be found for example in [21, 26]. The two states considered are: the twin-beam state and the squeezed state.

1.6.1 Twin-beam state

The twin-beam state is a quantum state of light originated in the spontaneous parametric down conversion (SPDC) process. In this process an intense coherent beam pumps a non-linear crystal. In the interaction with the non linear optical medium, one photon of the pump beam (having frequency ω_p) can generate two photons of lower frequencies, ω_1 and ω_2. The probability of this process is very low ($\sim 10^{-9}$), but sufficient to observe down-converted photons with current technologies. In Fig. 1.6 a scheme of the SPDC process is reported. In this process both energy and momentum are conserved:
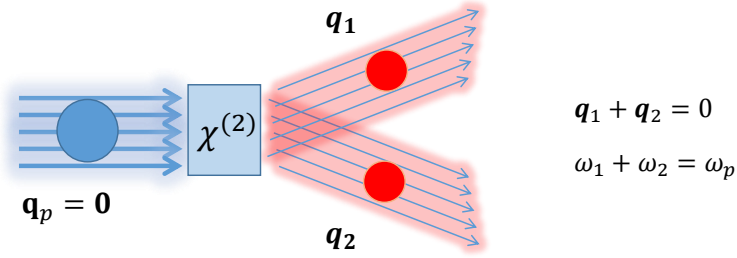
Figure 1.6: Scheme of the spontaneous parametric down conversion process (SPDC) inside a non-linear crystal. With a certain probability, one photon of the pump is down-converted into two photons, satisfying energy and momentum conservation. The state generated in this process is named twin-beam state and presents perfect number correlation between the two beams.

$$\omega_p = \omega_1 + \omega_2 \tag{1.95}$$

$$\mathbf{k}_p = \mathbf{k}_1 + \mathbf{k}_2 \tag{1.96}$$

where p refers to the pump photon, 1-2 to the two down-converted photons and $\mathbf{k}$ is the wave vector. It is useful to write ω_1 and ω_2 in terms of ω_p and Ω as:

$$\omega_1 = \frac{\omega_p}{2} + \Omega, \ \ \omega_2 = \frac{\omega_p}{2} - \Omega \tag{1.97}$$

The frequency $\omega_1 = \omega_2 = \frac{\omega_p}{2}$, corresponding to $\Omega = 0$, is named as degenerate frequency. It is useful to decompose $\mathbf{k}_p$ in the pump direction k_z and in the transverse component $\mathbf{q}$. For the transverse components it holds:

$$\mathbf{q}_p = 0 = \mathbf{q}_1 + \mathbf{q}_2 \tag{1.98}$$

thus leading to $\mathbf{q}_1 = -\mathbf{q}_2$. According to Eq.s 1.97-1.98, two conjugated photons can be identified by the modes $(\mathbf{q}, \Omega)$ and $(-\mathbf{q}, -\Omega)$.

The twin-beam state expression, while considering a single pair of conjugated modes $(\mathbf{q}, \Omega)$ and $(-\mathbf{q}, -\Omega)$, in the Fock basis, is:

$$|twb\rangle_{(\mathbf{q},\Omega),(-\mathbf{q},-\Omega)} = \sum_n c(n)|n\rangle_{\mathbf{q},\Omega}|n\rangle_{-\mathbf{q},-\Omega} \tag{1.99}$$

where $c(n)$ is a coefficient that, from the normalization condition, results $c(n) \propto \sqrt{\frac{1}{\langle n \rangle + 1} \left(\frac{\langle n \rangle}{\langle n \rangle + 1} \right)^n}$.

Extending this expression to the multi-mode situation, the multi-mode twb state can be written as:

$$|TWB\rangle = \otimes_{\mathbf{q},\Omega}|twb\rangle_{(\mathbf{q},\Omega),(-\mathbf{q},-\Omega)} \tag{1.100}$$

that is a tensor product of independent two modes twin-beam states. The coefficient $c(n)$ can be considered constant over the different modes. Being the modes independent, to describe the multi-mode twb properties it is sufficient to focus on the single mode case, i.e. fixing a specific $(\mathbf{q}, \Omega)$. A more exhaustive treatment of the multimode extension can be found in [27].

The twin-beam state can be obtained by letting the two mode vacuum state $|00\rangle_{a_1,a_2}$ evolving under the two modes squeezing operator $\hat{S}_{a_1,a_2}(\xi)$ (in Appendix A its derivation from the interaction hamiltonian is reported). Its expression assiming a plane wave pump is:

$$\hat{S}_{a_1,a_2}(\xi) = e^{\xi \hat{a}_1^\dagger \hat{a}_2^\dagger - \xi^* \hat{a}_1 \hat{a}_2}, \quad \xi = r e^{i\phi} \tag{1.101}$$

$$|twb\rangle_{a_1,a_2} = \hat{S}_{a_1,a_2}(\xi)|00\rangle_{a_1,a_2} \tag{1.102}$$

where, for the sake of simplicity, we name the two correlated modes as $\hat{a}_{\mathbf{q},\Omega} \to \hat{a}_1$ and $\hat{a}_{-\mathbf{q},-\Omega} \to \hat{a}_2$. In the following we will assume $\phi = 0$, thus $\xi = r$.

Photon statistics

From the twin-beam expression in Eq. 1.99, one of the main features of the this state immediately emerges: the two modes are entangled in the photon-number. This means that two correlated modes always have exactly the same number of photons.

The photon statistics of two correlated modes can be obtained considering the evolution of the operators $\hat{a}_i$ under the action of the operator $\hat{S}_{a_1,a_2}$. In the interaction picture the bosons operators evolve as:

$$\hat{b}_i = \hat{S}_{a_1,a_2}^\dagger \hat{a}_i \hat{S}_{a_1,a_2}, \quad i = 1,2 \tag{1.103}$$

To perform the calculation we exploit the following operator property:

$$e^{\hat{B}} \hat{A} e^{-\hat{B}} = \hat{A} + [\hat{B}, \hat{A}] + \frac{1}{2!}[\hat{B}, [\hat{B}, \hat{A}]] + \frac{1}{3!}[\hat{B}\hat{B}, [\hat{B}, \hat{A}]] + ... \tag{1.104}$$

The final expressions for the $\hat{b}_i$ operators are:

$$\hat{b}_1 = U_1 \hat{a}_1 + V_1 \hat{a}_2^\dagger \tag{1.105}$$

$$\hat{b}_2 = U_2 \hat{a}_2 + V_2 \hat{a}_1^\dagger \tag{1.106}$$

where:

$$U_1 = U_2 = \cosh(r) \tag{1.107}$$

$$V_1 = V_2 = \sinh(r) \tag{1.108}$$

From $\hat{b}_1$ and $\hat{b}_2$ it is possible to obtain the photon statistics of the twin-beam state. The normal ordered momenta of the photon statistics are:

$$\langle 00|(\hat{b}_i^\dagger)^m (\hat{b}_i)^m|00\rangle = m!\sinh^{2m}(r) \tag{1.109}$$

The momentum corresponding to $m = 1$, i.e. the mean photon number, is:

$$\langle \hat{n}_1 \rangle = \langle \hat{n}_2 \rangle = \sinh^2(r) \tag{1.110}$$

The momentum corresponding to $m = 2$ leads to the variance on the mean photon number:

$$\Delta^2 \hat{n}_1 = \langle : \hat{n}_1 \hat{n}_1 : \rangle - \langle \hat{n}_1 \rangle^2 + \langle \hat{n}_1 \rangle = 2\langle \hat{n}_1 \rangle^2 - \langle \hat{n}_1 \rangle^2 + \langle \hat{n}_1 \rangle = \tag{1.111}$$

$$= \langle \hat{n}_1 \rangle (1 + \langle \hat{n}_1 \rangle) = \Delta^2 \hat{n}_2 \tag{1.112}$$

where $\langle :\; : \rangle$ indicates the normally ordered product. Each mode of a twin-beam state, therefore, follows a thermal statistics (see Sec. 1.4). According to Eq. 1.86, if we consider M modes it follows:

$$\Delta^2 \hat{n}_1 = \langle \hat{n}_1 \rangle \left(1 + \frac{\langle \hat{n}_1 \rangle}{M} \right) \tag{1.113}$$

The covariance between the two correlated modes can be calculated. In particular,

$$\langle : \hat{n}_1 \hat{n}_2 : \rangle = \langle \hat{b}_1^\dagger \hat{b}_2^\dagger \hat{b}_1 \hat{b}_2 \rangle = 2\langle \hat{n}_1 \rangle^2 + \langle \hat{n}_1 \rangle \tag{1.114}$$

and

$$\langle \Delta \hat{n}_1 \Delta \hat{n}_2 \rangle = \langle : \hat{n}_1 \hat{n}_2 : \rangle - \langle \hat{n}_1 \rangle \langle \hat{n}_2 \rangle = \langle \hat{n}_1 \rangle (1 + \langle \hat{n}_1 \rangle) \tag{1.115}$$

Moreover, it can be demonstrated that:

$$\langle (\hat{n}_1 - \hat{n}_2)^M \rangle = 0, \quad \forall M \tag{1.116}$$

In Eq. 1.91 we define the noise reduction factor σ. Making use of the photon statistics reported in Eq. 1.115, let us now evaluate it for a twin-beam state:

$$\sigma^{twb} = \frac{\Delta^2 \hat{n}_1 + \Delta^2 \hat{n}_2 - 2\langle \Delta \hat{n}_1 \Delta \hat{n}_2 \rangle}{\langle \hat{n}_1 + \hat{n}_2 \rangle} = \tag{1.117}$$

$$= \frac{\langle \hat{n}_1 \rangle + \langle \hat{n}_1 \rangle^2 + \langle \hat{n}_1 \rangle + \langle \hat{n}_1 \rangle^2 - 2(\langle \hat{n}_1 \rangle^2 + \langle \hat{n}_1 \rangle)}{2\langle \hat{n}_1 \rangle} = 0 \tag{1.118}$$

Thus, in the ideal lossless case, two conjugated modes present perfect correlation in the photon number. As discussed in Sec. 1.5.2, $\sigma < 1$ is a signature for non classical correlations. We will provide examples of how to exploit the twin-beam non classicality in Ch.s 3-4-5.

Using the results presented in Sec.1.1.2, also the statistics of the detected photon number $\hat{N}_i$ can be obtained:

$$\langle \hat{N}_i \rangle = \eta_i \langle \hat{n}_i \rangle \tag{1.119}$$

$$\Delta^2 \hat{N}_i = \eta_i \langle \hat{n}_i \rangle (1 + \eta_i \langle \hat{n}_i \rangle) \tag{1.120}$$

$$\langle \Delta \hat{N}_1 \Delta \hat{N}_2 \rangle = \eta_1 \eta_2 \langle \hat{n}_1 \rangle (1 + \langle \hat{n}_1 \rangle) \tag{1.121}$$

Using these results, the detected noise reduction factor results:

$$\sigma_{det}^{twb} = \frac{\Delta^2 \hat{N}_1 + \Delta^2 \hat{N}_2 - 2\langle \Delta \hat{N}_1 \Delta \hat{N}_2 \rangle}{\langle \hat{N}_1 + \hat{N}_2 \rangle} = 1 - \bar{\eta} + \frac{(\eta_1 - \eta_2)^2}{2\bar{\eta}} \left(\langle n \rangle + \frac{1}{2} \right) \tag{1.122}$$

where $\bar{\eta} = (\eta_1 + \eta_2)/2$. For identical channel efficiencies $\eta_1 = \eta_2 = \eta$, Eq. 1.122 simplifies in:

$$\sigma_{det}^{twb} = 1 - \eta \tag{1.123}$$

Eq. 1.123 shows that, for balanced channels, the noise reduction factor always remains below the classical limit ($\sigma = 1$). This result shows that photon number correlations between the two modes are particularly robust to experimental imperfections. This feature paves the way for real applications. Otherwise, in the case of $\eta_1 \neq \eta_2$, there is an additional term (in Eq. 1.122) which comes from a non-perfect cancellation of the excess noise and which can lead to $\sigma_{det}^{twb} > 1$.

Eq.s 1.119-1.120-1.121 can be generalized to the multi-mode case (see [27] for more details) as:

$$\langle \hat{N}_i \rangle = M \eta_i \mu \tag{1.124}$$

$$\Delta^2 \hat{N}_i = M \eta_i \mu_i (1 + \eta_i \mu) \tag{1.125}$$

$$\langle \Delta \hat{N}_1 \Delta \hat{N}_2 \rangle = \eta_1 \eta_2 M \mu (1 + \mu) \tag{1.126}$$

where M is the number of spatio-temporal modes and μ is the mean number of photons per mode, i.e. $\langle \hat{n}_i \rangle = M\mu$.

Quadrature correlation

In the previous section we discussed the photon statistics of the twin-beam state, here we focus on its properties in terms of quadrature correlations between two conjugated modes. We can adopt the same approach, starting from the evolution of the

bosons operators under the two-mode squeezing operator $\hat{S}_{a_1,a_2}(\xi)$, see Eq. 1.105, and recalling the quadrature definition in Eq. 1.14. We obtain:

$$\hat{X}_{b_1} - \hat{X}_{b_2} = e^{-r}(\hat{X}_{a_1} - \hat{X}_{a_2}) \tag{1.127}$$

$$\hat{X}_{b_1} + \hat{X}_{b_2} = e^{r}(\hat{X}_{a_1} + \hat{X}_{a_2}) \tag{1.128}$$

and for the $\hat{Y}$:

$$\hat{Y}_{b_1} - \hat{Y}_{b_2} = e^{+r}(\hat{Y}_{a_1} - \hat{Y}_{a_2}) \tag{1.129}$$

$$\hat{Y}_{b_2} + \hat{Y}_{b_2} = e^{-r}(\hat{Y}_{a_1} + \hat{Y}_{a_2}) \tag{1.130}$$

where for example $\hat{X}_{b_1} = (\hat{b}_1 + \hat{b}_1^\dagger)/\sqrt{2}$. It is also possible to consider the variance on these quantities, in particular:

$$\Delta^2(\hat{X}_{b_1} \pm \hat{X}_{b_2}) = e^{\pm r}\Delta^2(\hat{X}_{a_1} \pm \hat{X}_{a_2}) \tag{1.131}$$

and for the $\hat{Y}$:

$$\Delta^2(\hat{Y}_{b_1} \pm \hat{Y}_{b_2}) = e^{\mp r}\Delta^2(\hat{Y}_{a_1} \pm \hat{Y}_{a_2}) \tag{1.132}$$

The variance on the difference of the amplitude quadrature is squeezed, this means that the two conjugated modes present amplitude quadrature correlation. This fact will be experimentally exploited in the experiment described in Ch. 5.

1.6.2   Single mode squeezed state

Single-mode vacuum squeezed state is obtained letting the coherent vacuum state $|0\rangle$ evolving under the operator $\hat{S}_a(\xi)$, named as single-mode squeezing operator:

$$|sq\rangle_a = \hat{S}_a(\xi)|0\rangle_a \tag{1.133}$$

$$\hat{S}_a(\xi) = e^{\xi^*\hat{a}^2/2 - \xi\hat{a}^{2\dagger}/2}, \quad \xi = re^{2i\phi} \tag{1.134}$$

In the following, we assume $\phi = 0$ so $\xi = r$ and we avoid to write the subscript a. r is usually referred as squeezing factor. The squeezed state expression in the Fock basis is:

$$|sq\rangle = \hat{S}(\xi)|0\rangle = \frac{1}{\cosh(r)} \sum_{n=0}^{\infty} (\tanh(r))^n \frac{\sqrt{(2n!)}}{n!2^n}|2n\rangle \tag{1.135}$$

Similarly to what done in the twin-beam case (see Eq. 1.103), it is useful to consider the action of $\hat{S}(\xi)$ on the annihilation and creation operators. It can be obtained [26]:

$$\hat{b} = \hat{S}^\dagger(\xi)\hat{a}\hat{S}(\xi) = \hat{a}\cosh(r) - \hat{a}^\dagger\sinh(r) = U\hat{a} + V\hat{a}^\dagger \tag{1.136}$$

$$\hat{b}^\dagger = \hat{S}^\dagger(\xi)\hat{a}^\dagger\hat{S}(\xi) = \hat{a}^\dagger\cosh(r) - \hat{a}\sinh(r) = U\hat{a}^\dagger + V\hat{a} \tag{1.137}$$

where $U = \cosh(r)$ and $U = \sinh(r)$.

Quadrature squeezing

From the relations in Eq.s 1.136-1.137 the evolution of the quadrature operators can be written as:

$$\hat{X}_b = \hat{S}^\dagger(r)\hat{X}_a\hat{S}(r) = \hat{X}_a e^{-r} \tag{1.138}$$

$$\hat{Y}_b = \hat{S}^\dagger(r)\hat{Y}_a\hat{S}(r) = \hat{Y}_a e^{r} \tag{1.139}$$

We can now derive some properties of the squeezed vacuum states, in particular the quadratures mean values and their associated variances. Instead of considering $\hat{X}$ and $\hat{Y}$ separately we consider the generalized quadrature defined in Eq. 1.14:

$$\langle \hat{X}_\theta \rangle = \langle 0|\frac{\hat{b}e^{-i\theta} + \hat{b}^\dagger e^{i\theta}}{\sqrt{2}}|0\rangle = \frac{\langle\hat{b}\rangle e^{-i\theta} + \langle\hat{b}^\dagger\rangle e^{i\theta}}{\sqrt{2}} = 0 \tag{1.140}$$

where the last equality follows from $\langle\hat{b}\rangle = U\langle\hat{a}\rangle + V\langle\hat{a}^\dagger\rangle = 0$, using Eq. 1.44. Similarly proceeding for $\langle\hat{X}_\theta^2\rangle$ we can write:

$$\langle \hat{X}_\theta^2 \rangle = \frac{1}{2}\langle 0|\hat{b}^2 e^{-2i\theta} + \hat{b}^{\dagger 2} e^{2i\theta} + \hat{b}\hat{b}^\dagger + \hat{b}^\dagger\hat{b}|0\rangle \tag{1.141}$$

$$\langle\hat{b}^2\rangle = \langle\hat{b}^{\dagger 2}\rangle = UV \quad \langle\hat{b}^\dagger\hat{b}\rangle = |V|^2 \tag{1.142}$$

Therefore, for a squeezed vacuum state, the variance on the generalized quadrature $\hat{X}_\theta$ is:

$$\langle \Delta^2 \hat{X}_\theta \rangle = \langle \hat{X}_\theta^2 \rangle = \frac{1}{2} + V(V + \sqrt{1+V^2}\cos(2\theta)) \tag{1.143}$$

Considering $\theta = 0$ and $\theta = \pi/2$, thus considering the amplitude and phase quadrature, it results:

$$\Delta\hat{X} = \frac{e^{-r}}{\sqrt{2}}, \quad \Delta\hat{Y} = \frac{e^{r}}{\sqrt{2}}, \tag{1.144}$$

Comparing this result with the one for coherent states, reported in Eq. 1.66, it emerges that for squeezed vacuum states the uncertainty in one quadrature is reduced below the coherent limit, at the expenses of the orthogonal one:

$$\Delta\hat{X}_{sq} = e^{-r}\Delta\hat{X}_{coh} \tag{1.145}$$

$$\Delta\hat{Y}_{sq} = e^{r}\Delta\hat{Y}_{coh} \tag{1.146}$$

Also for squeezed states the Heisenberg limit is saturated, $\Delta\hat{X}\Delta\hat{Y} = 1/2$. In Fig. 1.7 a vacuum squeezed state (green ellipse), is represented in the $(\hat{X}, \hat{Y})$ quadrature space. The coordinates of the center correspond to the quadratures mean values, i.e. $\langle\hat{X}\rangle = \langle\hat{Y}\rangle = 0$. The squeezing direction depend on ϕ, while the amount of squeezing depends on r.

A more general single-mode squeezed state can be obtained through the combined operation of the squeezing operator $\hat{S}(\xi)$ and the displacement operator $\hat{D}(\alpha)$ defined in Eq. 1.69:

$$|sq, \alpha\rangle = \hat{D}(\alpha)\hat{S}(\xi)|0\rangle \tag{1.147}$$
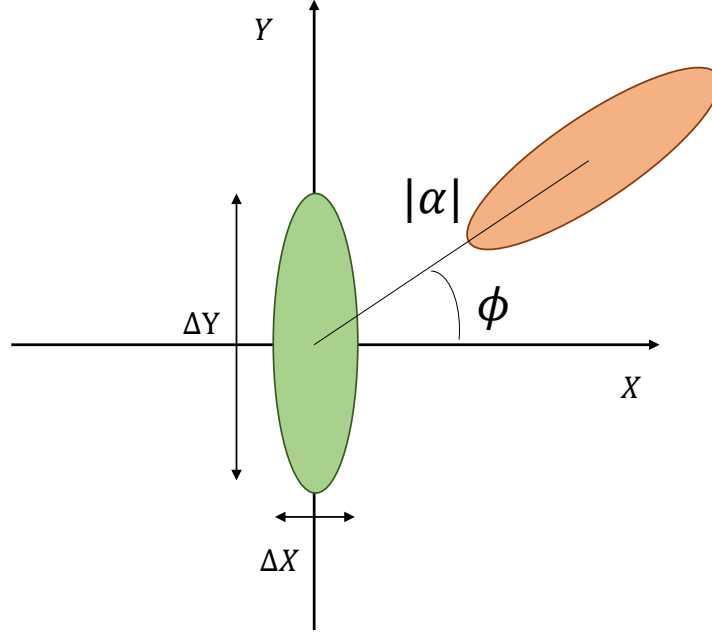
Figure 1.7: Squeezed states in the $(\hat{X}, \hat{Y})$ space. Green ellipse: squeezed vacuum state in the $\hat{X}$ quadrature ($\phi = 0$). Orange ellipse: displaced squeezed state in a generic $\hat{X}_\phi$ quadrature. The variance on one of the two quadrature is squeezed respect to the coherent case, while the conjugated one is anti-squeezed (compare with Fig. 1.4)

The evolution of $\hat{a}$ and $\hat{a}^\dagger$ in this case is ($\xi = r$ is assumed also in this case):

$$\hat{b} = \hat{S}^\dagger(\xi)\hat{D}^\dagger(\alpha)\hat{a}\hat{D}(\alpha)\hat{S}(\xi) = \hat{a}\cosh(r) + \hat{a}^\dagger\sinh(r) + \alpha \tag{1.148}$$

$$\hat{b}^\dagger = \hat{S}^\dagger(\xi)\hat{D}^\dagger(\alpha)\hat{a}^\dagger\hat{D}(\alpha)\hat{S}(\xi) = \hat{a}^\dagger\cosh(r) + \hat{a}\sinh(r) + \alpha^* \tag{1.149}$$

In this case, $\langle\hat{b}\rangle = \alpha \neq 0$, thus leading to:

$$\langle\hat{X}_\theta\rangle = \frac{\alpha e^{-i\theta} + \alpha^* e^{i\theta}}{\sqrt{2}} \tag{1.150}$$

The variance remains unchanged:

$$\langle\Delta^2\hat{X}_\theta\rangle = \langle\hat{X}_\theta^2\rangle = \frac{1}{2} + V(V + \sqrt{1 + V^2}\cos(2\theta)) \tag{1.151}$$

In Fig. 1.7 a displaced squeezed state (orange ellipse) is represented in the $(\hat{X}, \hat{Y})$ quadrature space. The coordinates of the center correspond to the quadratures mean values $(\text{Re}(\alpha), \text{Im}(\alpha))$.

Quadrature squeezing with losses

In the ideal situation of perfect detection efficiency a vacuum squeezed state presents variance on one quadrature below the classical limit, according to Eq.s 1.145-1.145. However, experimentally losses are always present, and their effect need to be taken into account. As described in Sec. 1.3.1, the quadrature is experimentally measured considering the difference of two independent currents (named as I_c and I_d in Eq.s 1.74-1.75). Using the results presented in Sec. 1.1.2, it follows ($\eta_c = \eta_d = \eta$):

$$\Delta^2 \hat{X}_{det} = \frac{1}{\sqrt{2}k\beta_0}(\Delta^2 N_c + \Delta^2 N_d) =$$

$$= \frac{1}{\sqrt{2}k\beta_0}(\eta^2\Delta^2 n_c + \eta(1-\eta)\langle n_c\rangle + \eta^2\Delta^2 n_d + \eta(1-\eta)\langle n_d\rangle) =$$

$$= \frac{1}{\sqrt{2}k\beta_0}(\eta^2\Delta^2\hat{X} + \eta(1-\eta)\langle n_c + n_d\rangle) \tag{1.152}$$

where $\Delta^2\hat{X}$ is the variance in presence of perfect detection efficiency. For an ideal coherent input state $|\alpha\rangle$:

$$\Delta^2\hat{X}_{coh} = \frac{1}{\sqrt{2}k\beta_0}(\Delta^2 n_c + \Delta^2 n_d) = \frac{1}{\sqrt{2}k\beta_0}(\langle n_c\rangle + \langle n_d\rangle) \tag{1.153}$$

The detected variance, normalized to the coherent case, is:

$$\frac{\Delta^2\hat{X}_{det}}{\Delta^2\hat{X}_{coh}} = \eta^2\frac{\Delta^2\hat{X}}{\Delta^2\hat{X}_{coh}} + \eta(1-\eta) \tag{1.154}$$

Considering a squeezed state it follows:

$$\frac{\Delta^2\hat{X}_{det,sq}}{\Delta^2\hat{X}_{coh}} = \eta^2\frac{\Delta^2\hat{X}_{sq}}{\Delta^2\hat{X}_{coh}} + \eta(1-\eta) = \eta^2 e^{-2r} + \eta(1-\eta) \tag{1.155}$$

and for the other quadrature:

$$\frac{\Delta^2\hat{Y}_{det,sq}}{\Delta^2\hat{Y}_{coh}} = \eta^2\frac{\Delta^2\hat{X}_{sq}}{\Delta^2\hat{Y}_{coh}} + \eta(1-\eta) = \eta^2 e^{2r} + \eta(1-\eta) \tag{1.156}$$

Photon statistics

Concerning the photon statistics, it holds [21]:

$$\langle\hat{n}\rangle = |\alpha|^2 + \sinh^2(r) \tag{1.157}$$

$$\Delta^2 n = |\alpha\cosh(r) - \alpha^* e^{2i\phi}\sinh(r)|^2 + 2\cosh^2(r)\sinh^2(r) \tag{1.158}$$

Commenting Eq.s 1.157-1.158 it can be observed that:

- For $\alpha = 0$, it follows $\langle\hat{n}\rangle \neq 0$. A vacuum squeezed state has a mean number of photons different from zero.

- The expression for $\Delta^2 \hat{n}$ is rather complicate, and can be higher or lower $\langle \hat{n} \rangle$ depending on ϕ. In particular, in correspondence of $\phi = 0$ it results $\Delta^2 n < \langle n \rangle$ (sub-poissonian statistics), while for $\phi = \pi/2$ it results $\Delta^2 n > \langle n \rangle$ (super-poissonian statistics).

Chapter 2

Experimental implementation of quantum states

In this chapter we discuss the experimental realization of some of the quantum states presented from the theoretical point of view in Ch. 1. The experimental set-ups are described in details, and some of the characterization measurements performed are reported. In particular we consider:

- Multi-mode twin beam state $|TWB\rangle = \otimes_{\mathbf{q},\Omega}|twb\rangle_{(\mathbf{q},\Omega),(-\mathbf{q},-\Omega)}$, theoretically described in Sec. 1.6.1 and experimentally used for the experiments in Ch.s 3-4.

- Squeezed vacuum state $|sq\rangle = \hat{S}(\xi)|0\rangle$, theoretically described in Sec. 1.6.2 and experimentally used for the experiment described in Ch. 5. The squeezer set-up has been provided by the U. L. Andersen quantum optics group at the Danish Technical Laboratories (DTU).

- Twin-beam like state, used in Ch. 5 as approximation of a real two mode twin-beam state.

2.1 Multi-mode twin-beam state

In Sec. 1.6.1 we present the twin-beam state from the theoretical point of view, arriving to the expression in Eq. 1.100:

$$|TWB\rangle = \otimes_{\mathbf{q},\Omega}|twb\rangle_{(\mathbf{q},\Omega),(-\mathbf{q},-\Omega)} = \otimes_{\mathbf{q},\Omega} \sum_{n=0}^{\infty} c(n)_{\mathbf{q},\Omega}|n\rangle_{\mathbf{q},\Omega}|n\rangle_{\text{-}\mathbf{q},-\Omega} \qquad (2.1)$$

In this section we describe how this multi-mode twin-beam state is produced in our laboratories, and we report some characterisation and preliminary measurements. In particular we focus on the non-classical intensity correlations between sets of conjugated modes, $(\mathbf{q}, \Omega)$ and $(-\mathbf{q}, -\Omega)$. We remind that $\mathbf{q}$ is the transverse momentum of the down-converted photon, while $\omega = \omega_{\text{pump}} \pm \Omega$ is its frequency.

2.1.1   Experimental set-up

In Fig. 2.1, we report the set-up used to produce the multi-mode twb state, and to detect the non-classical intensity correlations between its conjugated modes. The prin-
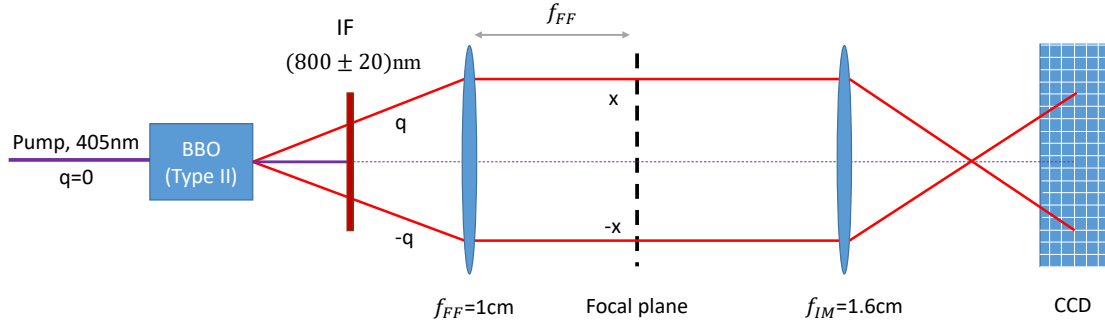

Figure 2.1: Scheme of the experimental set-up for multio-mode twin-beam generation and intensity correlation detection. In the Beta-Barium-Borate (BBO) crystal a photon of the pump (λ_{pump} = 405 nm) is converted into two photons, having opposite transverse momentum, **q** and -**q**. The interferential filter (IF) performs a spectral selection around the degenerate frequency, $\lambda_d = 2\lambda_{pump} = 810$ nm. In the far-field of the first lens, f_{FF}, the momentum correlation is converted into position correlation. The second lens, f_{IM}, images the focal plane to the CCD camera, with a magnification factor $M = 7.8$.

cipal elements of the system are:

- Laser source: a continuos wave laser-beam (OBIS405 Coherent) at $\lambda_p = 405$ nm, having maximum output power of 100 mW. The laser output is controlled by using an external digital signal coming from the camera. In particular, thanks to this synchronization, the laser emits only when the camera acquires. During the data storage time no light arrives at the detector, thus avoiding unwanted noise in the data.

- BBO crystal: it is a $(1cm)^3$ Type-II-Beta-Barium-Borate (BBO) non linear crystal. In this crystal the SPDC process occurs, converting one photon of the pump into two photons, satisfying energy and momentum conservation (see Eq.s 1.95-1.96).

- Interferential filter (IF) at (800±20)nm: it performs a spectral selection of the down-converted photons allowing only the photons around the degenerate frequency ($\lambda_d = 2\lambda_p = 810$ nm) to reach the detector.

- Far field lens: focal length $f_{FF} = 1$ cm. The far-field plane of the emission, where spatial correlation occurs, is realized in the focal plane of this lens.

- Imaging lens: focal length f_{IM} = 1.6 cm. Using this lens the far-field plane is imaged to the detection plane. In our case the magnification factor is M = 7.8.

- CCD camera: the detector is a charge-coupled-device (CCD) camera (Princeton Instrument Pixis 400BR Excelon), working in linear mode, with high quantum efficiency (nominally > 95% at 810 nm), 100% fill factor and low electronic noise, Δ_{el}. The detector is an array of 1024x1024 pixels, being the pixel size 13 μm. The pixels can be eventually grouped together into macro-pixels of user-settable size. The camera is mounted on a motorized stage, with resolution of about 1μm in order to precisely control its position. We typically work using an acquisition time of 50-100 ms and $10^3 - 10^4$ counts per pixel. Two digitization rates are possible: 100 kHz and 2 MHz. Note that a certain amount of time, usually named as readout time and mainly depending from the number of pixels considered, is necessary to store the data. The time required for each frame is therefore the sum of the acquisition time, the digitization time and the readout time.

2.1.2   Mode collection in the far field and coherence area estimation

In the far field of the crystal, realized in the focal plane of the first lens, any transverse mode $\mathbf{q}$ is associated with a position $\mathbf{x}$ according to the geometric transformation:

$$\mathbf{q} \rightarrow \frac{\omega}{2c f_{FF}} \mathbf{x}, \tag{2.2}$$

being c the speed of light and ω the frequency of the photon. From the momentum conservation law we know that, in the hypothesis of ideal pump having $\mathbf{q}_p = 0$, it holds:

$$\mathbf{q}_1 + \mathbf{q}_2 = 0 \tag{2.3}$$

Using the transformation presented in Eq. 2.2, in the far-field it holds:

$$\frac{\omega_1}{2c f_{FF}} \mathbf{x}_1 + \frac{\omega_2}{2c f_{FF}} \mathbf{x}_2 = 0 \tag{2.4}$$

Focusing around the degeneracy, i.e. $\omega_1 = \omega_2 = \omega_p/2$, the previous equation can be simplified as:

$$\mathbf{x}_1 + \mathbf{x}_2 = 0 \tag{2.5}$$

Therefore, conjugated photons at the degenerate frequency reach the camera in symmetric positions with respect to the pump intersection point ($\mathbf{x} = 0$). Experimentally the spectral selection is performed using interferential filters.

The perfect correlation in $\mathbf{x}$ holds only in the ideal situation of perfect plane wave pump. A more realistic Gaussian pump presents a spread $\Delta\mathbf{q}$, and Eq. 2.5 changes accordingly:

$$\mathbf{q}_1 + \mathbf{q}_2 = \Delta\mathbf{q} \rightarrow \mathbf{x}_1 + \mathbf{x}_2 = \Delta\mathbf{x} \tag{2.6}$$

where $\Delta\mathbf{x} = \frac{2cf_{FF}}{\omega_p}\Delta\mathbf{q}$ can be interpreted as the size of the area where, given a photon detected in position x_1, it is possible to find its conjugate around the position x_2. This area is named as coherence area, A_{coh}.

In Fig. 2.2 we report a typical image from the CCD camera. The frequencies of the detected photons are reported. If we limit to photons exactly at the degenerate frequency,
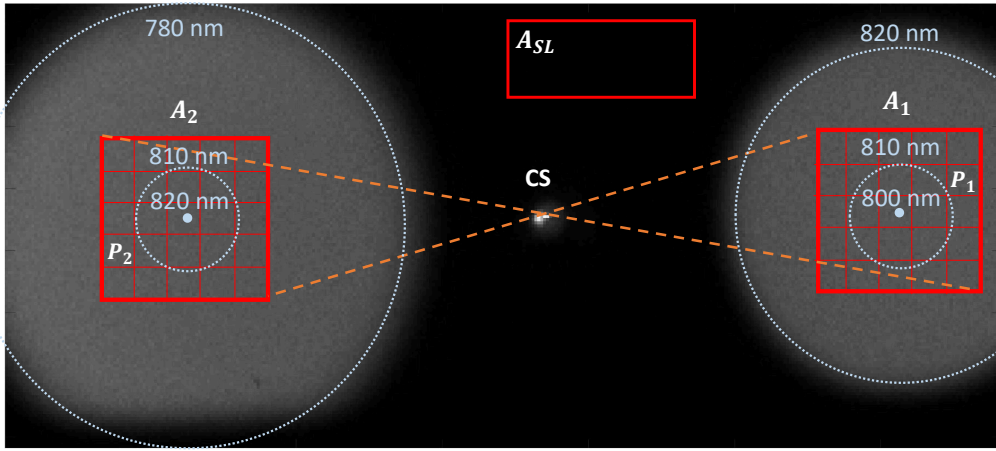
Figure 2.2: Example of a typical frame acquired at the CCD. The two areas of analysis, A_1 and A_2, are symmetric respect the center of symmetry *CS*. Each area is constituted by a certain number of pixels P_i, whose dimension can be set according to the experimental requirements. At full resolution the pixel size is 13μm. A_1 and A_2 are centered around the degenerate wavelength, $\lambda_d = 810$ nm. The interferential filter used transmits photons at (800 ± 20)nm. A_{SL} can be used to evaluate the stray-light photons.

λ_d nm (assuming it possible with real filters), we will see at the detector two circles (the dashed circles in correspondence of 810nm in the figure): this configuration could not allow to perform wide-field imaging, i.e. it would not be possible to image a sample occupying a finite area in one single frame. On the contrary, considering a certain bandwidth around the degenerate frequency (in our case 800 ± 20nm), wide-field imaging becomes possible. This situation corresponds to have the whole areas A_1 and A_2 enlighten, instead of having only the photons in correspondence of the 810nm circles. Note that for a small displacement from the degenerate frequency Eq. 2.6 remains, in first approximation, valid.

Experimentally, A_{coh} can be estimated considering the spatial cross-correlation between the two beams [28]:

$$C(\xi) = \sum_{\mathbf{x}} \frac{\langle \delta \hat{N}_1(\mathbf{x}) \delta \hat{N}_2(-\mathbf{x} + \xi) \rangle}{\sqrt{\langle [\delta \hat{N}_1(\mathbf{x})]^2 \rangle \langle [\delta \hat{N}_2(-\mathbf{x} + \xi)]^2 \rangle}} \qquad (2.7)$$

where $\xi = (\xi_1, \xi_2)$ is the shift respect to the ideal correlated pixel position and $\hat{N}_i(\mathbf{x})$ is the number of detected photons in the pixel in position $\mathbf{x}$.

An example of spatial cross correlation function corresponding to the typical working point of our experiment is reported in Fig. 2.3. There, the full resolution of the camera (physical pixel of 13 μm) is exploited. The peak corresponds to the position in which the regions are well correlated. Fitting the cross sections with a Gaussian function the coherence size can be estimated as the FWHM in the two directions ($2r_x$ and $2r_y$ respectively). Referring to the fits reported in Fig. 2.3, we obtain:

$$2r_x = (4.80 \pm 0.06)\text{pixels}$$
$$2r_y = (3.61 \pm 0.07)\text{pixels}$$

Which, at the focal plane, corresponds to:

$$2r_x = (8.0 \pm 0.1)\mu\text{m}$$
$$2r_y = (6.0 \pm 0.1)\mu\text{m}$$

2.1.3 Experimental noise reduction factor

As stated in Eq. 1.91, in ideal experimental conditions, for two correlated modes of a twin-beam state, we expect a null noise reduction factor, $\sigma = 0$. However, in Eq. 1.122 it is demonstrated that σ_{det} depends from the two channel efficiencies η_1 and η_2. In order to describe the experimental situation in the multi-mode case the model can be further generalized introducing the concept of collection efficiency, A. In Fig. 2.4 the quantities involved in the model are reported (further details can be found in [28]). Referring to this figure, P_1 and P_2 are two macro-pixels in the areas of analysis (see Fig. 2.2) and the circles correspond to the coherence area of the different modes of the field: each mode has its conjugate in the symmetric position respect to the center of symmetry. M_c is the number of modes in P_2 which are correlated to the modes collected in P_1, M_b is the number of modes on the border, M_u is the number of modes in P_2 that do not have a correlated mode in P_1.

The two efficiencies involved in the model can be defined as follows:

- Channel efficiency, η: the probability that a photon of the source is detected by the CCD.

- Collection efficiency, A: the probability that, given a photon in P_1, its conjugate falls in P_2, and not elsewhere.
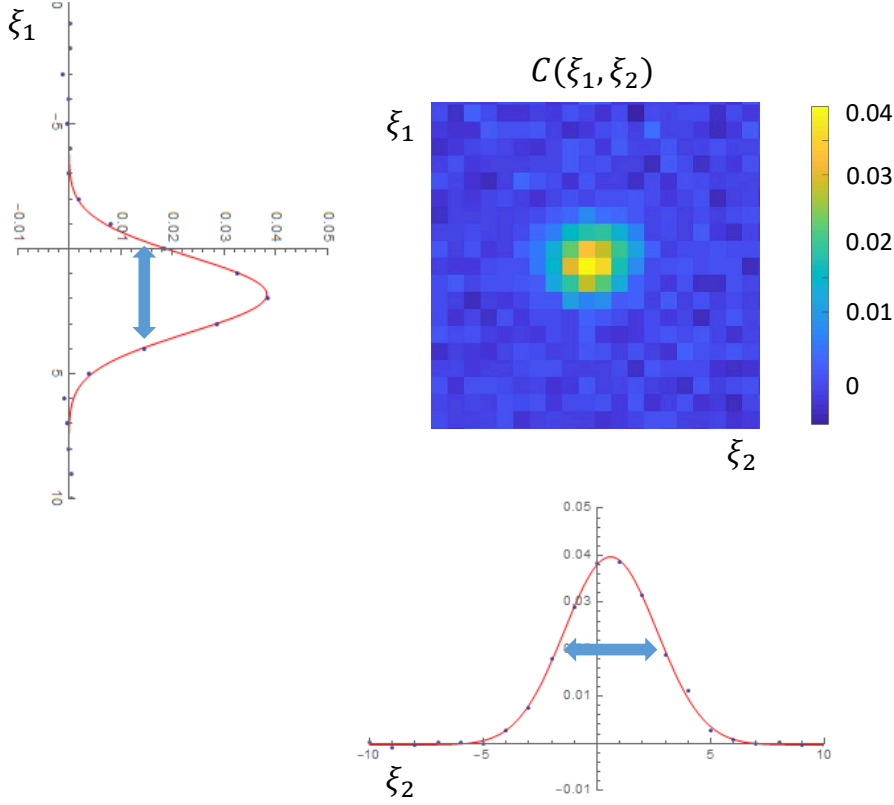
31

Figure 2.3: Spatial cross correlation function, evaluated according Eq. 2.7. We consider two regions, A_1 and A_2, of 40 x 40 pixels, chosen approximately in symmetric position at the detection plane. The full resolution of the camera is exploited (pixel size 13μm). The peak corresponds to the position in which the regions are well correlated pixel by pixel. The vertical and horizontal sections are shown in the two Cartesian plots and the data are fitted with a gaussian function. From the FWHM the size of the coherence area is estimated.

In real experiments A is not one, mainly for two reasons. On one side, some collected modes necessarily fall on the region border and therefore only a fraction of them can find its conjugate in the other region. On the other side, it is possible that there is a misalignment in the definition of the center of symmetry, which leads to collection of uncorrelated modes. The collection efficiency A can be written in terms of geometric quantities such as the dimensions of the macro-pixel L, the misalignment δ and the radius of the coherence area at the detection plane r as:

$$A = \frac{X(\pi\beta^2 - 2D(\mu + 1) - 2) + X^2 + 1}{X^2 + (\pi\beta - 2)X + 1}$$

(2.8)

where β is the fraction of M_b successfully collected, μ is the mean photon number per spatio-temporal mode, $X = L/2r$ is the ratio between the size of the macro-pixel and
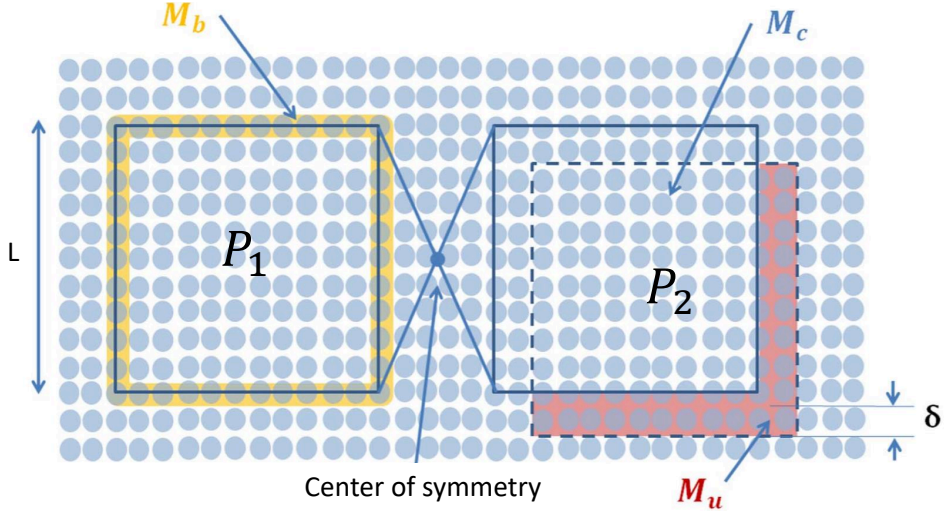
Figure 2.4: Model for the collection efficiency, A. L is the size of the macro-pixel considered. Given the macro-pixel P_1, in P_2 we collect M_c correlated modes, M_b border modes and M_u uncorrelated modes. δ is the misalignment of P_2 respect its ideal symmetric position.

the size of the coherence area, $D = \delta/2r$ is the ratio between the misalignment and the size of the coherence area. Experimentally, slightly moving the camera in the $x - y$ direction, it is possible to maximize A, i.e. to minimize the value of σ measured. It can be assumed that the experimental configuration where σ_{det} is minimum corresponds to $\delta \sim 0$. According to [27], it results that the collection efficiency behaves as an additional optical efficiency. In particular, for balanced channels, we have:

$$\sigma_{det} = 1 - \eta A \qquad (2.9)$$

Bigger is the size of the macro-pixel considered, lower is the effect of the modes on the border: in the limit $X \gg 1$, $A \sim 1$.

Trade-off between NRF and pixel size

Our CCD has physical pixels of $(13\mu m)^2$, but presents the option of hardware binning. Binning is the process of adding the data from adjacent pixels together to form a single pixel; hardware binning is performed on the CCD array before the signal is read out of the output amplifier, therefore the ratio between signal and readout noise is improved. Binning also reduces readout time and the burden on the computer memory, but at expenses of the resolution.

In order to detect a significant level of non-classical correlation the dimension of the macro-pixels considered must be comparable with, or larger than, the coherence area, $X \geq 1$. In Fig. 2.5, according to Eq. 2.9, σ_{det} in function of the pixel size L is reported. To

obtain this figure we set $\beta = 1/2$, a coherence radius at the detection plane of $r = 2.1$ pixels and a channel efficiency of $\eta = 0.76$. These values reproduce our experimental conditions. In the cases where the resolution is important, as in the experiment de-
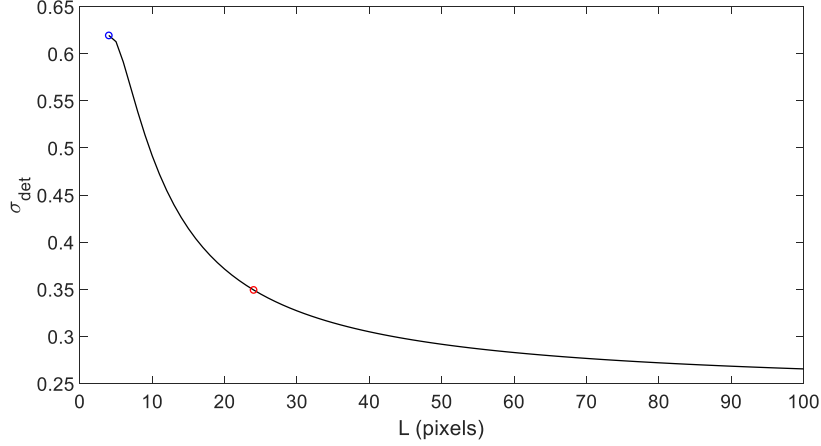

Figure 2.5: Detected noise reduction factor, σ_{det} in function of the macro-pixel size L. The curve is obtained replacing the expression of the collection efficiency A (Eq. 2.8) in Eq. 2.9. The values of the parameters used reproduce our experimental conditions: $\beta = 1/2$, $D \sim 0$, $r = 2.1$ pixels, $\eta = 0.76$. The red and the blue points correspond to the working point of the experiment described in 3 and Ch.s 4 respectively.

scribed in Ch. 4, we use the 3x3 hardware binning, roughly corresponding to the size of a spatial mode. This allows to match the highest resolution achievable in a ghost imaging experiment (exactly the coherence area) maintaining a still significant level of non classical correlation ($\sigma_{det} < 1$). This can be appreciated in Fig. 2.5, where the working point corresponding to the experiment described in Ch. 4 is reported in blue. In the cases where resolution is not the main concern, as in the experiment described in Ch. 3, an higher binning can be used (in our case 24x24) without any drawback. The working point corresponding to this situation is represented by the red point in Fig. 2.5.

Experimental procedure for NRF minimization

Experimentally it is fundamental to adjust the position of the different optical components in order to maximize the correlation level, thus minimizing the value of σ_{det}. For this purpose a "real time" σ estimation is performed using a Matlab program. Basically, a certain region A_1 of the CCD camera is fixed while the value of σ is evaluated at the varying of the position of A_2, in order to find the optimal one. A typical outcome of the program is reported in Fig. 2.6. Each pixel of the 2-D map reports the value of σ evaluated in correspondence of a specific position of A_2. The determination of the optimal
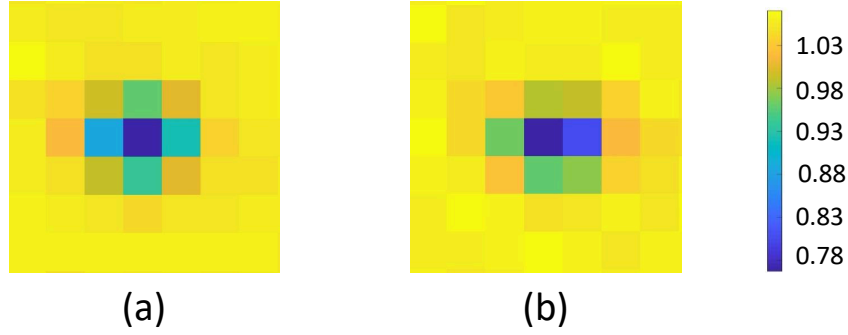
Figure 2.6: Output of the Matlab program used to test in real time the level of correlation achieved and to optimize the position of the detector. The 2-D map represents the noise-reduction factor, σ_{det}, at varying the center of symmetry around its optimal position. In (a) the figure obtained is symmetric. In (b) the figure obtained is not symmetric, this can be solved slightly moving the camera with sub-pixel movements.

position (the dip in Fig. 2.6), allows to calculate the center of symmetry (CS) of the correlation pattern. This CS is then used in the subsequent analysis. Note that it is possible to obtain figures of the kind in Fig. 2.6(b), where the correlation is shared between two pixels. To solve this problem sub-pixel micro-positioning of the camera can be used. As soon as the optimal value of σ is found, the sample is inserted and the acquisition launched. It is important that the experimental conditions remain constant during the acquisition. This is not straightforward since, for example for the experiment described in Ch. 4, the acquisition lasts several hours. In particular, drifts in temperature can have a detrimental effect in the alignment, thus lowering the experiment performances.

2.1.4   Raw data analysis

Before being used for the real analysis the data acquired by the CCD are preliminary processed. This preliminary process mainly consists into three steps:

- Background subtraction.

For technical reasons the baseline has been offset by adding a voltage to the signal to bring the output to a non-zero value, typically 500-600 counts. This ADC Offset is preset at the factory and is not user-changeable. However, this bias level is not noise and can be fully subtracted. In order to estimate the bias level, 100 frames with shutter closed are acquired in the same conditions of the real acquisition (in terms of acquisition time and digitization rate) and subsequently averaged. The resulting pattern is subtracted to the raw data. Moreover, from the same acquisition also the electronic noise, Δ_{el}, can be estimated. In linear mode (no electronic gain), at 100kHz digitization rate, it results $\Delta_{el} \sim 5$ counts$^-$/(pixel $\cdot$ frame), while at 2 MHz digitization rate, $\Delta_{el} \sim 13$ counts$^-$/(pixel $\cdot$ frame).

- Conversion from counts to electrons (e^-).

The output of the CCD is expressed in counts, to convert it into electrons we need to apply a conversion factor. In the typical working conditions of our experiments, this conversion factor is $g \sim 0.96$. The CCD gain calibration procedure is described in the following.

- Corrupted frames removal.

Some frames are corrupted by cosmic rays. Frames with cosmic rays present particularly bright pixels, as reported in Fig. 2.7. Frames where one pixel is above a certain threshold
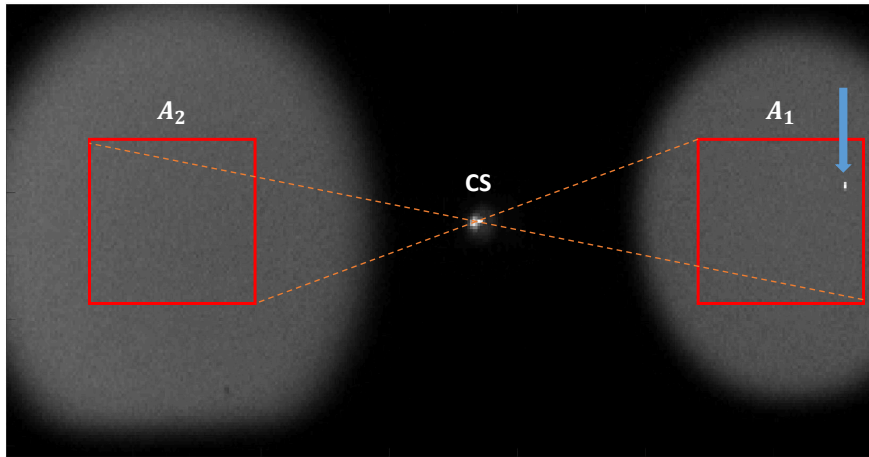
Figure 2.7: Example of frame acquired at the CCD presenting a cosmic ray in the region of interest (see blue arrow). Frames of this kind are removed.

are discarded. Percentage of discarded frames is usually $1 - 5\%$.

The remaining frames are ready for the analysis.

CCD gain calibration

In general, a CCD works converting photons into electrons, thanks to the photo-electric effect. The output of the CCD is expressed into units of counts. The conversion factor between the number of electrons and the number of counts is known as the CCD gain:

$$g = \frac{N_{e^-}}{N_c} \tag{2.10}$$

where N_{e^-} is the number of electrons and N_c is the number of corresponding counts. To experimentally evaluate the gain we can consider the variance on the mean number

of counts registered, $\Delta^2 N_c$. Here two contributions are present: the light photon noise, $\Delta^2 N_c^{pn}$, and the electronic noise of the CCD camera, $\Delta_{el,c}^2$. We can write:

$$\frac{\Delta^2 N_c}{\langle N_c \rangle} = \frac{\Delta^2 N_c^{pn} + \Delta_{el,c}^2}{\langle N_c \rangle} = \frac{\Delta^2 N_{e^-}^{pn} g}{g^2 \langle N_{e^-} \rangle} + \frac{\Delta_{el,c}^2}{\langle N_c \rangle} \tag{2.11}$$

Considering a coherent state, or, as in our case, a thermal state where the number of photons per spatio-temporal mode is sufficiently low, the photon statistics is poissonian (Eq. 1.58). In this limit we can approximate $\Delta^2 N_{e^-}/\langle N_{e^-} \rangle \sim 1$, thus obtaining:

$$\frac{\Delta^2 N_c}{\langle N_c \rangle} = \frac{1}{g} + \frac{\Delta_{el,c}^2}{\langle N_c \rangle} \tag{2.12}$$

and therefore:

$$\Delta^2 N_c = \frac{1}{g} \langle N_c \rangle + \Delta_{el,c}^2 \tag{2.13}$$

This equation suggests that evaluating $\mathrm{Var}(N_c)$ at varying the signal level $\langle N_c \rangle$ it is possible to extract the value of g fitting the data with a straight line and considering its slope.

In Fig. 2.8 the experimental data for g estimation are reported. We obtain each point acquiring 100 frames at the exposure time of 100 ms. $\Delta_{el,c}^2$ corresponds to the variance for no signal, and can be accurately estimated acquiring frames with the shutter closed. The value of g obtained from the fit is:
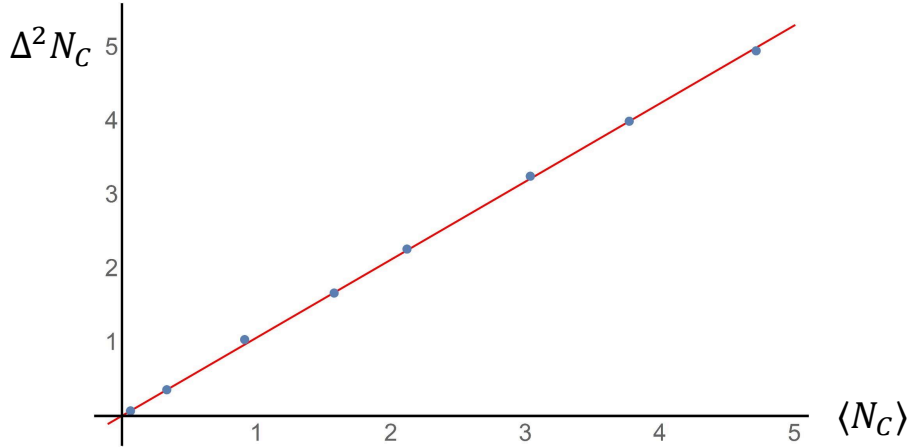

Figure 2.8: Linear fit for CCD gain estimation. The variance of the number of counts, $\mathrm{Var}(N_c)$, is evaluated at varying the signal level, $\langle N_c \rangle$. The data are fit with the model function in Eq. 2.13. The value of the gain obtained from the fit is $g = (0.9456 \pm 0.004)$.

$$g = (0.9456 \pm 0.004) \tag{2.14}$$

This is the value that will be used to convert the acquired data, expressed in counts, into photo-electrons units, according to Eq. 2.10.

2.1.5   Twin-beam for channel efficiency estimation

The experimental evaluation of σ and the model presented in Sec. 2.1.3 offer a method for evaluating the channel efficiencies, η_1 and η_2. This method is an extension of the Klyshko method [29] and is absolute, in the sense that it does not require the use of any calibrated devices. It is extensively discussed for example in [10]. Said A_1 and A_2 two conjugated regions, we introduce the quantity:

$$\gamma = \frac{\langle N_1 \rangle}{\langle N_2 \rangle} = \frac{\eta_1}{\eta_2} \tag{2.15}$$

where $\langle N_1 \rangle$ and $\langle N_2 \rangle$ are the mean number of photons detected in A_1 and A_2 respectively. This quantity, which represents the imbalance between the two channels, is proportional to the ratio of the two efficiencies η_1 and η_2. γ can be easily experimentally estimated and allows to balance the photon counts of the two channels. Accordingly, a new factor can be defined as:

$$\sigma_\gamma = \frac{\Delta^2(N_1 - \gamma N_2)}{\langle N_1 + \gamma N_2 \rangle} \tag{2.16}$$

In addition to losses, also the presence of spurious noise degrades the detected value of σ or σ_γ. In particular, there are two main sources of noise:

- Stray-light, $\langle N_{SL} \rangle$: it is due to fluorescence of the laser pump in the BBO crystal and in the interference filter. It can be estimated considering the mean number of photons detected per pixel in a "dark" region of the frame acquired, as A_{SL} in Fig. 2.2.

- Electronic noise, Δ^2_{el}: it can be estimated considering frames acquired with the shutter closed, where the only noise source is the electronic noise.

It is possible to take into account both these contributions, arriving to a corrected version of σ_γ [28]:

$$\sigma_{\gamma,B} = \sigma_\gamma \cdot \frac{\langle N_1 \rangle}{\langle N_1 - N_{SL} \rangle} - \frac{\Delta^2_{el} + \langle N_{SL} \rangle}{\langle N_1 - N_{SL} \rangle} \tag{2.17}$$

It turns out that $\sigma_{\gamma,B}$ can be written in terms of η_1 as:

$$\sigma_{\gamma,B} = \frac{1 + \gamma}{2} - \eta_1 A \tag{2.18}$$

being A the collection efficiency defined in Sec. 2.1.3. Inverting the expression in Eq. 2.18 and using the definition of γ, the two efficiencies can be estimated as:

$$\eta_1 = \frac{1 + \gamma}{2} - \sigma_{\gamma,B} A \tag{2.19}$$

$$\eta_2 = \frac{\eta_1}{\gamma} \tag{2.20}$$

In the experiments described in Ch.s 3 and 4 the efficiencies are estimated using this method, evaluating A according to the formula in Eq. 2.8, assuming $\beta = 1/2$ and $D \sim 0$. The uncertainty on the estimate is experimentally evaluated repeating the measurement several times and then considering the standard deviation of the values obtained.

2.2 Single mode squeezed state

The first signature of squeezed light was observed in 1985 by Slusher et al. [30], using the process of four-wave-mixing in an atomic vapor of sodium atoms (0.3 dB). Subsequently squeezing was generated exploiting other processes, as in the experiment realized by Wu et al. in 1986 [31], where the parametric down conversion process in a 2nd-order nonlinear crystal placed in an optical cavity was used. In this case a squeezing level of 3.5 dB was demonstrated, showing the potentialities of this technique. This type of configuration is known as Optical Parametric Oscillator (OPO) and seems to be the most efficient source of quadrature squeezed light. To date, squeezing factors of more than 10 dB have been directly observed in several experiments [32–34]. An interesting review about squeezed state production evolution can be found in [35].

In this section the two squeezer sources used for the experiment presented in Ch. 5 are briefly described. The realization of the two squeezer sources is not part of my PhD activity: both sources were provided by the Danish Technical University (DTU) laboratories. For using these sources the experiment was built in the danish laboratories and I spent 4 months there working at the set-up and acquiring data.

2.2.1 Experimental set-up

The squeezed light source is schematically depicted in Fig. 2.9; an exhaustive description of all the technical details can be found in [36]. It is based on parametric down-conversion process in a periodically poled potassium titanyl phosphate crystal (PPKTP) inside a cavity. In particulat, a semi-monolithic linear cavity, constituted by the edges of the crystal and a semi-transparent mirror of reflectivity 90%, is used. For locking the cavity length to the resonance, the cavity is seeded with 1064 nm light, opportunely phase modulated at a certain frequency (37.22MHz for the first squeezer and or 36.5MHz for the second one) by an electro-optical modulator (EOM). We refer to this beam as the control beam. The Pound-Drever-Hall (PDH) technique is used (see Appendix C) and the error signal is sent to a piezoelectric actuator (PZT) attached to the cavity mirror.

The same laser source used for producing the control beam also provides 532 nm radiation by an internal module for second harmonic generation. We refer to this beam as pump beam. In order to have a clean TEM_{00} mode the pump beam is sent trough
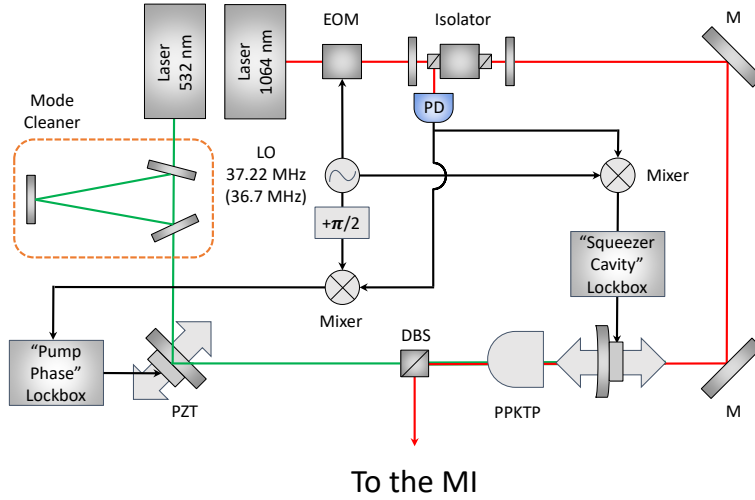
Figure 2.9: Schematic of the squeezed light source. PPKTP: potassium titanyl phosphate crystal. DBS: dichroic beam splitter. PZT: piezoelectric actuators. EOM: electro-optical modulator. LO: local oscillator. PD: photo-diode.

a mode-cleaner: a resonant mode cleaner cavity, consisting in tree high reflective mirrors, is used. Its working principle is based on the fact that the resonant frequencies of higher-order modes are different from the resonant frequency of the fundamental TEM_{00} mode, see [36] for all the details. After the mode cleaner the beam is directed to the locked cavity, where the parametric down conversion process takes place. To establish a phase-match condition between the pump and the control beam, the crystals temperature is actively stabilised. According to [37], the phase relation between pump and control beam determines the orientation of the squeezing ellipse and therefore needs to be locked appropriately. In particular, if we lock to the bright fringe i.e to the amplification, results in phase squeezing while if we lock it to the dark fringe, i.e. to the deamplification, results in amplitude squeezing. The error signal for locking to the amplitude squeezing is sent to a PZT actuator mounted on a mirror on the pump path. Finally, a dichroic beam splitter (DBS) is used at the output of the squeezer to separate the 1064 nm component from the unwanted 532 nm one. The output of the squeezer consists in a displaced squeezed state with displacement provided by the control beam. The squeezed state generated is very sensitive to losses, therefore high reflective mirrors ($R \sim 99\%$) need to be used.

The control beam perfectly spatially overlaps the generated squeezed light, therefore it is useful for alignment and mode-matching optimization.

2.2.2 Characterisation measurements

To detect the squeezing level of the state produced, we perform an homodyne measurement, according to Sec. 1.3.1. A scheme of this measurement is reported in Fig. 1.5: the squeezed beam and the local oscillator (LO) are interfered on a BS. The phase is periodically varied by a phase shifter and the subtracted output is sent to a spectrum analyzer. This approach offers to measure the quadratures of the field, thus allowing to estimate the noise reduction in the squeezing case. The output of the spectrum analyzer, at 13.5MHz, is presented in Fig. 2.10. The blue line refers to the coherent case, where the squeezed beam is blocked and the measurement is performed with only the LO. The green curve refers to the squeezed case. Both curves are normalized to the coherent case. It emerges that for certain *t*, corresponding to certain phases between
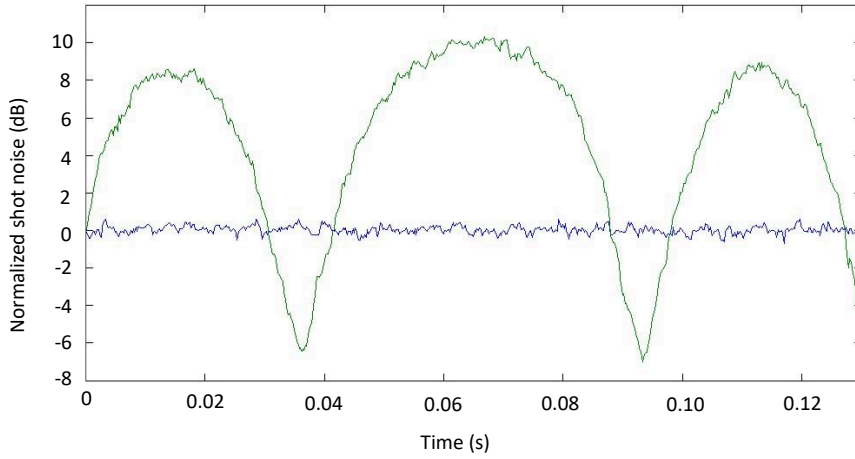
Figure 2.10: Squeezing level produced by the system in Fig. 2.9, detected via an homodyne measurement. The normalized amplitude, expressed in dB, is plotted in function of time (i.e. phase shift between the local oscillator and the field). The blue line corresponds to the classical case, while the green line corresponds to squeezing injection. A detected squeezing level of 6.5 dB is demonstrated.

the squeezed beam and the LO, the noise on the quadrature is below the coherent case (we refer to the minimum value as squeezing level), while for other phases the noise is higher (we refer to the maximum value as anti-squeezing level). In the ideal case of perfect efficiency we expect the squeezing and anti-squeezing level to be equal, i.e. $V_{sq}^{dB} = -V_{anti-sq}^{dB}$. However, in real experiments losses produce an imbalance between the two. In particular, in our case we have:

$$V_{sq}^{dB} = 10\log\frac{\Delta^2 X_{sq}}{\Delta^2 X_{coh}} = -6.5 \text{ dB} \tag{2.21}$$

41

$$V_{anti-sq}^{dB} = 10\log\frac{\Delta^2 Y_{sq}}{\Delta^2 Y_{coh}} = 10 \text{ dB} \tag{2.22}$$

From these values it is possible to estimate the squeezing level at the source, and the efficiency of the system. According to Eq.s 1.155-1.156, it holds:

$$V_{sq} = \eta V + (1 - \eta) \tag{2.23}$$

$$V_{anti-sq} = \eta/V + (1 - \eta) \tag{2.24}$$

where V is the amount of squeezing produced by the squeezer, and η includes both transmission efficiency (η_t) and mode-matching between the squeezed beam and the LO (η_m). Solving the system having independently estimated $\eta_m = 0.99$, we obtain:

$$V^{dB} = 10.6 \text{ dB} \tag{2.25}$$

$$\eta_t = 0.85 \tag{2.26}$$

We conclude that our source produces a squeezed state of around 10.6 dB, however, losses induced by optical components and mode-matching necessarily decrease the squeezing level. The results obtained for the second squeezer are totally analogous and therefore are not reported.

2.3 Approximate Twin-beam state

If two single-mode squeezed states presenting squeezing in orthogonal quadratures are overlapped on a symmetric BS ($\tau = 0.5$), a twin-beam state is produced. In particular, the output state presents squeezing in the amplitude quadrature difference, according to what presented in Sec. 1.6.1. This result can be obtained considering the beam splitter transformations in Eq. 1.21 and the definition of quadrature in Eq. 1.10, as described in [26]. A scheme of this technique is reported in Fig. 2.11(a). Referring to this figure, and recalling the properties of squeezed states presented in Sec. 1.6.2, we can write :

$$X_{b_1'} = e^{-r}X_{a_1'}, \ Y_{b_1'} = e^{r}Y_{a_1'}, \tag{2.27}$$

$$X_{b_2'} = e^{r}X_{a_2'}, \ Y_{b_2'} = e^{-r}Y_{a_2'} \tag{2.28}$$

$$b_1 = \frac{1}{\sqrt{2}}(b_1' - b_2'), \ b_2 = \frac{1}{\sqrt{2}}(b_1' + b_2') \tag{2.29}$$

For convenience the vacuum modes in a_1' and a_2' can be considered as originated by two other vacuum modes, a_1 and a_2, incident on a symmetric BS:

$$a_1' = \frac{1}{\sqrt{2}}(a_1 + a_2), \ a_2' = \frac{1}{\sqrt{2}}(a_2 - a_1) \tag{2.30}$$
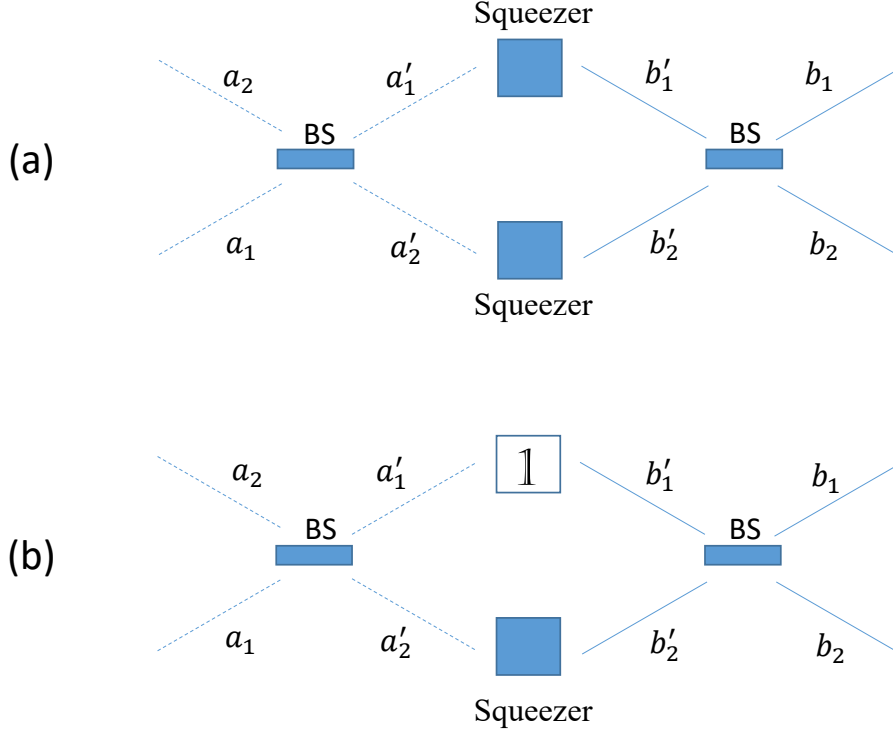
Figure 2.11: (a) Scheme showing how a twin-beam state can be obtained from the interference of two single mode squeezed states at a BS. (b) If a vacuum state and a single mode squeezed state interfere on a BS the output state presents, if limiting to one of the two quadratures, the same properties of a twin-beam state. Dashed lines show a fictitious beam splitter transformation of a pair of vacuum states. See Sec. 2.3 for all the details.

For the quadratures of the output modes it follows:

$$X_{b_1} = \frac{b_1 + b_1^\dagger}{2} = \frac{1}{\sqrt{2}} \frac{b_1' - b_2' + b_1'^\dagger - b_2'^\dagger}{\sqrt{2}} = \frac{1}{\sqrt{2}}(X_{b_1'} - X_{b_2'}) =$$

$$= \frac{1}{\sqrt{2}}(e^{-r}X_{a_1'} - e^{r}X_{a_2'}) \tag{2.31}$$

and similarly for the other mode:

$$X_{b_2} = \frac{1}{\sqrt{2}}(e^{-r}X_{a_1'} + e^{r}X_{a_2'}) \tag{2.32}$$

Considering the sum and the difference between the quadratures of the output states and writing the result in terms of a_1 and a_2, for the X quadrature it is obtained:

$$X_{b_1} - X_{b_2} = e^{-r}(X_{a_1} - X_{a_2}) \text{ and } X_{b_1} + X_{b_2} = e^{r}(X_{a_1} + X_{a_2}) \tag{2.33}$$

and for the Y:

$$Y_{b_1} - Y_{b_2} = e^r(Y_{a_1} - Y_{a_2}) \text{ and } Y_{b_1} + Y_{b_2} = e^{-r}(Y_{a_1} + Y_{a_2}) \tag{2.34}$$

As we wanted to demonstrate, we obtain exactly the same results presented in Eq.s 1.127-1.128-1.129-1.130 for a twin-beam state.

Let us now consider the situation presented in Fig. 2.11(b), where one of the squeezer is replaced with an identity operator. This case experimentally corresponds to split a single-mode squeezed state at a balanced BS. The same approach used to obtain Eq. 2.33 can be adopted, simply substituting the expressions in 2.27 with:

$$X_{b_1'} = X_{a_1'} \text{ and } Y_{b_1'} = Y_{a_1'} \tag{2.35}$$

The final results for the difference of the two quadrature are:

$$X_{b_1} - X_{b_2} = e^{-r}(X_{a_1} - X_{a_2}) \tag{2.36}$$

$$Y_{b_1} - Y_{b_2} = e^r(Y_{a_1} - Y_{a_2}), \tag{2.37}$$

While for the sum:

$$X_{b_1} + X_{b_2} = X_{a_1} + X_{a_2} \tag{2.38}$$

$$Y_{b_1} + Y_{b_2} = Y_{a_1} + Y_{a_2}, \tag{2.39}$$

We can conclude that the output state presents squeezing in the difference of the X quadrature, exactly as a real twin-beam state. On the contrary, considering the sum of the quadratures it behaves classically. It presents exactly the same twin-beam properties when focusing on the opportune quantity (i.e. amplitude quadrature difference), in this sense this state can be considered as a twin beam state approximation. For the sake of simplicity, in order to demonstrate the equivalence we are interested in, we chose the argument above, however it can be made more rigorous using the approach of local operators presented in [**takahashi10**].

2.3.1 Experimental set-up

In the experiment described in Ch. 5 a twin-beam like state, obtained using the approximate method described in the previous paragraph is used. Experimentally its implementation is straightforward: it is sufficient to send a squeezed beam to a symmetric BS, and to consider the two output modes. The squeezed beam is generated using one of the squeezers described in Sec. 2.2.1. A scheme of the set-up for twin-beam like state generation is presented in Fig. 2.12.
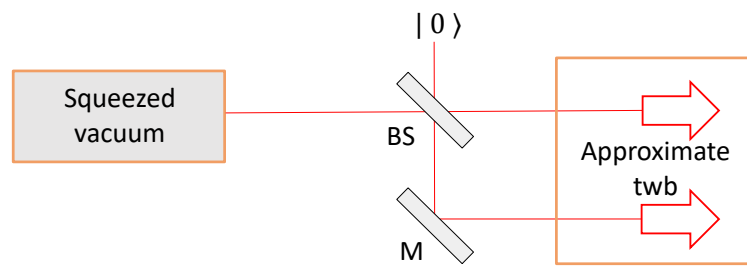
Figure 2.12: Schematic of the experimental set-up used to produce a twin-beam like state. This state is obtained splitting a squeezed vacuum state on a balanced BS.

45

Chapter 3

Quantum enhanced absorption measurement

In this chapter a first application of quantum states of light for quantum enhanced measurements is presented. In particular it is demonstrated how using the stronger than classical correlations in twin beam states it is possible to increase the sensitivity in absorption estimation measurements beyond the classical limits. After a brief introduction to estimation theory, the absorption estimation problem is faced both theoretically, in Sec.s 3.2-3.3.1, and experimentally, in Sec. 3.5. Different estimation strategies are compared, discussing the role of experimental imperfections, such as detector noise and not unitary channel efficiency, as well as their relation with the ultimate quantum limit, i.e. the ultimate limit allowed by quantum mechanics laws. The theoretical model is experimentally validated and a quantum enhancement of (1.51 ± 0.02), compared to the best classical strategy for same probe intensity and channel efficiency, is demonstrated. These results have been published in [17] in 2017, representing at that time, to our knowledge, the best quantum enhancement ever obtained in absorption estimation.

3.1   Basic elements of estimation theory

Often it is not possible to directly access a quantity of interest, i.e. estimating its value through a direct measurement. In these cases indirect measurements are the only option available. Aim of an indirect measurement is to infer the value of the quantity of interest from its influence on a given probe. At the same time it is important to keep the uncertainty associated to the estimate as low as possible. Solving a parameter estimation problem means looking for a measurement scheme, (i.e. probe, quantity measured, estimator), able to estimate the parameter of interest, with the smaller uncertainty. In this paragraph we briefly review some elements of the parameter estimation theory, in particular focusing on one of its main results: the Cramer-Rao inequality, which sets a lower bound on the variance of any estimator in terms of the Fisher information.

Moreover, the quantum version of the Cramer-Rao inequality, written in terms of the quantum Fisher information is discussed.

To formalize the concepts introduced so far, let us consider the scenario schematically depicted in Fig. 3.1: N independent measurements are performed on N copies of
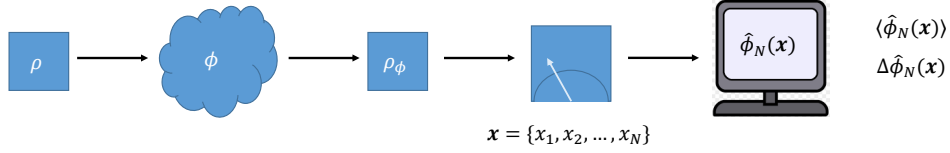

Figure 3.1: Scheme describing the key elements of estimation theory. A probe state ρ interacts with the sample under investigation, described by the parameter ϕ. In the interaction the initial state evolves in ρ_ϕ. N measurements are performed on ρ_ϕ, giving as output $\mathbf{x} = \{x_1, ..., x_N\}$. An unbiased estimator $\tilde{\phi}(\mathbf{x})$ allows to estimate the parameter of interest ϕ. An important feature for an estimator is its associated variance, $\langle \Delta^2 \tilde{\phi}_N \rangle$, which should be kept as low as possible.

the probe system ρ and we are given the N results, $\mathbf{x} = \{x_1, x_2, ..., x_N\}$. For the sake of simplicity we assume the support of x_i to be real numbers. Each x_i is the realization of a random variable X_i, distributed according to a probability density function (PDF), $p_\phi(X)$, equal for all i. The PDF depends from ϕ, which is the parameter we want to determine. Here we assume the N results being independent of each other. Under this assumption $p_\phi(\mathbf{x}) = p_\phi(x_1) \cdot ... \cdot p_\phi(x_N)$. However, the formalism is valid for an arbitrary joint-probability distribution.

Our aim is to find an estimator $\tilde{\phi}_N(\mathbf{x})$ that, opportunely elaborating $\mathbf{x}$, gives an accurate estimate of the parameter ϕ. Note that $\tilde{\phi}_N(\mathbf{x})$ is function of random data thus being a random variable itself: it is important to reduce its fluctuations as much as possible. The approach used here, usually referred as frequentist or Fisher information approach, assumes that ϕ is a deterministic variable with an unknown value that could be stated to any precision, at least in principle. Given an estimator $\tilde{\phi}_N(\mathbf{x})$ its performances can be evaluated considering:

- Mean value, $\langle \tilde{\phi}_N \rangle = \int p_\phi(\mathbf{x}) \, \tilde{\phi}_N(\mathbf{x}) \mathrm{d}^N \mathbf{x}$. If $\langle \tilde{\phi}_N \rangle = \phi$, the estimator is said unbiased.

- Variance, $\langle \Delta^2 \tilde{\phi}_N \rangle = \langle (\tilde{\phi}_N(\mathbf{x}) - \phi)^2 \rangle = \int p_\phi(\mathbf{x})(\tilde{\phi}_N(\mathbf{x}) - \phi)^2 \mathrm{d}^N \mathbf{x}$. The estimator with smaller variance should be preferred.

For an unbiased estimator, $\langle \Delta^2 \tilde{\phi}_N \rangle$ cannot be reduced arbitrarily, on the contrary a lower

bound can be fixed. Let us consider the following chain of equalities (see [38]):

$$1 = \frac{\partial}{\partial \phi} \langle \tilde{\phi}_N \rangle = \int d^N \mathbf{x} \frac{\partial}{\partial \phi} p_\phi(\mathbf{x}) \tilde{\phi}_N(\mathbf{x}) = \int d^N \mathbf{x} p_\phi(\mathbf{x}) \left(\frac{\partial}{\partial \phi} \ln p_\phi(\mathbf{x}) \right) \tilde{\phi}_N(\mathbf{x}) =$$

$$= \int d^N \mathbf{x} p_\phi(\mathbf{x}) \left(\frac{\partial}{\partial \phi} \ln p_\phi(\mathbf{x}) \right) (\tilde{\phi}_N(\mathbf{x}) - \phi) = \langle \frac{\partial \ln p_\phi}{\partial \phi} \cdot (\tilde{\phi}_N(\mathbf{x}) - \phi) \rangle \qquad (3.1)$$

where in the step before the last one it is exploited the fact that $\phi(\partial/\partial_\phi)\langle 1 \rangle = 0$. The last expression can be interpreted as the scalar product between the quantities $\partial \ln p_\phi / \partial \phi$ and $(\tilde{\phi}_N(\mathbf{x}) - \phi)$. The (classical) Cramer-Rao bound can be obtained simply applying the Cauchy-Schwarz inequality to this scalar product. In particular:

$$1 = \langle \frac{\partial \ln p_\phi}{\partial \phi} \cdot (\tilde{\phi}_N(\mathbf{x}) - \phi) \rangle^2 \leq \langle \left(\frac{\partial \ln p_\phi}{\partial \phi} \right)^2 \rangle \langle (\tilde{\phi}_N(\mathbf{x}) - \phi)^2 \rangle \qquad (3.2)$$

Thus it follows:

$$\langle \Delta^2 \tilde{\phi}_N \rangle \geq \frac{1}{F_\phi^{(N)}} \qquad (3.3)$$

where $F_\phi^{(N)}$ is the (classical) Fisher information, defined as:

$$F_\phi^{(N)} = \int d^N \mathbf{x} p_\phi(\mathbf{x}) \left(\frac{\partial \ln p_\phi(\mathbf{x})}{\partial \phi} \right)^2 = \int d^N \mathbf{x} \frac{1}{p_\phi(\mathbf{x})} \left(\frac{\partial p_\phi(\mathbf{x})}{\partial \phi} \right)^2 \qquad (3.4)$$

The Fisher information is a measure of distinguishability: the higher the Fisher information the easier we can distinguish between p_ϕ and a $p_{\phi+\delta\phi}$ From Eq. 3.4 it emerges that the Fisher information is additive, therefore, for independent and identically distributed samples $F_\phi^{(N)} = N F_\phi^{(1)}$. In general the Fisher information is a function of ϕ, therefore, depending on the true value of the parameter, the Cramer-Rao bound puts weaker or stronger constraints on the minimal variance attainable. Moreover, it can be shown that, for independently drawn and identically distributed samples, it always exists an estimator, called maximum-likelihood (ML) estimator, which for an infinitely large sample (i.e. $N \to \infty$) saturates the bound. The ML estimator is formally defined as:

$$\tilde{\phi}_N^{ML}(\mathbf{x}) = \text{argmax}_\phi p_\phi(\mathbf{x}) \qquad (3.5)$$

It is the function that, for a given $\mathbf{x}$, gives the value of ϕ for which that data sample is the most probable. For finite N the ML estimator is biased, but becomes unbiased asymptotically.

These results (for a deeper discussion see for example [38, 39]) can be extended to the quantum domain. According to quantum mechanics, the state of a system can be described with a density matrix $\hat{\rho}$, with $\text{Tr}(\hat{\rho}) = 1$. After the interaction with the sample,

whose properties are encoded in ϕ, $\hat{\rho}$ will depends on ϕ, assumed here as a classical parameter. We indicate the density matrix after the interaction with the sample as $\hat{\rho}_\phi$. The scenario is analogous to the one presented for the classical case: we measure some observable $\hat{\mathbf{x}}$ of the system $\hat{\rho}_\phi$, whose statistics depends on ϕ. Then, starting from the data measured, we want to estimate ϕ with the highest possible precision. In the quantum framework, measurements can be described by the POVM operators, which generalize the projective von Neumann measurements. They are a set of positive operators M_x obeying the completeness relation $\int M_x dx = 1$. x labels the possible measurement outcomes, also here we assume real x. Given a state $\hat{\rho}_\phi$, a POVM generates a probability distribution:

$$p_\phi(x) = \text{Tr}(\hat{\rho}_\phi \hat{M}_x) \tag{3.6}$$

Using this relation it is possible to extend the classical estimation theory to the quantum framework, mapping the problem of estimating a parameter of a quantum state to the problem of parameter estimation previously described. In particular, replacing 3.6 into the Fisher information definition in Eq. 3.4 for $N = 1$, we have:

$$F_\phi^{(1)} = \int \left[\frac{1}{\text{Tr}(\hat{\rho}_\phi \hat{M}_x)} \left(\text{Tr}\left(\frac{\partial \hat{\rho}_\phi}{\partial \phi} \hat{M}_x \right) \right)^2 \right] dx =$$

$$= \int \left[\frac{1}{\text{Tr}(\hat{\rho}_\phi \hat{M}_x)} \left(\text{Tr}\left(\frac{1}{2}(\hat{\rho}_\phi L_{\rho_\phi} + L_{\rho_\phi} \hat{\rho}_\phi) \hat{M}_x \right) \right)^2 \right] dx \tag{3.7}$$

where L_{ρ_ϕ}, in analogy with the classical logarithmic derivative $\partial \ln p_\phi / \partial \phi$, is called symmetric logarithmic derivative and is implicitly defined as:

$$\frac{\partial \hat{\rho}_\phi}{\partial \phi} = \frac{1}{2}(\hat{\rho}_\phi L_{\rho_\phi} + L_{\rho_\phi} \hat{\rho}_\phi) \tag{3.8}$$

As highlighted in [38], compared to the classical case, in the quantum mechanical setting there is the additional freedom of choosing a suitable measurement $\hat{M}_x$ in order to obtain a distribution $p_\phi(x)$ that contains as much information as possible on the parameter ϕ. Varying the set of $\hat{M}_x$, F_ϕ varies accordingly. The quantum Fisher information is defined as:

$$QF_\phi = \max_{\{\hat{M}_x\}} F_\phi(\hat{M}_x) \tag{3.9}$$

In particular, it holds:

$$F_\phi \leq QF_\phi = \text{Tr}(\rho_\phi L_{\rho_\phi}^2) \tag{3.10}$$

Note that QF_ϕ only depends on ρ_ϕ, thus not referring to one particular measurement strategy or estimator, but including all the possibilities. As the classical Fisher information, also the quantum Fisher information is additive when calculated on product states, in particular it holds $QF_\phi[\rho_\phi^{\otimes N}] = N \cdot QF_\phi[\rho_\phi]$. The inequality in Eq. 3.10 can be

saturated with a POVM consisting in the projectors onto L_{ρ_ϕ} eigenstates. Replacing the result of Eq. 3.10 in Eq. 3.3, the so called quantum Cramer-Rao bound is obtained:

$$\langle \Delta^2 \tilde{\phi}_N \rangle \geq \frac{1}{QF_\phi^{(\otimes N)}} = \frac{1}{N \cdot QF_\phi} \tag{3.11}$$

where the last equality holds when N uncorrelated sub-systems are considered. The quantum Cramer-Rao bound establishes the ultimate sensitivity in estimating a parameter ϕ, being already optimized for all possible estimators and all possible measurements (POVM). Moreover, it can be always saturated in the limit of infinite measurements ($N \to \infty$) and choice of the optimal POVM (consisting of projectors onto the eigenstates of L_{ρ_ϕ}) [38, 39].

In practice, once an explicit estimator $\tilde{\phi}$ is demonstrated to saturate the quantum Cramer-Rao bound we are sure that it is not possible to further increase the measurement sensitivity.

3.2 Ultimate quantum limit vs classical limit in absorption measurement

Using the estimation theory tools presented in Sec. 3.1 it is possible to derive the ultimate quantum limit achievable in the estimation of a generic parameter ϕ. In this section we focus on absorption coefficient estimation, presenting the ultimate quantum limit in this context. Moreover, the limit achievable while limited to classical resources is discussed.

Several theoretical works have been devoted to understand the ultimate quantum limit in estimating an absorption coefficient. Depending on the point of view, an absorption from the environment can be considered as a loss, therefore various works refer to the absorption estimation problem as to the loss estimation problem. We will use the two expressions as equivalent. In [40, 41], the ultimate quantum limit for gaussian states is obtained, while in [42] the discussion is extended to non Gaussian states.

Formally, gaussian states are defined as states having a gaussian Wigner function [21], and include coherent states, thermal light and squeezed light. Among the non gaussian states we will focus on Fock states.

In order to present how the quantum estimation theory can be used in practice, the procedure followed by Monras and Paris in [40] is reviewed in the following:

- The evolution of a state $\hat{\rho}$ in a lossy channel, characterized by the loss parameter ζ, is given by $\hat{\rho}_\zeta = E_\zeta(\hat{\rho})$, being E_ζ an opportune map associated to the system evolution. The evolution is described by the Lindblad master equation:

$$\dot{\hat{\rho}} = \frac{\zeta}{2} \mathscr{L}[\hat{a}]\hat{\rho}, \tag{3.12}$$

where $\mathscr{L}[\hat{a}]\hat{\rho} = 2\hat{a}^\dagger \hat{rho}\hat{a} - \hat{a}^\dagger \hat{a}\hat{\rho} - \rho\hat{a}^\dagger \hat{a}$.

- The probe state is constrained to have finite mean energy: $\mathrm{Tr}(\hat{\rho}\hat{a}^\dagger \hat{a}) = \bar{n}$

- Any gaussian state of a single bosonic mode may be represented as a thermal state $\hat{\rho}_\mu$ under the action of a squeezing and displacement operation: $\hat{\rho} = \hat{D}(\beta)\hat{S}(\xi)\hat{\rho}_\mu \hat{S}^\dagger(\xi)\hat{D}^\dagger(\beta)$. This allows to consider all the gaussian states at once, eventually considering specific limits at the end.

- The aim is to find the gaussian state $\hat{\rho}$ which is mapped in $\hat{\rho}_\zeta$ with the highest QF_ζ. It can be demonstrated that it is sufficient to limit the research to pure states: $\hat{\rho} = \hat{D}(\beta)\hat{S}(\xi)|0\rangle\langle 0|\hat{S}^\dagger(\xi)\hat{D}^\dagger(\beta)$, with $\beta = se^{i\theta}$ and $\xi = re^{-2i\phi}$.

- The optimization problem can be reduced to the determination of two parameters: the ratio of squeezing energy to total energy $y = \sinh^2 r/\bar{n}$ and the displacement phase θ.

- The evolution of the state parameters under the action of the channel is explicitly evaluated, as well as the symmetric logarithmic derivative L_ζ.

- From L_ζ, QF_ζ can be computed according to Eq. 3.10. It is an expression in terms of the state parameters y, θ and the loss parameter ζ.

- The last step consists in optimizing QF_ζ thus obtaining the ultimate quantum limit. Its explicit expression results:

$$\langle \Delta^2 \phi_{uql} \rangle = \frac{1}{4\bar{n}N} \tag{3.13}$$

where $\bar{n}$ is the average number of photons in the probe, N is the number of repetition of the measurement, and ϕ is connected to ζ by the parameterization $e^{-\zeta t} = \cos^2 \phi$.

A measurement strategy (probe state $\hat{\rho}$ and estimator $\tilde{\phi}$) leading to $\langle \Delta^2 \tilde{\phi} \rangle = \langle \Delta^2 \phi_{uql} \rangle$ is said optimal. It is also found that an optimal measurement can be implemented through photon counting. This result is particularly important in view of real experimental applications. Moreover, it is concluded that, for low losses and low probe energy, the squeezed vacuum state is an optimal probe. It is also demonstrated that this is the ultimate limit also having access to the environment degrees of freedom.

Considering $y = 0$, i.e. null ratio between the squeezing energy and the total energy, means considering the coherent case. In this case maximizing the QF_ζ leads to:

$$\langle \Delta^2 \phi_{coh} \rangle = \frac{(1 + \tan^2 \phi)}{4\bar{n}N\tan^2 \phi} \tag{3.14}$$

This represents the best sensitivity that can be obtained when restricted to classical resources. It is evident that using quantum states of light, as squeezed states, allows to increase the sensitivity respect to the coherent case, in particular for small values of ϕ.

In [42], the ultimate limit in absorption estimation for non gaussian states is considered. Also in this case the approach of the quantum information theory is followed and the same $\Delta\phi_{uql}$ of Eq. 3.13 is found. It is demonstrated that Fock states saturate $\Delta\phi_{uql}$ unconditionally for any value of the loss. Moreover, the measurement strategy identified requires only photon counting. This is an interesting result, both from the theoretical side and in view of real applications. The saturation of the ultimate quantum limit with gaussian states holds only asymptotically, and in the nonphysical limits of infinitesimal or infinite loss. In the realistic regime of intermediate loss the Gaussian based estimation remains always sub-optimal. In order to investigate the sample with less than one photon, also superposition of Fock states, $|\psi^{(k)}\rangle = \sum_{n=0}^{k} c_n|n\rangle$, are considered. It emerges that, numerically optimizing the complex weights c_n for $\bar{n}$ and ϕ, it is possible to surpass the performances offered by gaussian states, asymptotically attaining the ultimate quantum limit for $k \to \infty$.

In the following we use a different parameterization, connected to the previous one by the relation:

$$\alpha = \sin^2(\phi) = 1 - e^{-\zeta t} \tag{3.15}$$

We refer to the parameter α as to the absorption coefficient. It is convenient to rewrite the theoretical limits presented so far in terms of α. Let us consider:

$$\langle\Delta^2\alpha\rangle = \frac{\langle\Delta^2\phi\rangle}{|\partial\phi/\partial\alpha|^2} = \frac{1}{4\bar{n}N}(2\sin\phi\cos\phi)^2 = \frac{\alpha(1-\alpha)}{\bar{n}N} \tag{3.16}$$

Thus, the ultimate quantum limit can be written as:

$$U_{uql} = \sqrt{\frac{\alpha(1-\alpha)}{\bar{n}N}} \tag{3.17}$$

While the limit in the presence of only classical resources, in Eq. 3.14, becomes:

$$\Delta\alpha_{coh} = \sqrt{\frac{1-\alpha}{\bar{n}N}} \tag{3.18}$$

In both [40, 42] the optimality of various probe states is analyzed, respectively within the single-mode gaussian states and non-gaussian states, while the possibility of entangled probes is not considered. This issue is discussed in [43], where also the possibility of a twin-beam state as a probe is taken into account. It is demonstrated that using twin-beam states for loss estimation the ultimate quantum limit remains the U_{uql} reported in Eq. 3.17 and is in principle attainable.

3.3   Possible absorption estimators

In Sec. 3.2 the ultimate quantum limit for α estimation and the limit if restricted to classical resources are identified (see Eq. 3.17-3.18). Moreover, in [43], the possibility of attaining the UQL using a twin-beam state is demonstrated. However, the existence of an experimental estimator, as well as its explicit expression, does not emerge from the theoretical analysis.

In this section we adopt an operative approach: we consider different specific estimators (S_α,S'_α,S''_α) and we discuss their performances at varying the probe state. Both classical and quantum probe states are considered, in order to demonstrate how quantum resources can enhance the sensitivity beyond the classical limits. It will be shown how the twin-beam state allows to attain the UQL, for all energy regimes and all values of the loss parameter α.

In view of real applications, the role of experimental imperfections is of the utmost importance and therefore it is extensively discussed. In particular, the performances of the estimators at varying the channel efficiency is considered.

3.3.1 S_α

A simple measurement strategy to estimate a loss α, firstly analyzed by Jakeman and Rarity in [44], consists in evaluating the ratio between the photon number measured after the lossy interaction, N'_P, with a reference value, N_R, representing the number of photons which would have been detected in absence of the sample. N_R can be evaluated in a previous moment, before placing the absorbing sample, or using a second beam. We refer to these strategies as single-mode and two-mode respectively. Referring to Fig. 3.2, this estimator is defined as:

$$S_\alpha = 1 - \gamma \frac{N'_P}{N_R} \tag{3.19}$$

where $\gamma = \langle N_R \rangle / \langle N_P \rangle$ is a factor which compensates for possible imbalance between the probe and reference beams. Using a two mode strategy, γ can be easily evaluated with a calibration measurement, i.e. a measurement without the sample (Fig.3.2(c)). On the contrary, using a pure single-mode strategy there is no way for evaluating γ, and the stability of the reference beam (i.e. $\gamma = 1$) needs to be assumed for having an unbiased estimator. As it will be discussed deeper in the following, this represents one of the main drawbacks of single-mode strategies.

In Sec. 1.1.2 we discuss how losses affect the photon statistics. This argument can be applied in this context, to model the effect of the probe interaction with the lossy sample. In particular, using Eq.s 1.32-1.33 and the Fano Factor definition in Eq. 1.90, it follows:

$$\langle N'_P \rangle = (1-\alpha)\langle N_P \rangle \tag{3.20}$$

$$\langle \Delta^2 N'_P \rangle = [(1-\alpha)^2(F_P - 1) + 1 - \alpha]\langle N_P \rangle \tag{3.21}$$
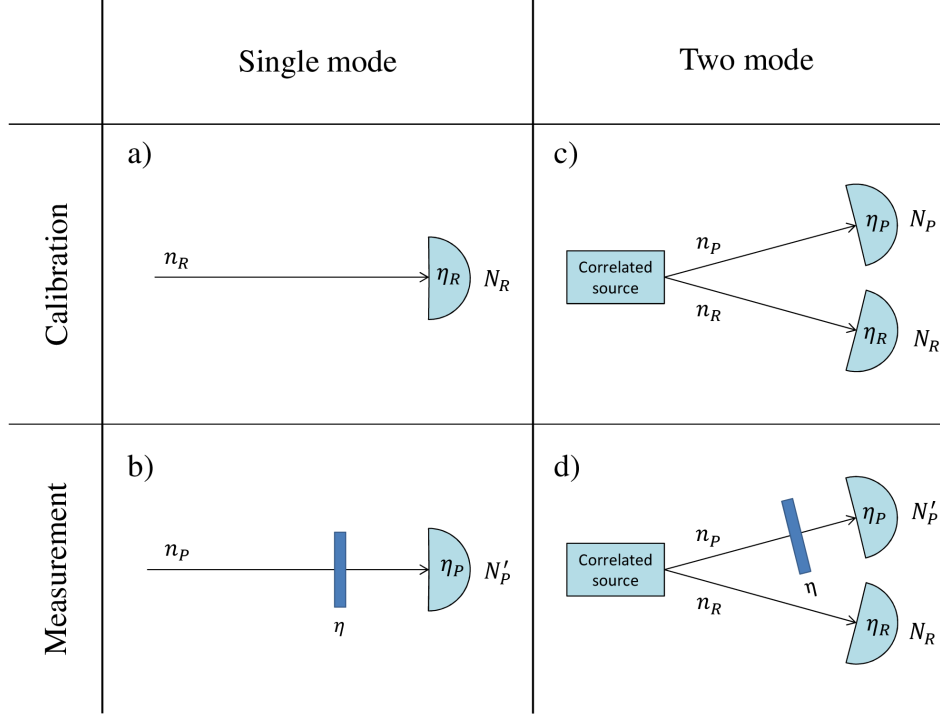
Figure 3.2: Scheme of two possible estimation strategies for the absorption α. (a) and (b) refer to the single-mode case. In these cases there is no correlation between probe and reference beam, i.e. $\langle \Delta N_P \Delta N_R \rangle = 0$ (c) and (d) refer to the two-mode strategy. Here it can be $\langle \Delta N_P \Delta N_R \rangle \neq 0$. Different possibilities of input states and absorption estimators for both the schemes are discussed in the text.

Let us now consider the mean value of the estimator proposed in Eq. 3.19:

$$\langle S_\alpha \rangle = 1 - \gamma \langle \frac{N'_P}{N_R} \rangle = 1 - \gamma \langle \frac{\langle N'_P \rangle + \Delta N'_P}{\langle N_R \rangle + \Delta N_R} \rangle = 1 - \gamma \langle \frac{\langle N'_P \rangle + \Delta N'_P}{\langle N_R \rangle (1 + \Delta N_R / \langle N_R \rangle)} \rangle \sim$$

$$\sim 1 - \gamma \langle \frac{\langle N'_P \rangle + \Delta N'_P}{\langle N_R \rangle} \left(1 - \frac{\Delta N_R}{\langle N_R \rangle} \right) \rangle = 1 - \gamma \frac{\langle N'_P \rangle}{\langle N_R \rangle} + \gamma \frac{\langle \Delta N'_P \Delta N_R \rangle}{\langle N_R \rangle^2} =$$

$$= 1 - \frac{\langle N'_P \rangle}{\langle N_P \rangle} + \frac{\langle \Delta N'_P \Delta N_R \rangle}{\langle N_R \rangle \langle N_P \rangle} = \alpha + (1 - \alpha) \frac{\langle \Delta N_P \Delta N_R \rangle}{\langle N_R \rangle \langle N_P \rangle} =$$

$$= \alpha + (1 - \alpha) \frac{\langle \Delta N_P \Delta N_R \rangle}{\langle N_P \rangle \langle N_R \rangle} \tag{3.22}$$

It emerges that S_α is not unconditionally unbiased. This derivation holds under the condition:

$$\frac{\Delta N_R}{\langle N_R \rangle} \ll 1 \tag{3.23}$$

This hypothesis is necessary to stop to the first order the expansion of the term $(1 + \Delta N_R/\langle N_R \rangle)^{-1}$, namely $(1 + \Delta N_R/\langle N_R \rangle)^{-1} \sim (1 - \Delta N_R/\langle N_R \rangle)$. For a multi-mode twin-beam state, said M the number of spatio-temporal modes and $\mu = \langle n \rangle / M$ the number of photons per mode, according to Eq.s 1.124-1.125-1.126, the condition in Eq. 3.23 becomes:

$$\frac{\Delta N_R}{\langle N_R \rangle} = \sqrt{\frac{1}{M}\left(1 + \frac{1}{\mu\eta}\right)} \ll 1 \rightarrow (M-1)\mu\eta \gg 1 \tag{3.24}$$

As it will be clear in Sec. 3.5, our experiment respects this condition being $\mu \ll 1$, $M \gg 1$ and $(M-1)\mu\eta \sim M\mu\eta = \langle N_R \rangle \sim 1000 \gg 1$. Moreover, considering that the efficiency η is of the order of the unity, the result in Eq. 3.24 implies for the covariance between N_P and N_R:

$$\frac{\langle \Delta N_R \Delta N_P \rangle}{\langle N_R \rangle \langle N_P \rangle} = \frac{\eta_P \eta_R M \mu (1 + \mu)}{\eta_P \eta_R \mu^2 M^2} = \frac{1}{M}\left(1 + \frac{1}{\mu}\right) \ll 1 \tag{3.25}$$

Therefore, under the condition discussed, the estimator S_α is unbiased. Situations where the condition in Eq. 3.23 is not fulfilled could be explored considering higher order of expansion.

To discuss if and in which conditions the estimator proposed attains the ultimate quantum limit we need to consider the uncertainty on S_α, $\langle \Delta^2 S_\alpha \rangle$. Propagating the uncertainty of N_P' and N_R on S_α according to the formula:

$$X = \frac{A}{B} \rightarrow \langle \Delta^2 X \rangle = \frac{\langle \Delta^2 A \rangle}{B^2} + \frac{A^2}{B^4}\langle \Delta^2 B \rangle - 2\frac{A}{B^3}\langle \Delta A \Delta B \rangle \tag{3.26}$$

and rewriting the expression in terms of $\langle N_P \rangle$, $\langle N_R \rangle$ and their variances, it follows:

$$\langle \Delta^2 S_\alpha \rangle = \frac{1}{\langle N_R \rangle}(1 - \alpha)[2\sigma_\gamma(1 - \alpha) + \gamma\alpha] \tag{3.27}$$

It is useful to write Eq. 3.27 in terms of U_{uql} as:

$$\langle \Delta^2 S_\alpha \rangle = U_{uql,\langle N_P \rangle}^2 + \frac{(1-\alpha)^2}{\langle N_P \rangle}\frac{2\sigma_\gamma}{\gamma} \tag{3.28}$$

Here, $U_{uql,\langle N_P \rangle}^2 = \frac{\alpha(1-\alpha)}{\langle N_P \rangle}$ has the form of the UQL in Eq. 3.17, but refers to the number of detected photons (N_P) rather than the number of photons incident on the sample (n_P). Said η_d the channel efficiency after the sample, the two expressions are simply related by: $U_{uql,\langle n_P \rangle}^2 = U_{uql,\langle N_P \rangle}^2 \eta_d$. σ_γ, defined in Eq. 2.16, represents the extension of the noise reduction factor in Eq. 1.91 to the case of unbalanced beams. In terms of the covariance between N_P and N_R it can be written as:

$$\sigma_\gamma = \frac{\langle \Delta^2(N_R - \gamma N_P) \rangle}{\langle N_R + \gamma N_P \rangle} = \frac{\langle \Delta^2 N_R \rangle + \gamma^2 \langle \Delta^2 N_P \rangle - 2\gamma \langle \Delta N_P \Delta N_R \rangle}{\langle N_R + \gamma N_P \rangle} \tag{3.29}$$

For $\gamma = 1$, σ_γ is exactly the noise reduction factor, and the value $\sigma = 1$ sets the bound between classical and quantum correlations. Only using quantum states of light it is possible to have $\sigma < 1$, eventually saturating the ultimate quantum limit in correspondence of $\sigma_\gamma = 0$.

Let us now focus on different possibility of probe states, both classical and quantum, dividing them according to the presence or absence of correlation between the probe and the reference beams.

First we consider measurement strategies where the two beams are not correlated, i.e. $\langle \Delta N_P \Delta N_R \rangle = 0$. For single-mode strategies, where reference and probe beams are measured in two independent moments, this condition necessarily holds.

- Fock states.

  Using uncorrelated quantum states of light it is possible to have $\sigma_\gamma = 0$. This is true considering the product of two unperturbed Fock states: $|n\rangle_P \otimes |n\rangle_R$, with $n \neq 0$. As stated in Eq. 1.50, these states present a fixed number of photons, leading to $\langle \Delta^2 N_R \rangle = \langle \Delta^2 N_P \rangle = 0$, and consequently $\sigma_\gamma = 0$. As anticipated in Sec. 3.2, Fock states allow to reach the UQL for all the values of α.

$$\langle \Delta^2 S_\alpha^{(Fock)} \rangle = U^2_{uql,\langle n_P \rangle} \tag{3.30}$$

  Note that Fock states are defined for integer numbers, and therefore the number of photons in the probe cannot be arbitrarily small but it must be $\langle n_P \rangle \geq 1$. Moreover, this result holds only in the presence of perfect detection efficiency, since Fock statistics are dramatically degraded by losses (see Sec. 1.1.2).

- Coherent states.

  Considering a pair of uncorrelated coherent states, $|coh\rangle_P \otimes |coh\rangle_R$, is particularly relevant for its simple experimental implementation. Recalling the coherent states photon statistics presented in Sec. 1.3 and the definition of the imbalance factor γ, it follows:

$$\langle \Delta^2 S_\alpha^{(Coh)} \rangle = U^2_{uql,\langle N_P \rangle} + \frac{(1-\alpha)^2}{\langle N_P \rangle} \frac{1+\gamma}{\gamma} \tag{3.31}$$

  If classical beams are used, the ultimate quantum limit is not attainable. However, under the condition $\gamma \gg 1$, we have:

$$\langle \Delta^2 S_\alpha^{(Coh,\gamma\gg1)} \rangle = U^2_{uql,\langle N_P \rangle} + \frac{(1-\alpha)^2}{\langle N_P \rangle} = \frac{1-\alpha}{\langle N_P \rangle} = U^2_{coh,\langle N_P \rangle} \tag{3.32}$$

  This means that, for a reference beam having much more energy than the transmitted probe, a pair of uncorrelated coherent states allows to saturate the classical bound, detection efficiency apart ($U^2_{coh,\langle n_P \rangle} = U^2_{coh,\langle N_P \rangle} \eta_d$). Having $\gamma \gg 1$ corresponds to measure N_R with higher precision compared to N_P, in fact, from

$\langle N_R \rangle \gg \langle N_R \rangle$ and assuming a poissonian distribution, it follows $\frac{\Delta N_R}{\langle N_R \rangle} \ll \frac{\Delta N_P}{\langle N_P \rangle}$. Experimentally, in a single mode strategy, this situation can be reproduced considering a longer measurement time in the calibration phase rather than in the measurement itself.

- Arbitrarily uncorrelated states, $|\psi\rangle_P \otimes |\psi\rangle_R$.

  More in general, for $\langle \Delta N_P \Delta N_R \rangle = 0$, σ_γ can be written in terms of the detected Fano factors (see Eq. 1.90) as:

  $$\sigma_\gamma^{(unc)} = \frac{\langle \Delta^2 N_R \rangle + \gamma^2 \langle \Delta^2 N_P \rangle}{\langle N_R \rangle + \gamma \langle N_P \rangle} = \frac{F_R + \gamma F_P}{2} \qquad (3.33)$$

  Replacing this result in Eq. 3.28 it follows:

  $$\langle \Delta^2 S_\alpha^{(unc)} \rangle = U_{uql,\langle N_P \rangle}^2 + \frac{(1-\alpha)^2}{\langle N_P \rangle}\left(\frac{1}{\gamma} F_R + F_P\right) \qquad (3.34)$$

  where F_R and F_P represent the detected Fano factors, for the probe and the reference beams respectively. As demonstrated by Eq. 1.90, losses deteriorate these factors according to: $F_j = \eta_j F_j^{(0)} + 1 - \eta_j > F_j^{(0)}$ (being $j = R, P$). This prevents from the real possibility of reaching the ultimate quantum limit in real experiments, where $\eta_j < 1$.

Let us now consider the possibility of having correlated states of light, i.e. $\langle \Delta N_P \Delta N_R \rangle \neq 0$. Also in this case a classical option and a quantum option are considered.

- Twin beam state, $|twb\rangle_{PR}$.

  This is the bipartite state described in Sec. 1.6.1, and presents perfect correlation in the photon number between the two modes. In particular, in absence of losses ($\eta_P = \eta_R = 1$), $\gamma = 1$ and $\sigma_\gamma = \sigma = 0$. Substituting these values in Eq. 3.28, it follows:

  $$\langle \Delta^2 S_\alpha^{(twb)} \rangle = U_{uql,\langle n_p \rangle}^2 \qquad (3.35)$$

  thus demonstrating that twin-beam states, in case of perfect detection efficiency and in the respect of condition in Eq. 3.23, saturate the ultimate quantum limit. To better understand the influence of losses we can consider how losses affect the detected noise-reduction factor. For the sake of simplicity we report the expression in the case of equal channel efficiencies, $\eta_P = \eta_R = \eta$. Replacing Eq. 1.5.2 in Eq. 3.28, it is obtained:

  $$\langle \Delta^2 S_\alpha^{(twb,\eta)} \rangle = U_{uql,\langle N_P \rangle}^2 + 2\frac{(1-\alpha)^2}{\langle N_P \rangle}(1-\eta) \qquad (3.36)$$

  This expression highlights how in real experiments, where $\eta < 1$, losses prevent to attain the UQL, even if twin-beam states are used. In particular, the highest detachment from the UQL is in the presence of small absorption, i.e. $\alpha \ll 1$.

- Classical correlated beams (CCB).

Classically correlated beams can be obtained by splitting a classical thermal beam with a BS of splitting ratio τ. This situation is described in Sec. 1.4. In this case $\gamma = (1 - \tau)/\tau$ and $\sigma_\gamma = (2\tau)^{-1}$, which is independent from the statistics of the incoming beam. Using this expression of σ_γ, the uncertainty on α becomes:

$$\langle \Delta^2 S_\alpha^{(CCB)} \rangle = U_{uql,\langle N_P \rangle}^2 + \frac{(1-\alpha)^2}{\langle N_P \rangle} \frac{1+\gamma}{\gamma} = \langle \Delta^2 S_\alpha^{(coh)} \rangle \tag{3.37}$$

Classically, correlation between two beams is possible, but not sufficiently "strong" to allow to reach the UQL. The minimum uncertainty attainable is in correspondence of $\tau \sim 0$. In this regime $\frac{1+\gamma}{\gamma} \to 1$ and $\langle \Delta^2 S_\alpha^{(CCB)} \rangle = \frac{1-\alpha}{\langle N_P \rangle} = U_{coh,\langle N_P \rangle}^2$. Let us now focus on the specific case of balanced correlated classical beams (bCCB), corresponding to $\tau = 1/2$ and $\gamma = 1$. In this case $\sigma_\gamma = \sigma = 1$, independently from the losses level: $\sigma_{det} = \sigma\eta + 1 - \eta = \eta + 1 - \eta = 1$. It follows that $\langle \Delta^2 S_\alpha^{(bCCB,\eta)} \rangle$ is immune from detection losses (but always worse than the $\langle \Delta^2 S_\alpha^{(twb,\eta)} \rangle$ reported for the twin-beam case):

$$\langle \Delta^2 S_\alpha^{(bCCB,\eta)} \rangle = U_{uql,\langle N_p \rangle}^2 + 2\frac{(1-\alpha)^2}{\langle N_P \rangle} = \frac{(1-\alpha)(2-\alpha)}{\langle N_P \rangle} \tag{3.38}$$

3.3.2 S_α'

In [45], an optimized version of S_α is proposed. In particular, aim of the optimization procedure is to reduce the uncertainty on α in the presence of experimental imperfections, such as losses. Following [45], we report the procedure for defining the new optimized estimator, S_α'.

In order to take into account and to correct for the random fluctuation of the detected photon number, N_P' is substituted with $N_{Pk}' = N_P' - k\Delta N_R$. ΔN_R is the deviation of N_R from its mean value, i.e. $\Delta N_R = N_R - \langle N_R \rangle$, and k is a parameter of the form $k = C_1 N_P'$, where C_1 is a constant to be determined that will be defined in the following. In these terms α is estimated as:

$$S_{\alpha k} = 1 - \frac{N_{Pk}'}{\langle N_R \rangle} = 1 - \frac{N_P' - k\Delta N_R}{\langle N_R \rangle} \tag{3.39}$$

There are two main issues connected to the estimator defined in Eq. 3.39:

- Its uncertainty depends on k: minimizing it respect to k allows to find the optimal value for k.

- It is necessary to check if it is unbiased. If this is not the case it will be necessary to properly adjust its expression.

Concerning the first point, minimizing the uncertainty on $S_{\alpha k}$ is equivalent to minimize the uncertainty on N'_{Pk}. Let us therefore calculate the detected variance:

$$\langle \Delta^2 N'_{Pk} \rangle = \langle \Delta^2 [N'_P (1 - C_1 \Delta N_R)] \rangle = \langle \Delta^2 N'_P \rangle \langle 1 - C_1 \Delta N_R \rangle^2 +$$

$$+ \langle N'_P \rangle^2 \langle \Delta^2 (1 - C_1 \Delta N_R) \rangle + 2 \langle N'_P \rangle \langle 1 - C_1 \Delta N_R \rangle \langle \Delta N'_P \Delta (1 - C_1 \Delta N_R) \rangle =$$

$$= \langle \Delta^2 N'_P \rangle + \langle N'_P \rangle^2 C_1^2 \langle \Delta^2 N_R \rangle - 2C_1 \langle N'_P \rangle \langle \Delta N'_P \Delta N_R \rangle =$$

$$= \langle \Delta^2 N'_P \rangle + \langle k \rangle^2 \langle \Delta^2 N_R \rangle - 2 \langle k \rangle \langle \Delta N'_P \Delta N_R \rangle \tag{3.40}$$

The detected variance, in analogy with Eq. 1.33, can be written in terms of the mean photons number at the source $\langle N \rangle$, assumed equal in both channels, as:

$$\langle \Delta^2 N_i \rangle = \eta_i \langle N \rangle + \beta \eta_i^2 \langle N \rangle^2 = \langle N_i \rangle + \beta \langle N_i \rangle^2 \tag{3.41}$$

where the first term represents the shot noise and the second terms takes into account possible super-poissonian fluctuations. Similarly, for the covariance it holds:

$$\langle \Delta N'_P \Delta N_R \rangle = \eta_P \eta_R (1 - \alpha) \langle \Delta^2 N \rangle == \eta_P \eta_R (1 - \alpha) \langle N \rangle (1 + \beta \langle N \rangle) \tag{3.42}$$

Replacing Eq.s 3.41-3.42 in Eq.3.40, we obtain:

$$\langle \Delta^2 N'_{Pk} \rangle = \eta_P (1 - \alpha) \langle N \rangle (1 + \eta_P (1 - \alpha) \beta \langle N \rangle) + k^2 \eta_R \langle N \rangle (1 + \eta_R \beta \langle N \rangle) +$$

$$- 2k \eta_P \eta_R (1 - \alpha) \langle N \rangle (1 + \beta \langle N \rangle) \tag{3.43}$$

Minimizing this expression respect to k, the optimal value for k results:

$$\langle k \rangle = \frac{\eta_P (1 - \alpha)(1 + \beta \langle N \rangle)}{1 + \beta \langle N \rangle \eta_R} \tag{3.44}$$

Note that this parameter can be written in terms of experimental quantities, rendering its use possible in practice. From the Fano Factor definition in Eq. 1.90 we have:

$$F_{det,i} = \frac{\langle \Delta^2 N_i \rangle}{\langle N_i \rangle} = \frac{\langle N_i \rangle + \beta \langle N_i \rangle^2}{\langle N_i \rangle} \longrightarrow \beta \langle N_i \rangle = F_{det,i} - 1 \tag{3.45}$$

thus following:

$$\langle k \rangle = \frac{(1 - \alpha)(\eta_P + F_P - 1)}{F_R} = \frac{\eta_P + F_P - 1}{F_R \langle N_R \rangle} \langle N'_P \rangle = C_1 \langle N'_P \rangle \tag{3.46}$$

This result allows us to identify the expression for C_1. C_1 is a constant that can be evaluated from a calibration measurement without the absorbing sample inserted.

Concerning the second point, we need to consider if $\langle N'_{Pk} \rangle = \langle N'_P \rangle$, or equivalently $\langle k \Delta N_R \rangle = 0$. If this is not the case, the estimator proposed in the form of Eq. 3.39 is not unbiased, and its definition needs to be changed accordingly.

$$\Delta E = \langle k \Delta N_R \rangle = \langle k \rangle \langle \Delta N_R \rangle + \text{Cov}(k, \Delta N_R) = C_1 \text{Cov}(N'_P, \Delta N_R) =$$

$$= C_1 \text{Cov}(N'_P, N_R) = C_1(1-\alpha)\text{Cov}(N_P, N_R) = \frac{C_1 \text{Cov}(N_P, N_R)}{\langle N_R \rangle} N'_P = C_2 N'_P \qquad (3.47)$$

where C_2, similarly to C_1, is a constant that can be evaluated from a calibration measurement. We found $\Delta E = \langle k \Delta N_R \rangle \neq 0$, therefore using the definition in Eq. 3.39 would lead to a biased estimation of α. The optimized estimator needs to be changed in:

$$S'_\alpha = 1 - \frac{N'_P - k\Delta N_R + \Delta E}{\langle N_R \rangle} \qquad (3.48)$$

This estimator is unbiased and optimized for the presence of experimental losses. k and ΔE are computed independently for each single frame as $k = C_1 N'_P$ and $\Delta E = C_2 N'_P$. C_1 and C_2 can be measured in a calibration phase of the experiment.

Propagating the uncertainty on Eq. 3.48, it is possible to obtain $\langle \Delta^2 S'_\alpha \rangle$. For the sake of simplicity, we report the expression corresponding to symmetric channels, i.e. $\eta_P = \eta_R = \eta$ and $F_P = F_R = F$:

$$\langle \Delta^2 S'_\alpha \rangle = U^2_{uql,\langle N_P \rangle} + \frac{(1-\alpha)^2}{\langle N_P \rangle} \sigma \left(2 - \frac{\sigma}{F} \right) \qquad (3.49)$$

For a twin-beam state with low number of photons per spatio-temporal mode, the expression in Eq. 3.49 can be further simplified in:

$$\langle \Delta^2 S'^{(twb,\eta)}_\alpha \rangle = U^2_{uql,\langle N_P \rangle} + \frac{(1-\alpha)^2}{\langle N_P \rangle} \sigma(1 - \eta^2) \qquad (3.50)$$

where it has been used the result in Eq. 1.5.2 and the fact that, in the presence of low number of photons per spatio-temporal mode, $F \sim 1$. In case of perfect efficiency $\eta = 1$, $\langle \Delta^2 S'_\alpha \rangle = U^2_{uql,\langle N_P \rangle}$. We conclude that both $S'^{(twb)}_\alpha$ and $S^{(twb)}_\alpha$, are optimal measurement strategies.

3.3.3 S''_α

In [46] a further absorption estimator is proposed:

$$S''_\alpha = \frac{N_R - \gamma N'_P}{\langle N_R \rangle} \qquad (3.51)$$

Its uncertainty can be written in terms of experimental quantities such as $\sigma_\gamma, F_P, \langle N_P \rangle$. It results:

$$\langle \Delta^2 S''_\alpha \rangle = \frac{[2(1-\alpha)\sigma_\gamma + \alpha + (F_R - 1)\alpha^2]}{\gamma \langle N_P \rangle} \qquad (3.52)$$

Replacing in Eq. 3.52 the parameters values corresponding to the ideal twin-beam case ($\sigma_\gamma = 0$ and $\gamma = 1$), it follows:

$$\langle \Delta^2 S''^{(twb,\eta=1)}_\alpha \rangle = \langle \Delta^2 \alpha_{uql} \rangle + \frac{F_R \alpha^2}{\langle N_P \rangle} \qquad (3.53)$$

This estimator is in general not optimal. It becomes optimal only asymptotically, in the limit $F_R \alpha^2 / \langle N_P \rangle \to 0$. Considering twin-beam state produced by SPDC, the photon number per spatio temporal mode is typically very low, thus leading to $F_R \sim 1$. In this regime, therefore, the condition of optimality becomes $\alpha^2 / \langle N_P \rangle \to 0$.

3.4   Comparison among the different estimators

In order to compare the performances of the different measurement strategies presented so far, in Fig.s 3.3-3.4-3.5 the variance on α (normalized to $\langle N_P \rangle$) in terms of its mean value is plotted. In particular we report the curves corresponding to:

- ultimate quantum limit (U_{uql}, in Eq. 3.17), black dashed-dotted line

- limit in the presence of classical resources ($\Delta \alpha_{coh}$, in Eq. 3.18), black dashed line

- ΔS_α using twb ($\Delta S_\alpha^{(twb,\eta)}$, in Eq. 3.36), blue line

- ΔS_α using balanced correlated classical beams ($\Delta S_\alpha^{(bCCB,\eta)}$, in Eq. 3.38), black dotted line

- $\Delta S_\alpha'$ using twb ($\Delta S_\alpha'^{(twb,\eta)}$, in Eq. 3.50), yellow line

- $\Delta S_\alpha''$ using twb ($\Delta S_\alpha''$, in Eq. 3.52), green line

for different values of the channel efficiecy ($\eta_P = \eta_R$ is assumed)

Fig. 3.3 represents the ideal situation: in this case the curves are obtained under the hypothesis of $\eta_P = \eta_R = 1$, $\sigma_\gamma = 0$, $\gamma = 1$. It results $U_{uql} = \Delta S_\alpha^{(twb)} = \Delta S_\alpha'^{(twb)}$, meaning that both S_α and S_α' are optimal if an ideal twin-beam is used. Moreover, for $\alpha \to 0$, also $S_\alpha''^{(twb)}$ is optimal, according to Eq. 3.53. Both the classical strategies, in the presence of low absorption, are significantly detached from the ultimate quantum limit.

Fig. 3.4 represents the situation for $\eta < 1$. In particular this plot corresponds to $\eta_P = \eta_R = 0.95$. Both $\Delta S_\alpha^{(twb,\eta)}$ and $\Delta S_\alpha'^{(twb,\eta)}$ start detaching from the U_{uql}. The advantages offered by the optimized estimator S_α' over S_α are almost negligible.

The situation in the presence of higher losses ($\eta_P = \eta_R = 0.25$) is presented in Fig. 3.5. In this case the difference between S_α and S_α' is evident: while $\Delta S_\alpha^{(twb,\eta)}$ is worse than $\Delta \alpha_{coh}$, $\Delta S_\alpha'^{(twb,\eta)}$ always remains below the classical limit.

3.5   Experimental set-up

Aim of our experiment is to validate the theoretical model presented in the previous sections, demonstrating the advantages of using twin-beam states. A scheme of the experimental set-up is reported in Fig. 3.6. To produce the twin beam state of light the
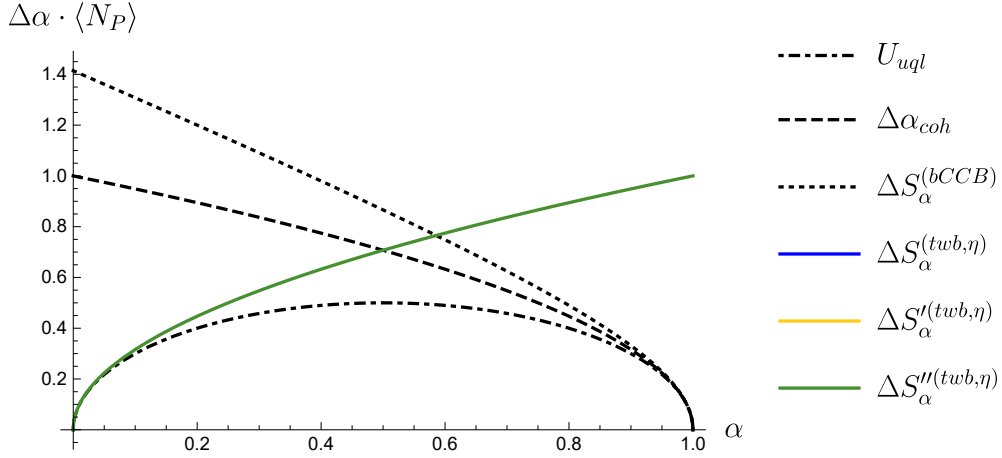
Figure 3.3: Estimation uncertainty of the absorption coefficient in function of its mean value α. The uncertainty is normalized for the number of detected photons in the probe beam $\langle N_P \rangle$. The performances of different measurement strategies are compared (see text for more details). $\eta_P = \eta_R = 1$. The green, blue and yellow curves overlap.
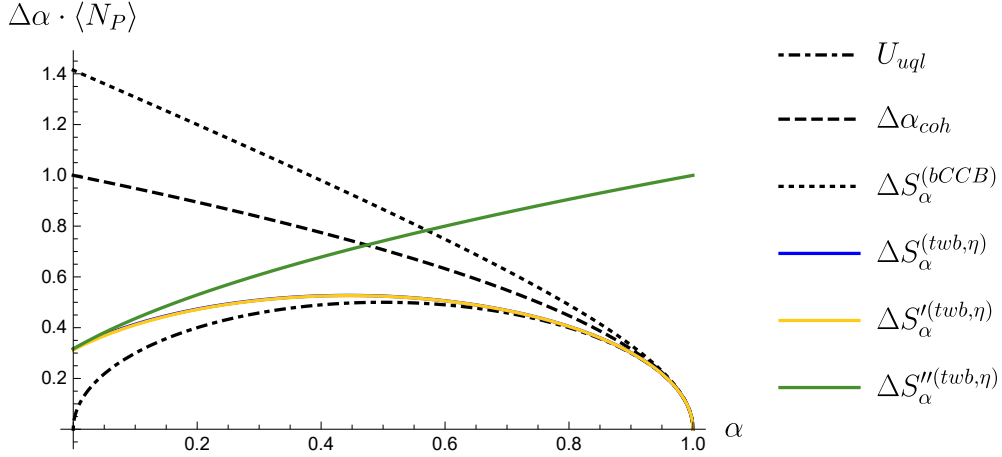

Figure 3.4: Estimation uncertainty of the absorption coefficient in function of its mean value α. The uncertainty is normalized for the number of detected photons in the probe beam $\langle N_P \rangle$, in function of the mean absorption α. The performances of different measurement strategies are compared (see text for more details). $\eta_P = \eta_R = 0.95$. The blue and yellow curves overlap.

SPDC process in a BBO crystal is exploited. A non linear crystal is pumped with a laser of $\lambda = 405$nm and power of 100 mW. The laser emission is triggered by a digital signal coming from the camera, i.e. the laser emits only in correspondence of the camera acquisition time. Using a system of two lenses, the correlations in momentum between two down-converted photons are mapped into spatial correlations at the detection plane.
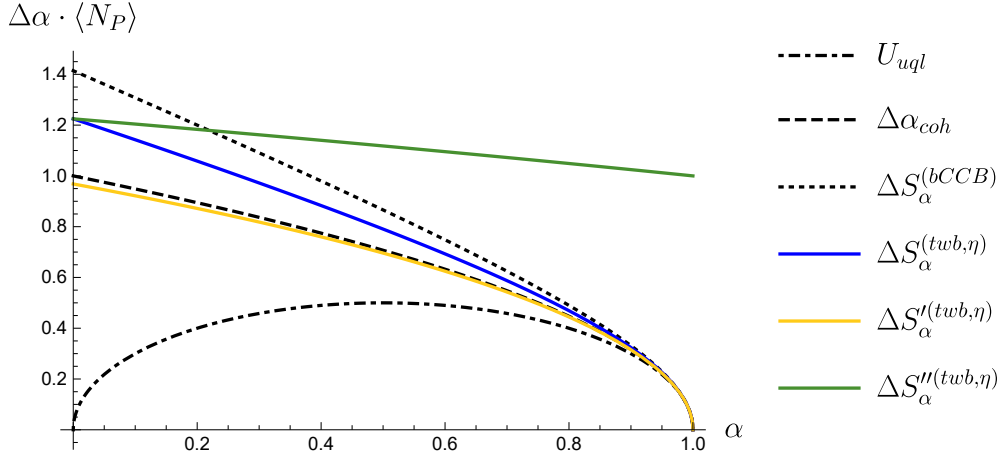
Figure 3.5: Estimation uncertainty of the absorption coefficient in function of its mean value α. The uncertainty is normalized for the number of detected photons in the probe beam $\langle N_P \rangle$, in function of the mean absorption α. The performances of different measurement strategies are compared (see text for more details). $\eta_P = \eta_R = 0.25$.
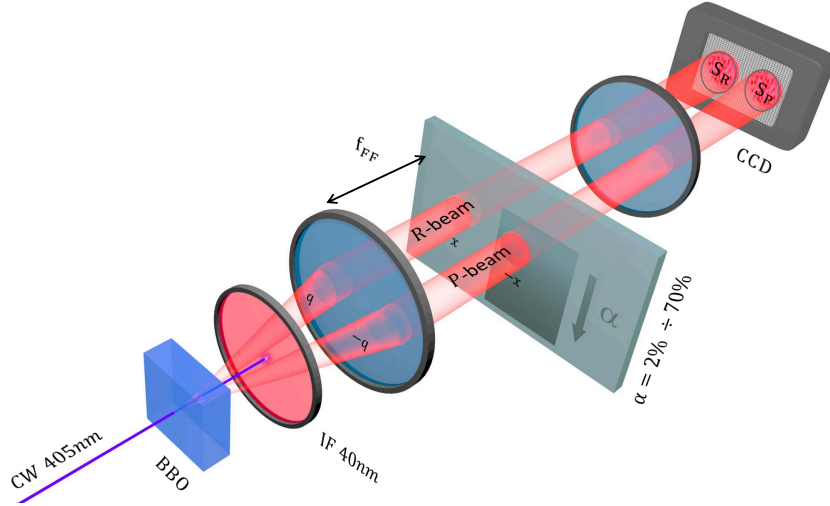

Figure 3.6: Scheme of the experimental set-up. In the BBO crystal a twin-beam state is generated. The probe beam passes through the sample and then is detected in the S_P region of the CCD, while the reference beam goes directly to S_R, without interacting with the sample. The sample consists in a glass slide with a deposition of different absorption coefficient ($\alpha = 2 \div 70\%$). More details are presented in the text.

Placing an interferential filter at (800 ± 20)nm allows to consider only photons around the degenerate wavelength ($\lambda_d = 2\lambda_{pump}$). This is the same mechanism at the basis of the experiment described in Ch. 4, and is extensively discussed in Ch. 2 (see in particular Sec. 2.1). The detector is the CCD camera Princeton Inst. Pixis 400BR Excelon described

in Sec. 2.1.1. We operate in linear mode and we cool it down to -70C. The chosen digitization rate is 100kHz. In this experiment we are not interested in spatial resolution, being the aim of the experiment the estimation of the mean absorption coefficient of the sample, therefore we use an hardware binning of 24x24, leading to macro-pixels measuring $(312\text{x}312)\mu m^2$. This procedure allows to increase the signal detected with respect to the read-out noise and to reduce the readout time. The two detection areas, corresponding to the reference and probe beams, are named as S_R and S_P respectively and each of them contains 56 macro-pixels. For the analysis the signals in S_P and S_R are integrated, we indicate as N_P and N_R the total number of photons detected in each region.

The sample consists in a coated glass-slide with a deposition of variable absorption coefficient α, $\alpha \sim 0.02 \div 0.70$. Moving the sample in the vertical direction, data for 9 different values of α are collected. As shown in Fig. 3.6, the sample is positioned in the focal plane of the far-field lens, where spatial correlations occur. It is then imaged to the detection plane by the imaging lens, with a magnification factor of $M = 7.8$. Only the probe beam intercepts the deposition, while the reference beam passes in an empty portion of the glass-slide.

In order to validate the theoretical model at varying η_R, neutral filters of different absorption can be eventually positioned on the reference beam path. We consider three different values for η_R. Without any filter and having maximized the set-up performances, the value of η_R is $\eta_R = 0.76$. The other values considered are: $\eta_R = 0.49$ and $\eta_R = 0.43$.

In order to estimate the mean photons number per spatio-temporal mode we can consider that:

- The typical number of detected photons is $\langle N_R \rangle \sim 50 \cdot 10^4$.

- The number of detected modes is given by the product of temporal and spatial modes, namely: $M = M_{sp}M_t$.

- The acquisition time for each frame is 100ms. Being the SPDC coherence time around 10^{-12}s, it follows $M_t \sim 10^{11}$.

- Comparing the dimension of the coherence area, estimated as described in Sec. 2.1.2, with the one of the detection areas considered here, it follows $M_{sp} \sim 3500$.

Therefore, $\mu = \dfrac{\langle N_R \rangle}{M} \sim 1.4 \cdot 10^{-9}$. In this regime, as shown in Eq. 1.86, the single mode of a twin-beam state is well described by a poissonian statistics.

In order to estimate η_P, η_R, γ, σ_γ, F_P and F_R an acquisition with no deposition on the probe path is performed. The channels efficiencies are estimated using the method presented in Sec. 2.1.5, while γ, σ_γ, F_P and F_R are estimated according to their definitions in terms of $\langle N_P \rangle$ and $\langle N_R \rangle$. The best value of σ_γ obtained, corresponding to $\eta_P \sim \eta_R \sim 0.76$ is $\sigma_\gamma = 0.24 \pm 0.03$ and $\gamma = 1.006$.

We refer to η_P and η_R as channel efficiencies so far, this means that the number of detected photons can be written as $\langle N_P \rangle = N \eta_P$ (and analogously for $\langle N_R \rangle$), being N the number of photons produced at the source in correspondence of the detection areas S_P and S_R. The channel efficiency can be further decomposed into different contributions, that can be independently estimated. Referring to Fig. 3.7, we can write:
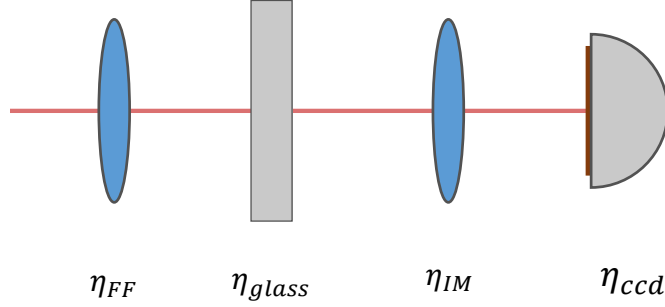

Figure 3.7: Scheme of the different efficiencies concurring to the total channel efficiency η_P (or η_R). $\eta_P = \eta_{FF} \cdot \eta_{glass} \cdot \eta_{IM} \cdot \eta_{ccd}$

$$\eta_P = \eta_{FF} \cdot \eta_{IM} \cdot \eta_{glass} \cdot \eta_{ccd} \tag{3.54}$$

η_{FF} is the collection efficiency of the far field lens and takes into account that only a fraction of the produced photons pairs enters the lens (on the contrary, optical losses due to the lens itself are almost negligible). η_{IM} is the collection and optical transmittance of the imaging lens. η_{ccd} is the efficiency of the CCD, considering also the interferential filter mounted just before the detector. η_{glass} takes into account the optical losses in the glass used for the deposition. In order to decouple the different efficiencies, we perform the following acquisitions:

- Acquisition with the far-field lens in the position used in our experiment and the CCD in its focal plane. The channel efficiency estimated in this configuration, evaluated using the extension of the Klyshko method described in Sec. 2.1.5, corresponds to $\eta_{ccd}\eta_{FF}$. We find $\eta_{ccd}\eta_{FF} = 0.81 \pm 0.03$.

- Acquisition with the far-field lens much closer to the crystal, in order to consider $\eta_{FF} \sim 1$ and the CCD in its focal plane. In this configuration we measure $\eta_{ccd} = 0.83 \pm 0.03$.

- The absorption of the glass slide has been independently measured: $\eta_{glass} = 0.98$.

From these results we obtain:

$$\eta_{IM} = (0.96 \pm 0.06) \tag{3.55}$$

It can be useful to estimate the efficiency after the sample: $\eta_d = \eta_{IM}\eta_{ccd} = 0.79 \pm 0.08$. This allows to estimate the number of photons arriving on the sample as $\langle n_P \rangle = \langle N_P \rangle / \eta_d$.

3.6 Experimental results

In Fig.s 3.8-3.9-3.10 the experimental results are reported. The three figures differ for the value of the efficiency on the reference path, η_R, and report the uncertainty on α at varying its mean value. For evaluating $\Delta\alpha$ and its standard deviation (represented in the plots by the error bars) we divide the total amount of frames acquired (2000) into 10 groups. Given a group, α is estimated from each frame using the different estimators and $\Delta\alpha$ is evaluated as the standard deviation of the obtained values. The standard deviation of the $\Delta\alpha$ obtained in the various groups gives us the uncertainty on $\Delta\alpha$ reported as the error bars in the graphs.
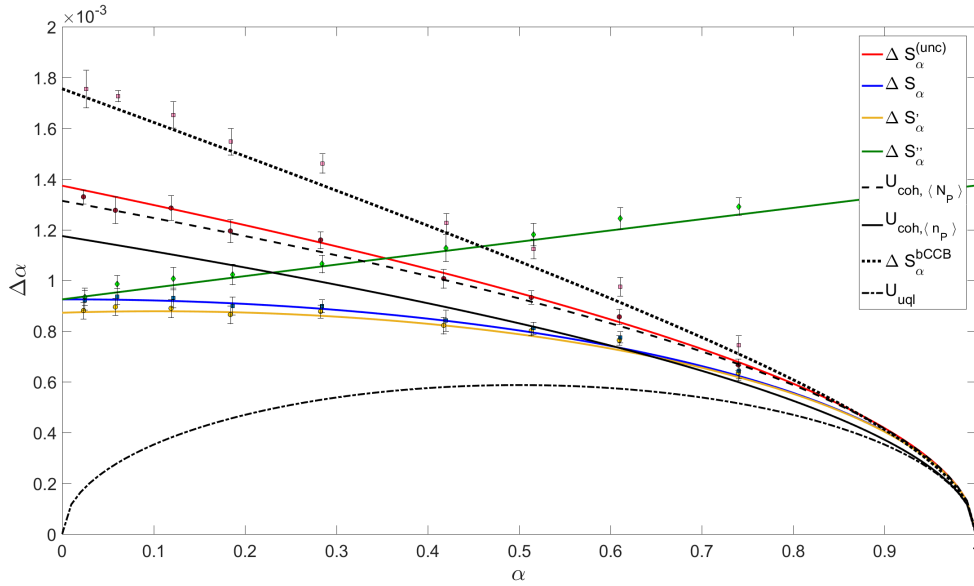

Figure 3.8: Uncertainty estimation of the absorption coefficient in function of its mean value α. The different estimators presented in the text are considered. Markers are the experimental data, with the corresponding error bars. Solid lines are the theoretical curves, dashed and dotted lines represent few significant theoretical limits (see text for details). The channel efficiencies are $\eta_P \sim \eta_R \sim 0.76$.
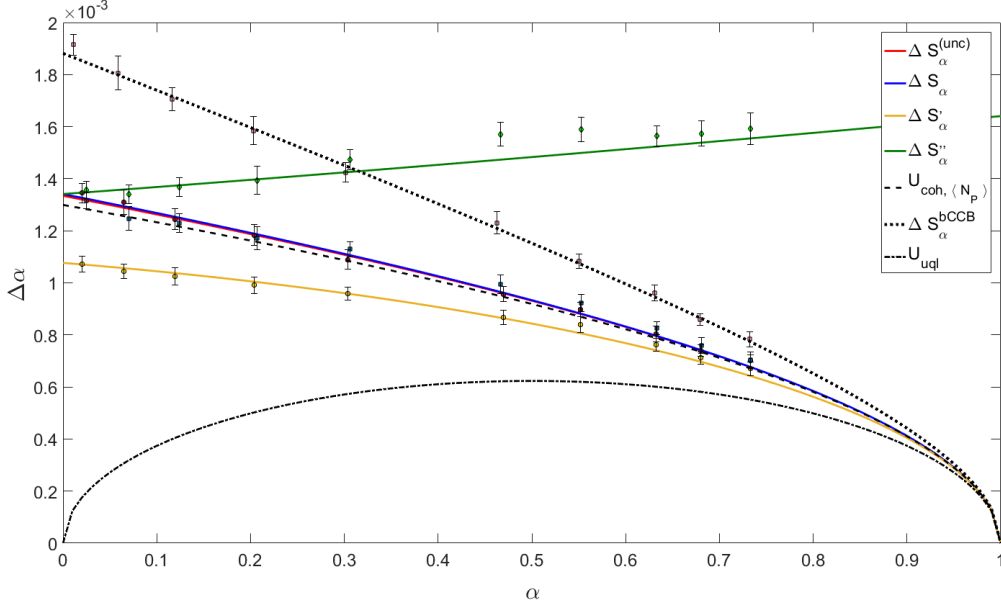
Figure 3.9: Uncertainty estimation of the absorption coefficient in function of its mean value α. The different estimators presented in the text are considered. Markers are the experimental data, with the corresponding error bars. Solid lines are the theoretical curves, dashed and dotted lines represent few significant theoretical limits (see text for details). The channel efficiencies are $\eta_P \sim 0.76$ and $\eta_R \sim 0.49$.

The acquired data are analyzed according to the different strategies theoretically investigated in Sec. 3.3. In particular:

- $S_\alpha^{(twb)}$. This is the estimator firstly proposed by Rarity in [44] and discussed in Sec. 3.3.1. S_P and S_R are chosen in order to exploit quantum correlations in the twin-beam state.

- $S_\alpha^{(bCCB)}$. To reproduce the situation of two classically correlated beams with quasi-poissonian statistics, we consider as reference region a region S_R', displaced from S_R. Quasi poissonian beams should not show correlation in principle. However, possible unwanted super-poissonian excess noise, for example due to the laser power fluctuations can not be removed by this procedure.

- $S_\alpha^{(unc)}$. To reproduce this case we simply consider the probe beam, using as $\langle N_R \rangle$ the value obtained in a preliminary acquisition, without deposition inserted. Being $\langle N_P \rangle / M \ll 1$ the single beam can be well approximated with a coherent beam.

- $S_\alpha'^{(twb)}$. This is the estimator proposed by Moreau in [45], which requires independent evaluation of η_P and η_R but offers interesting advantages in the presence of
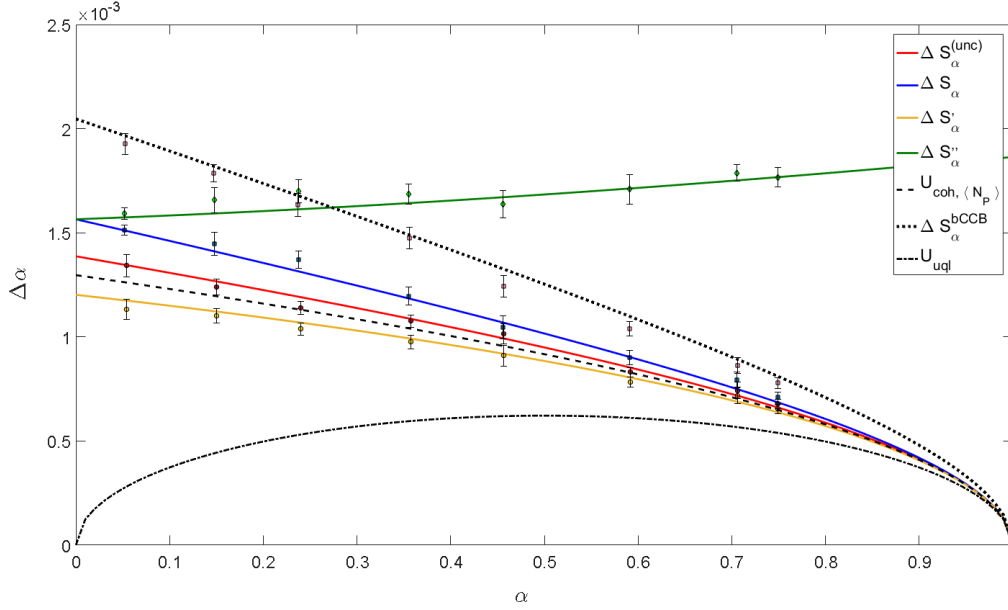
Figure 3.10: Uncertainty estimation of the absorption coefficient in function of its mean value α. The different estimators presented in the text are considered. Markers are the experimental data, with the corresponding error bars. Solid lines are the theoretical curves, dashed and dotted lines represent few significant theoretical limits (see text for details). The channel efficiencies are $\eta_P \sim 0.76$ and $\eta_R \sim 0.43$.

high losses (see Sec. 3.3.2).

- $S_\alpha''^{(twb)}$. This is the estimator proposed by Brambilla in [46], which performs similarly to S_α in the limit $\alpha \to 0$.

Moreover the theoretical curves are reported. The coloured curves are obtained replacing the experimental parameters ($\langle N_P \rangle$, $\langle N_R \rangle$, η_P, η_R, γ =, σ_γ, F_P and F_R) in the Eq.s 3.34-3.36-3.49-3.52. The black curves are the theoretical limits. In particular, the dashed-dotted line is the ultimate quantum limit: $U_{uql} = \sqrt{\dfrac{\alpha(1-\alpha)}{\langle n_P \rangle}}$, where $\langle n_P \rangle$ is the number of photons which interacts with the sample. Dashed line is the limit corresponding to the best classical strategy when the same mean energy of the probe and the same detection efficiency are considered, i.e. $U_{coh,\langle N_P \rangle} = \sqrt{\dfrac{1-\alpha}{\langle N_P \rangle}}$. In Fig. 3.8 the continue black line represents the classical limit for same mean energy of the probe but unitary efficiency of the detector, i.e. $U_{coh,\langle n_P \rangle} = \sqrt{\dfrac{1-\alpha}{\langle n_P \rangle}}$. The dotted line represents the uncertainty on α in case of classically correlated beams (balanced case), according to Eq. 3.38.

Note that the value of $\langle n_P \rangle$ can be estimated from the detected photons number $\langle N_P \rangle$ as $\langle n_P \rangle = \langle N_P \rangle / \eta_d$.

3.7   Discussion and conclusions

From the experimental results shown in Sec. 3.6 we conclude that the theoretical model presented in Sec. 3.3 is validated. In particular, the presence of experimental imperfections is properly taken into account. The curves obtained substituting the values of the experimental parameters, independently estimated, in the theoretical expressions are in good accordance with the experimental data. For almost all the cases the theoretical curves intercept the error bars associated to the corresponding experimental data.

Referring to Fig. 3.8, we demonstrate state of the art sensitivity per photon in loss estimation, without any kind of post selection. The enhancement reported is probably the best ever reported at the time of our publication [17]. In particular, to the best of our knowledge, the best reported result was a quantum enhancement of 1.21 ± 0.02 respect to the optimal classical option, in [45]. In our experiment the quantum strategy leads, for $\alpha \sim 2\%$, to an enhancement compared to the classical case of $U_{coh,\langle N_P \rangle}(\alpha)/\Delta S'_\alpha = 1.51 \pm 0.13$, where same probe mean energy and channel efficiency are considered. The quantum enhancement remains even considering the classical limit for perfect detection efficiency. However, in this case it is lowered to $U_{coh,\langle n_P \rangle}/\Delta S'_\alpha = 1.32 \pm 0.14$. As expected from the theory, in case of relatively high η (in this case $\eta_P \sim \eta_R \sim 0.76$), the difference between S_α and S'_α is almost negligible, and the use of S_α can be more practical since does not require calibration of the set-up or high stability of the system. Note that having $\eta_R, \eta_P \neq 1$ significantly detaches the experimental uncertainty from the ultimate quantum limit.

In Fig. 3.9 and 3.10 lower values of η_R are considered. In these cases the differences between S_α and S'_α are more significant. In particular, for $\eta \sim 0.5$, $\Delta S_\alpha^{(twb)}$ is similar to the classical strategy $\Delta S_\alpha^{(unc)}$, while for $\eta \sim 0.43 < 0.5$, S_α performs even worse than it. However, in both cases, $\Delta S'_\alpha$ remains below the classical limit, thus offering a way to go below the shot-noise-limit in practical situations, where η_R can be low.

For the sake of simplicity, in Eq.s 3.36-3.49, we assume $\eta_P \sim \eta_R$. The expressions for the general case are not reported; in Fig.s 3.11-3.12 their behaviour, normalized to the coherent case, can be graphically appreciated. In Fig. 3.11, η_P is fixed to $\eta_P = 0.76$, the value of our experiment, and the dependence on η_R and α is reported. On the contrary, in Fig. 3.12, η_R is fixed to 0.76 and the dependence from η_P and α is reported.

From Fig. 3.11 it emerges that the advantages of S'_α over S_α are relevant in the presence of high losses. Thanks to the optimization procedure, for all the possible parameters values the uncertainty on S'_α always remains below the one of the other estimators, eventually approaching their behaviour in particular limits (such as $\Delta S'^{(twb)}_\alpha \sim \Delta S_\alpha^{(twb)}$ for η_R sufficiently high, or $\Delta S'^{(twb)}_\alpha \sim \Delta S_\alpha^{(coh)}$ for η_R sufficiently low). From Fig. 3.12 it can be concluded that the role of η_P is less relevant respect to the one of η_R. For $\eta_R \sim 0.76$, as it is in the figure, at varying η_P the enhancement offered by S'_α is almost negligible.

In view of real applications, we conclude commenting on the importance of a two-mode strategy. Adopting a single mode strategy, it is necessary to perform a calibration
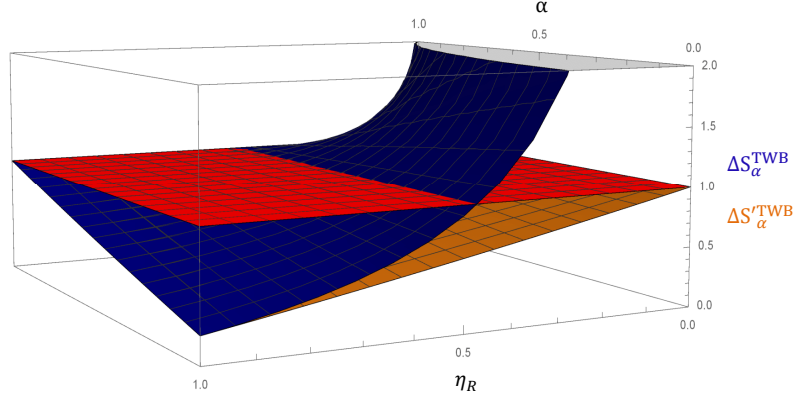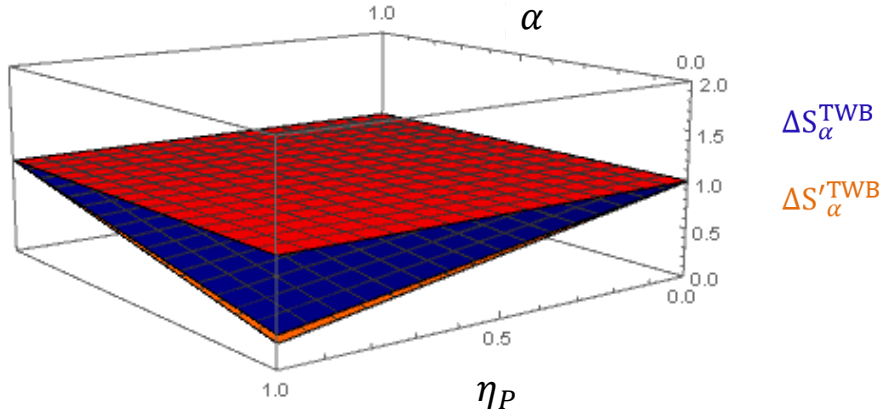
70

Figure 3.11: Uncertainty on the loss coefficient α, normalized to the single mode coherent case (U_{coh}, $\langle N_P \rangle$, red surface), using twin-beam state as input state and the two different estimators presented in the text in function of the reference path efficiency, η_R, and the mean absorption α. Blue surface refers to S_α while the orange surface refers to S'_α. η_P is fixed to $\eta_P = 0.76$.

Figure 3.12: Uncertainty on the loss coefficient α, normalized to the single mode coherent case ($U_{coh,\langle N_P \rangle}$, red surface), using twin-beam state as input state and the two different estimators presented in the text in function of the probe path efficiency, η_P, and the mean absorption α. Blue surface refers to S_α while the orange surface refers to S'_α. η_R is fixed to $\eta_R = 0.76$.

measurement, i.e. a measurement without the sample, in order to estimate $\langle N_R \rangle$. This measurement is necessarily performed in a different moment respect to the measurement with the sample inserted. To obtain an unbiased estimation of α, it is necessary to assume the stability of the system between the two measurements, in particular the stability of the source is of the utmost importance. Theoretically this is not a problem, but from the experimental point of view it represents an issue, leading to a bias estimation of the parameter α, which can result in a consistent deviation especially if α is small. To solve this problem, in many practical measurements an auxiliary detector is used to monitor power drifts and to correct for them. In addition also the detectors performances can be influenced by temperature. For these reasons, a two mode strategy, where $\langle N_P \rangle$ and $\langle N_R \rangle$ are measured at the same time, should be preferred. In fact, it is reasonable to assume that the temporal drifts of the set-up affect both reference and probe channels in the same way. Experimentally, it is much less demanding maintaining $\gamma = \frac{\langle N_R \rangle}{\langle N_P \rangle} = \frac{\eta_R}{\eta_P}$ constant over time than controlling the power stability of the individual beam (i.e. $\langle N_P \rangle$ constant over time). Some commercial devices adopt a two mode strategy, typically with an unbalanced splitting ratio between probe and reference, in order to get closer to the classical limit (see Eq. 3.37). In our experiment we focus on the balanced two mode strategy, measuring a quantum enhancement of $\Delta S_\alpha^{(bCCB)} / \Delta S_\alpha' = 2.00 \pm 0.16$. S_α and S_α'' do not require the knowledge of the mean individual intensity of the two beams, nor the absolute values of the channels efficiencies, but only the estimation of the arms imbalance, γ. This factor can be estimated in a calibration measurement: the estimation of α is reliable if γ remains constant between the calibration phase and the measurement with the sample inserted. As discussed above this condition can be easily experimentally satisfied. On the contrary, S_α', requires the absolute knowledge of η_R, and assumes that this value remains constant over time. If these conditions are sufficiently well verified, it leads to important advantages over S_α, in particular for low channels efficiencies. In conclusion, there is no a univocal solution for the estimator choice but, depending on the situation, i.e. especially the values of η_P and η_R, and in accordance to the discussion above, the most suitable should be chosen.

Chapter 4

Quantum differential ghost imaging

Quantum correlations are at the basis of different quantum enhanced measurement protocols. In Ch. 3 we discuss how they can be exploited in absorption estimation, in this chapter we focus on a possible imaging application. In particular, we consider the so called ghost imaging technique (GI), particularly interesting since it allows the reconstruction of the image in environmentally difficult conditions. Exploiting the non classical correlations in twin-beam state (see Sec. 1.6.1), a great quantum enhancement is possible, when considering low brightness conditions. Here, an improved variant of the GI protocol, named as differential ghost imaging (DGI) and originally proposed for bright thermal light, is presented and extended to the quantum domain. In particular, the low-brightness regime, where quantum fluctuations and experimental imperfections play an important role, is deeply analyzed. Note that this regime can be extremely relevant in case of delicate or photo-sensitive samples. While it is shown that the direct extension of the DGI protocol in the low brightness regime presents some drawbacks, we elaborate an optimized version of the DGI with better performance compared with the existent protocols. Finally, an experiment in the low-brightness regime, using twin-beam state is performed. The theoretical results are validated and, in view of real applications, the protocol is applied for the reconstruction of biological objects.

4.1   Introduction to the ghost imaging technique

The fundamental scheme of the ghost imaging technique is presented in Fig. 4.1. Two correlated beams are used: one goes to the object and then to a bucket detector, i.e. a detector without spatial resolution, while the other goes directly to a spatial resolving detector, without interacting with the object. It is clear that considering the two beams separately it is not possible to recover the absorption profile of the object. However, its reconstruction is possible by exploiting the spatial correlations between the two beams.
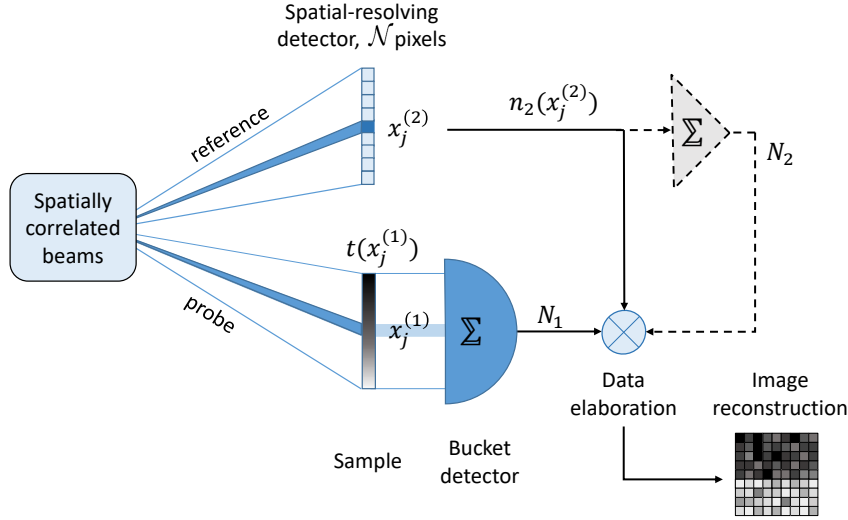
Figure 4.1: Schematic representation at the basis of any ghost imaging protocol. Two spatially correlated beams are exploited. One of the two, the probe beam, interacts with the sample and then impinges on a detector without spatial resolution (bucket detector). The other beam, the reference beam, is detected by a spatial resolving detector. The one-to-one correspondence between the pixel $x_j^{(2)}$ of the resolving detector and the resolution cell $x_j^{(1)}$ at the object plane is exploited. For the image reconstruction the number of photons detected by the bucket detector, N_1, and the one detected by each pixel of the resolving detector, $n_2(x_j^{(2)})$, are used. Eventually, also the equivalent bucket detector N_2 can be evaluated without requiring any modification in the experimental set-up.

This technique was theoretically proposed by Belinskii and Klyshko in 1994 [47] and experimentally realised one year later by Pittman et al. [48]. This first demonstration was realized exploiting SPDC correlated photon pairs, measuring their temporal coincidences with detectors consisting in avalanche photodiode operating in Geiger mode. Also classical beams can present spatial correlation and can therefore be used for GI reconstruction. In particular, split thermal light has been used in several GI experiments demonstrating that also classical correlation allows image reconstruction [49–53], although with a smaller signal-to-noise ratio (SNR) [54–56]. Also GI with intense TWBs has been experimentally implemented [57]. A lot of theoretical and experimental works were devoted to understand the role of quantum resources in GI protocol, a systematic study of this topic can be found in [55]. A comprehensive review on the physics at the basis of the ghost imaging protocol can be found in [56].

The great interest on this technique and the existence of several variants are strongly

justified by GI potentialities in difficult experimental conditions, hostile to direct imaging. Typical situations that can take advantage of this technique are:

- Lack of space for placing a resolving detector and a proper imaging system. This is for example the case in some extreme experimental conditions, such as cryogenic temperatures or high magnetic field [58].

- Presence of turbulence or diffusive media on the object path. GI is immune to turbulence or scattering between the sample and the bucket detector [59–61].

- Necessity of probing the sample with a wavelength inappropriate for currently available resolving detectors and imaging systems [62, 63].

4.1.1 Conventional GI protocol

Let us now discuss the details of the conventional protocol. As shown in Fig. 4.1, the data available for the elaboration and the image reconstruction are:

- N_1, number of photons detected by the bucket detector.

- $n_2(x_j^{(2)})$, the output from the resolving detector, i.e. a matrix where each element is the number of photons detected by the pixel $x_j^{(2)}$

The GI protocol is not a single-shot imaging technique, on the contrary H frames are acquired, thus providing H values of N_1 and $n_2(x_j^{(2)})$.

We name $S(x_j)$ the function used to reconstruct the object absorption profile. In general it is function of the joint outputs distribution of the two detectors:

$$S(x_j) = f(\langle \hat{N}_1 \rangle, \langle \hat{n}_2(x_i) \rangle, \langle \hat{N}_1 \hat{n}_2(x_i) \rangle, ... \langle \hat{N}_1^p \hat{n}_2(x_i)^q \rangle) \tag{4.1}$$

where, in general, i can be different from j. In the conventional GI technique $S(x_j)$ is the covariance between the two outputs:

$$S(x_j)_{GI} = \langle \delta\hat{N}_1 \delta\hat{n}_2(x_j) \rangle = \langle \hat{N}_1 \hat{n}_2(x_j) \rangle - \langle \hat{N}_1 \rangle\langle \hat{n}_2(x_j) \rangle \tag{4.2}$$

The goal is now to demonstrate that this quantity is related to the transmission profile of the object. The key point is the spatial correlation of the two beams: the spatial selection performed in the reference beam by the pixel in $x_j^{(2)}$ automatically identifies a small area where the correlated probe photons are expected to impinge on the object plane, centered in $x_j^{(1)}$. This area represents the ultimate spatial resolution cell of the GI scheme. We also assume that the pixel is larger than the coherence area (see Sec. 2.1.2): from this assumption it follows that resolution cells (at the object plane) identified by two adjacent pixels (of the resolving detector) do not overlap. This implies that the outcome of two different pixels can be considered as uncorrelated:

$$\langle \delta\hat{n}_2(x_i) \delta\hat{n}_2(x_j) \rangle = 0, \text{for } i \neq j \tag{4.3}$$

75

Similarly:

$$\langle \delta\hat{n}_1(x_i)\delta\hat{n}_1(x_j)\rangle = \langle \delta\hat{n}_1(x_i)\delta\hat{n}_2(x_j)\rangle = 0, \text{for } i \neq j \tag{4.4}$$

where $\hat{n}_1(x_j)$ is the number of photons in the resolution cell x_j that would be detected by a resolving detector on the object path. With this notation, the signal from the bucket detector can be written as $\hat{N}_1 = \sum_1^{\mathcal{N}} \hat{n}_1(x_1)$. Given this one-to-one correspondence between object plane and reference detection plane, hereinafter we will omit the suffixes 1 and 2, identifying $x_j^{(2)}$ and $x_j^{(1)}$ simply as x_j. Said $t(x_j)$ the transmission profile of the object and $\mathcal{N}$ the number of pixels in the resolving detector, Eq. 4.2 can be written as:

$$S(x_j)_{GI} = \langle \delta \sum_{i=1}^{\mathcal{N}} \hat{n}_1(x_i)\delta\hat{n}_2(x_j)\rangle = \langle \sum_{i=1}^{\mathcal{N}} \delta\hat{n}_1(x_i)\delta\hat{n}_2(x_j)\rangle = \sum_{i=1}^{\mathcal{N}}\langle \delta\hat{n}_1(x_i)\delta\hat{n}_2(x_j)\rangle =$$

$$= \sum_{i\neq j}\langle \delta\hat{n}_1(x_i)\delta\hat{n}_2(x_j)\rangle + \langle \delta\hat{n}_1(x_j)\delta\hat{n}_2(x_j)\rangle = \langle \delta\hat{n}_1(x_j)\delta\hat{n}_2(x_j)\rangle \tag{4.5}$$

Said $n_1'(x_j)$ and $n_2'(x_j)$ the mean number of photons at the source in the reference and probe beams respectively, the mean numbers of detected photons are: $\langle \hat{n}_1(x_j)\rangle = n_1'(x_j)\eta_1 t(x_j)$ and $\langle \hat{n}_2(x_j)\rangle = n_2'(x_j)\eta_2$, being $\eta_{1,2}$ the probe and reference channel efficiencies. In the reasonable hypothesis of spatially uniform beams and efficiencies, $\langle \hat{n}_2(x_j)\rangle$ is constant over the pixeled detector, i.e. $\langle \hat{n}_2(x_j)\rangle \equiv n_2$. Moreover, in the model we assume that the efficiency is the same in the two channels, i.e. $\eta_1 = \eta_2 = \eta$. This assumption does not decrease the generality of the result since an imbalance between η_1 and η_2 can be included in the transmission profile of the object. In particular, said $\gamma = \eta_2/\eta_1$, $t(x_j)$ can be redefined as $t'(x_j) = t(x_j)/\gamma$, leading to $\langle \hat{n}_1(x_j)\rangle = n_1'\eta\frac{t(x_j)}{\gamma} = n_1'\eta t'(x_j)$. This is schematically exemplified in Fig. 4.2.

The quantity resulting in Eq. 4.5, $S_{GI}(x_j) = \langle \delta\hat{n}_1(x_j)\delta\hat{n}_2(x_j)\rangle$, depends on the state of light used. Here we focus on two cases:

- Equally split thermal light (*th*). Note that, according to the results presented in Sec. 1.3 split coherent beam do not present any correlation and therefore cannot be used in this context.

- Multi-mode twin-beam state (*tw*).

Referring to the light statistics discussed in Sec.s 1.4 and 1.6.1, and considering that $t(x_j)$ can be considered as a detection loss (Sec. 1.1.2) we have:

$$S(x_j)_{GI}^{th} = \langle \delta\hat{n}_2(x_j)\delta\hat{n}_1(x_i)\rangle^{th} = \frac{t(x_i)n_2^2(x_j)}{M}\delta_{i,j} \tag{4.6}$$

$$S(x_j)_{GI}^{tw} = \langle \delta\hat{n}_2(x_j)\delta\hat{n}_1(x_i)\rangle^{tw} = t(x_i)\left(\frac{n_2^2(x_j)}{M} + \eta n_2(x_j)\right)\delta_{i,j} \tag{4.7}$$
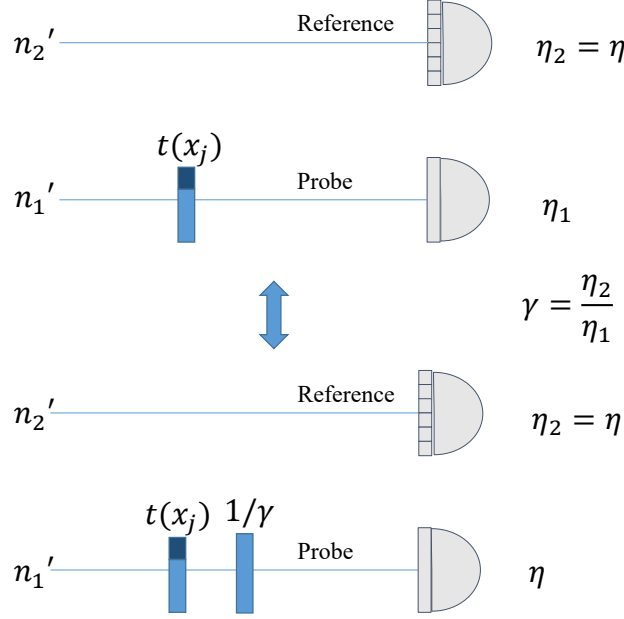
Figure 4.2: Scheme which demonstrates how it is possible to take into account possible imbalance between the two channels efficiencies ($\gamma = \eta_2/\eta_1 \neq 1$) redefining the absorption profile of the object as $t'(x_j) = t(x_j)/\gamma$. In the model it is assumed $\eta_1 = \eta_2 = \eta$, without loss of generality.

where M is the number of spatio-temporal modes collected by the pixel x_j. Typically this quantity can be considered constant over all the resolving detector area ($M(x_j) \equiv M$). This result demonstrates, on one side, that the expression of $S(x_j)$ is a good choice since it leads to an expression proportional to $t(x_j)$ and, on the other side, that both SPDC and thermal light allow the image reconstruction.

In order to quantitatively compare the GI performance under different conditions, the absolute value of the signal $S(x_j)$ is not important, but it is necessary to consider the signal to noise ratio (SNR).

For the sake of simplicity in developing the theoretical model we consider a two level object, with R_+ pixels of transmission level t_+ and R_- pixels of transmission level t_- ($t_+ > t_-$). This situation is exemplified in Fig. 4.3. We define ϵ as the fraction of the object with transmission t_-:

$$\epsilon = \frac{R_-}{\mathscr{N}} = \frac{R_-}{R_+ + R_-} \tag{4.8}$$

In terms of ϵ the mean transmission coefficient of the sample, $\bar{t}$, can be written as:

$$\bar{t} = \frac{t_- R_- + t_+ R_+}{R_- + R_+} = t_- \epsilon + t_+(1 - \epsilon) \tag{4.9}$$
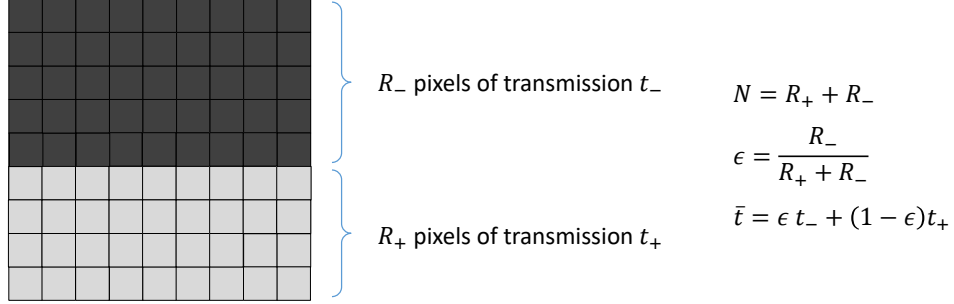
Under these hypothesis the SNR can be defined as:

R_- pixels of transmission t_-

R_+ pixels of transmission t_+

$N = R_+ + R_-$

$\epsilon = \dfrac{R_-}{R_+ + R_-}$

$\bar{t} = \epsilon \, t_- + (1 - \epsilon)t_+$

Figure 4.3: Example of a two level object: the different quantities used in the theoretical model ($R_+, R_-, \mathcal{N}, \epsilon, \bar{t}, t_+, t_-$) are graphically presented.

$$\text{SNR} = \frac{|\langle S_+\rangle - \langle S_-\rangle|}{\sqrt{\delta^2\langle S_+\rangle + \delta^2\langle S_-\rangle}}, \tag{4.10}$$

where $\langle S_\pm\rangle$ and $\delta^2\langle S_\pm\rangle$ are respectively the mean value of the reconstructed image in correspondence of $t_\pm$ and its associated variance. Being H the number of frames used to estimate S, from the central limit theorem it follows that the uncertainty on the mean value scales as $\sqrt{H}$, e.g. $\delta^2\langle S(x_j)\rangle = \delta^2 S(x_j)/H$. Therefore, acquiring an arbitrary big number of frames, it is always possible, at least in principle, to sufficiently increase the SNR thus recovering the image. However, there are several practical issues that need to be taken into account, as the stability of the system, the amount of time required, the limitation in the photon dose to be sent on the sample. Lowering the number of frames necessary to have a SNR sufficiently high to distinguish the image from the noise (SNR = 1 is conventionally considered as the benchmark) is therefore of the utmost importance.

In Eq. 4.6 and 4.7 the expected values of $S(x_j)$ in both thermal and twin-beam cases are reported (being $S_\pm$ simply $S(x_j)$ with $x_j \in R_\pm$). Concerning the variance on these quantities we have:

$$\delta^2\langle S_\pm\rangle = \frac{\langle(\delta\hat{N}_1\delta\hat{n}_2(x_j))^2\rangle - \langle\delta\hat{N}_1\delta\hat{n}_2(x_j)\rangle^2}{H} \sim \frac{1}{H}\langle\delta\hat{N}_1\rangle^2\langle\delta\hat{n}_2(x_j)\rangle^2 \tag{4.11}$$

where $x_j \in R_\pm$ respectively. The first equality is the definition of variance. Concerning the second equality, in the hypothesis of $R_\pm$ sufficiently big, we can assume that, given $n_2(x_j)$ and N_1, the fluctuations on N_1 are dominated by uncorrelated noise (in all N_1 fluctuations only the fluctuations of $n_1(x_j)$ are correlated with the fluctuations of $n_2(x_j)$). Therefore, the variance of their product can be factorized into the product of their variances. In the last expression in Eq. 4.11 there is no difference between thermal

or SPDC cases. Being two resolution cells uncorrelated, we can write $\langle \delta^2 \hat{N}_1 \rangle$ as:

$$\langle \delta^2 \hat{N}_1 \rangle = \sum_j \langle \delta^2 \hat{n}_1(x_j) \rangle = \sum_{x_j \in R_+} \langle \delta^2 \hat{n}_1(x_j) \rangle + \sum_{x_j \in R_-} \langle \delta^2 \hat{n}_1(x_j) \rangle, \qquad (4.12)$$

that can be evaluated by substituting the expressions for the variance of multi-thermal distribution in Sec. 1.4.

For the sake of simplicity, we report here the SNR analytic expressions in the case of no electronic background, $\Delta_{el} = 0$, and a binary object of transmission $t_- = 0$ and $t_+ = 1$. Replacing into the definition 4.10 the results from Eq.s 4.6-4.7-4.11, it is obtained:

$$\text{SNR}_{\text{GI}}^{th} = \sqrt{H} \frac{1}{\sqrt{2\mathcal{N}(1-\epsilon)}} \frac{n_2}{n_2 + M}, \qquad (4.13)$$

$$\text{SNR}_{\text{GI}}^{tw} = \sqrt{H} \frac{1}{\sqrt{2\mathcal{N}(1-\epsilon)}} \frac{n_2 + M\eta}{n_2 + M} \qquad (4.14)$$

In both cases, SNR $\propto \sqrt{H/\mathcal{N}}$. Thus, in the following we will sometime consider the SNR normalized for the number of frames and the area of the reconstructed region. This means considering the quantity $\text{SNR}' = \text{SNR}\sqrt{\frac{\mathcal{N}}{H}}$.

In order to highlight the advantage of quantum light, let us consider the ratio of the two expressions (note that the result holds for every value of t_+, t_- and Δ_{el}, and not only for the special values used for deriving Eq.s 4.13-4.14):

$$\frac{\text{SNR}_{\text{GI}}^{tw}}{\text{SNR}_{\text{GI}}^{th}} = \frac{n_2 + M\eta}{n_2} = 1 + \frac{M\eta}{n_2} \qquad (4.15)$$

It emerges that the advantage of quantum light over its classical counter part is relevant when the number of photons emitted per spatio-temporal mode is sufficiently low, i.e. $M\eta/n_2 \gg 1$. In the opposite regime the performances of splitted thermal beams and SPDC light are exactly the same. This result is exemplified in Fig. 4.4.

4.2 Differential ghost imaging

This protocol was firstly proposed by Ferri et al. in [64] in 2010, in the specific case of bright thermal light. Also an experimental demonstration of the advantages of this protocol was presented, both in [64] and [61], always considering bright thermal light.

The main idea of the differential ghost imaging (DGI) is to exploit also the integrated signal over the pixeled detector (i.e. $\hat{N}_2 = \sum_{i=1}^{\mathcal{N}} \hat{n}_2(x_i)$), in order to increase the SNR of the reconstruction. Note that this new approach does not require any modification of the conventional GI set-up, but simply a different analysis of the data. In particular, the
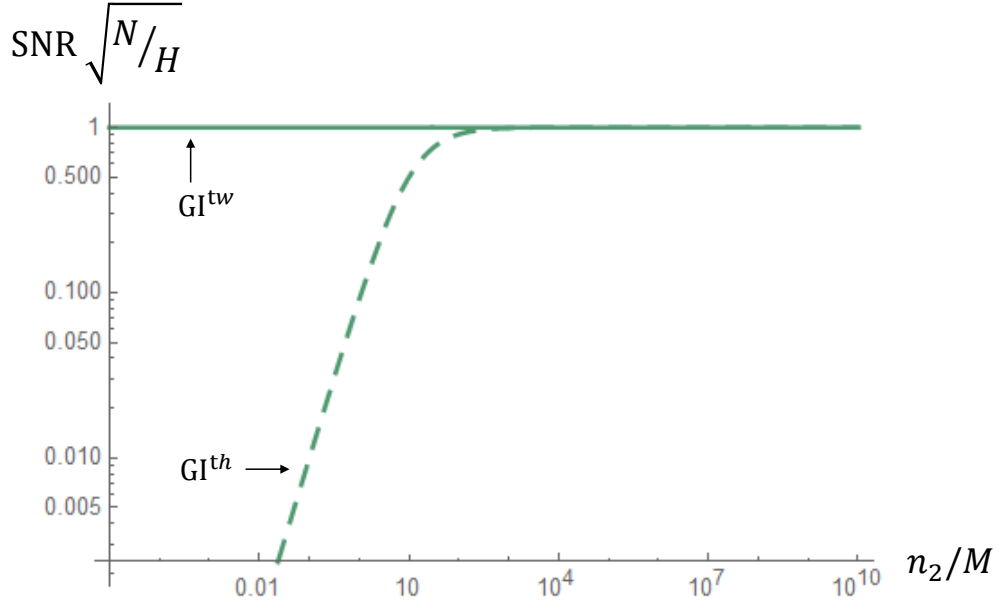
Figure 4.4: SNR, normalized for the number of frames and the area of the reconstructed region, versus the number of detected photons per mode (n_2/M). The other parameters being $\eta = 1$, $\Delta_{el} = 0$, $t_+ = 1$, $t_- = 0$, $\epsilon = 0.5$.

following quantity is introduced:

$$\hat{N}_{DGI} = \hat{N}_1 - \frac{\langle \hat{N}_1 \rangle}{\langle \hat{N}_2 \rangle} \hat{N}_2 \tag{4.16}$$

and the image is reconstructed as:

$$S(x_j)_{DGI} = \langle \delta \hat{n}_2(x_j) \delta \hat{N}_{DGI} \rangle = S_{GI}(x_j) - \frac{\langle \hat{N}_1 \rangle}{\langle \hat{N}_2 \rangle} \langle \delta^2 \hat{n}_2(x_j) \rangle \tag{4.17}$$

where the last equality follows from the absence of correlation between modes collected from two different pixels of the resolving detector.

4.2.1 Differential ghost imaging with bright thermal light

Making use of the results presented in Sec. 1.4 for thermal light, it is possible to write Eq. 4.17 in terms of the object absorption profile $t(x_j)$. For the thermal case, it follows:

$$S^{th}_{DGI}(x_j) = n_2 \left[\frac{n_2}{M} \delta t(x_j) - \bar{t} \right] \tag{4.18}$$

where $\bar{t}$ is the average transmission level of the object, $\bar{t} = (1/\mathcal{N}) \sum_{i=1}^{\mathcal{N}} t(x_i)$, and $\delta t(x_j) = t(x_j) - \bar{t}$. Note that the average transmission $\bar{t}$ can be evaluated as $\bar{t} = \langle N_1 \rangle / \langle N_2 \rangle$. The bright thermal light regime corresponds to consider Eq. 4.18 in the limit $n_2/M \gg 1$. Under this assumption we have:

$$S_{DGI}^{th} \propto \delta t(x_j) \tag{4.19}$$

The fact that DGI is sensitive to the spatial change in the transmission rather than to the transmission itself (as it happens for standard GI in Eq. 4.6) suggests that this protocol can offer significant improvements when considering small or highly transparent objects. This result is presented in [64] and confirmed by our model. Here, we do not report the details of the SNR derivation since it follows the same line adopted for GI and reported in Sec. 4.1.1. In the limit $n_2/M \gg 1/\epsilon$, neglecting the electronic noise ($\Delta_{el}^2 \ll n_2$) and considering $t_- = 0$ and $t_+ = 1$, the ratio of the SNR for the two protocols can be written as:

$$\frac{\mathrm{SNR}_{DGI}^{th}}{\mathrm{SNR}_{GI}^{th}} = \frac{1}{\sqrt{\epsilon}} \tag{4.20}$$

The theoretical curves of our model, considering the parameters of a typical GI experiment with bright thermal light, are plotted in Fig. 4.5. A two-level object of transmission $t_- = 0$ and $t_+ = 1$ is considered. The SNR, normalized to the number of frames and pixels in the reconstructed area, is reported in function of the object occupation fraction ϵ. Interestingly the DGI advantage is not sensitive to losses: the curves corresponding to different loss levels (i.e. $\eta = 1, 0.7, 0.2$ are considered) are perfectly overlapping. It can be concluded that, in this regime, DGI offers important improvements in the reconstruction of small object in the field of view. For example, considering a totally absorbing object occupying 2% of the reconstructed area we have: $\mathrm{SNR}_{DGI}' \sim 5$, while $\mathrm{SNR}_{GI}' \sim 0.7$.

The advantage in the reconstruction of highly transparent objects is demonstrated in Fig. 4.6. In this case the occupation fraction is fixed to $\epsilon = 0.9$. The SNR, normalized to the number of frames and pixels in the reconstructed area, is reported in function of the object transmission coefficient, t_- (while $t_+ = 1$). SNR_{DGI} remains constant at varying t_-, while GI performance rapidly decreases. For example, considering an object of $t_- = 0.9$, for the normalized SNR we have: $\mathrm{SNR}_{DGI} \sim 2.5$, while $\mathrm{SNR}_{GI} \sim 0.08$.

4.2.2   Extension to the quantum regime

The great performances, in terms of SNR, of the DGI protocol presented in Sec. 4.2.1 for the bright thermal case, justify the interest in extending this protocol to the quantum regime. As emerged considering the GI conventional protocol in Sec. 4.1.1, only quantum correlations allow the image reconstruction in the low brightness regime ($n_2/M \ll 1$), and this regime can be of the utmost importance when it is necessary to keep low the photon dose.

Starting from the DGI expression in Eq. 4.17 and making use of the twin-beam light statistics in Eq. 1.113, we obtain:
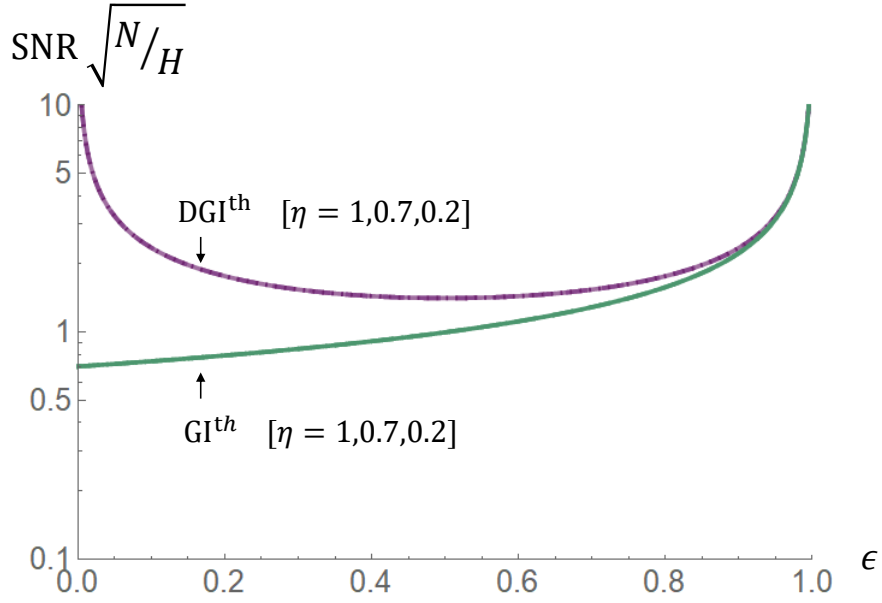
Figure 4.5: SNR, normalized for the number of frames and the area of the reconstructed region, versus the object occupation fraction ϵ, in the bright thermal regime. Green curve refers to the conventional GI protocol, while purple curve refers to the DGI. The other parameters are $n_2/M \sim 10^8$ (i.e. bright thermal light), $\Delta_{el} = 0$, $t_+ = 1$, $t_- = 0$. Different values of the channels efficiency η are considered ($\eta = 1,0.7,0.2$) resulting in perfectly overlapping curves.

$$S_{DGI}^{tw}(x_j) = n_2 \left[\left(\frac{n_2}{M} + \eta \right) \delta t(x_j) - \bar{t}(1-\eta) \right] \tag{4.21}$$

where η is the overall detection efficiency of the experiment, including both detector and channels efficiencies.

We do not report the details of the SNR derivation since it follows the same line adopted for the GI protocol, reported in Sec. 4.1.1. Similarly to what is obtained for the conventional protocol, also for DGI, in the bright regime, i.e. $n_2/M \gg 1$, it holds:

$$\text{SNR}_{DGI}^{th} \sim \text{SNR}_{DGI}^{tw} \tag{4.22}$$

Therefore, all the results presented in Sec. 4.2.1 for bright thermal beams are valid also when twin-beam with high number of photons per spatio-temporal mode are considered. In the limit $n_2/M \gg 1/\epsilon$, neglecting the electronic noise ($\Delta_{el}^2 \ll n_2$) and considering $t_- = 0$ and $t_+ = 1$, the ratio of the SNR in the two cases can be written as:

$$\frac{\text{SNR}_{DGI}^{tw}}{\text{SNR}_{GI}^{tw}} = \frac{\text{SNR}_{DGI}^{th}}{\text{SNR}_{GI}^{th}} = \frac{1}{\sqrt{\epsilon}} \tag{4.23}$$
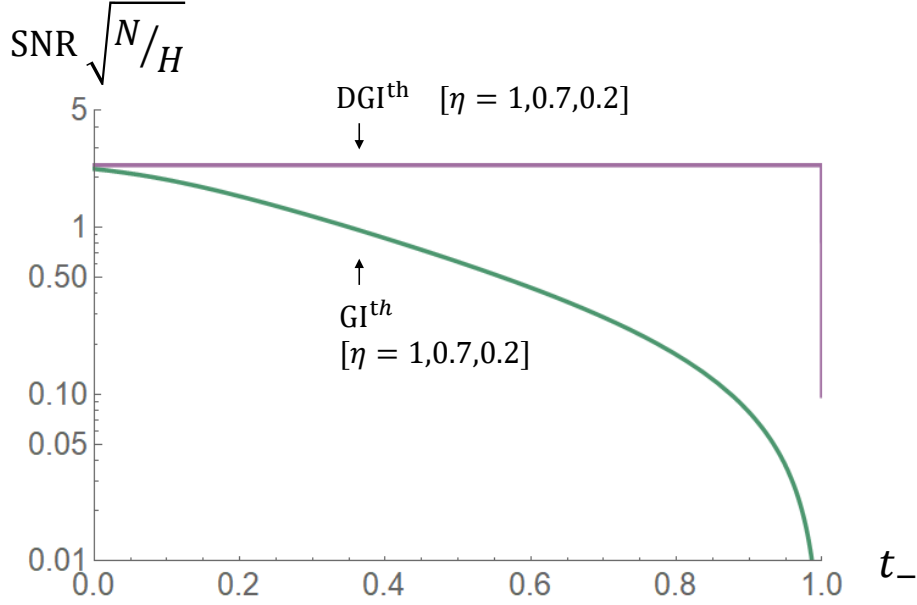
Figure 4.6: SNR, normalized for the number of frames and the area of the reconstructed region, versus t_-, in the bright thermal regime. Green curve refers to the conventional GI protocol, while purple curve refers to the DGI. The other relevant parameters are $n_2/M \sim 10^8$ (i.e. bright thermal light), $\Delta_{el} = 0$, $t_+ = 1$, $\epsilon = 0.9$.

It follows that, if we want to work in the bright regime, the twin-beam state does not offer any advantage over its classical counter part: if there are no issues with investigating the sample with bright light, using split thermal beams is probably the most practical solution.

However, as extensively discussed in Sec. 1.5.3, there are relevant situations where the intensity cannot be arbitrarily increased. With this motivation in mind, we will explore the quantum low brightness regime both theoretically, in this section, and experimentally, in Sec. 4.5.

Considering Eq. 4.21, in the limit $n_2/M \ll 1$, we have:

$$S_{DGI}^{tw} \sim n_2[\eta \delta t(x_j) - \bar{t}(1 - \eta)] \tag{4.24}$$

Therefore, in the twin-beam case, the sensitivity of DGI to the object profile reaches a finite constant value, proportional to the channel efficiency in the limit of low brightness. On the other side, in the thermal case (see Eq. 4.18), in the same limit, the sensitivity to the object transmission profile is lost.

For the sake of simplicity we report the expression of the ratio of the SNRs for the two protocols neglecting the electronic noise and always considering $t_- = 0$ and $t_+ = 1$:

$$\frac{\text{SNR}_{DGI}^{tw}}{\text{SNR}_{GI}^{tw}} = \frac{1}{\sqrt{2(\eta - 1/2)(\epsilon - 1) + 1}} \tag{4.25}$$

From Eq. 4.25 it is confirmed that losses in the low intensity regime have a significant impact. In particular we can observe that:

- For $\eta = 1$ the same result of Eq.(4.23) is recovered.

- As soon as $\eta < 1$ the DGI advantage is drastically reduced.

- For high losses, i.e. $\eta < 1/2$, DGI performs worse than the conventional GI protocol.

The strong dependence, at low brightness, of the SNR from the channel efficiency can be appreciated in Fig.s 4.7-4.8. The SNR, normalized for the number of frames and pixels in the reconstructed area, is plotted in function of ϵ for different values of η. In Fig. 4.7 both GI and DGI are considered: for $\eta = 0.7$ DGI is slightly better than GI, while for $\eta = 0.2$ the DGI performs worst than GI. Fig. 4.8 shows that, as soon as $\eta < 1$ (e.g. $\eta = 0.95$), the rising of SNR_{DGI} for low ϵ is lost. Of course, in real experiments η is necessarily below one, for example the efficiency of our set-up is $\eta \sim 0.8$ (see Sec. 4.4).
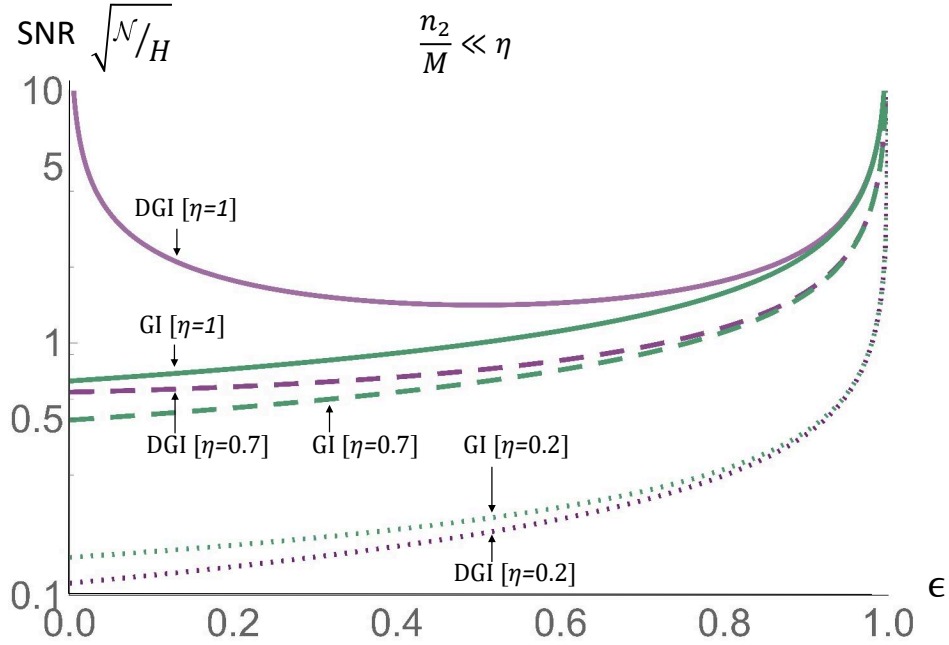

Figure 4.7: SNR, normalized for the number of frames and the area of the reconstructed region, versus the object occupation fraction ϵ, in the low-brightness SPDC regime. Green curves refer to the conventional GI protocol, while purple curves refer to the DGI. The plain lines correspond to ideal efficiency $\eta = 1$, while dashed and dotted lines correspond to $\eta = 0.7$ and $\eta = 0.2$ respectively. The other relevant parameters are $n_2/M \sim 10^{-8}$ (i.e. low-brightness), $\Delta_{el} = 0$, $t_+ = 1$, $t_- = 0$.
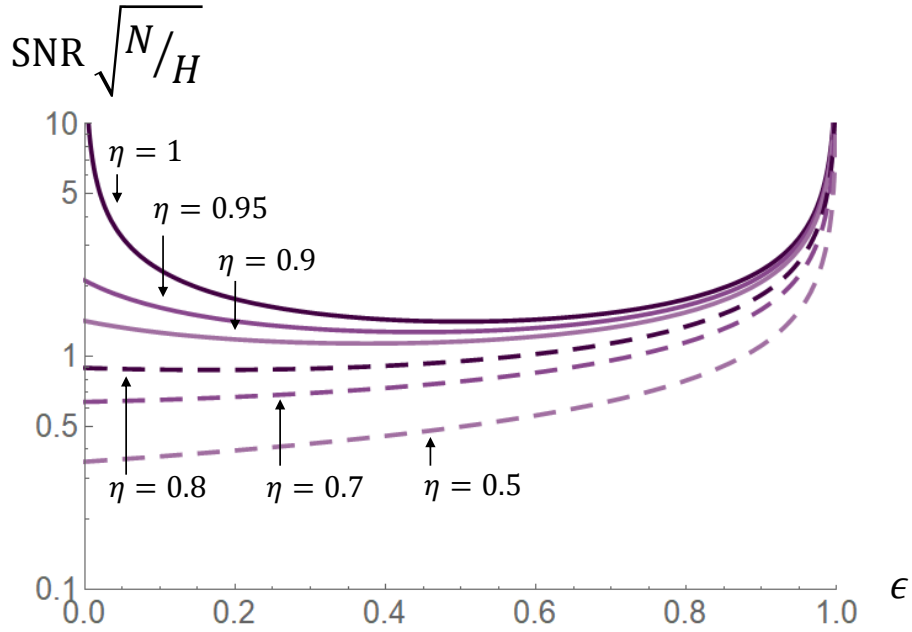
Figure 4.8: SNR, normalized for the number of frames and the area of the reconstructed region, versus ϵ, in the low-brightness SPDC regime. Only DGI is considered for different values of η: starting from the first curve from above, $\eta = 1, 0.95, 0.9, 0.8, 0.7, 0.5$ respectively. The other relevant parameters are $n_2/M \sim 10^{-8}$ (i.e. low-brightness), $\Delta_{el} = 0$, $t_+ = 1, t_- = 0$.

We can conclude that the DGI extension to the low brightness regime, where only quantum correlation allows the reconstruction of the image with an affordable number of frames, is extremely affected from experimental imperfection. This consideration is the motivation of the work described in the next section. In fact, in Sec.4.3 we propose a new optimized protocol, able to partially compensate for the detrimental effect of losses and electronic noise.

4.3   Optimized differential ghost imaging

After presenting the advantages of the DGI protocol when bright thermal light is used (see Sec. 4.2.1), in Sec. 4.2.2 we extended this protocol to the quantum domain, focusing in particular to the low-brightness regime. From this extension it emerges that losses play a key role in this context, lowering the enhancement offered by DGI. In this section we propose an optimized differential ghost imaging protocol, ODGI, able to partially compensate for the detrimental effect of losses and electronic noise.

In particular, we propose a generalization of the DGI protocol replacing $\hat{N}_{DGI}$ in Eq.

4.17 with $\hat{N}_k = \hat{N}_1 - k\hat{N}_2$:

$$S_k(x_j) = \langle \delta \hat{N}_k \delta \hat{n}_2(x_j) \rangle = S_{GI}(x_j) - k \langle \delta^2 \hat{n}_2(x_j) \rangle \tag{4.26}$$

where k is a parameter that can be set in order to minimize the SNR of the reconstruction. For $k = 0$ and for $k = \langle \hat{N}_1 \rangle / \langle \hat{N}_2 \rangle$ the GI and the DGI protocols are retrieved. Similarly to what done in Eq. 4.11, the uncertainty on $\langle S_k \rangle$ can be written as:

$$\delta^2 \langle S_k(x_j) \rangle = \frac{\langle \delta^2 \hat{N}_k \delta^2 \hat{n}_2(x_j) \rangle - \langle \delta \hat{N}_k \delta \hat{n}_2(x_j) \rangle^2}{H} \sim \frac{1}{H} \langle \delta^2 \hat{N}_k \rangle \langle \delta^2 \hat{n}_2(x_j) \rangle \tag{4.27}$$

where

$$\langle \delta^2 \hat{N}_k \rangle = \langle \delta^2 \hat{N}_1 \rangle + k^2 \langle \delta^2 \hat{N}_2 \rangle - 2k \langle \delta \hat{N}_1 \delta \hat{N}_2 \rangle \tag{4.28}$$

The optimization procedure consists in writing the SNR in terms of k and then in maximizing the expression respect to it. In this way an optimal value of k, function of the experimental quantities considered in our model, is found. We define S_{ODGI} as:

$$S_{ODGI}(x_j) = S_{GI}(x_j) - k_{opt} \langle \delta^2 \hat{n}_2(x_j) \rangle \tag{4.29}$$

The general expressions for k_{opt}, for the thermal and twin-beam case, are respectively:

$$k_{opt}^{th} = \frac{n_2^2 \bar{t}}{n_2^2 + M(n_2 + \Delta_{el}^2)} \tag{4.30}$$

$$k_{opt}^{tw} = \frac{n_2(n_2 + M\eta)\bar{t}}{n_2^2 + M(n_2 + \Delta_{el}^2)} \tag{4.31}$$

The only difference between the two expressions is in the term $M\eta$.

Let us now consider the expressions of k_{opt} in the limit of high and low brightness:

$$n_2/M \gg 1 \ : \ k_{opt}^{tw} = k_{opt}^{th} = \bar{t} = \frac{\langle \hat{N}_1 \rangle}{\langle \hat{N}_2 \rangle} \tag{4.32}$$

$$n_2/M \ll \eta \ : \ k_{opt}^{tw} = \frac{n_2}{n_2 + \Delta_{el}^2} \eta \frac{\langle \hat{N}_1 \rangle}{\langle \hat{N}_2 \rangle} \tag{4.33}$$

From these expressions it can be concluded that:

- In the limit of high brightness the ODGI coincides with the DGI. In this regime, the differential ghost imaging protocol is the best possible choice among all the estimators of the form $S_k = S_{GI} - k \langle \delta^2 \hat{n}_2(x_j) \rangle$.

- In the low brightness regime and ideal conditions (i.e. $\eta = 1$ and $\Delta_{el} = 0$) $k_{opt}^{tw} = \frac{\langle \hat{N}_1 \rangle}{\langle \hat{N}_2 \rangle}$. In this situation, again, the ODGI protocol reduces to the DGI.

- In the low brightness regime and realistic conditions ODGI departs from DGI, performing better than it. We will analyze the enhancement offered by ODGI in detail in the next sections.

- The experimental evaluation of k_{opt} requires the measurement of the channel efficiency η and the electronic noise of the camera Δ_{el}. To estimate these quantities a characterisation measurement is required.

Now, we would like to highlight a similarity between the optimized protocol presented here and the optimized absorption estimator proposed by Moreau et al. [45] and discussed in Sec. 3.3.2. In both contexts there are two strategies: one easier to be implemented since it does not require a characterization of set-up (in this context corresponding to the DGI protocol) and the other (in this context corresponding to the ODGI protocol) which, being optimized, performs better but requires the knowledge of various experimental parameters. Moreover, the two strategies coincide in ideal conditions, while the advantages offered by the optimization procedure become more and more relevant drifting away from $\eta = 1$ and $\Delta_{el} = 0$.

In the following the expressions which show the SNR improvement offered by the ODGI respect to GI and DGI are reported ($t_+ = 1, t_- = 0, \Delta_{el}^2 \ll n_2, n_2/M \ll \eta$):

$$\frac{\text{SNR}_{ODGI}^{tw}}{\text{SNR}_{GI}^{tw}} = \frac{1}{\sqrt{\eta^2(\epsilon - 1) + 1}} \tag{4.34}$$

$$\frac{\text{SNR}_{ODGI}^{tw}}{\text{SNR}_{DGI}^{tw}} = \sqrt{\frac{(\epsilon - 1)(\eta - 1) + 1}{\eta^2(\epsilon - 1) + 1}} \tag{4.35}$$

In Eq. 4.34, differently than in Eq. 4.25, the denominator is always smaller than 1 (being $0 < \epsilon < 1$). This confirms that ODGI always performs better than GI. In the ideal case of $\eta = 1$ we find back the scaling $1/\sqrt{\epsilon}$, as in Eq. 4.23. Similarly, in Eq. 4.35, the numerator is smaller than the denominator (being $\eta - 1 < \eta^2$), confirming that ODGI is always better than DGI. The improvement of ODGI respect to both DGI and GI can be appreciated in Fig. 4.9, in this case $\epsilon = 0.1$ is chosen. The best advantage over the two protocols at the same time is achieved for η such that the expressions in Eq. 4.34 and in Eq. 4.35 are equal. This condition is satified for $\eta = 0.5$. In correspondence of this value the ODGI advantage is maximum for $\epsilon \to 0$. In this limit:

$$\frac{\text{SNR}_{ODGI}^{tw}}{\text{SNR}_{GI}^{tw}} = \frac{\text{SNR}_{ODGI}^{tw}}{\text{SNR}_{DGI}^{tw}} = \frac{1}{\sqrt{0.5^2(\epsilon - 1) + 1}} \sim \frac{1}{\sqrt{0.75}} = 1.15 \tag{4.36}$$

Therefore, the optimization procedure in this regime is able to offer an SNR increment of 15%. However, the advantage of ODGI with respect to either GI or DGI separately can be much higher, respectively for low and large efficiency values, as shown in Fig. 4.9.
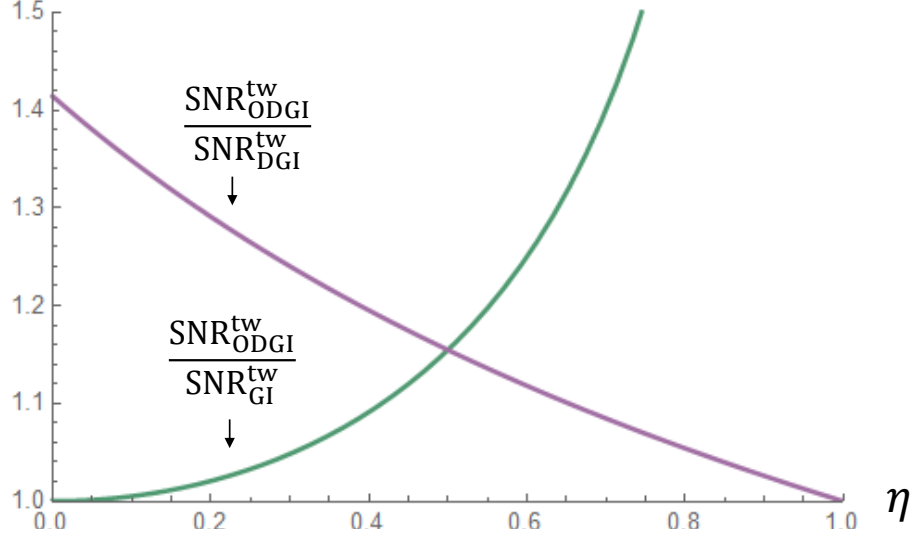
Figure 4.9: ODGI advantage over GI (green curve) and DGI (purple curve), in terms of SNR, in the low-brightness SPDC regime, in function of the channel efficiency η. The other relevant parameters are $n_2/M \sim 10^{-8}$ (i.e. low-brightness), $\Delta_{el} = 0$, $t_+ = 1$, $t_- = 0$, $\epsilon = 0.01$.

Finally, in Fig. 4.10, the enhancements offered by S_{DGI} and S_{ODGI} over the conventional protocol are reported as function of both efficiency, η, and number of detected photons per mode, n_2/M. Considering the front cut plane, corresponding to $n_2/M = 0.01$, the results discussed in the limit $n_2/M \ll 1$ are confirmed. Moreover, it emerges that, increasing the brightness of the source, the higher advantage of ODGI over both GI and DGI is achieved for lower values of η. This fact suggests that an optimal trade-off between the different parameters included in our model, e.g. efficiency and brightness, can be specifically designed in order to maximize the SNR of the reconstruction in the specific experimental situation considered.

4.4 Experimental set-up

In Sec.s 4.1.1, 4.2 and 4.3 we present three different ghost imaging protocols (S_{GI}, S_{DGI}, S_{ODGI} respectively), and we develop a theoretical model, in terms of experimental quantities and taking into account non- idealities (in particular the channel efficiency η and the electronic noise of the detector Δ_{el}). This is a full quantum model, describing both thermal and twin-beam sources in the high or low brightness regime. In this and in the following sections we experimentally validate the theoretical model in the low-brightness regime, using twin-beam states.
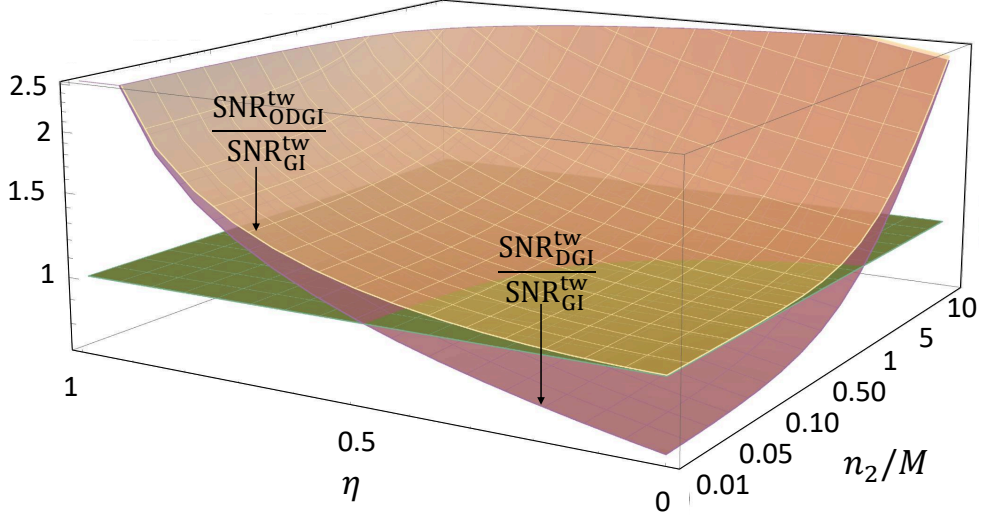
Figure 4.10: DGI and ODGI are compared in terms of SNR with GI, at varying both the channel efficiency, η, and the brightness of the source, n_2/M. The other relevant parameters are, $\Delta_{el} = 0$, $t_+ = 1$, $t_- = 0$, $\epsilon = 0.1$.

A scheme of the experimental set-up is reported in Fig. 4.11. To produce the twin-beam state we exploit the SPDC process in a BBO crystal. In particular, the non linear crystal is pumped with a laser of $\lambda = 405$ nm and power of 100 mW. The laser emission is triggered by a digital signal coming from the camera, i.e. the laser emits only in correspondence of the camera acquisition time. Using a system of two lenses, the correlation in momentum between two down-converted photons is mapped into spatial correlation at the detection plane. This is the same mechanism at the basis of the experiment described in Ch. 3, and is extensively discussed in Ch. 2 (see in particular Sec. 2.1). The detector is the same CCD camera used in the experiment described in Ch. 3. In this case we use 3 x 3 hardware binning: each macro-pixel measures 39μm, corresponding to 5μm at the object plane (being the magnification factor M=7.8). This value represents the ultimate resolution limit of our system. The binned pixel size roughly corresponds to the coherence area: this guarantees that the condition of statistical independence between two adjacent pixels assumed by our model is respected. At the same time, the resolution is maximized.

In our case both the beams go to the CCD, there is no real bucket detector. To simulate the outcome of the equivalent bucket detector, N_1, it is sufficient to integrate the CCD signal over the region of interest. Moreover, in our experiment the bucket detector is placed at the same distance as the pixeled detector, however, this is not strictly required.
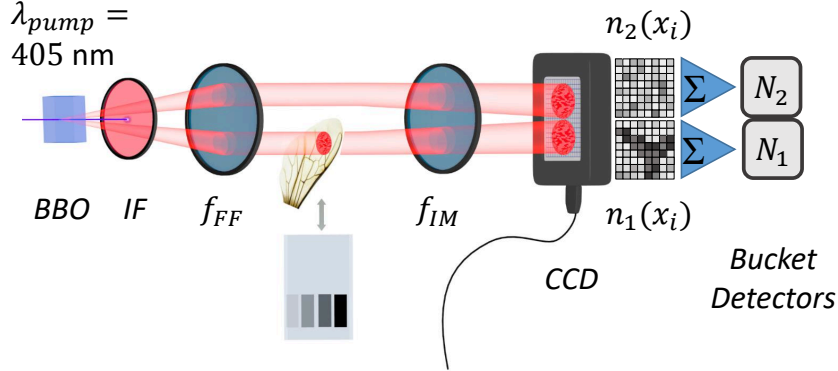
Figure 4.11: Scheme of the experimental set-up. In the Beta Barium Borate non linear crystal (BBO) a twin-beam state is generated. One of the two perfectly correlated beams interacts with the sample and is then detected by the charge coupled device camera (CCD). The other beam goes directly to the camera. The equivalent bucket detector on both channels can be easily simulated integrating over the two regions of interest. In a first part of the experiment a set of uniform depositions of different transmittance t_- is considered, while in a second part different kinds of insect wings are suspended in air and imaged. BBO: Beta Barium Borate non linear crystal, IF: interferential filter, f_{FF} = 1cm: focal length of the far-field lens, f_{IM} = 1.6cm: focal length of the imaging lens, CCD: coupled device camera.

In a first part of the experiment we reconstruct simple uniform objects of different absorption coefficients. They consist in metallic depositions of different thickness over a coated glass. The simplicity of these objects allow to quantitatively evaluate the SNR. In a second part of the experiment biological objects are considered, in order to demonstrate the potentialities of the technique towards real applications. In particular, a polistes wasp wing, a green bug wing and a ant wing are suspended in air and imaged.

4.4.1 Experimental parameters of the set-up

In this section we report on the experimental values of the parameters used in the model.

- η: the channel efficiency is estimated through an acquisition in absence of the absorbing sample, using the method described in Sec. 2.1.5. The values slightly differ from one acquisition to the other due to unavoidable modifications in the environment. The imbalance between the two channels is almost negligible, $\gamma \sim 1$. A typical value of measured efficiency is $\eta = 0.794 \pm 0.003$.

- n_2: the average number of photons detected per pixel per frame is $n_2 \sim 10^3$

- M: the number of modes detected per pixel per frame can be written as $M = M_{sp}M_{temp}$, where M_{sp} and M_{temp} are the number of spatial and temporal modes respectively. Being the dimension of a physical pixel roughly equal to the coherence area, $M_{sp} \sim 1$. To estimate M_{temp} we can consider that the coherence time of the SPDC process is $\sim 10^{-12}$ s and that the acquisition time for a frame is 50 ms. It follows that $M_{temp} \sim 5 \cdot 10^{10}$. It can be concluded: $M \sim 5 \cdot 10^{10}$. The number of photons emitted per spatio-temporal mode results $n_2/(M\eta) \sim 2.5 \cdot 10^{-8}$. Also if this is a rough estimate, it allows us to assert that we are in the low brightness regime, corresponding to the limit $n_2/(M\eta) \ll 1$.

- Δ_{el}: the electronic noise of the camera is experimentally estimated as described in Ch. 2. We have: $\Delta_{el} = 5e^-/(\text{pixel} \cdot \text{frame})$ for 100 kHz digitization rate and $\Delta_{el} = 13e^-/(\text{pixel} \cdot \text{frame})$ for 2 MHz digitization rate.

- H: the number of frames acquired differs in the different cases and will be always specified. Typical number of acquired images, while using a digitization rate of 100 kHz, is $H \sim 10^4 \div 10^5$. The time necessary for collecting this number of frames is few hours. This is due to the fact that acquiring data from a region of $\sim 5 \cdot 10^4$ pixels, as it is necessary in this application, the read-out time of a single frame dramatically increases.

- $\mathcal{N}$: the number of pixels of the reconstructed area are 28 x 34 when considering the metallic deposition and 57 x 57 (corresponding to an area of $(285 \ \mu\text{m})^2$ at the object plane) for the biological objects.

- t_+: this parameter is well defined only in the case of the two level objects. In our case the high transmittance part of the objects is roughly $t_+ \sim 1$ (the deposition covers only a part of the field of view, the coated glass is present in both channels and its losses are therefore included in the channel efficiency, evaluated with the glass inserted)

- t_-: this parameter is well defined only in the case of the two level objects. In our case we use four different samples of transmittance $t_- = 0, 0.25, 0.34, 0.52$

- ϵ: this parameter is well defined only in the case of the two level objects. It represents the fraction of the reconstructed area of lower transmittance. $0 < \epsilon < 1$, low values of ϵ correspond to "small" objects in the field of view.

4.5 Experimental validation of the theoretical model

In this section we report the experimental results obtained using the set-up described in Sec. 4.4, with the aim of validating the theoretical model. In particular, the SNR dependence from ϵ, t_- and η, for the three protocols, is experimentally explored. Since the protocols performances are evaluated in terms of the SNR, in Sec. 4.5.1 the details of the

SNR experimental estimation are discussed. For this analysis the two level transmission objects are used.

4.5.1 Evaluation of the SNR

According to Eq. 4.10 for experimentally evaluating the SNR, in the case of a two level object of transmission t_+ and t_-, it is necessary to estimate:

- $\langle S_+ \rangle$ and $\langle S_- \rangle$, mean values of the reconstructed image over the regions of transmittance t_+ and t_- respectively.

- $\delta^2 \langle S_+ \rangle$ and $\delta^2 \langle S_- \rangle$, their associated variances.

This can be easily done considering the spatial statistics on two different regions of the reconstructed image, in correspondence of $t = t_+$ and $t = t_-$. Fig. 4.12(a) reports an example of direct image obtained averaging over 5000 frames, in this case $t_- = 0.75$ and $\epsilon = 0.53$. Fig. 4.12(b) is the reconstructed image obtained using the GI protocol. To obtain the SNR the two regions, A and B, are considered. Simply calculating the average and the standard deviation of $S(x_j)$ in these two regions the values of $\langle S_\pm \rangle$ and $\delta^2 \langle S_\pm \rangle$ are estimated. Regions A and B are chosen in order to avoid border effects, but at the same time wide enough to provide sufficient statistics.
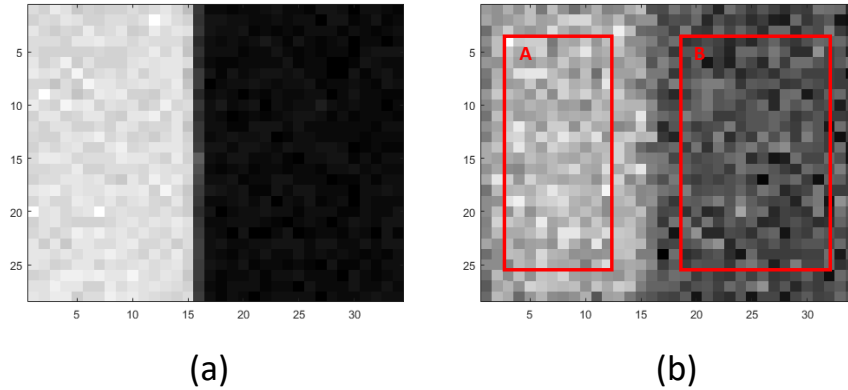

(a)   (b)

Figure 4.12: (a) direct image, averaging over 5000 frames, of the two level object considered (in this case $t_- = 0.25$). (b) reconstructed image, using 40000 frames. The two regions A and B are the regions used to evaluate the experimental signal-to-noise ratio (SNR) of the reconstruction.

The direct image in Fig. 4.12(a) is obtained selecting a 28 x 34 region from the full-frame image acquired. An example of full-frame image is reported in Fig. 4.13. Varying the region considered (as for example the R_1-R_2-R_3 regions in figure), different values

of the object occupation fraction ϵ can be explored. We consider regions corresponding to $\epsilon = 0.17, 0.29, 0.41, 0.53, 0.65, 0.76$.
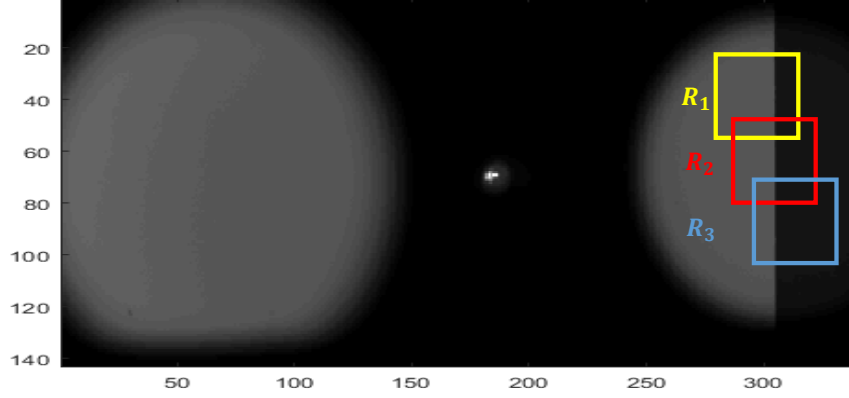

Figure 4.13: Example of a full-frame direct image acquired by the camera. Considering regions R_1-R_2-R_3 the reconstructed image allows to obtain different occupation fraction ϵ.

4.5.2 SNR vs object occupation fraction

In Fig.s 4.14-4.15-4.16-4.17 the SNR is plotted in function of the occupation fraction ϵ, for the four available depositions. Green color refers to GI, purple to DGI and yellow to ODGI protocol. The dots are the experimental data, obtained using the procedure described in Sec. 4.5.1. For each deposition $H \sim 3 \cdot 10^4$ frames are acquired at the digitization rate of 100 kHz. The experimental data are fitted using the model theoretical expressions (e.g. Eq. 4.14 for GI), leaving the efficiency η as a free parameter. The dashed lines are the fitting curves. The coloured area corresponds to the 1σ confidence region. It is obtained propagating the uncertainty on the different parameters in the expressions of the SNR. As uncertainty on η, the value provided by the fit procedure is used. Below, we report the values of η estimated from the fits of each data series, with their 2-σ uncertainty, and the corresponding value independently estimated (using the method described in Sec. 2.1.5), $\bar{\eta}$.

$$t_- = 0$$
$$\text{GI} \quad \eta_{GI} = (0.800 \pm 0.013)$$
$$\text{DGI} \quad \eta_{DGI} = (0.787 \pm 0.008)$$
$$\text{ODGI} \quad \eta_{DGI} = (0.787 \pm 0.008)$$
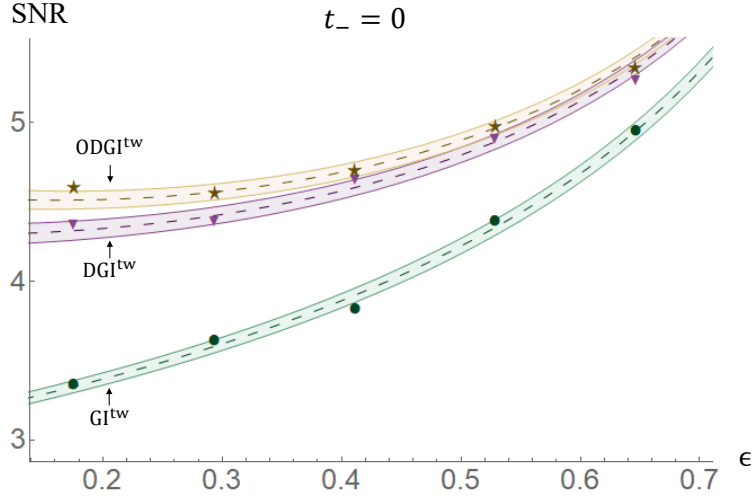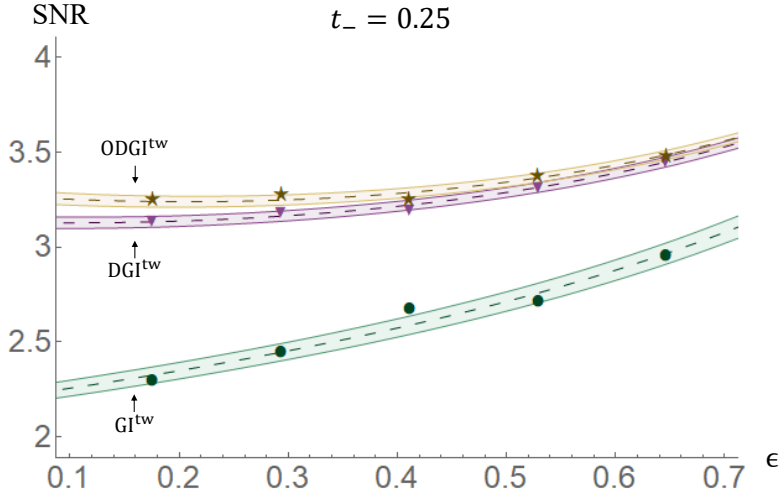$$\bar{\eta} \quad (0.794 \pm 0.004)$$

93

Figure 4.14: SNR in function of the object occupation fraction ϵ, for lower transmission of the two level object $t_- = 0$. Green color refers to GI, purple to DGI and yellow to ODGI. The dots are the experimental data, obtained for number of frames acquired $H \sim 3 \cdot 10^4$ and a total number of pixels of the image $\mathcal{N} = 952$. The dashed lines are obtained fitting the data with the theoretical model, considering η as free parameter. The confidence region at 1σ is reported as colored bands around the curves

$$t_- = 0.25$$

GI	$\eta_{GI} = (0.80 \pm 0.02)$
DGI	$\eta_{DGI} = (0.795 \pm 0.003)$
ODGI	$\eta_{DGI} = (0.790 \pm 0.005)$
$\bar{\eta}$	(0.792 ± 0.004)

$$t_- = 0.34$$

GI	$\eta_{GI} = (0.78 \pm 0.02)$
DGI	$\eta_{DGI} = (0.794 \pm 0.007)$
ODGI	$\eta_{DGI} = (0.804 \pm 0.007)$
$\bar{\eta}$	(0.797 ± 0.004)

$$t_- = 0.52$$

GI	$\eta_{GI} = (0.786 \pm 0.009)$
DGI	$\eta_{DGI} = (0.798 \pm 0.006)$
ODGI	$\eta_{DGI} = (0.798 \pm 0.006)$
$\bar{\eta}$	(0.794 ± 0.004)

Figure 4.15: SNR in function of the object occupation fraction ϵ, for lower transmission of the two level object $t_- = 0.25$. Green color refers to GI, purple to DGI and yellow to ODGI. The dots are the experimental data, obtained for number of frames acquired $H \sim 3 \cdot 10^4$ and a total number of pixels of the image $\mathcal{N} = 952$. The dashed lines are obtained fitting the data with the theoretical model, considering η as free parameter. The confidence region at 1σ is reported as colored bands around the curves

In order to consider the performances of the three protocols in the presence of higher losses, a neutral filter is placed on the beams path and the SNR is evaluated for different values of ϵ. In Fig. 4.18 the experimental results referring to this experimental condition are reported. As before, the dots are the experimental data, the dashed lines are the fitting curves, obtained leaving η as free parameter, the coloured area is the 1σ confidence region. The 2σ statistical uncertainty obtained from the fit for η, as well as the value independently estimated, are reported. Note that in this case DGI does not offer any advantage over the GI.On the contrary, the optimized protocol offers an improvement over both of them. For $\epsilon = 0.17$ we have an advantage of roughly 12%.

$$t_- = 0, \eta \sim 0.5$$

$$\text{GI} \quad \eta_{GI} = (0.529 \pm 0.003)$$
$$\text{DGI} \quad \eta_{DGI} = (0.536 \pm 0.009)$$
$$\text{ODGI} \quad \eta_{DGI} = (0.524 \pm 0.006)$$
$$\bar{\eta} \quad (0.529 \pm 0.003)$$

From the presented results we conclude that the experimental data validate our theoretical model. In all the cases considered the data are properly fitted by the curves, falling almost all of them into the 1σ confidence region. A further element of consistency is given by the comparison between the value of $\bar{\eta}$ obtained using a Klishko-like
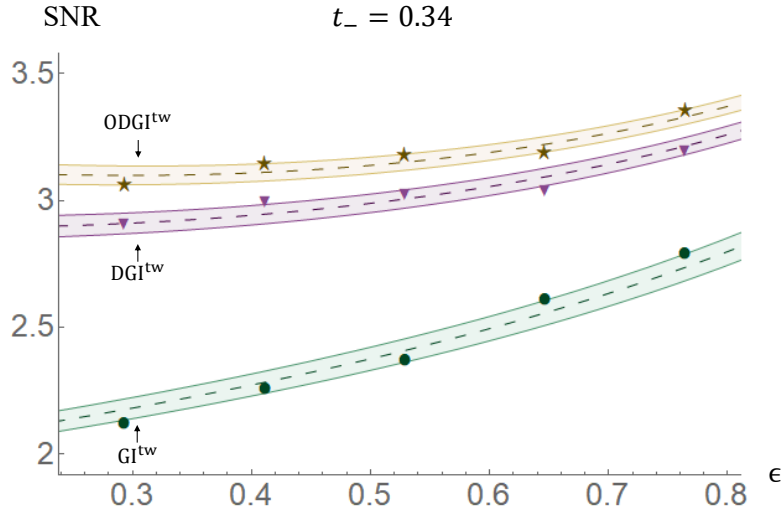
Figure 4.16: SNR in function of the object occupation fraction ϵ, for lower transmission of the two level object $t_- = 0.34$. Green color refers to GI, purple to DGI and yellow to ODGI. The dots are the experimental data, obtained for number of frames acquired $H \sim 3 \cdot 10^4$ and a total number of pixels of the image $\mathcal{N} = 952$. The dashed lines are obtained fitting the data with the theoretical model, considering η as free parameter. The confidence region at 1σ is reported as colored bands around the curves

method (see Sec. 4.4.1) and the values of η obtained from the fit. In all the cases these values are compatible with a confidence level of 95%.

4.5.3 SNR vs object contrast

Fig. 4.19 reports, for the three protocols considered, the SNR in function of the lower transmittance of the two-level deposition, t_-. Since the highest transmission is fixed to $t_+ = 1$, this corresponds to vary the object contrast. The experimental data are obtained by fixing the value of ϵ (i.e. $\epsilon = 0.52$). The SNR for the four available depositions is evaluated according to the procedure described in Sec. 4.5.1. Green colour refers to GI protocol, purple to DGI and yellow to ODGI. The dots correspond to the experimental data, the dashed curves are obtained fitting the experimental data with the theoretical model, leaving η as a free parameter, the coloured areas are the 1σ confidence regions. The confidence intervals for η obtained from the fit, as well as the value independently estimated, $\bar{\eta}$, are reported below.
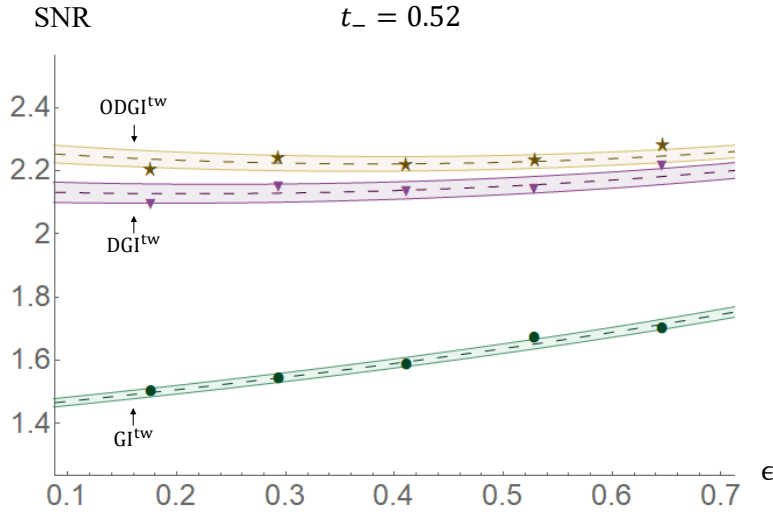
Figure 4.17: SNR in function of the object occupation fraction ϵ, for lower transmission of the two level object $t_- = 0.52$. Green color refers to GI, purple to DGI and yellow to ODGI. The dots are the experimental data, obtained for number of frames acquired $H \sim 3 \cdot 10^4$ and a total number of pixels of the image $\mathcal{N} = 952$. The dashed lines are obtained fitting the data with the theoretical model, considering η as free parameter. The confidence region at 1σ is reported as colored bands around the curves

$$t_- = 0.52$$

GI	$\eta_{GI} = (0.80 \pm 0.03)$
DGI	$\eta_{DGI} = (0.794 \pm 0.009)$
ODGI	$\eta_{DGI} = (0.792 \pm 0.018)$
$\bar{\eta}$	(0.795 ± 0.004)

Also in this case we conclude that the theoretical model is in good agreement with the experimental data. All the experimental data are in the 1σ confidence region and the values of η obtained from the fit are compatible, with a confidence level of 95%, with the value independently estimated.

4.6   Reconstruction of a biological object

In this section we use the set-up and the different protocols considered to reconstruct different biological objects, in order to demonstrate how the technique could be used in real applications. A polistes wasp wing, a green bug wing and a ant wing are considered.
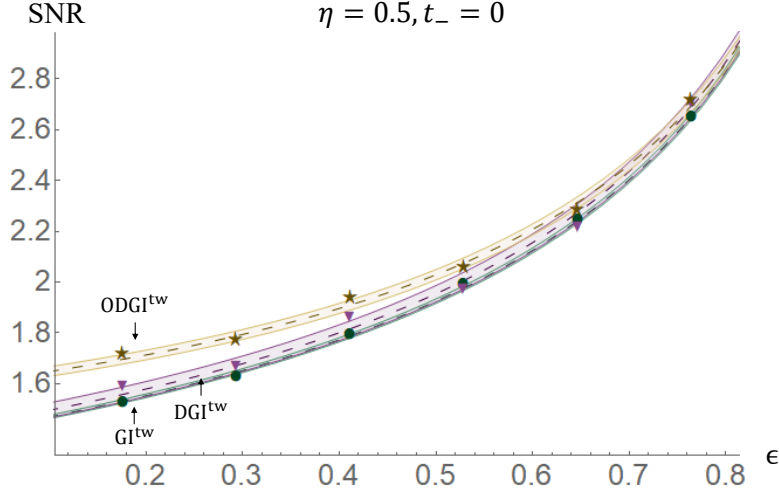
Figure 4.18: SNR in function of the object occupation fraction ϵ, for lower transmission of the two level object $t_- = 0$. In this case a neutral filter is placed on the beams path in order to lower the channel efficiencies to $\eta \sim 0.5$. Green color refers to GI, purple to DGI and yellow to ODGI. The dots are the experimental data, obtained for number of frames acquired $H \sim 3 \cdot 10^4$ and a total number of pixels of the image $\mathcal{N} = 952$. The dashed lines are obtained fitting the data with the theoretical model, considering η as free parameter. The confidence region at 1σ is reported as colored bands around the curves

4.6.1 Polistes wasp wing

The wasp wing is suspended in air and $2 \cdot 10^5$ frames were acquired at 2MHz digitization rate. In Fig. 4.20(a) the direct image of the detail considered (57 x 57 pixels), averaged over 5000 frames, is reported. Fig. 4.20(b) and Fig. 4.20(c) are the ghost-imaging reconstructions, using S_{GI} and S_{ODGI} respectively. At this digitization rate the electronic noise is higher than in the other case, and it lowers the improvement offered by the ODGI protocol. However, it can be appreciated at sight that the ODGI image is less noisy than the GI one, and few more details can be appreciated, as the edge of the wing in the left side. The channel efficiency corresponding to this acquisition is $\eta \sim 0.8$: as it emerges from the theoretical analysis presented in Sec. 4.3, in this high-efficiency regime the improvement offered from the optimized protocol over the differential one are quite limited, and cannot be appreciated at sight, this is why the DGI reconstructions are not reported. The resolution achieved in the reconstruction, corresponding to the coherence area at the object plane, is $5\mu m$. We didn't focus on improving this value, we mention that it is aligned with the other ghost imaging experiments present in literature (as for example [63]).
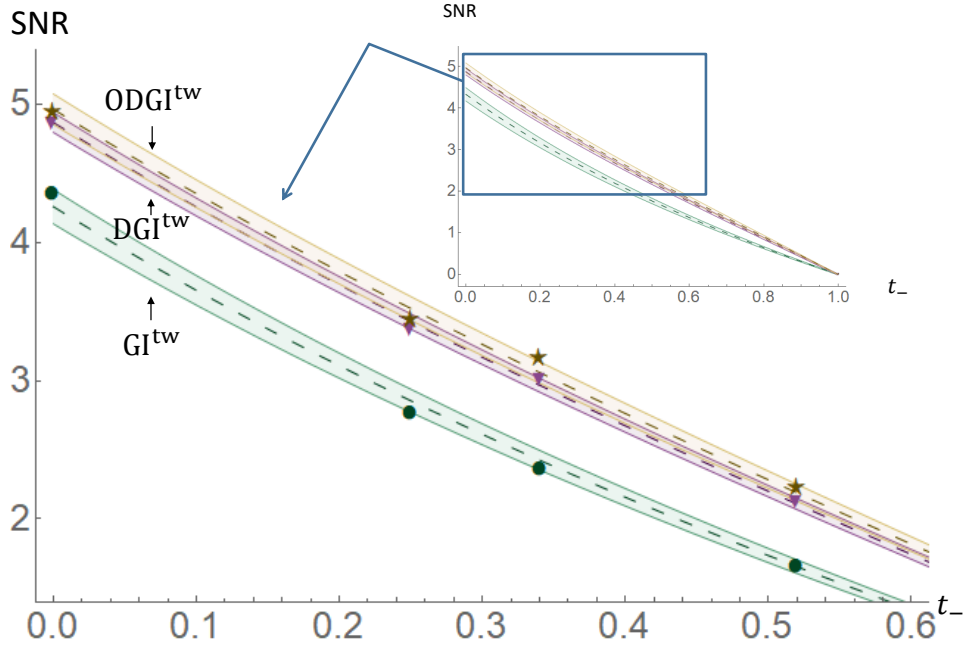
Figure 4.19: SNR in function of the lower transmission of the two level object t_-, for the object occupation fraction $\epsilon = 0.52$. Green color refers to GI, purple to DGI and yellow to ODGI. The dots are the experimental data, obtained for number of frames acquired $H \sim 3 \cdot 10^4$ and a total number of pixels of the image $\mathcal{N} = 952$. The dashed lines are obtained fitting the data with the theoretical model, considering η as free parameter. The confidence region at 1σ is reported as colored bands around the curves

Reconstruction of the total images, technical notes

The total dimension of the biological detail reconstructed is (57 x 57) pixels. In order to achieve a sufficiently high SNR with a reasonable acquisition time the total area is divided into 9 sub regions of (19 x 19 pixels), and each region is reconstructed independently. The 9 reconstructions are finally placed side by side. This process is particularly straightforward while considering the GI protocol, while few more data elaboration is necessary in the other cases. As stated in Eq.s 4.6-4.7 for the GI protocol the reconstructed matrix $S_{GI}(x_j)$ is proportional to the absorption profile of the object, with a constant that, at least in principle, is invariant from one sub-region to the other. Therefore, simply placing side by side the 9 reconstruction, the total image is recovered. This is shown in Fig. 4.21. When considering the DGI (or ODGI) protocol the situation is different since, as it emerges in Eq. 4.21, $S_{DGI}(x_j)$ (or $S_{ODGI}(x_j)$) is not proportional to $t(x_j)$. This is the quantity we are interested in, which is continuous from one sub-region to the other, and which we need to recover.Simply placing side by side the reconstructions the result is the one presented in Fig. 4.22. In order to recover a quantity proportional
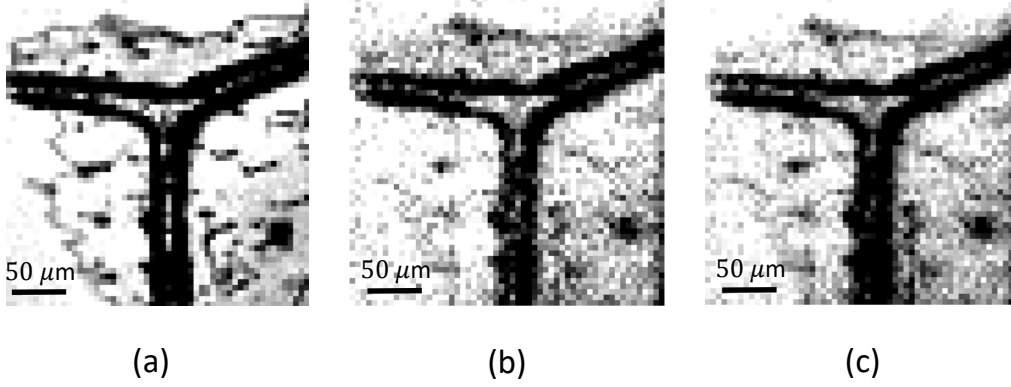
Figure 4.20: Images of a wasp wing with spatial resolution of $(5\mu m)^2$. (a) direct image, obtained averaging 5000 frames. (b)-(c) reconstruction using the GI and ODGI protocol respectively. The total region is divided into 9 sub-region, the protocol is applied to each of them and finally the complete image is recovered. 40 blocks of 5000 images acquired at 2MHz digitization rate are processed.
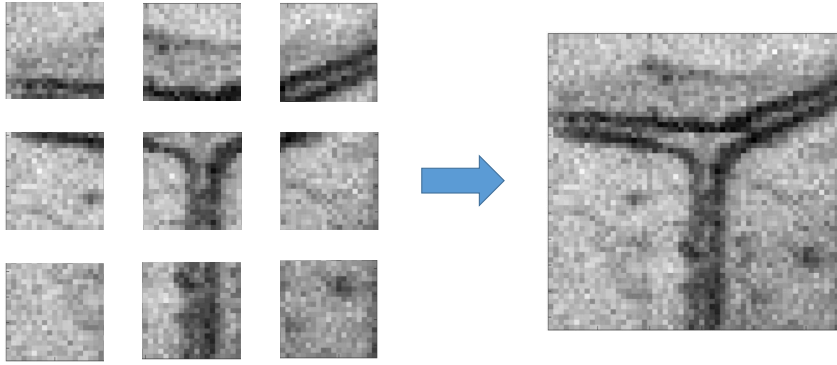

Figure 4.21: Intermediate step for the reconstruction of a (57 x 57) pixels detail of a wasp wing. The total area is divided in 9 sub-regions and each region reconstructed independently using the GI protocol. The resulting reconstructions are then placed side by side to obtain the total image.

to the absorption profile, $t(x_j)$, we exploit the relation between GI and DGI (or ODGI) in Eq. 4.26 (being $S_k(x_j) \equiv S_{DGI}(x_j)$ or $S_{ODGI}(x_j)$):

$$t(x_j) \propto S_{GI}(x_j) = S_k(x_j) + k\langle \delta^2 \hat{n}_2(x_j)\rangle \tag{4.37}$$

where k ($k = \langle \hat{N}_1\rangle/\langle \hat{N}_2\rangle$ for DGI and $k = k_{opt}$ for ODGI) and $\langle \delta^2 \hat{n}_2(x_j)\rangle$ can be both independently evaluated. Note that, depending on the mean absorption of the sub-region, $\langle \hat{N}_1\rangle$ (and consequently k) is different from one sub-region to the other.

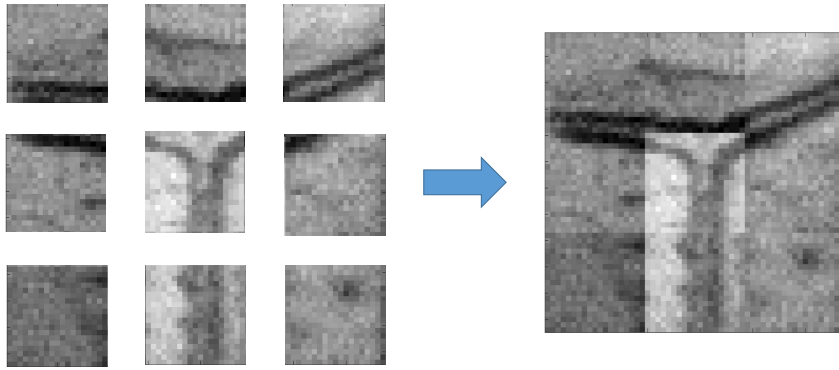Using this method the total image is recovered, without any discontinuity from one

Figure 4.22: Intermediate step for the reconstruction of a (57 x 57) pixels detail of a wasp wing. The total area is divided in 9 sub-regions and each region reconstructed independently using the ODGI protocol. The resulting reconstructions are then placed side by side to obtain the total image. The resulting reconstruction presents evident discontinuity from one sub-region to the next one.

sub-region to the other one. An example is reported in Fig. 4.23. Furthermore, in order
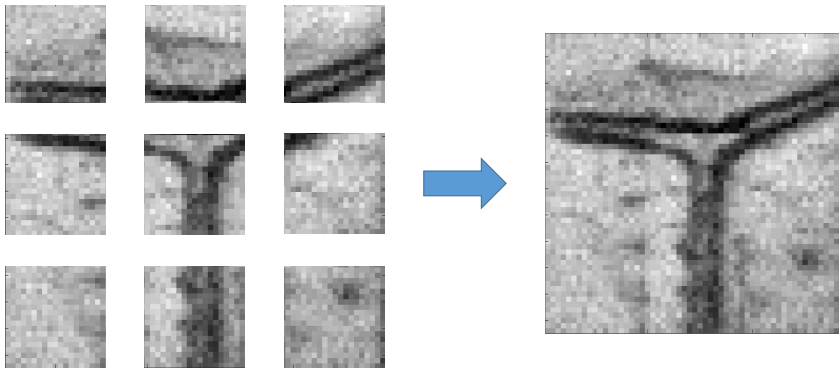

Figure 4.23: Intermediate step for the reconstruction of a (57 x 57) pixels detail of a wasp wing. The total area is divided in 9 sub-regions and each region reconstructed independently using the ODGI protocol. The resulting reconstructions are processed as described in the text and then placed side by side to obtain the total image. The discontinuity observed in Fig. 4.22 disappears.

to better appreciate the difference between the protocols it is possible to adjust the contrast. This procedure is used to obtain the final images in Fig. 4.20. The procedure described here is repeated for all the biological samples considered.

4.6.2   Green bug wing

The green bug wing is suspended in air and $4 \cdot 10^4$ acquired at 100kHz digitization rate. Fig. 4.24(a) shows the direct image of a portion of the wing (57 x 57 pixels), averaged over 5000 frames. The reconstruction of two details is reported in Fig. 4.24(b) and 4.24(c). In Fig. 4.24(c) it can be appreciated how the edge, which is almost lost in the noise when conventional protocol is used, emerges as more defined using S_{ODGI}. Fig. 4.24(b) illustrates that the ODGI protocol requires less frames to properly reconstruct the object. In particular, we notice that the SNR of the reconstruction using 40000 frames and the conventional GI protocol is comparable to the reconstruction using 20000 frames and the optimized protocol. This result is in agreement with the prediction of our model. Having estimated the values of the different parameters as $t_- = 0.36, t_+ = 0.8, \eta = 0.78, \epsilon = 0.07$ we obtain:

$$\frac{\text{SNR}_{ODGI}}{\text{SNR}_{GI}} \sim 1.35 \qquad (4.38)$$

This means that, to reach the same ODGI performances while using the conventional protocol, the number of frames needs to be increased by a factor $1.35^2 \sim 1.82$. Decreasing the number of frames, and therefore the acquisition time, can be of the utmost importance in real situations, where unavoidable drifts in temperature and in the source should be taken into account. Moreover, the reduction of acquisition time corresponds to reduction in the photon dose for the sample investigated. According to what discussed in Sec. 1.5.3, this aspect can be relevant in many practical situations, in particular when dealing with biological samples.

The channel efficiency corresponding to this acquisition is $\eta \sim 0.8$: as it emerges from the theoretical analysis presented in 4.3, in this high-efficiency regime the improvement offered from the optimized protocol over the differential one is quite limited, and cannot be appreciated at sight in the examples reported here. The resolution achieved in the reconstruction, corresponding to the coherence area at the object plane, is 5μm.

4.6.3   Ant wing

The ant wing is suspended in air and $4 \cdot 10^4$ acquired at 100kHz digitization rate. In Fig. 4.25(a) the direct image of size 57 x 57 pixels, averaged over 5000 frames, is reported. Also in this case the resolution achieved is 5μm. In Fig.s 4.25(b)-(c) we report the ghost-imaging reconstructions, using S_{GI} and S_{ODGI} respectively. The direct image presents several details and complex structures, which are successfully reconstructed with both protocols. Also if a SNR quantitative analysis is not possible, being the object too complex, it can be appreciated at sight that the ODGI image is slightly less noisy than the GI one. It can be also noted that the brighter spots in the direct image are not present in the reconstructions. This is due to the fact that these spots are not due to a very low transmittance of the sample (being the number of photons in those pixels even higher than the number of photons in absence of the sample), but they can be attributed to some scattering effect. Scattering deflects the photons, thus deleting the
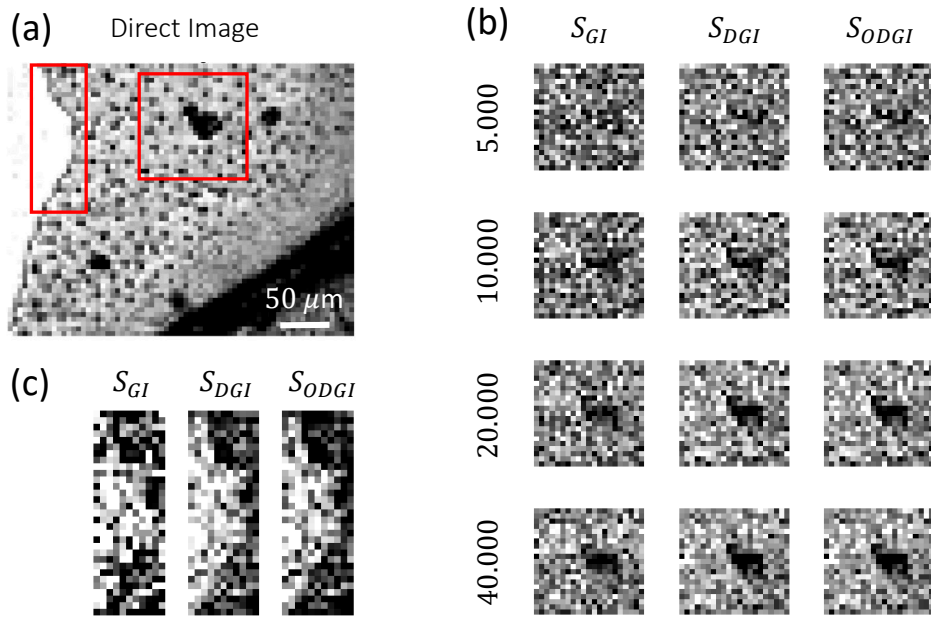
Figure 4.24: Images of a green bug wing with spatial resolution of $(5\mu m)^2$. (a) direct image, obtained averaging 5000 frames. (b)-(c) reconstruction of two details using the GI, DGI and ODGI protocol respectively. In (b) the reconstructions obtained for different number of frames are reported, while in (c) the total amount of available frames (8 blocks of 5000 images) is used. In this case the 100kHz digitization rate is used.

pixel-to-pixel correlations. This fact could be exploited to use GI (and its variants) for distinguishing actual transmission losses from other spurious effects as scattering. Note that this distinction is not possible with direct imaging.
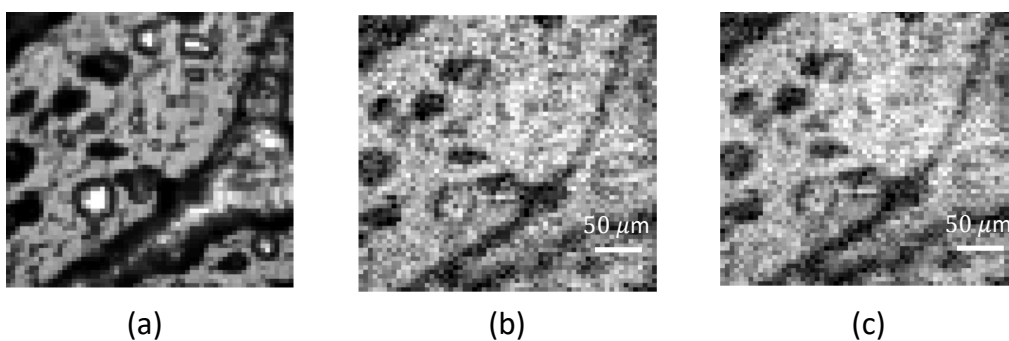

Figure 4.25: Images of a ant wing with spatial resolution of $(5\mu m)^2$. (a) direct image, obtained averaging 5000 frames. (b)-(c) reconstruction using the GI and ODGI protocols respectively. 8 blocks of 5000 images, acquired at 100kHz digitization rate are processed.

Chapter 5

Quantum enhanced correlated interferometry

The advantages of using squeezed states of light in one interferometer are well known. In particular, the advantage in terms of phase sensitivity has been demonstrated both theoretically [65] and experimentally [16]. Nevertheless, the potentialities of quantum light in correlated interferometry have received much less attention. In this chapter, experimental results demonstrating how quantum light can enhance the sensitivity of this kind of systems are presented. In particular, two different quantum states of light are considered and their performances compared.

The chapter is organized as follows:

- In Sec. 5.1, following Caves' reasoning [65], we demonstrate how a squeezed vacuum state, injected from the classically unused interferometer port, enhances the phase sensitivity of a single interferometer.

- In Sec. 5.2, Hogan's theory [66], which shows how correlated interferometry could be useful for probing quantum gravity effects and which inspired our work, is briefly presented.

- In Sec. 5.3, the theoretical results demonstrating how quantum light can enhance the sensitivity in correlation measurements are discussed. In particular, we refer to [67, 68].

- In Sec. 5.4 the experimental set-up I worked on is described. Having joined the experiment in an advanced phase, I advice [69] for all the technical details. This set-up has been built in the Technical University of Denmark (DTU), in collaboration with the U. L. Andersen group.

- Finally, in Sec.s 5.5-5.6, the experimental results are reported and discussed.

5.1 Quantum light in one interferometer

The idea of using quantum light in one interferometer dates back 1981, when Caves in [65] demonstrated how the injection of a squeezed vacuum state in an interferometer can lead to an enhancement in its phase sensitivity. Nowadays, this idea is exploited in gravitational wave detectors such as LIGO and GEO [16, 70, 71], and allows to increase the sensitivity below the shot-noise limit. Being the opportunities of squeezed vacuum in one single interferometer particularly relevant to understand the potentialities of quantum light in more complicated interferometric systems, we report here the demonstration of how this quantum state leads to a phase sensitivity enhancement.

5.1.1 Ideal case, without losses

Let us consider a simple Michelson interferometer (MI) of phase ϕ. According to Sec. 1.1.3, the MI can be modeled as a beam splitter of transmittance $\tau = \cos^2 \frac{\phi}{2}$, see Fig. 5.1. Aim of a measurement is to estimate the phase ϕ with the smallest possible uncertainty.
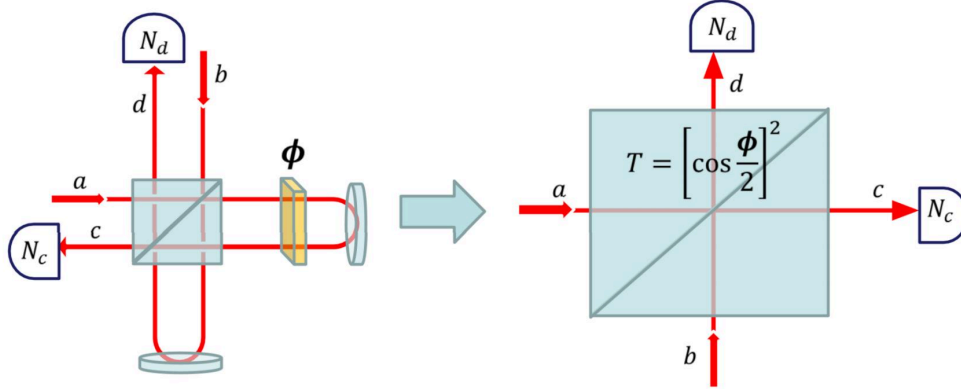
.

Figure 5.1: Scheme describing the equivalence between a MI of phase ϕ and a BS of transmittance $\tau = \cos^2 \phi/2$.

We cannot directly measure the phase, but we can estimate it through another observable, i.e. an hermitian combination of the output modes. In particular, here we consider the intensity at the anti-symmetric port, $\hat{N}_c = \langle \hat{c}^\dagger \hat{c} \rangle$. As input states we use:

- $\hat{b} \to |\sqrt{\mu}e^{i\theta}\rangle$, coherent state. Without loss of generality we can set $\theta = 0$.

- $\hat{a} \to \hat{S}(\psi)|0\rangle$, squeezed vacuum state (see Sec. 1.6.2). $\psi = |\psi|e^{i\xi}$, without loss of generality we can set $\xi = 0$. We retrieve the classical case, where $\hat{a}$ corresponds to the coherent vacuum, considering $\psi = 0$.

Using Eq. 1.24 and the results on the quadratures obtained in Eq. 1.140, we have:

$$\langle \hat{c}^\dagger \hat{c} \rangle = \tau \langle \hat{a}^\dagger \hat{a} \rangle + (1-\tau)\langle \hat{b}^\dagger \hat{b} \rangle + i\sqrt{\tau(1-\tau)}\langle \hat{b}^\dagger \hat{c} - \hat{c}^\dagger \hat{b} \rangle =$$

$$= \tau\lambda + (1-\tau)\mu + \sqrt{\tau(1-\tau)}\sqrt{2\mu}\langle \hat{X}_{\phi+\frac{\pi}{2}} \rangle = \tau\lambda + (1-\tau)\mu \tag{5.1}$$

where we name the mean number of photons in the two input modes as $\langle \hat{n}_b \rangle = \langle \hat{b}^\dagger \hat{b} \rangle = \mu$ and $\langle \hat{n}_a \rangle = \langle \hat{a}^\dagger \hat{a} \rangle = \lambda = \sinh^2|\psi|$. By definition, the variance on $\hat{N}_c$ is:

$$\Delta^2 \hat{N}_c = \langle \hat{c}^\dagger \hat{c} \hat{c}^\dagger \hat{c} \rangle - \langle \hat{c}^\dagger \hat{c} \rangle^2 \tag{5.2}$$

The evaluation of the first term leads to:

$$\langle \hat{c}^\dagger \hat{c} \hat{c}^\dagger \hat{c} \rangle = \tau^2 \langle \hat{n}_a^2 \rangle + (1-\tau)^2 \langle \hat{n}_b^2 \rangle - \tau(1-\tau)\langle (\hat{a}^\dagger \hat{b} - \hat{b}^\dagger \hat{a})^2 \rangle + 2\tau(1-\tau)\langle \hat{n}_a \hat{n}_b \rangle \tag{5.3}$$

which, for the input states considered, simplifies in:

$$\langle \hat{c}^\dagger \hat{c} \hat{c}^\dagger \hat{c} \rangle = \tau^2 \langle \hat{n}_a^2 \rangle + (1-\tau)^2 \langle \hat{n}_b^2 \rangle - \tau(1-\tau)(\mu+\lambda) + 4\tau(1-\tau)\lambda\mu - \tau(1-\tau)\mu(\langle \hat{a}^{\dagger 2} \rangle + \langle \hat{a}^2 \rangle) \tag{5.4}$$

For the term $\langle \hat{c}^\dagger \hat{c} \rangle^2$ we have:

$$\langle \hat{c}^\dagger \hat{c} \rangle^2 = \tau^2 \lambda^2 + (1-\tau)^2 \mu^2 + 2\tau(1-\tau)\lambda\mu \tag{5.5}$$

In conclusion, the variance on $\hat{N}_c$ can be written as:

$$\Delta^2 \hat{N}_c = \tau^2 \Delta^2 \hat{n}_a + \tau(1-\tau)\lambda + (1-\tau)\mu[1 + 2\tau\lambda - 2\tau\sqrt{\lambda(1+\lambda)}\cos(2\theta)] =$$

$$= \tau^2 \Delta^2 \hat{n}_a + \tau(1-\tau)\lambda + (1-\tau)\mu[1 + \tau e^{-2|\psi|} - \tau] \tag{5.6}$$

where in the last equation we use $\theta = 0$. A further assumption is necessary at this point: we consider the case of $\tau \sim 1$. This assumption corresponds to the experimental situation of working close to the dark fringe, $\phi \sim 0$. In this condition almost all the power injected returns back toward the laser. At the same time a strong coherent beam is assumed, in particular we consider that the power detected at the output port is mainly given by the coherent photons:

$$(1-\tau)\mu \gg \tau\lambda \tag{5.7}$$

Considering Eq. 5.6 in the limit of Eq. 5.7, we have:

$$\Delta^2 \hat{N}_c \sim 2\lambda(1+\lambda) + \tau(1-\tau)\mu e^{-2|\psi|} + (1-\tau)^2 \mu \sim \tau(1-\tau)\mu e^{-2|\psi|} + (1-\tau)^2 \mu =$$

$$= \cos^2(\phi/2)\sin^2(\phi/2)\mu e^{-2|\psi|} + (\sin^2(\phi/2))^2 \mu \tag{5.8}$$

and for the mean value:

$$\langle \hat{N}_c \rangle = \langle \hat{c}^\dagger \hat{c} \rangle \sim (1-\tau)\mu = \sin^2(\phi/2)\mu \tag{5.9}$$

Being interested in ϕ estimation, we propagate the uncertainty using the conventional uncertainty propagation rule:

$$\Delta\phi = \frac{\Delta(\hat{c}^\dagger\hat{c})}{|\partial_\phi\langle\hat{c}^\dagger\hat{c}\rangle|} = \frac{\sqrt{\sin^2\frac{\phi}{2} + \cos^2\frac{\phi}{2}e^{-2|\psi|}}}{\cos\frac{\phi}{2}\sqrt{\mu}} \tag{5.10}$$

In the classical limit, i.e. $|\psi| = 0$, using also the dark-fringe condition, we have:

$$\Delta\phi_{cl} = \frac{\sqrt{2}}{\sqrt{\mu(1 + \cos\phi)}} \sim \frac{1}{\sqrt{\mu}} \propto \frac{1}{\sqrt{P}} \tag{5.11}$$

where $P = \mu\hbar\omega$ is the power of the coherent beam entering the interferometer. Note that the typical shot-noise scaling, discussed in Sec. 1.5.3, is retrieved. This is the best possible achievement while using classical states of light. In this case, in order to increase the ϕ sensitivity, the only possibility is to increase the input power. In practical situations this is not always possible, for example because a further increase in the power would lead to the appearance of new sources of noise such as thermal and radiation pressure noise.

The injection of a squeezed vacuum state through the $\hat{a}$ port, working close to the dark fringe, allows the following quantum enhancement:

$$\frac{\Delta\phi_{sq}}{\Delta\phi_{cl}} = \sqrt{\sin^2\frac{\phi}{2} + \cos^2\frac{\phi}{2}e^{-2|\psi|}} \sim e^{-|\psi|} \tag{5.12}$$

The higher is the squeezing factor $|\psi|$, the higher is the advantage over the classical counter part.

5.1.2 Role of losses

In Sec. 5.1.1 the potentiality of squeezing in a single ideal interferometer is demonstrated. However, the hypothesis of no losses and perfect detection efficiency do not reproduce the typical experimental working conditions. To take into account losses, we model the lossy experimental set-up as an ideal experimental set-up whose output passes through a beam-splitter of transmittance η, and is then detected by an ideal photo-detector. This idea is presented in Fig. 5.2. In η both detector and channel efficiencies are included. Using the beam-splitter input-output relations (see Sec. 1.1.1), the mode detected, which is the one we can experimentally access, is:

$$\hat{c}' = \sqrt{\eta}\hat{c} + i\sqrt{1 - \eta}\hat{v} \tag{5.13}$$

where $\hat{v}$ indicates the vacuum mode entering the beam splitter. Using Eq.s 1.32 -1.33 we obtain:

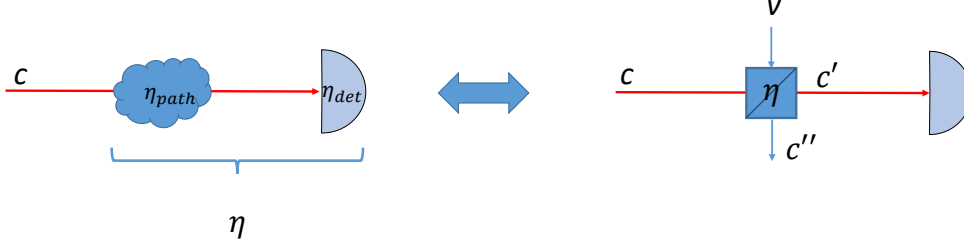$$\langle\hat{N}_{c'}\rangle = \eta\langle\hat{N}_c\rangle \tag{5.14}$$

Figure 5.2: A system which presents losses (both in the channel and in the detector, lowering the overall efficiency to η) can be modeled as an ideal system where a BS of transmittance η is inserted, as shown on the right. From the unused port of the BS the vacuum state $|0\rangle$ enters.

and

$$\Delta^2 N_{c'} = \eta^2 \Delta^2 \hat{N}_c + \eta(1-\eta)\langle \hat{N}_c \rangle \tag{5.15}$$

Propagating the uncertainty to ϕ and using the results obtained in Eq.s 5.9- 5.6, under dark-fringe condition, we have:

$$\Delta\phi = \frac{\Delta\hat{N}_{c'}}{|\partial_\phi \langle \hat{N}_{c'} \rangle|_\phi} = \Delta\phi_{cl,\eta=1} \sqrt{e^{-2|\psi|} + \frac{1-\eta}{\eta}} \tag{5.16}$$

From Eq. 5.16 some considerations follow:

- The role of losses in the classical case is retrieved for $|\psi| = 0$. In this case, $\Delta\phi_{cl,\eta} = \sqrt{\frac{1}{\eta}} \cdot \Delta\phi_{cl,\eta=1}$, where $\Delta\phi_{cl,\eta=1}$ is the phase uncertainty in case of perfect efficiency.

- In the limit of $|\psi| \to \infty$, corresponding to a squeezed state extremely far from a vacuum coherent state, we have: $\Delta\phi_{sq,\eta} = \sqrt{\frac{1-\eta}{\eta}} \cdot \Delta\phi_{cl,\eta=1}$. Therefore, for $\eta < 1/2$, the presence of losses prevents from beating the theoretical shot-noise-limit $\Delta\phi_{cl,\eta=1}$, for any squeezing level. However, an advantage over the classical case if same η is considered always remains.

In conclusion, losses heavily affect the advantages due to squeezing injection and therefore it is extremely important to reduce them as much as possible in the experimental realization.

5.2 Correlated interferometry

In this section we present the possibility of interferometric systems constituted by two interferometers. This kind of systems is currently used in different contexts and

aims at detecting, for various purposes, phase noise correlation between the two interferometers. The key idea is that the shot noise is uncorrelated in the two systems and therefore, considering the outputs correlation, is statistically washed away. In this sense, a system of two interferometers allows to go beyond the shot noise level of the single interferometer: longer is the integration time higher is the enhancement respect to the single interferometer. Nowadays the main applications of correlated interferometry are:

- Study on the stochastic gravitational wave background [72, 73].

- Search for traces of primordial blackholes [74].

- Search of possible effects of Planck scale physics [66, 75–77].

In this work we focus on the last application. We refer to the experimental set-up, named Holometer, realised at Fermilab by Hogan and his collaborators [74]. The Holometer consists in a pair of large MIs (arm length $L \sim 40$m) and has been designed to work with only classical light.

5.2.1 The Fermilab Holometer and the holographic noise

One of the main challenges in contemporary physics is to merge quantum theory and general relativity into a unified framework, the so-called quantum gravity (QG). Unfortunately, QG effects are expected to be relevant only at the Planck scale (being the Planck energy $E_P = 1.22 \cdot 10^{19}$ GeV, the Planck time $t_P = 5.39 \cdot 10^{-44}$ s and the Planck length $l_P = 1.62 \cdot 10^{-35}$ m), and therefore extremely difficult to be experimentally investigated. In the last years several efforts have been devoted toward an "experimental quantum gravity" [78]. In this context several heuristic quantum gravity theories have been developed. Many of them propose a non null commutator between the position variables. In [66, 79] Hogan proposes:

$$[\hat{x}_i, \hat{x}_j] = \hat{x}_k i c t_p \epsilon_{i,j,k} / \sqrt{4\pi} \tag{5.17}$$

where $\hat{x}_i, i = 1,2,3$ are the position operators and $\epsilon_{i,j,k}$ the antisymmetric 3-tensor. According to quantum mechanics laws, this non null commutator is associated to an uncertainty principle, named holographic uncertainty principle:

$$\Delta x_i \Delta x_j \geq \langle \hat{x}_k \rangle c t_p / \sqrt{4\pi} \tag{5.18}$$

This fact can be interpreted as the consequence of a new noise source, dubbed as holographic noise (HN), which makes the bodies wondering around their mean position. Being the commutator of the order of the Planck scale, this effect is completely negligible at ordinary scales. In order to be experimentally detected with current technologies, HN needs to be amplified by orders of magnitude. In [66] Hogan explores the effects of HN in a simple MI and concludes that this system is able to "accumulate" this conjectured

noise. It emerges that HN is proportional to $\sqrt{L}$, being L the length of the interferometer arms. Moreover, always in [66], considering the interferometer auto-correlation function, a statistical analysis of the HN noise is presented, as well as its expected spectrum.

A single interferometer is a useful device to amplify the HN, but is still not sufficient. Considering $L \sim 40$ m the maximum of the spectrum is expected to be $\sim 10^{-20}$ m/$\sqrt{\text{Hz}}$ in a frequency bandwidth upper limited to 1MHz, which is challenging from the experimentally point of view. Moreover, as it will be clarified in the following paragraphs, considering only one interferometer does not offer the possibility of testing all the HN peculiar properties.

For these two reasons, Hogan proposed, and experimentally realized at Ferimilab, the Holometer [74, 75], an interferometric system constituted by two independent power-recycling MIs of $L \sim 40m$. The distance d between the two BS is small ($d/L < 0.1$) and the two arms can be placed into two configurations, named as parallel ($\parallel$) and perpendicular ($\perp$). The configurations are reported in Fig. 5.3. HN is expected to have different
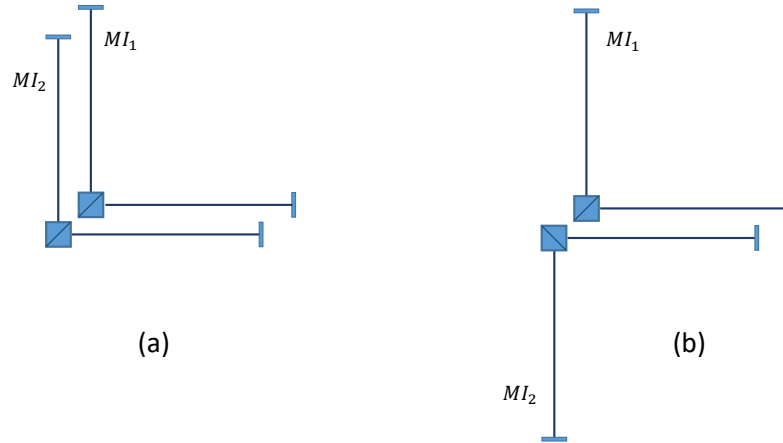

Figure 5.3: The two holometer configurations. (a) parallel ($\parallel$) configuration: due to overlapping of the light cones of the two MIs the HN is expected to be correlated between them. (b) perpendicular ($\perp$) configuration: in this case HN should be uncorrelated between the two MIs.

consequences in the two configurations, in particular:

- Parallel configuration, Fig. 5.3(a): if the two interferometers are sufficiently close, they share the same time-space volume and therefore HN is correlated between them. This induce a correlation in the two interferometers output.

- Perpendicular configuration, Fig. 5.3(b): in this case the two MIs space-time cones do not overlap, the HN is present, but is uncorrelated. There is no correlation between the interferometer outputs.

Due to the quantum nature of light shot-noise is necessarily present. However, differently from HN, the shot-noise is always uncorrelated between the two interferometers. Considering the correlation between the two MIs outputs and integrating for sufficiently long time, the uncorrelated contribution is statistically washed away, allowing the correlated component to emerge. In particular, focusing to sufficiently high frequencies, where mechanical or thermal noises are negligible, we can consider the phase noise as dominated by two contributions, the HN and the shot noise:

$$\delta\phi_1 = \delta\phi_{1sn} + \delta\phi_{1hn} \text{ and } \delta\phi_2 = \delta\phi_{2sn} + \delta\phi_{2hn}, \tag{5.19}$$

Repeating the measurement N times, i.e. acquiring for $t_{obs} = 2NL/c$, the cross-correlation at zero-delay is:

$$\text{Cov}(\phi_1, \phi_2)_\parallel = \langle\delta\phi_1\delta\phi_2\rangle_N = \frac{(\delta\phi_{sn})^2}{\sqrt{N}} + (\delta\phi_{hn})^2 \tag{5.20}$$

$$\text{Cov}(\phi_1, \phi_2)_\perp = \langle\delta\phi_1\delta\phi_2\rangle_N = \frac{(\delta\phi_{sn})^2}{\sqrt{N}} + \frac{(\delta\phi_{hn})^2}{\sqrt{N}} \tag{5.21}$$

Therefore, the detection of a difference in the phase cross-correlation between the two configurations would be a signature for HN. In particular, HN should emerge in the parallel configuration, while the perpendicular configuration offers a reference measurement. For more details, in [66] an accurate theoretical analysis is presented. The first measurements of the Holometer are reported in [75]. The cross-correlation between the two output is performed, obtaining, in the MHz range and averaging over $2 \cdot 10^8$ independent spectral measurements, a $2.1 \cdot 10^{-20}$ m/$\sqrt{\text{Hz}}$ sensitivity to stationary signals. With this sensitivity, no evidence of HN has been found.

5.3   Quantum light in a system of two interferometers

Aim of this section is to analyze, from the theoretical point of view, the advantages of quantum light in correlated interferometry. We refer to an holometer-like system, and we are interested in the sensitivity in a phase noise correlation measurement. The main references are two theoretical papers by I. Ruo-Berchera and collaborators [67, 68]. In Fig. 5.4 all the notations used are summarised:

- MI_1, MI_2 are the two power-recylcing Michelson interferometers constituting the holometer. Each interferometer can be modeled as a beam-splitter of transmittance $\tau_i = \cos^2 \frac{\phi_i}{2}, i = 1,2$.

- ϕ_1, ϕ_2 are the interferometers phases. We define $\phi_{10,20}$ the central phases and $\delta\phi_{1,2}$ the fluctuations around them. Since the effects of HN are expected to be extremely faint, we work in the hypothesis of small fluctuations. This allows to consider only the first term when expanding $\phi_{1,2}$ around its mean value. Moreover, we work close to the dark fringe, $\phi_{10,20} \sim 0$.
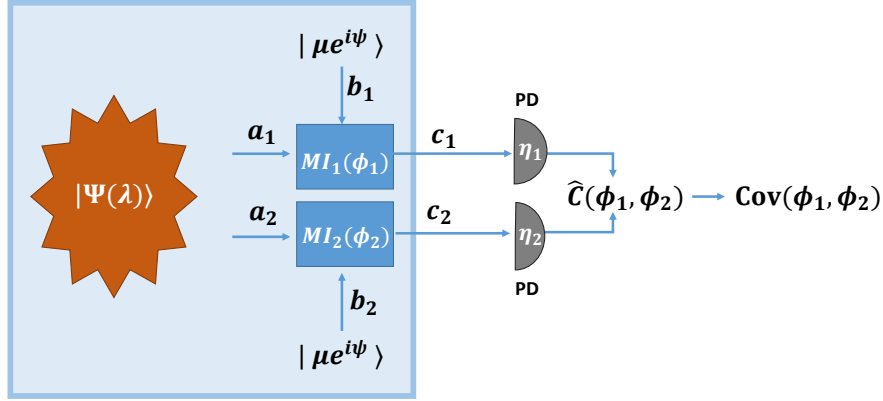
Figure 5.4: Scheme of the quantum enhanced holometer. This system consists in a couple of power-recycling MI_is of phase ϕ_i, and aims at measuring the covariance between the two phases. From the $\hat{b}_i$ port a coherent state enters, while from the $\hat{a}_i$ port a quantum state $|\psi(\lambda)\rangle$ is injected. Classically, vacuum states enter the interferometer from the $\hat{a}_i$ ports. Two possible quantum states $|\psi(\lambda)\rangle$ are discussed in the text: two single-mode vacuum squeezed states, $|\psi(\lambda)\rangle = |sq\rangle_{a1} \otimes |sq\rangle_{a2}$, and the twin-beam state, $|\psi(\lambda)\rangle = |twb\rangle_{a1,a2}$.

- $\hat{b}_1$ and $\hat{b}_2$ are the input modes entering from the symmetric ports. We consider the injection of a bright coherent state of mean photon number μ: $|\sqrt{\mu}e^{i\psi_1}\rangle$ and $|\sqrt{\mu}e^{i\psi_2}\rangle$.

- $\hat{a}_1$ and $\hat{a}_2$ are the input modes entering from the anti-symmetric ports. Two different quantum states $|\psi(\lambda)\rangle$ are considered (see Sec.s 5.3.1-5.3.2). λ refers to the mean number of photons in the state. Classically the coherent vacuum $|0\rangle_{a1} \otimes |0\rangle_{a2}$ enters from there. We indicate as $\hat{\rho}_{1,2}$ the density matrix of the input state.

- $\hat{C}(\phi_1, \phi_2)$ is the observable that we measure in order to estimate the correlation between ϕ_1 and ϕ_2, i.e. $\langle \delta\phi_1 \delta\phi_2 \rangle$.

- $\hat{c}_1$ and $\hat{c}_2$ are the anti-symmetric output ports. Experimentally we can have access to these modes measuring the photo currents on two photodiodes (proportional to the number of output photons, $\langle \hat{c}_1^\dagger \hat{c}_1 \rangle$ and $\langle \hat{c}_2^\dagger \hat{c}_2 \rangle$).

- $\eta_{1,2}$ are the efficiencies in the two MIs. In this factor both the detector efficiencies and the optical components efficiency are included.

We measure an observable $\hat{C}(\phi_1\phi_2)$ and we aim at estimating $\langle \delta\phi_1 \delta\phi_2 \rangle$ in the parallel configuration, with the smallest possible uncertainty. Expanding $\hat{C}(\phi_1\phi_2)$ around ϕ_{10} and ϕ_{20}, it has been demonstrated that [67]:

$$E_\parallel[\delta\phi_1 \delta\phi_2] = \frac{E_\parallel[\hat{C}(\phi_1, \phi_2)] - E_\perp[\hat{C}(\phi_1, \phi_2)]}{\langle \partial^2_{\phi_1\phi_2} \hat{C}(\phi_{10}, \phi_{20}) \rangle} \tag{5.22}$$

with uncertainty:

$$\mathcal{U}(\delta\phi_1\delta\phi_2) = \frac{\sqrt{\text{Var}_\parallel[\hat{C}(\phi_1, \phi_2)] + \text{Var}_\perp[\hat{C}(\phi_1, \phi_2)]}}{\langle\partial^2_{\phi_1\phi_2}\hat{C}(\phi_{10}, \phi_{20})\rangle} \tag{5.23}$$

The contribution of the zero-th order is:

$$\mathcal{U}^{(0)}(\delta\phi_1\delta\phi_2) = \frac{\sqrt{2\text{Var}[\hat{C}(\phi_{10}, \phi_{20})]}}{\langle\partial^2_{\phi_1\phi_2}\hat{C}(\phi_{10}, \phi_{20})\rangle} \tag{5.24}$$

In Eq.s 5.22-5.23-5.24 the symbols $E_i[x]$ and $\text{Var}_i[x]$, $i = \parallel, \perp$, are formally defined as $E_i[x] = \int\langle x\rangle f_i(\phi_1, \phi_2)\mathrm{d}\phi_1\mathrm{d}\phi_2$ and $\text{Var}_i[x] = E_i[x^2] - E_i^2[x]$, where $f_i(\phi_1, \phi_2)$ are the joint probability density functions in the two configurations and reproduce the statistical properties of the phase fluctuations induced by HN. For a deep discussion on these properties see [67, 68].

The goal is now to find a quantum state $\hat{\rho}_{a1,a2}$ and an observable $\hat{C}(\phi_1, \phi_2)$ that allow to reduce $\mathcal{U}^{(0)}(\delta\phi_1\delta\phi_2)$ as much as possible. Two different scenarios are considered:

- $|\psi(\lambda)\rangle_{a1,a2} = |sq\rangle_{a_1} \otimes |sq\rangle_{a_2}$, i.e. two independent vacuum squeezed states are injected from the classically unused ports. This is probably the more obvious extension of using quantum light in one single interferometer. See Sec. 5.3.1.

- $|\psi(\lambda)\rangle_{a1,a2} = |twb\rangle_{a_1,a_2}$, i.e. the two modes of a twin beam state are injected from the classically unused ports. This approach has no equivalent when only one interferometer is considered. See Sec. 5.3.2.

5.3.1 Two independent single mode squeezed states

When two independent squeezed states are used we consider as $\hat{C}(\phi_1\phi_2)$ the covariance between the number of photons detected at the output port $\hat{c}_i$. In particular, we define $\hat{C}(\phi_1\phi_2)$ as:

$$\hat{C}(\phi_1\phi_2) = \Delta\hat{N}_1(\phi_1)\Delta\hat{N}_2(\phi_2) = (\hat{N}_1 - \langle\hat{N}_1\rangle)(\hat{N}_2 - \langle\hat{N}_2\rangle) \tag{5.25}$$

Being the two squeezed states independent, the variance on this quantity can be written as:

$$\text{Var}(\hat{C}(\phi_1\phi_2)) = \langle(\hat{N}_1 - \langle\hat{N}_1\rangle)^2\rangle\langle(\hat{N}_2 - \langle\hat{N}_2\rangle)^2\rangle = \Delta^2\hat{N}_1\Delta^2\hat{N}_2 \tag{5.26}$$

Substituting Eq. 5.26 in Eq. 5.24, we have:

$$\mathcal{U}^{(0)}(\delta\phi_1\delta\phi_2) = \sqrt{2}\frac{\Delta\hat{N}_1}{|\partial_{\phi_1}\hat{N}_1(\phi_{1,0})|}\frac{\Delta\hat{N}_2}{|\partial_{\phi_2}\hat{N}_2(\phi_{2,0})|} \tag{5.27}$$

Both factors have exactly the form of Eq. 5.10. Eq. 5.27 demonstrates that, enhancing the sensitivity of the two MIs independently, the sensitivity in a correlation measurement is improved. Using the expression in Eq. 5.16, which is valid in the dark-fringe condition and takes into account for detection losses, it follows:

$$\mathcal{U}^{(0)}(\delta\phi_1\delta\phi_2) = \sqrt{2}\,\mathcal{U}^{(0)}_{1,cl}\sqrt{e^{-2r_1} + \frac{1-\eta_1}{\eta_1}}\mathcal{U}^{(0)}_{2,cl}\sqrt{e^{-2r_2} + \frac{1-\eta_2}{\eta_2}} \tag{5.28}$$

where $\mathcal{U}^{(0)}_{1,cl} = \left(\cos^2\frac{\phi_{1,0}}{2}\sqrt{\mu}\right)^{-1}$, and $r_{1,2} = |\psi_{1,2}|$ are the squeezing factors.

In the ideal situation of $\eta_1 = \eta_2 = 1$ and $\phi_{10} = \phi_{20} = 0$ it holds: $\mathcal{U}^{(0)}(\delta\phi_1\delta\phi_2) = \frac{\sqrt{2}e^{-r_1}e^{-r_2}}{\mu}$. In this case the uncertainty is reduced by a factor proportional to the geometric mean of the squeezing factors. The advantage of squeezing injection in the presence of losses can be quantified considering the ratio (for the sake of simplicity we set $\eta_1 = \eta_2 = \eta$ and $r_1 = r_2 = r$):

$$\mathcal{R}_{sq} = \frac{\mathcal{U}^{(0)}_{sq}}{\mathcal{U}^{(0)}_{cl}} = \eta\left(e^{-2r} + \frac{1-\eta}{\eta}\right) \tag{5.29}$$

In Fig. 5.5 the dashed curves show the squeezing advantage at varying η, for different numbers of photons in the squeezed state ($\lambda = \sinh^2 r$, according to Eq. 1.157). The squeezing advantage is reduced by losses, nonetheless is not washed away and remains relevant also for values of η achievable with current technologies. In Fig. 5.6 the dependence of $\mathcal{R}^{(0)}$ from ϕ_0 is reported for different values of η (Eq. 5.29 is obtained in the approximation of $\phi_0 \sim 0$, nonetheless $\mathcal{R}^{(0)}$ depends in the general case from the central phase ϕ_0). It can be appreciated that, when two single mode squeezed states are injected (dashed lines), $\mathcal{R}^{(0)}$ reaches a plateau for ϕ_0 sufficiently small, and a further decrease of ϕ_0 does not further increase the quantum advantage.

5.3.2   Twin-beam state

Let us now consider as quantum input state $|\psi(\lambda)\rangle = |twb\rangle_{a_1,a_2}$. As in the previous case the input modes $\hat{b}_1$ and $\hat{b}_2$ are excited in two coherent states while $\hat{a}_1$ and $\hat{a}_2$ are now entangled in a twin-beam state. As presented in Sec. 1.6.1, one of the main features of the twin-beam state is the perfect correlation in the photon number between the two modes. According to Eq. 1.116:

$$_{a_1,a_2}\langle twb|(\hat{N}_{a_1} - \hat{N}_{a_2})^M|twb\rangle_{a_1,a_2} = 0, \forall M \tag{5.30}$$

To take advantage of this peculiarity, we consider as observable:

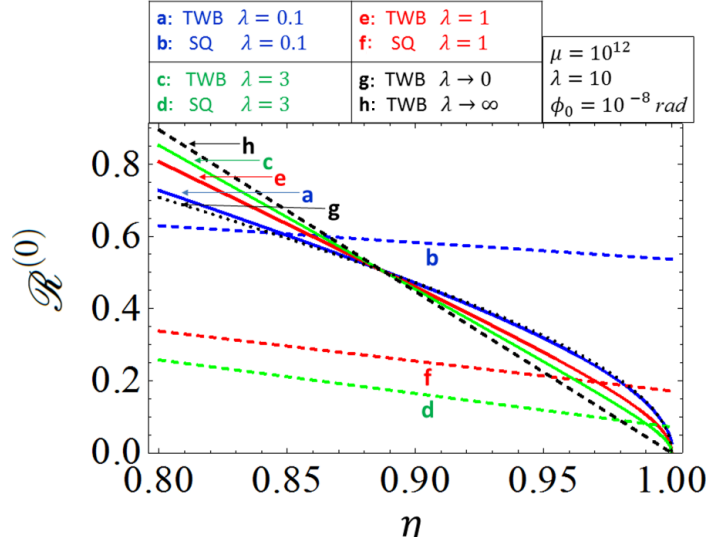$$\hat{C}(\phi_1,\phi_2) = (\hat{N}_1 - \hat{N}_2)^2 \tag{5.31}$$

Figure 5.5: Quantum enhancement in the case of two independent single mode squeezed vacuum state ($\mathscr{R}_{sq}^{(0)}$, dashed lines) and in the case of twin-beam state ($\mathscr{R}_{twb}^{(0)}$, continuous lines) in terms of the efficiency of the system, η. The curves corresponding to different values of the number of photons in the quantum state injected, λ, are reported. The other parameters are: $\mu = 3 \cdot 10^{12}$, $\phi_0 = 10^{-8}$, $\psi = \pi/2$. This figure is extracted from [68].

Its variance can be calculated as:

$$\Delta^2 \hat{C}(\phi_1, \phi_2) = \langle (\hat{N}_1 - \hat{N}_2)^4 \rangle - \langle (\hat{N}_1 - \hat{N}_2)^2 \rangle^2 \tag{5.32}$$

The evaluation of this quantity is extensively discussed in [67, 68], here we limit to present some of the main results, without reporting analytical expressions.

The most interesting result is the consequence of working at the dark-fringe, under the assumption of ideal detection efficiency. If we consider $\phi_{10} = \phi_{20} = 0$ each interferometer behaves as a transparent medium: the coherent states are totally transmitted in $\hat{d}_1$ and $\hat{d}_2$ and therefore the perfect correlation in the photon number between $\hat{a}_1$ and $\hat{a}_2$ is transferred to the output modes $\hat{c}_1$ and $\hat{c}_2$. It follows that the numerator in Eq. 5.24 is identically null, while the denominator is different from zero. Therefore, using a twin-beam state, at the first order, we have:

$$\mathscr{U}_{twb}^{(0)} = 0 \tag{5.33}$$

Differently from the $|sq\rangle_{a1} \otimes |sq\rangle_{a2}$ case, where we work close to the dark fringe but not exactly at that point (to respect the condition in Eq. 5.7, $\phi_{10} = \phi_{20} = 0$ is not acceptable), in this case it would be necessary to work exactly at the dark-fringe.

The result presented in Eq. 5.33 is obtained under the assumption of working perfectly at the dark fringe and with ideal detection efficiency, $\eta = 1$. Therefore, although
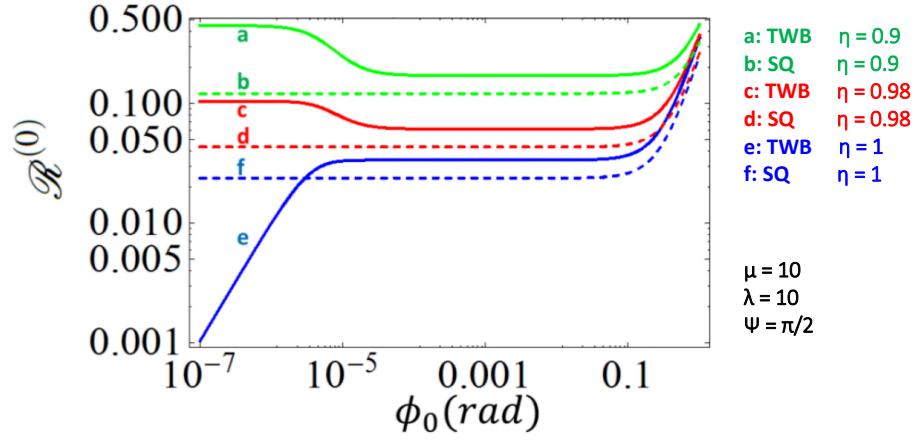
Figure 5.6: Quantum enhancement in the case of two independent single mode squeezed vacuum state ($\mathscr{R}_{sq}$, dashed lines) and in the case of twin-beam state ($\mathscr{R}_{twb}$, continuous lines) in terms of the central phase, ϕ_0. The curves corresponding to different values of the efficiency, η, are reported. The other parameters are: $\mu = 3 \cdot 10^{12}$, $\lambda = 10$, $\psi = \pi/2$. This figure is extracted from [68].

it remains very interesting from the theoretical point of view, it is also important to study what are the consequences of experimental imperfections. To take into account losses we can proceed as done in Sec. 5.1.2, modeling the real system as an ideal system of perfect efficiency with a beam splitter of transmittance η just before an ideal photo detector. In Fig.s 5.5-5.6 the advantage offered by twb respect to the best classical case $\mathscr{R}^{(0)}_{twb} = \frac{\mathscr{U}^{(0)twb}}{\mathscr{U}^{(0)}_{cl}}$ is presented in function of η and ϕ_0 respectively (see continuous lines). It emerges that for lower efficiencies, as well as away from the dark-fringe, the twin-beam advantage is highly affected.

Referring to Fig. 5.6, two regimes can be identified (see [68] for an extensive discussion):

- "Photon-number entanglement regime", left-side of the plot: extremely close to the dark fringe, and for $\eta \sim 1$, the effect of photon-number entanglement manifests in $\mathscr{R}^{(0)}_{twb}$ rapidly decreasing toward zero. With the existing technologies this regime is extremely challenging, due to the difficulties in locking an interferometric system at $\phi_0 = 0$ and to the presence of losses in the detection process.

- "Quadrature correlation regime", right-side of the plot: for ϕ sufficiently away from the dark fringe the twin-beam state qualitatively behaves as the two-single mode squeezed state. In this case the enhancement is based on quadrature correlation

117

between the two modes. This regime does not allow to obtain the surprising uncertainty reduction in Eq. 5.33.

Despite the fact that in the ideal situation the twin-beam offers the major improvement respect to the classical strategy, in real situations the two-independent squeezed states configuration performs better. This is represented in Fig. 5.7, where $\mathscr{R}_{twb}^{(0)}$ and $\mathscr{R}_{sq}^{(0)}$ are compared in terms of η and λ.
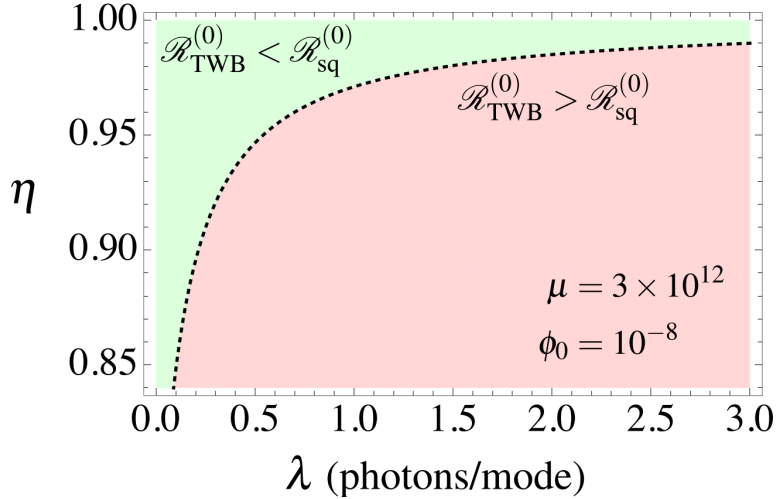

Figure 5.7: The green region represents the values of η and λ for which the quantum enhancement offered by the twin-beam strategy is higher than the one offered by the two independent squeezed states strategy ($\mathscr{R}_{twb} < \mathscr{R}_{sq}$). The red region represents the values of η and λ corresponding to the opposite situation. η is the efficiency of the set-up, λ the mean number of photons in the quantum state. The other parameters are: $\mu = 3 \cdot 10^{12}$, $\phi_0 = 10^{-8}$, $\psi = \pi/2$. This figure is extracted from [68].

5.4   Experimental set-up: brief description

A simplified schematic of the experimental set-up is presented in Fig. 5.8. It consists in a couple of power recycling MIs placed close to each other, eventually fed with quantum light from the classically unused ports (in the following we may refer to these ports also as anti-symmetric ports or dark ports). A more detailed scheme of each MI, concerning the classical part, is depicted in Fig. 5.9. A picture of the experimental set-up is reported in Fig. 5.10.

The length of each arm is $L \sim 92$ cm, while the distance between the two beam splitters (BS) is $d \sim 8$ cm. Differently from the Holometer realised at Fermilab, ours is a table-top experiment. Even if our experiment is conceived as a proof of principle experiment and is not specifically devoted to the search of HN, being $d \ll L$ the condition
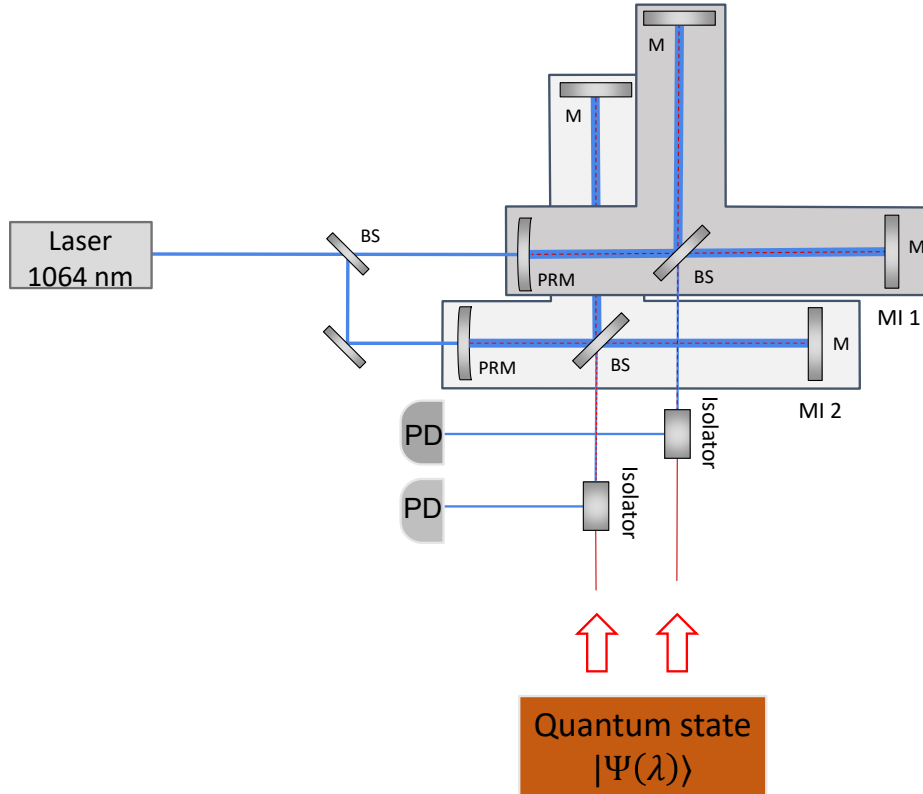
Figure 5.8: Simplified schematic of the experimental set-up. Our system consists in two power-recycling Michelson interferometers (*MI*), eventually fed with the quantum state $|\psi(\lambda)\rangle$ through their anti-symmetric ports. The output of each MI is separated from the input state $|\psi(\lambda)\rangle$ using a Faraday isolator and is then sent to a photo-detector (PD). The collected data are subsequently analyzed. PRM: power recycling mirror. BS: beam splitter. M: end mirror.

of space time volumes superposition (see Sec. 5.2.1) is fulfilled.

Both MIs are fed with a Nd-YAG laser of wavelength $\lambda = 1064$ nm. The input power is maintained around $P_{in} = 1.5$ mW. The same laser is also used for squeezed light generation. In order to have a TEM$_{00}$ mode the light is fiber coupled.

Each power-recycling MI is formed by a power-recycling mirror (PRM) having radius of curvature of 1.5 m and reflectivity 90%, a 50-50 BS, and two plane end-mirrors M_1 and M_2 (reflectivity $\sim$ 99.9%). These mirrors are mounted on piezoelectric actuators (PZT), used for maintaining the interferometer at the desired working point (the locking scheme is described in Sec. 5.4.1). In one arm of each MI we place an electro-optical modulator (EOM). This device is involved in the locking scheme and can be connected to a noise generator, thus allowing to test the system for injection of different kinds of noise. Another EOM is present before entering the interferometer: it is also used in the locking system. Two Faraday isolators permit to separate the light exiting the
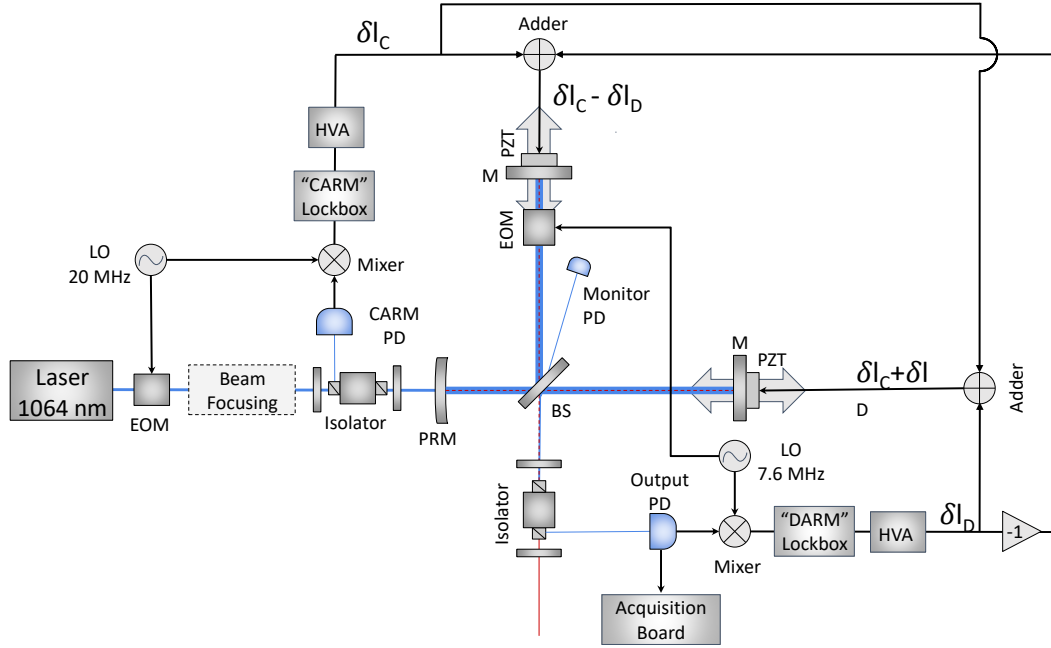
Figure 5.9: Schematic of the single power recycling MI, concerning the classical part. In this scheme all the details concerning the locking schemes are reported, see text for more details. EOM: electro-optical-modulator. PD: photo-diode. BS: beam-splitter. M: end mirror. PRM: power recycling mirror. PZT: piezoelectric actuators. HVA: high voltage amplifier. LO: local oscillator.

interferometers from the entering quantum states. Three photodiodes (PD) are used:

- Output PD: it is a custom InGaAs photodiode with high quantum-efficiency (99%) and low noise (noise equivalent power $1.2 \cdot 10^{-11} \mathrm{W}/\sqrt{\mathrm{Hz}}$). It has two DC-outputs and two 100 kHz high passed AC-outputs. One DC-output and one AC-output are sent to the acquisition board. The other AC-output is used for locking while the remaining DC-output is used for real time monitoring.

- CARM PD: as the previous one, it is a custom InGaAs photodiode with high quantum-efficiency (99%) and low noise (noise equivalent power $1.2 \cdot 10^{-11} \mathrm{W}/\sqrt{\mathrm{Hz}}$). It is used for locking the *CARM* degree of freedom (see next section).

- Monitor PD: this is a commercial detector and it monitors a spurious reflection of the BS, allowing to measure the power circulating in the MIs.

The acquisition board consists in a 14 bit data acquisition system with 4 channels (DC and AC for each MI) and acquisition rate 500 kSample/s. The DC signal from the output PD is collected without any further processing, while the AC signal is down mixed
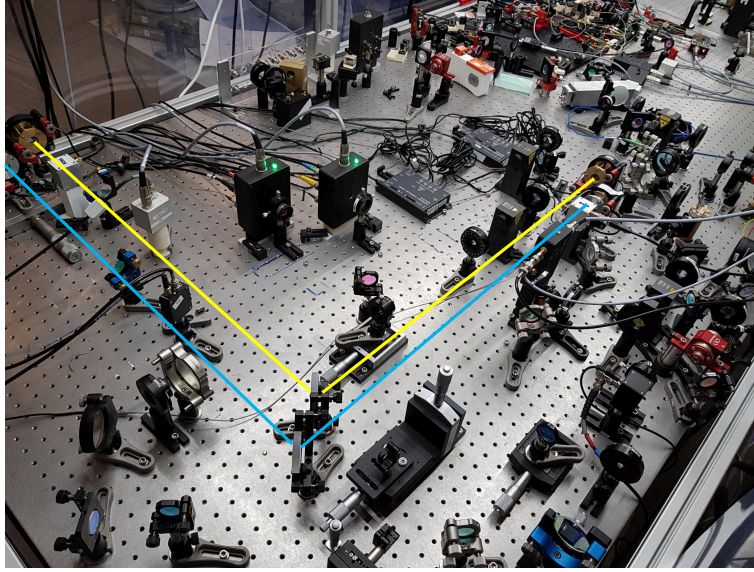
Figure 5.10: Picture of our experimental set-up, the two MIs are highlighted in yellow and blue respectively. The arm length is $L \sim 92$ cm, and the distance between the two beam-splitters is $d \sim 8$ cm.

at 13.5 MHz, preamplified and low passed at 100 kHz. A detailed scheme of the data acquisition system is depicted in Fig. 5.11.
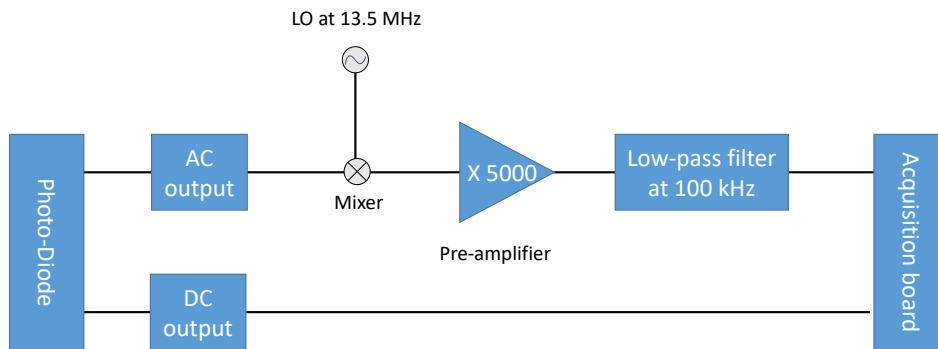

Figure 5.11: Scheme of the acquisition system. The photodiode monitoring the output port of the MI has both AC and DC outputs: the DC signal is directly acquired while the AC signal is further processed. The acquisition rate is 500 kSample/s.

Two different quantum states $|\psi(\lambda)\rangle$ are eventually injected from the classically un-used port. The squeezer set-up used for generating a single mode vacuum squeezed state

has been provided by the DTU laboratories and is described in Sec. 2.2. We have two independent squeezer, therefore the experimental implementation of the state $|\psi(\lambda)\rangle_{a1,a2} = |sq\rangle_{a_1} \otimes |sq\rangle_{a_2}$ is straightforward. Concerning the state $|\psi(\lambda)\rangle_{a1,a2} = |twb\rangle_{a_1,a_2}$, we do not produce a real twin-beam state but an approximation of it. In particular, we obtain a twin-beam like state splitting one single mode squeezed vacuum at a balanced BS. As discussed in Sec. 2.3, the state obtained presents, in terms of quadrature correlation between the two modes, the same properties as a real twin-beam state. A scheme of the implementation of the two states considered is reported in Fig. 5.12.
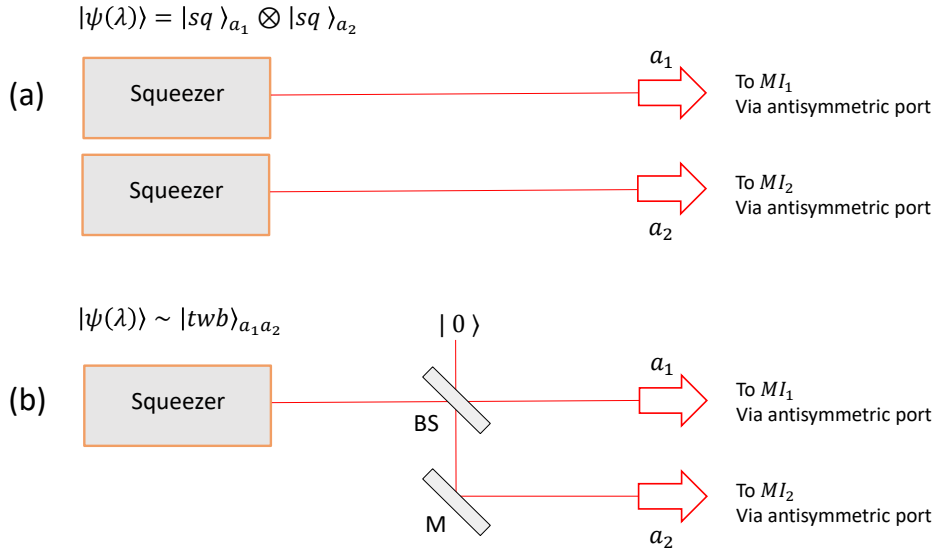

Figure 5.12: Two different options of quantum states $|\psi(\lambda)\rangle$ are experimentally implemented: two independent squeezed vacuum states (a) and twin-beam like state (b). In both cases the bipartite quantum state is injected in the two MIs via their anti-symmetric ports.

5.4.1 Power-recycling MI locking schemes

Let us firstly consider a simple MI, i.e. without power recycling mirror. The laser field entering from the input port is splitted into two fields at the BS that propagate in each arm of the interferometer, before being reflected back towards the BS, where they interfere. The intensity of the output light (sensed by the output PD) depends on the interferometer phase, or, in other terms, on the difference between the two arms length. We refer at this quantity as differential arm length ($DARM = L - L'$). The $DARM$ value corresponding to constructive interference is called bright fringe while the one corresponding to destructive interference is called dark fringe. In latter case most of the power is reflected back towards the laser, but can be recycled by placing a PRM.

In a power-recycling MI, the simple MI, that close to the dark fringe can be considered as a high-reflective compound mirror, and the PRM form a cavity of equivalent length $CARM = \frac{L+L'}{2}$. For appropriate $CARM$ lengths the cavity is resonant and the power in the cavity increases.

Therefore, a power-recycling MI presents two degrees of freedom ($DARM$ and $CARM$) that need to be locked to the desired values. In our case:

- $DARM = n\lambda + \delta$, being $n \in Z$ and $\delta \ll \lambda$,

- $CARM = m\lambda$, being $m \in Z$

The $CARM$ is locked by the Pound-Drever-Hall technique (see Appendix C.1), while for the $DARM$ the internal modulation technique is employed (see Appendix C.3). Both techniques require to impress sidebands on the carrier field: this is done generating phase modulations, at 20 MHz and 7.6 MHz respectively, using EOMs. The PD outputs are down-mixed, at 20 MHz and 7.6 MHz respectively, and sent to the corresponding Lockbox (see Fig. 5.9), consisting in a proportional-integral controller (PI). The phase between the electronic local oscillator (LO) and the AC output signal from the photodetector has to be adjusted properly to maximize the slope of the error signal.

The error signal generated by the $CARM$ Lockbox, δl_C, is sent equally (phase concordance) to both M_1 and M_2, passing through a high voltage amplifier (HVA). The error signal generated by the $DARM$ Lockbox, δl_D, is sent differentially (i.e with a relative phase of π) to M_1 and M_2, passing through an HVA. By this procedure it is possible to decouple the control of the two degrees of freedom, facilitating the control of the system. The $CARM$ remains unchanged for δl_D applied differentially (i.e. $L + L' = L + \delta l_D + L' - \delta l_D$). Analogously, the $DARM$ remains unchanged for δl_C applied equally (i.e. $L - L' = L + \delta l_C - (L' + \delta l_C)$).

Working point of the experiment

In typical working conditions we fix the $DARM$ and the $CARM$ such as:

- $P_{out} \sim 0.35$ mW

- $G \sim 9$

P_{out} is the power at the anti-symmetric port, while G is the gain of the power-recycling cavity. It is defined as:

$$G = \frac{P_{cav}}{P_{cav\ off}} \tag{5.34}$$

where P_{cav} is the power in the cavity at the resonance and $P_{cav\ off}$ is the power in the cavity without resonance (this situation is reproduced slightly misaligning the PRM). These two values can be experimentally estimated using the Monitor PD.

5.4.2   Squeezing injection and quantum noise locking

In Sec. 2.2 we describe how the squeezed light is produced. The squeezed beam and the corresponding control beam, are injected in the MIs through their anti-symmetric ports, after being separated from the pump beam using a dichroic BS.

The control beam perfectly overlaps the generated squeezed light. For this reason it is used to align and to adjust the spatial mode matching between the laser beam and the squeezed beam. At the same time it is used for locking the quadrature of the field to the squeezed one. The corresponding locking scheme is represented in Fig. 5.13. A phase modulation at 37.22 MHz and 36.5 MHz for the two squeezers respectively is impressed on the control beam using an EOM (in our case this is the same EOM used to impress sidebands on the pump beam in the squeezer (see Sec. 2.2)). The signal from the output PD is demodulated at these frequencies by an inbuilt mixer and sent to a PI module, named as "Phase Lockbox" in the figure. The error signal is generated such that the point of squeezed quadrature corresponds to the maximum slope point of the error signal. It is then sent to a PZT with a phase shifter mounted on it, placed on the squeezed beam path, thus locking the squeezed state to the wished quadrature.
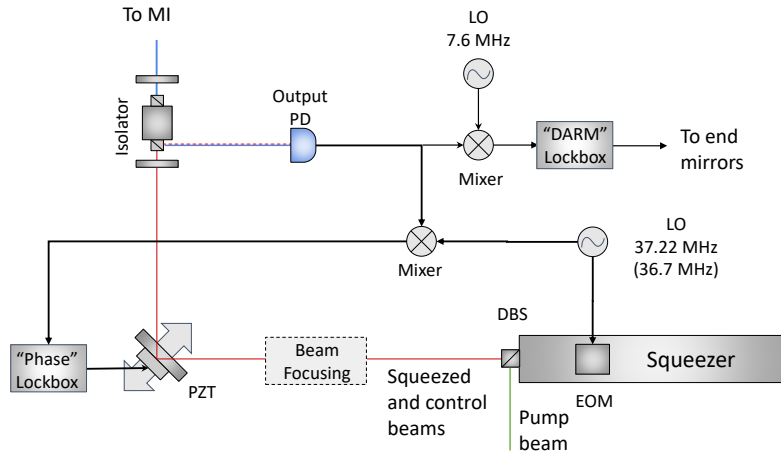

Figure 5.13: Scheme of the quantum noise locking system. Exploiting the sidebands in the control beam and the MI output, it is possible to lock the squeezed beam quadrature to the squeezed one. If the quadrature is properly locked, the photon noise can be reduced below the shot-noise level. PD: photo-diode. PZT: piezoelectric actuators. LO: local oscillator. DBS: dichroic beam-splitter. EOM: electro-optical-modulator. MI: Michelson interferometer.

The locking procedure is similar for both the quantum states considered. The only difference is that in the twin-beam-like case both sidebands are at 36.5 MHz since only

one squeezer is used.

5.4.3 Relevant characterization measurements

In this section we briefly report on some characterization measurements performed on the system. For a more detailed discussion, see [69].

Visibility

Visibility is a figure of merit used to quantify the contrast between the dark and the bright fringe. It is defined as:

$$V = \frac{P_{max} - P_{min}}{P_{max} + P_{min}} \tag{5.35}$$

being P_{max} and P_{min} the maximum and minimum power measured at the output port varying the $DARM$. In ideal conditions of perfect interference $P_{min} = 0$ and $V = 1$. Losses and experimental imperfections necessarily lower this value below one.

If the powers circulating in the two arms, P_1 and P_2, are unequal the normalized visibility is given by $V' = V/v$ where

$$v = \frac{2\sqrt{P_1 P_2}}{P_1 + P_2}. \tag{5.36}$$

To measure the visibility in our system, in the simple Michelson configuration, the PZT actuator mounted on one of the end mirror is modulated with the help of a function generator and a HVA. In Fig. 5.14 the signal from the output PD is reported in function of the PZT voltage. From this graph the visibility in the first MI is estimated to be $V_1 = (99.01 \pm 0.04)$. Similar results are obtained for the second MI, $V_2 = (99.08 \pm 0.05)$.

Noise vs power scaling

Squeezed states of light allow to increase the sensitivity below the classical shot-noise limit. If the sensitivity of the system is limited by other noise sources rather than the laser shot noise, the squeezing injection is almost useless. Therefore, it is of the utmost importance to verify that the system, in the classical configuration, is shot noise limited. As discussed in Sec. 1.5.3, if N photons arrive at the PD the associated shot noise is $\Delta N = \sqrt{N}$.

Usually low frequencies are dominated by mechanical noise, thermal noise and other source of noises. It is experimentally impossible to get rid of these noise sources, but we can avoid the problem limiting our analysis to sufficiently high frequencies. In particular, as described in Sec. 5.4, at the acquisition board we down mix the signal from the PD at 13.5 MHz, thus focusing our analysis around this frequency.

We can verify that the experiment is shot-noise limited both in the time and frequency domain. The measurements are performed after locking the simple MI close to
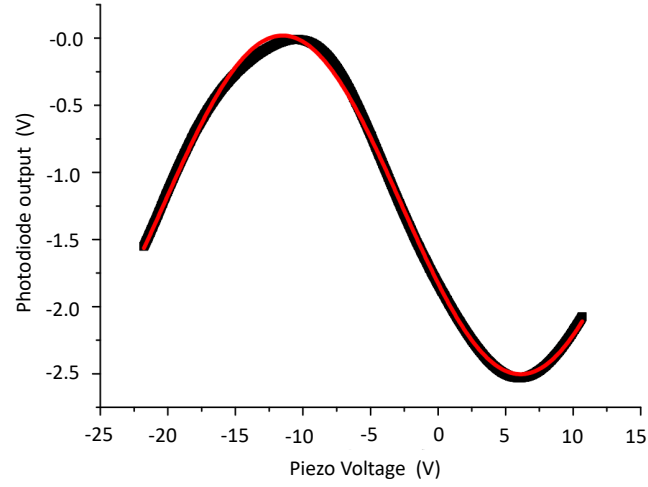
125

Figure 5.14: Output of the MI at varying the voltage feeding the PZT at the end mirror (this corresponds to periodically modulate the *DARM*). From the maximum and minimum values registered the visibility can be estimated. In our case we have $V \sim 99\%$ for both MIs.

the dark fringe, at varying the optical input power. In the time domain, we evaluate the mean value and the variance of the time series after down mixing. A previous photodiode calibration allows to convert from V (unit of measurement of the PD signal) to W. In Fig. 5.15 the variance of the signal for different power levels is reported. The dots are the experimental data, the red dashed line represents the shot-noise limit. It is obtained fitting the first data points with a straight line.

It can be concluded that the experiment, at 13.5 MHz, is shot-noise limited until around 0.6 mW. Therefore, we always work respecting this condition.

In the frequency domain we consider the power spectral density (PSD). Intuitively, the PSD describes how the power of a certain signal is distributed with respect to the frequency. It is defined as the Fourier transform of the auto-correlation function of the time series. As discussed in more details in Appendix B.1, said $X(t)$ a stationary signal, its auto correlation function is:

$$R_{XX}(\tau) = \langle X(t)X(t + \tau) \rangle \tag{5.37}$$

and the associated PSD:

$$\text{PSD}_X(\omega) = S_{XX}(\omega) = \frac{1}{Nf_S} \sum_{\tau=0}^{N} R_{XX}(\tau)e^{-2\pi j\omega\tau} \tag{5.38}$$

where N is the length of the time series and f_S its sampling frequency. From the PSD it is possible to define the linear spectral density (LSD) as the square root of the PSD (see Appendix B.2). In Fig. 5.16 the PSDs for different power levels are reported. The smooth
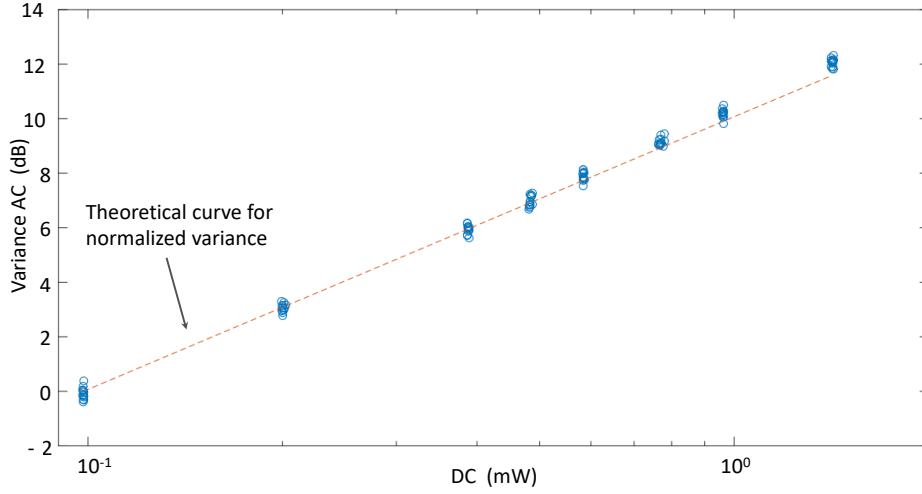
126

Figure 5.15: Normalized variance of the output power at varying the input optical power of the laser. The blue points are the experimental data, while the red line, obtained fitting the first data with a straight line, represents the shot noise limit (Var(P) $\propto$ P). It emerges that our system, at 13.5 MHz, is shot-noise limited until around 0.6 mW.

lines correspond to the theoretical PSD level of the shot-noise limited case. Also with this approach we conclude that we are shot noise limited until ~0.6 mW.

Sensitivity calibration

The signal recorded at the acquisition board is expressed in V, and therefore the corresponding PSD and LSD are expressed in V^2/Hz and $V/\sqrt{Hz}$ respectively (see Appendix B.1 for further details). However, we are interested in evaluating the strain sensitivity of our system, expressed in $m/\sqrt{Hz}$. This quantity gives us information about which is the minimum displacement that we can appreciate per unit of frequency. Moreover, expressing the sensitivity in $m/\sqrt{Hz}$ allows us to compare the performance of our experiment with other similar set-ups, that typically use this unit.

In order to obtain the conversion factor we need to consider the equivalent displacement ΔX_{rms} caused by the EOM when fed with an input root-mean-square voltage V_{rms}. The relation between these quantities is:

$$\Delta X_{rms}[\text{m}] = \frac{\lambda V_{rms}}{2V_\pi}, \tag{5.39}$$

where V_π is the half-wave voltage and is defined as the voltage required for inducing a phase shift of π.
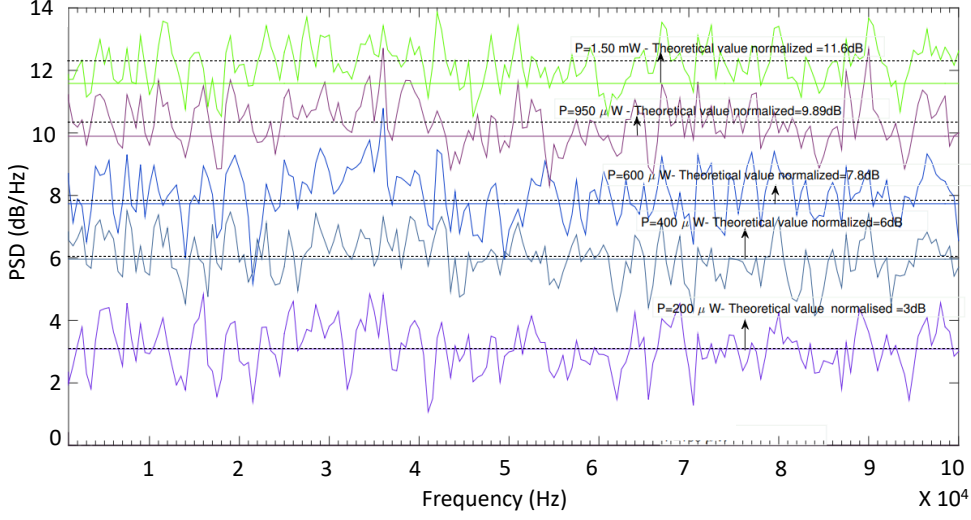
Figure 5.16: Normalized PSDs for various input powers. The straight lines are the theoretical PSDs in the shot-noise limited situation, while the noisy lines are the PSDs experimentally obtained. Dashed black lines represent the average values of the experimental PSD. As in Fig. 5.15, also here it emerges that our experiment, at 13.5 MHz, is shot-noise limited until around 0.6 mW.

Considering the measurement bandwidth, *BW*, we have:

$$\Delta x_{rms}[\mathrm{m}/\sqrt{\mathrm{Hz}}] = \frac{\lambda V_{rms}}{2V_{\pi}} \frac{1}{\sqrt{BW}} \tag{5.40}$$

This relation allows us to convert the LSDs (and the cross-linear spectral density, CLSDs see Appendix B.4) from V/$\sqrt{\mathrm{Hz}}$ to m/$\sqrt{\mathrm{Hz}}$. In all the plots reported we will always use the latter unit.

In principle, V_{π} can be theoretically evaluated in terms of the physical properties of the crystal [80], however we estimate this quantity experimentally. All the details about the procedure can be found in [69]. The resulting values of V_{π} for the EOMs placed in the two MIs are respectively $V_{\pi,1} = (988 \pm 7)$V and $V_{\pi,2} = (1000 \pm 11)$V.

Squeezing measurement in the MI

In Sec. 2.2.2 we describe the homodyne measurement performed on the squeezed state produced, reporting ~ 6.5 dB of squeezing, respect to the shot noise level. Here we report the measurements for evaluating the squeezing level at the output of the interferometers. The 6.5 dB enhancement at the output of the squeezer cavity is degraded, due to all the losses inside the MI (e.g. detection losses of the PD, transmission losses due to isolators and other optics, not perfect mode-matching).

In Fig. 5.17 the photon noise normalized to the shot noise level in function of time is reported. For performing this measurement the interferometer is locked at the typical working point and the phase shifter on the squeezed beam path is modulated. The blue curve is the shot noise level (obtained blocking the squeezed beam), the green curve is the noise in case of squeezing injection. It can be observed that for some phases the photon noise is below the shot-noise level.
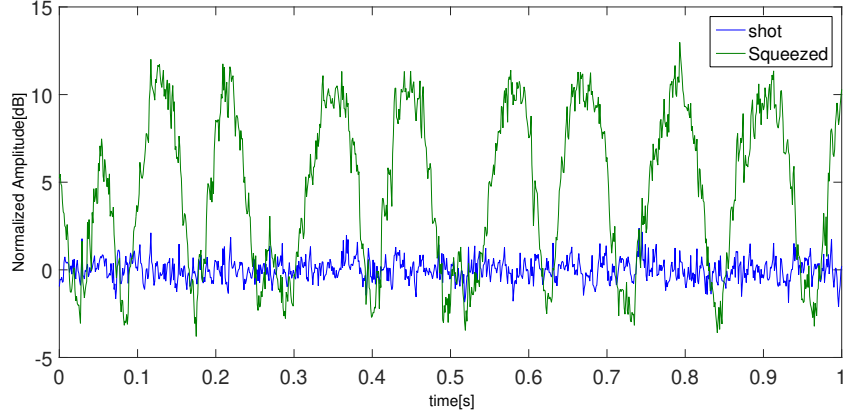

Figure 5.17: Photon noise, normalized to the shot noise level, of the MI output (temporal domain). The measurement is performed modulating the phase between the squeezed beam and the interferometer through a PZT placed on the squeezed beam path. The blue line corresponds to the classical case (obtained blocking the squeezed beam), the green line refers to squeezing injection: for certain phases the photon noise is below the shot noise level.

Using the locking technique discussed in Sec. 5.4.2, the phase is locked to the squeezed quadrature, in order to maintain the noise below the shot noise level. The result is shown in Fig. 5.18. Squeezing injection allows to reduce the photon noise below the shot-noise level: the achieved squeezing levels are 2.5 dB for the first MI and 3 dB for the second one.

5.5 Experimental results with two single mode squeezed states

In this section the experimental results corresponding to the injection of two independent squeezed states ($|\psi(\lambda)\rangle = |sq\rangle_{a1} \otimes |sq\rangle_{a2}$) are presented. The squeezed states are produced and injected as described in Sec.s 2.2-5.4.2. Data, consisting in both DC and AC outputs of the photodiode at the output port, are acquired according to Sec. 5.4. To reproduce the classical case the squeezed light is blocked before entering the MIs.

In order to measure the sensitivity of our system in phase correlation measurement
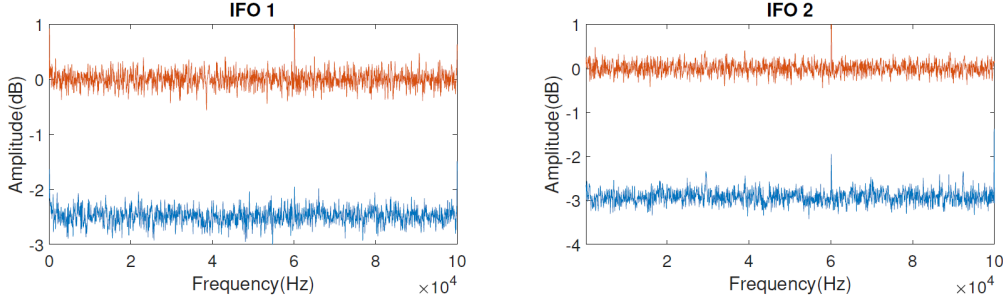
Figure 5.18: Photon noise, normalized to the shot-noise level, of the MIs output (frequency domain). This measurement is performed after locking the quadrature to the squeezed one. The blue line corresponds to squeezing injection, while the red line represents the shot-noise limit and is obtained blocking the squeezed beam. The squeezing levels measured are 2.5 dB for the first MI and 3 dB for the second one.

and to quantify the quantum enhancement two different situations are considered:

- Correlated white noise injected: we inject an artificial phase noise through the EOM inside the MIs. The noise generator allows to have perfectly correlated noise between the two channels. This situation emulates the parallel configuration of the holometer, where HN is correlated between the two MIs.

- No noise injected: in this case only the photon noise is present. Being the two squeezed states independent, the photon noise is expected to be uncorrelated between the two MIs.

Note that our experiment is not focused on the search of HN, but to demonstrate that quantum light can enhance the sensitivity of cross-correlation measurement. The noise injected is below the shot noise (around 1/5 of the shot noise level), but is higher than the expected HN, and its spectrum is not related to the one conjectured by Hogan in [81]. Moreover, our set-up does not present the two holometer configurations, parallel and perpendicular (see Sec. 5.2.1). The parallel configuration, where phase correlation due to HN is expected, corresponds to the case of correlated white noise injection; the perpendicular configuration, where HN is uncorrelated and therefore no phase correlation is expected, corresponds to the case of no external noise injected.

The analysis can be performed both in the temporal and in the frequency domains, the results are reported according to this classification.

5.5.1 Analysis in the temporal domain

The analysis in temporal domain follows direcly from the acquired AC signal of the output PDs, $\hat{X}_j(t)$ ($j = 1,2$ refers to MI_1 and MI_2 respectively). This quantity is proportional to the number of detected photons, $\hat{N}_j(t)$, which is the quantity considered

in the theoretical discussion. For the sake of simplicity, $X_j(t)$ is redefined as $\hat{X}_j(t) = \hat{X}_j(t) - \langle \hat{X}_j(t) \rangle$. According to Eq. 5.25, the quantity considered in the subsequent analysis is the covariance between the two interferometers output:

$$\hat{C}(\phi_1, \phi_2) = \hat{X}_1(\phi_1)\hat{X}_2(\phi_2) \tag{5.41}$$

In the photocurrent fluctuations two different components are present: one induced by the photon noise (*pn*) and one corresponding to the white noise (*wn*, when injected). Since photon noise and white noise injected are uncorrelated, it follows:

$$X_j(t) = X_{j,pn}(t) + X_{j,wn}(t) \tag{5.42}$$

$$\mathrm{Var}(X_j(t)) = \mathrm{Var}(X_{j,pn}(t)) + \mathrm{Var}(X_{j,wn}(t)) \tag{5.43}$$

The photon noise is uncorrelated between the two MIs, while the white noise is correlated. In the classical case $\mathrm{Var}(X_{j,pn})$ corresponds to the shot noise limit:

$$\mathrm{Var}(X_{j,pn}^{(cl)}) = \mathrm{Var}(X_{j,sn}) = X_{j,sn}. \tag{5.44}$$

With squeezing injection it is lowered below it:

$$\mathrm{Var}(X_{j,pn}^{(sq)}) \sim \mathrm{Var}(X_{j,sn})/g, \text{ being } g > 1. \tag{5.45}$$

Considering the covariance between $X_1(t)$ and $X_2(t)$, the correlated noise emerges from the uncorrelated photon-noise contribution:

$$\mathrm{Cov}(X_1(t), X_2(t)) = \mathrm{Cov}(X_{1pn}(t), X_{2pn}(t)) + \mathrm{Cov}(X_{1pn}(t), X_{2wn}(t)) + \tag{5.46}$$

$$+ \mathrm{Cov}(X_{1wn}(t), X_{2pn}(t)) + \mathrm{Cov}(X_{1wn}(t), X_{2wn}(t)) = \mathrm{Cov}(X_{1wn}(t), X_{2wn}(t)) \tag{5.47}$$

In the temporal domain the quantity of interest is the cross-correlation coefficient, $\rho_{1,2}(\tau)$. This quantity is defined as:

$$\rho_{1,2}(\tau) = \frac{|R_{1,2}(\tau)|}{\sqrt{\mathrm{Var}(X_{1sn})\mathrm{Var}(X_{2sn})}} \tag{5.48}$$

where $R_{1,2}(\tau)$ is the cross-correlation function:

$$R_{1,2}(\tau) = \mathrm{Cov}(X_1(t), X_2(t+\tau)) = \mathrm{Cov}(X_{1wn}(t), X_{2wn}(t+\tau)) \tag{5.49}$$

This quantity is different from zero only for null delay, $\tau = 0$. Experimentally $\rho_{1,2}(\tau)$ is estimated using a finite number of frames, and therefore is subject to fluctuations. Estimating these fluctuations is of the utmost importance. The variance of $\rho_{1,2}(\tau)$ is estimated as:

$$\Delta^2(\rho_{1,2}(\tau)) = \langle \rho_{1,2}(\tau)^2 \rangle - \langle \rho_{1,2}(\tau) \rangle^2 =$$

$$= \frac{\langle \text{Cov}(X_1(t)X_2(t+\tau))^2 \rangle - \langle \text{Cov}(X_1(t)X_2(t+\tau)) \rangle^2}{\langle \text{Var}(X_{1sn}) \rangle \langle \text{Var}(X_{2sn}) \rangle} \tag{5.50}$$

Said N the number of samples acquired, the first term at the numerator can be evaluated considering:

$$\langle \text{Cov}^2(X_1, X_2) \rangle = \frac{1}{N^2} \sum_{i,j=1}^{N} \langle X_{1i}X_{2i}X_{1j}X_{2j} \rangle =$$

$$= \frac{1}{N^2} \left[\sum_{i=j} \langle X_{1i}^2 X_{2i}^2 \rangle + \sum_{i \neq j} \langle X_{1i}X_{2i} \rangle \langle X_{1j}X_{2j} \rangle \right] = \frac{1}{N^2} [N \langle X_1^2 X_2^2 \rangle + N(N-1)\langle X_1 X_2 \rangle^2] =$$

$$= \frac{\langle X_1^2 X_2^2 \rangle}{N} + \left(1 - \frac{1}{N}\right) \langle X_1 X_2 \rangle^2 \tag{5.51}$$

Replacing this result in Eq. 5.50 and using the fact that, being $\langle X_1 \rangle = \langle X_2 \rangle = 0$ it follows $\text{Cov}(X_1 X_2) = \langle X_1 X_2 \rangle$, we have:

$$\Delta^2 \rho_{1,2}(\tau) = \frac{1}{N} \frac{\text{Var}(\text{Cov}(X_1, X_2))}{\text{Var}(X_{1sn})\text{Var}(X_{2sn})} \tag{5.52}$$

From Eq. 5.52 it emerges that the uncertainty in the estimation of $\rho_{1,2}(\tau)$ scales with $1/\sqrt{N}$. This means that acquiring enough samples any correlated signal emerges. However, the use of quantum light allows to decrease the number of samples necessary to detect the correlated signal. Decreasing the acquisition time ($\propto$ to the number of samples) can be extremely relevant in real situations.

To appreciate the effects of squeezing injection we can substitute X_j with $X_j^{(cl)} = X_{j,pn}^{(cl)} + X_{j,wn}$ and $X_j^{(sq)} = X_{j,pn}^{(sq)} + X_{j,wn}$. The difference between the two cases is in the photon noise variance (compare Eq.s 5.44-5.45). For the classical case we obtain:

$$\Delta^2(\rho_{12}(\tau))_{cl} = \frac{1}{N} + \frac{\text{Var}(\text{Cov}(X_{1wn}(t), X_{2wn}(t+\tau))}{N\text{Var}(X_{1sn}(t))\text{Var}(X_{2sn}(t))} \tag{5.53}$$

While with squeezing injection:

$$\Delta^2(\rho_{12}(\tau))_{sq} = \frac{\text{Var}(X_{1sq}(t))\text{Var}(X_{2sq}(t))}{N\text{Var}(X_{1sn}(t))\text{Var}(X_{2sn}(t))} + \frac{\text{Var}(\text{Cov}(X_{1wn}(t), X_{2wn}(t+\tau))}{N\text{Var}(X_{1sn}(t))\text{Var}(X_{2sn}(t))} \tag{5.54}$$

Comparing Eq. 5.53 with Eq. 5.54 we conclude that the first term is reduced by the factor $\frac{\text{Var}(X_{1sq}(t))\text{Var}(X_{2sq}(t))}{\text{Var}(X_{1sn}(t))\text{Var}(X_{2sn}(t))} \sim g_1 \cdot g_2$. g_i can be experimentally evaluated measuring the photon noise without any other noise injected, with and without squeezing. This measurement is reported in Fig. 5.18 and leads to:

$$MI_1 \; : \; -3 \text{ dB} = 10\log_{10}\left(\frac{\text{Var}(X_{1sq})}{\text{Var}(X_{1sn})}\right) \rightarrow g_1 = \frac{\text{Var}(X_{1sn})}{\text{Var}(X_{1sq})} = 10^{3/10} = 2 \tag{5.55}$$

$$MI_2 \; : \; -2.5 \text{ dB} \rightarrow g_2 = \frac{\text{Var}(X_{2sn})}{\text{Var}(X_{2sq})} = 10^{2.5/10} = 1.77 \tag{5.56}$$

Signal to noise ratio

We have now all the elements to quantitatively evaluate the emergence of the signal from the noise floor. To this purpose we consider the signal to noise ratio (SNR), figure of merit defined as:

$$\text{SNR} = \frac{\langle \rho_{12}(\tau = 0) \rangle - \langle \rho_{12}(\tau \neq 0) \rangle}{\langle \rho_{12}(\tau \neq 0) \rangle} \tag{5.57}$$

To theoretically evaluate the SNR, the absolute value of the cross-correlation, $R_{12}(\tau)$ can be approximated as:

$$\langle |R_{12}(\tau)| \rangle = \langle |\text{Cov}(X_1(t)X_2(t+\tau))| \rangle \sim \sqrt{\langle \text{Cov}^2(X_1 X_2) \rangle} \tag{5.58}$$

According to Eq. 5.51, this approximation holds in the limit $N \to \infty$. In this limit $\langle \text{Cov}^2(X_1, X_2) \rangle = \langle X_1 X_2 \rangle^2$ and therefore $\sqrt{\langle \text{Cov}^2(X_1, X_2) \rangle} = |\langle X_1 X_2 \rangle|$. Under this assumption, the general expression for $\langle \rho_{1,2}(\tau) \rangle$ is:

$$\langle \rho_{1,2}(\tau) \rangle = \frac{\sqrt{\frac{\langle X_1^2 X_2^2 \rangle}{N} + (1 - \frac{1}{N})\langle X_1 X_2 \rangle^2}}{\sqrt{\text{Var}(X_{1sn})\text{Var}(X_{2sn})}} \tag{5.59}$$

Let us now consider the cases of $\tau = 0$ and $\tau \neq 0$ separately:

- $\tau \neq 0$

In this case, since X_{1pn} and X_{2pn} are uncorrelated: $\langle X_1^2 X_2^2 \rangle = \langle X_1^2 \rangle \langle X_2^2 \rangle = \text{Var}(X_1)\text{Var}(X_2)$ and $\langle X_1 X_2 \rangle = 0$. Therefore:

$$\langle \rho_{1,2}(\tau \neq 0) \rangle = \frac{\sqrt{\text{Var}(X_1)\text{Var}(X_2)}}{\sqrt{N\text{Var}(X_{1sn})\text{Var}(X_{2sn})}} \tag{5.60}$$

- $\tau = 0$

In this case, being the white noise correlated: $\langle X_1 X_2 \rangle = \langle X_{1wn} X_{2wn} \rangle$. It follows:

$$\langle \rho_{1,2}(\tau = 0) \rangle = \frac{\sqrt{\frac{\text{Var}(X_1)\text{Var}(X_2)}{N} + (1 - \frac{1}{N})\langle X_{1wn} X_{2wn} \rangle^2}}{\sqrt{\text{Var}(X_{1sn})\text{Var}(X_{2sn})}} \tag{5.61}$$

Using Eq.s 5.60-5.61 it is possible to write the general expression for the SNR:

$$\text{SNR} \sim \sqrt{1 + \frac{N\langle X_{1wn} X_{2wn} \rangle^2}{\text{Var}(X_1)\text{Var}(X_2)}} - 1 \tag{5.62}$$

It results that, for sufficiently high N, the SNR scales $\propto \sqrt{N}$. The quantum enhancement offered by squeezing injection is defined as:

$$\mathscr{R} = \frac{\text{SNR}_{sq}}{\text{SNR}_{cl}} \sim \sqrt{\frac{\text{Var}(X_{1sn})\text{Var}(X_{2sn})}{\text{Var}(X_{1sq})\text{Var}(X_{2sq})}} = \sqrt{g_1 \cdot g_2} \tag{5.63}$$

where the limit of high N is assumed. Experimentally the SNR can be estimated considering the mean value of $\rho_{1,2}$ at zero delay, i.e. $\tau = 0$, and its mean value for $\tau \neq 0$.

In Fig. 5.19 we report $\rho_{12}(\tau)$ for different N. These data are obtained while injecting a correlated white noise (noise level $\sim 1/5$ of the shot noise) in the two MIs. The blue curves correspond to the classical case, while the red curves are obtained with squeezing injection. When injecting quantum light the peak emerges better from the noise.
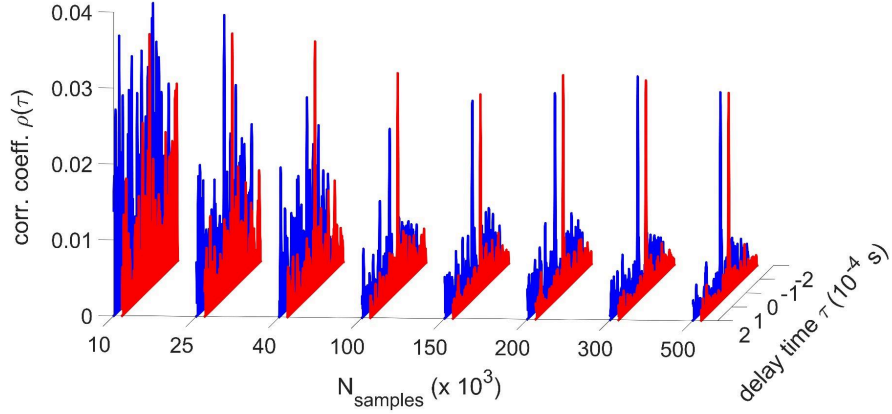

Figure 5.19: Analysis in the temporal domain, considering the injection of two independent squeezed vacuum states ($|\psi(\lambda)\rangle = |sq\rangle_{a_1} \otimes |sq\rangle_{a_2}$). The cross-correlation of the MIs output $\rho_{1,2}(\tau)$ is reported for different number of samples. The red curves correspond to the squeezing injection while the blue curve are obtained in the classical configuration. The correlation peak emerges for smaller N when squeezing is injected.

Evaluating $\rho_{12}(\tau)$ for different sets of samples, we calculate the SNR (and its uncertainty) for different N. The result is reported in Fig. 5.20. Also the ratio $\mathscr{R}$ is reported. Dots are the experimental data (error bars are too small to be appreciated), blue refers to the classical case, red refers to the squeezing injection. Black dots are obtained as ratio between the two cases. Blue and red curves are obtained fitting the experimental data with a fitting function defined as:

$$\text{SNR}(N) = \sqrt{1 + N \cdot k} - 1 \tag{5.64}$$

which reproduces the theoretical model reported in Eq. 5.62. The quantum enhancement factor $\mathscr{R}$ is evaluated fitting the black dots with a constant function (not considering
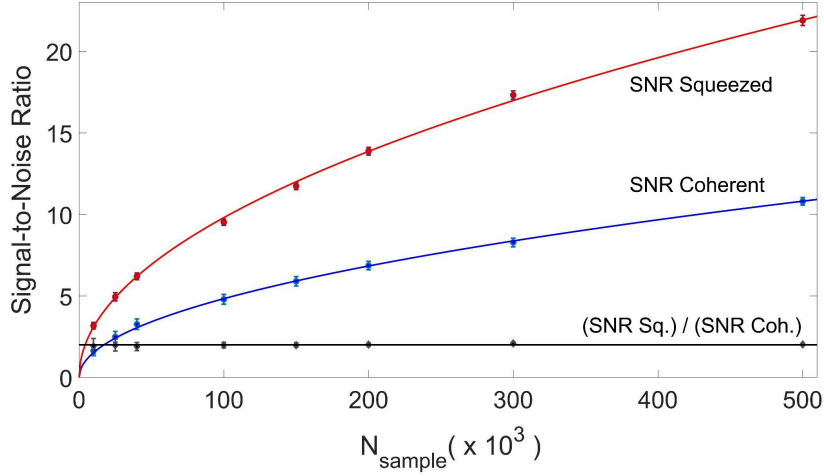
Figure 5.20: Signal to noise ratio (SNR) of the cross-correlation reported in Fig. 5.19, as a function of the number of samples *N*. Dots are the experimental data (error bars are too small to be appreciated). Blue data correspond to the classical case, red data to the squeezing injection case. The coloured curves are obtained fitting the data with the model function reported in Eq. 5.64. Black data are the ratio between squeezed and coherent SNR values, their are expected to be constant for *N* sufficiently high.

the first points in order to work in the approximation of high *N*). The values obtained from the fits are:

$$
\begin{array}{ll}
k_{cl} & (3.70 \pm 0.14) \cdot 10^{-4} \\
k_{sq} & (1.51 \pm 0.03) \cdot 10^{-3} \\
\mathscr{R} & (2.19 \pm 0.05)
\end{array}
$$

The value of $\mathscr{R}$ obtained from the fit is compatible (with 95% significativity) with the one estimated as $\sqrt{k_{sq}/k_{cl}}$. Since, according to Eq. 5.62, for $N \to \infty$, SNR $\propto \sqrt{N}$, a quantum enhancement of $\mathscr{R} \sim 2$ corresponds to a reduction of a factor $\mathscr{R}^2 \sim 4$ in the acquisition time. This factor can be extremely relevant in practical situations, where, among other factors, the stability of the system needs to be taken into account.

Moreover, $\mathscr{R} \sim 2$ is also comparable with the squeezing levels independently measured. In particular, we measure $g_1 = 2$ and $g_2 = 1.77$ (see Eq.s 5.55-5.56) and therefore, according to Eq. 5.63, we expect $\mathscr{R} \sim \sqrt{2 * 1.77} \sim 1.88$. The fact that we find an higher value can be due to the presence of a different squeezing level between the two measurements (the 3 dB and 2.5 dB refer to a calibration measurement, taken in a previous moment without noise injected).

135

5.5.2 Analysis in the frequency domain

In the frequency domain the function of interest is the cross-linear spectral density (CLSD, see Appendix B.4). It is evaluated as the square root of the cross-power spectral density (CPSD), defined as the discrete Fourier transform of the cross-correlation function:

$$S_{12}(\omega) = \sum_{\tau=0}^{N} R_{12}(\tau) e^{-j\omega\tau} \tag{5.65}$$

where, according to Eq. 5.49, $R_{12}(\tau) = \langle X_1(t) X_2(t+\tau) \rangle$ and N is the finite number of samples acquired. Considering the discrete Fourier transform rather than its continuous version, various problems emerge and different methods can be used to solve them. This topic is briefly reviewed in Appendix B.1. In particular, we use the Welch method, implementing the algorithm in a Labview code (see [69] for all the details). The time series are divided in $N_{spectra}$ bins and for each bin the CPSD is calculated, then the average of the $N_{spectra}$ CPSDs is evaluated and, by the square root, the CLSD is found. The CLSD is in general a complex function, therefore we always consider its magnitude. The mesurement unit of the CLSD, being the time series X_j expressed in V, is $V/\sqrt{Hz}$. Using the procedure described in Sec. 5.4.3 we convert it into $m/\sqrt{Hz}$.

Being related by a Fourier transform, the results in the frequency domain are in analogy with the ones obtained in the temporal domain in Sec. 5.5.1. Similarly to what obtained in Eq. 5.51, for the cross-linear spectral density we have:

$$\text{CLSD}(\omega) = \sqrt{S_{12}(\omega)} = \sqrt{\text{FFT}(R_{12}(\tau))} =$$

$$= \sqrt[4]{\frac{\text{PSD}_1 \text{PSD}_2}{N_{spectra}} + (1 - \frac{1}{N_{spectra}})[S_{12}^{wn}(\omega)]^2} \sim \sqrt[4]{\frac{\text{PSD}_1 \text{PSD}_2}{N_{spectra}} + [S_{12}^{wn}(\omega)]^2} \tag{5.66}$$

where PSD_1 and PSD_2 are the PSD of the two times series separately (see Eq. 5.38) and $S_{12}^{wn}(\omega)$ is the CPSD of the injected correlated white noise. From Eq. 5.66 some properties of the CLSD emerges:

- In absence of white noise injected, i.e. $S_{12}^{wn}(\omega) = 0$, it follows that $\text{CLSD} \propto N_{spectra}^{-1/4}$. This means that increasing the number of spectra allows to wash away the uncorrelated noise contribution potentially reaching an arbitrary high displacement sensitivity.

- In the presence of correlated white noise, $S_{12}^{wn}(\omega) \neq 0$. The contribution of this term to the CLSD is unaffected by increasing the number of spectra and therefore, sufficiently increasing $N_{spectra}$, the correlated noise can emerge from the background.

- Squeezing injection affects the PSDs, lowering the photon noise below the shot noise limit. It allows the correlated noise to emerge from the background with a lower number of frames compared to the classical case.

In Fig. 5.21 the CLSDs, plotted for a bandwidth of 100kHz and corresponding to the two different experimental situations, are reported. All the spectra are calculated from the read-out signals down-mixed at 13.5 MHz. Blue lines refer to the classical case, while red lines correspond to the two independent squeezed states injection. Thick lines are obtained in absence of white noise, while faint lines correspond to white noise injection (the injected noise level is 1/5 of the shot noise level). Moreover, the LSDs of the first interferometer are reported as faint dashed lines. When squeezing is injected the traces corresponding to absence and presence of white noise are more separated than in the classical case.

Each acquisition (with and without noise respectively) lasts 20 s, being the acquisition rate of 500 kSample/s, we collect $N_{samples} = 10^7$. Fig. 5.21 is obtained with $N_{spectra} = 1000$. Considering different values for the number of spectra and averaging, for each value, the CLSDs on the bandwidth considered, Fig. 5.22 is obtained. The dots correspond to the mean CLSD for a certain $N_{spectra}$. For example, the dots in the circle are obtained as mean values of the CLSDs plotted in Fig. 5.21. Plain lines refer to no-noise injected, while dashed lines refer to correlated white noise injected.
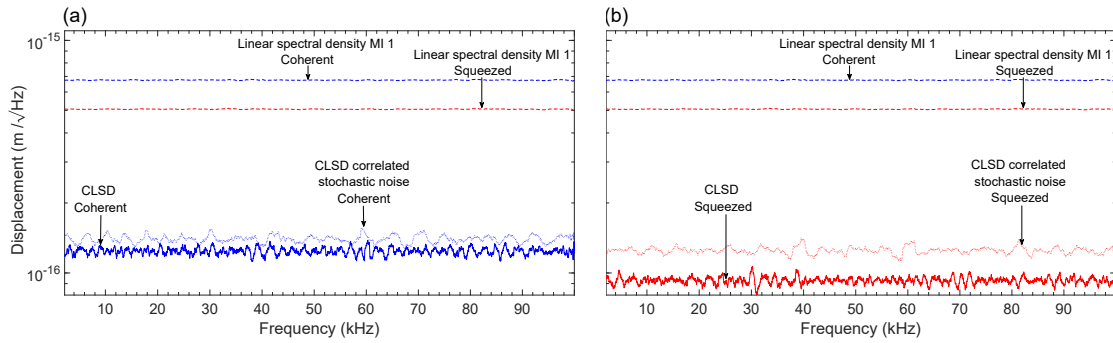

Figure 5.21: Cross Linear Spectral Densities (CLSDs, expressed in m/$\sqrt{\text{Hz}}$) in a bandwidth of 100 kHz around 13.5 MHz, for $N_{spectra} = 1000$. Figure (a) refers to the classical case, while Figure (b) corresponds to squeezing injection. Thick lines are obtained without any injected noise, thus corresponding to the background photon noise. Faint lines correspond to the injection of white noise (correlated in the two MIs and of amplitude $\sim 1/5$ of the shot noise). As a reference, the Linear Spectral Densities (LSDs) of the first MI, with and without squeezing, are also reported.

For the higher value considered of $N_{spectra}$ we demonstrate a maximum sensitivity of $(3.210 \pm 0.016) \cdot 10^{-17}$ m/$\sqrt{\text{Hz}}$. This value corresponds to roughly 1/20 of the shot noise level. This level is estimated using the LSD in the single interferometer, and results to be $(6.745 \pm 0.002) \cdot 10^{-16}$ m/$\sqrt{\text{Hz}}$. This sensitivity is obtained thanks to two contributions: the cross correlation technique and the squeezing injection. Referring to Fig. 5.21 and comparing the classical LSD with the classical CLSD we can conclude that the cross-correlation allows to go $\sim$10 dB below the shot noise limit of the single MI. On the other side, if we compare the classical LSD with the LSD in the presence of squeezing,
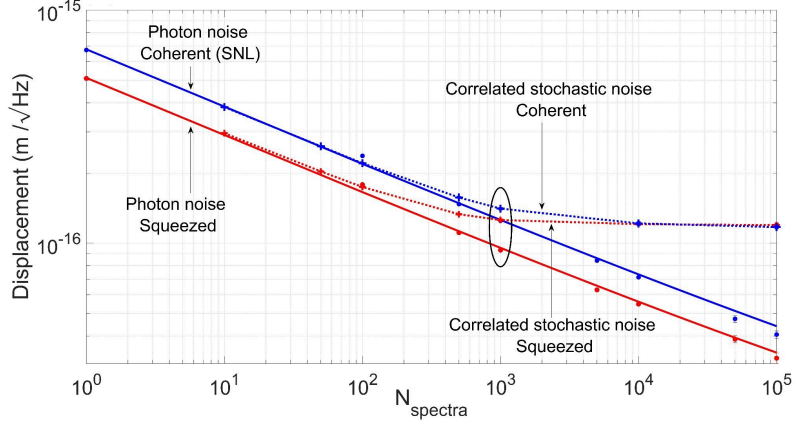
Figure 5.22: Average level of the Cross Linear Spectral Densities (CLSDs, expressed in m/$\sqrt{\text{Hz}}$) at varying $N_{spectra}$. Both the cases of presence and absence of injected white noise are considered. Red curves refer to squeezing injection, blue curves to the classical case. Dots are the experimental data, the thick solid lines are the fitting curves: the scaling of the displacement sensitivity $\propto N_{spectra}^{-1/4}$ is confirmed. The values in the circle correspond to the mean values of the CLSDs plotted in Fig. 5.21

it emerges that squeezing injection offers 3 dB of further advantage.

According to Eq. 5.66, in absence of noise we have CLSD $\propto 1/\sqrt[4]{N_{spectra}}$. To check the validity of this model we fit the experimental data in absence of noise, with and without squeezing injection, with the fitting function:

$$\text{CLSD}(N_{spectra}) = \left(\frac{A}{N_{spectra}} + c \right)^{1/4} \tag{5.67}$$

The resulting fit functions are reported as plain lines in Fig. 5.22. The obtained fit parameters are:

$$
\begin{array}{ll}
A_{cl} & (12.96 \pm 0.01) \cdot 10^{-13} \\
A_{sq} & (4.174 \pm 0.002) \cdot 10^{-13} \\
c_{cl} & (1.6 \pm 1.9) \cdot 10^{-20} \\
c_{sq} & (0.7 \pm 1.1) \cdot 10^{-20}
\end{array}
$$

As expected, in both cases, c is compatible with zero. The quantum enhancement can be evaluated from the ratio A_{cl}/A_{sq}. For reaching same sensitivity the number of frames required when squeezing is injected is smaller by a factor $A_{cl}/A_{sq} \sim 3.1$. When correlated noise is injected, the CLSDs, for $N_{spectra}$ sufficiently high, present a plateau of amplitude corresponding to the noise amplitude. With squeezing injection the plateau is reached for a lower number of frames.

5.6   Experimental results with twin-beam state

In this section the experimental results corresponding to the injection of a twin-beam state ($|\psi(\lambda)\rangle = |twb\rangle_{a_1,a_2}$) are presented. As pointed out in Sec. 5.4, we do not produce a real twin-beam state but we split a single-mode squeezed state with a 50-50 beam-splitter. In Sec. 2.3 we demonstrate that, in terms of quadrature correlation between the two modes, they behave exactly the same. On the contrary, the state obtained with this implementation does not present photon number entanglement between the two modes, preventing us from working in the "photon-number entanglement" regime. However, the experimental losses present in our setup are relevant, rendering the "quadrature correlation regime" the only accessible.

Similarly to the two-single mode squeezed case (Sec. 5.5), the acquired data consist in both DC and AC signals of the output PD. The observable we consider in this case is the difference between the two outputs:

$$\hat{C}(\phi_1, \phi_2) = \hat{X}_1(\phi_1) - \hat{X}_2(\phi_2) \tag{5.68}$$

Note that in the theoretical discussion in Sec. 5.3.2 a different observable is proposed, in particular, according to Eq. 5.31: $\hat{C}(\phi_1, \phi_2) = \text{Var}(\hat{X}_1(\phi_1) - \hat{X}_2(\phi_2))$. We have recently extended the data analysis considering this observable and thus recovering the desidered quantity $\langle\delta\phi_1\delta\phi_2\rangle$. These results have been obtained too late for being included in this thesis, however this new analysis can be found in the latest version of [19]. From the output difference, in Eq. 5.68, it is not possible to estimate the phase correlation $\langle\delta\phi_1\delta\phi_2\rangle$ between the two outputs. However, considering this quantity, allows to test and characterize the injected quantum state properties.

In order to demonstrate how the injection of a twin-beam state can enhance the sensitivity of our system, measurements in different experimental conditions are performed:

- No noise injected, in this case the only noise source is the photon noise.

- Uncorrelated white noise injected. Also if this is not the case of HN, there are several significant situations where detecting uncorrelated noises can be of interest (such as in case of scattering or unwanted resonances).

- Correlated white noise injected. Since we consider the output difference a noise of this kind is washed away. However, it can be useful as test measurement.

- Single frequency tone in one of the two MI.

The analysis can be performed both in the temporal and frequency domain.

5.6.1 Analysis in the temporal domain

No noise injected

In order to properly subtract X_1 and X_2 it is necessary to take into account possible imbalance between the two interferometers, in particular differences in the electronic gain. The normalization is performed considering the DC values, P_1 and P_2 and calculating the gain of the two detectors as:

$$g_1 = \frac{\text{Var}(X_1)}{P_1}, g_2 = \frac{\text{Var}(X_2)}{P_2} \tag{5.69}$$

Fig. 5.23 reports the variance of the output difference, opportunely normalized as $\hat{X}_1(t)-\sqrt{\frac{g_2}{g_1}}\hat{X}_2(t+\tau)$, at varying τ. The values are normalized to the classical case (blue line). When considering twin-beam injection (red line), the variance is always lower, for every
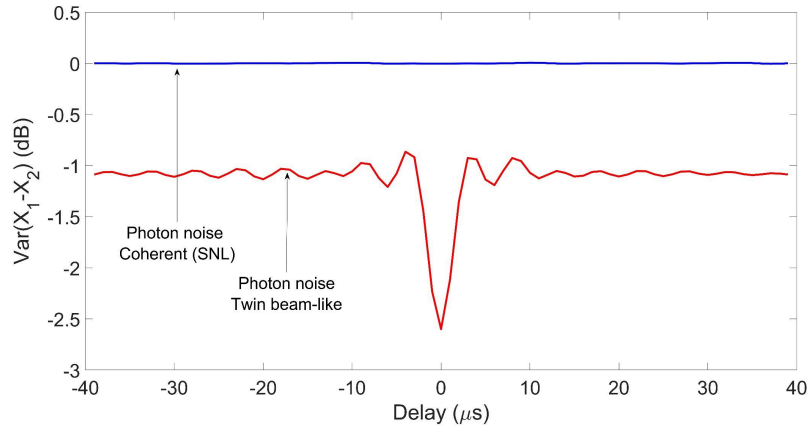

Figure 5.23: Variance of the photocurrent difference at varying the time delay τ, normalized to the classical case. In this case no external noise is injected. Blue trace refers to the coherent case, red trace to the twin-beam like state injection. With the quantum strategy a noise reduction of 2.5 dB is demonstrated for $\tau = 0$.

τ. For $\tau \neq 0$, the noise reduction is due to the residual squeezing in the two beams separately (each of them can be thought as a squeezed state incurring in 50% losses, induced by the beam splitter), and has nothing to do with the quadrature correlation between the two modes. For $\tau = 0$, where quadrature correlation occurs, an advantage of 2.5 dB is demonstrated.

Uncorrelated white noise injection

In this case, as variance on the output difference, we expect:

$$\text{Var}(X_1 - X_2) = \text{Var}((X_{1pn} + X_{1wn}) - (X_{2pn} + X_{2wn})) =$$

$$= \mathrm{Var}(X_{1pn} - X_{2pn}) + \mathrm{Var}(X_{1wn} - X_{2wn}) =$$
$$= \mathrm{Var}(X_{1pn} - X_{2pn}) + \mathrm{Var}(X_{1wn}) + \mathrm{Var}(X_{2wn}) - 2\mathrm{Cov}(X_{1wn}, X_{2wn}) =$$
$$\mathrm{Var}(X_{1pn} - X_{2pn}) + \mathrm{Var}(X_{1wn}) + \mathrm{Var}(X_{2wn}) \tag{5.70}$$

where the last equality holds because the noise injected is uncorrelated. The result in Eq. 5.70 shows that the variance reported in Fig. 5.23, when no noise is injected and the only contribution is the photon noise, increases by the quantity $\mathrm{Var}(X_{1wn}) + \mathrm{Var}(X_{2wn})$. This is confirmed in Fig. 5.24, where $\mathrm{Var}(X_1 - X_2)$ at varying τ is reported both in presence or absence of noise. In terms of dB, the injection of noise in the twin-beam case causes the dip reducing by ~ 1 dB. If only classical light is used, the change induced by the noise injection is of only 0.3 dB. We conclude that in the twin-beam case the noise injected emerges better from the background noise.
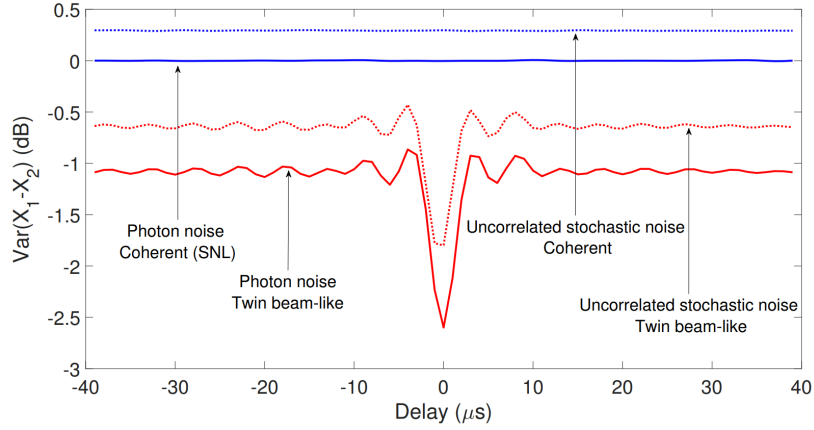

Figure 5.24: Variance of the photocurrent difference at varying the time delay τ, normalized to the classical case without noise injection. Continuous lines refer to no external noise injected, dotted lines are obtained injecting an uncorrelated white noise. Blue trace refers to the coherent case, while red trace to the twin-beam like state injection. Using the quantum strategy the noise injected emerges better from the background (the difference is of 0.3 dB for the classical case and 1 dB with the twin-beam-like state).

Correlated white noise injection

In this case $\mathrm{Cov}(X_{1wn}, X_{2wn}) \neq 0$. As variance on the output difference, we expect:

$$\mathrm{Var}(X_1 - X_2) = \mathrm{Var}(X_{1pn} - X_{2pn}) + \mathrm{Var}(X_{1wn}) + \mathrm{Var}(X_{2wn}) - 2\mathrm{Cov}(X_{1wn}, X_{2wn}) \tag{5.71}$$

In case of perfectly correlated noise ($X_{1wn} = X_{2wn} = X_{wn}$), for $\tau = 0$, it follows:

$$\mathrm{Var}(X_1 - X_2) = \mathrm{Var}(X_{1pn} - X_{2pn}) + 2\mathrm{Var}(X_{wn}) - 2\mathrm{Var}(X_{wn}) = \mathrm{Var}(X_{1pn} - X_{2pn}) \tag{5.72}$$

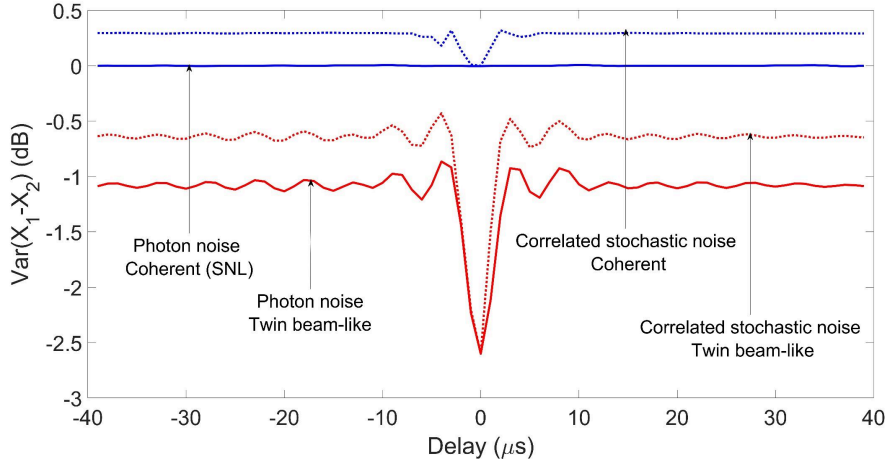For $\tau = 0$, we expect no difference between noise and no noise injection. This is confirmed in Fig. 5.25. .

141

Figure 5.25: Variance of the photocurrent difference at varying the time delay τ, normalized to the classical case without noise injection. Continuos lines refer to no external noise injected, while dotted lines are obtained injecting a correlated white noise. Blue trace refers to the coherent case, while red trace to the twin-beam like state injection. The correlated noise is washed away in the output subtraction for $\tau = 0$.

5.6.2 Analysis in the frequency domain

In the frequency domain we consider the PSD of the output difference for $\tau = 0$ (opportunely normalized as $\hat{X}_1(t) - \sqrt{\frac{g_2}{g_1}}\hat{X}_2(t)$). The PSD is evaluated using the method reported in Appendix B.1 and normalized to the classical case. The PSDs in presence and absence of injected uncorrelated noise are reported in Fig. 5.26. Blue lines refer to the classical case, red lines to the twin-beam-like state injection. The spectra are calculated in a bandwidth of 100 kHz from the read-out signals down-mixed at 13.5 MHz. The results obtained in the time domain are confirmed in the frequancy domain: in the quantum enhanced case, the injected noise emerges better from the photon noise. The difference is 1 dB with squeezing and 0.3 dB with only classical light.

As further example, we consider the injection of a single tone in one of the two MIs. The corresponding results are reported in Fig.s 5.27-5.28. In Fig. 5.27(a)-(b) there are the PSDs for the single MIs, in a bandwidth of 4 kHz and normalized for the classical case. A remaining squeezing level of 1 dB is present in both the interferometers. Considering the output subtraction (see Fig. 5.28) almost the entire squeezing level is recovered, leading to a noise reduction of $\sim$ 2 dB. .
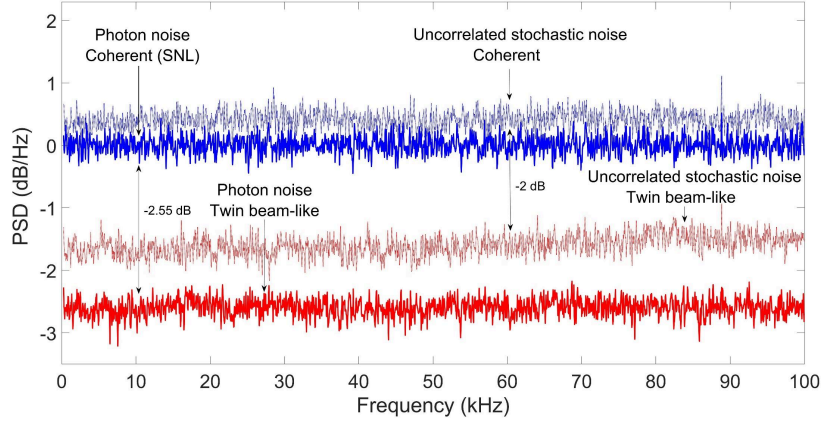
Figure 5.26: Power Spectral Densities (PSDs) of the output signals subtraction, normalized to the shot noise limit. The spectra are shown in a bandwidth of 100 kHz and the read-out signals are down-mixed at 13.5 MHz. Red curves refer to the twin-beam-like state injection and blue curves to the classical case. Thick lines are obtained in absence of external noise, faint lines correspond to uncorrelated white noise injection.
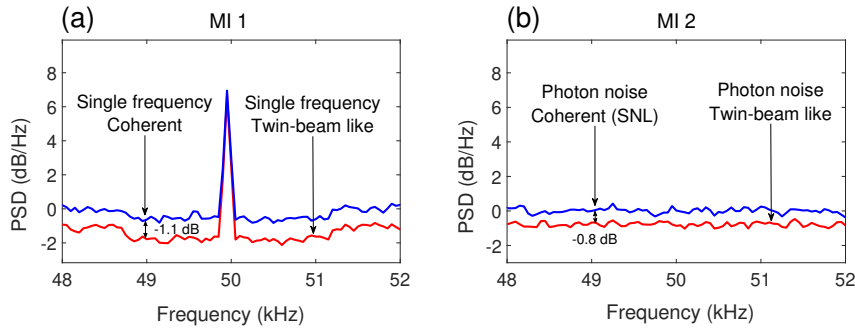

Figure 5.27: Power Spectral Densities (PSDs) of the output signal from the single interferometers, normalized to the shot-noise limit. A single-frequency tone at 13.55 MHz is injected in the first MI. The signal is down-mixed at 13.5 MHz and a bandwidth of 4kHz is reported. Red lines correspond to the twin-beam-like state injection, blue lines to the classical strategy.

5.7 Conclusion

In this chapter we discussed the potentialities of quantum light in correlated interferometry. We considered a system of two power recycling Michelson Interferometers, inspired by the classical system built at Fermilab and named "holometer". That system is devoted to search of holographic noise, a conjectured source of noise arising from
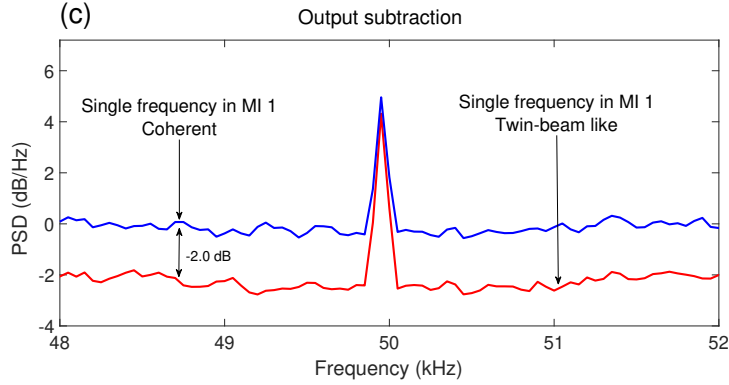
143

Figure 5.28: Power Spectral Densities (PSDs), normalized to the shot-noise limit, of the read-out signals subtraction. The quadrature correlation between the two modes leads to 2 dB of squeezing. The signal is down-mixed at 13.5 MHz and a bandwidth of 4kHz is reported. Red lines correspond to the twin-beam-like state injection, blue lines to the classical strategy.

Planck scale physics effects. However, correlated interferometry can be useful in different contexts, such as detection of gravitational wave background or search for traces of primordial blackholes.

Aim of our experiment is to demonstrate that quantum light can enhance the sensitivity in phase correlation measurements. Two quantum states of light are considered entering the classically unused doors: two independent squeezed vacuum states and a twin-beam state. The first case in the most straightforward extension of using quantum light in one interferometer, as currently done in many gravitational wave detectors. The second case has no analogous when only one interferometer is considered. The theoretically results, discussed in [67] and [68] are presented. It emerges that the use of quantum light can lead to important quantum enhancement in phase correlation measurements. In case of perfect efficiency and working exactly at the dark port, twin-beam state allows to lower the uncertainty on the phase correlation measurement to zero.

In Sec.s 5.5-5.6 the experimental results obtained with our set-up are reported. The feasibility of quantum enhanced correlated interferometry is demonstrated: it is the first time that the potentialities of quantum light are exploited in a system of this kind. The experiment has been done in collaboration with the Danish Technical University, for this reason I had the opportunity of spending four months of my PhD in Denmark, working at the experimental set-up and collecting data.

Concerning the injection of two independent squeezed states, we demonstrate a 2.5 dB and 3 dB enhanced sensitivity in each interferometer. Injecting a correlated phase signal in the two interferometers and performing a joint measurement, we demonstrate

a signal-to-noise ratio enhancement of a factor of 2 compared to the classical case (corresponding to around 3dB of quantum enhancement). This would allow to obtain the same sensitivity of the classical case reducing by a factor of 4 the measurement time: this can be extremely useful in practical situations. The absolute sensitivity obtained after only 20 s measurement time is $(3.21 \pm 0.16) \times 10^{-17} \mathrm{m}/\sqrt{\mathrm{Hz}}$, which corresponds to around 1/20 times the sensitivity of a single, shot noise limited interferometer. Incidentally, these results also pose a limit to holographic noise in a different frequency region respect to the one investigated at Fermilab.

Furthermore, we consider a twin-beam like state, presenting the same properties of a real twin-beam state in terms of quadrature correlations, by splitting a single mode squeezed state on a balanced beam splitter. In this case the squeezing levels observed in the individual interferometers are 1.1 dB and 0.9 dB respectively. The total original squeezing level is recovered when the subtraction of the signals is considered: 2.6 dB of noise reduction respect to the shot noise limited case is demonstrated in the subtraction of the two interferometers outputs. This approach can be useful in the presence of uncorrelated noise sources such as the ones due to scattering or resonances.

In conclusion, our experiment represents a first feasibility test for realization of quantum enhanced correlated phase interferometry, paving the way for practical applications.

Appendix A

Hamiltonian for the twin-beam state

In the previous paragraph we directly presented the twb expression in the Fock basis, focusing on the state properties. Here we describe how the twb expression can be obtained from the interaction hamiltonian $H_I(t)$.

As many other quantum states of light, the twb state originates from the interaction of an intense optical field with a non linear medium. The dielectric polarization vector P can be expanded as:

$$P = \chi^{(1)}E + \chi^{(2)}EE + \chi^{(3)}EEE + \dots \qquad \text{(A.1)}$$

In linear media $\chi^{(n)} = 0$ for $n > 1$, while in non linear media $\chi^{(n)} \neq 0$, remaining $\chi^{(2)} \ll \chi^{(1)}$. If considering a high strength of the electric field E, the higher order terms can be relevant.

Assuming non-linear effects relevant up to the second order the expression of the field hamiltonian, in a non-magnetic medium, is:

$$H(t) = \int_V \frac{1}{2}\mathbf{E} \cdot (\epsilon_0\mathbf{E}(r,t) + \vec{P}(r,t))\mathrm{d}V = \int_V \left[\frac{1}{2}\epsilon_0 E^2(r,t) + X_1(r,t) + X_2(r,t)\right]\mathrm{d}V \quad \text{(A.2)}$$

where V indicates the volume of the non linear medium and:

$$X_1(r,t) = \frac{1}{2}\chi_{i,j}^{(1)}E_iE_j \qquad \text{(A.3)}$$

$$X_2(r,t) = \frac{1}{3}\chi_{i,j,k}^{(2)}E_iE_jE_k. \qquad \text{(A.4)}$$

The expression in Eq. A.4 represents the non linear interaction and is the term on which we will focus on:

$$H_I(t) = \int_V \frac{1}{3}\chi_{i,j,k}^{(2)}E_iE_jE_k\mathrm{d}V \qquad \text{(A.5)}$$

147

In order to describe the process in the quantum mechanics framework it is necessary to consider the corresponding operator $\hat{H}(t)$. In particular, considering the field quantization process (see for example [21]), the electric field can be written in terms of the boson operators as:

$$\hat{E}_j(\mathbf{r}, t) \propto \int [\hat{a}_{k_j} e^{i(\mathbf{k}_j \mathbf{r} - \omega_j t)} + H.C.] \mathrm{d}^3 \mathbf{k}_j \tag{A.6}$$

This quantum description is necessary for the down-converted photons ($\hat{E}_1, \hat{E}_2$), while can be omitted while considering the intense pump field. In particular, considering a monochromatic pump propagating along z, it can be written:

$$E_p(\mathbf{r}, t) = A_p(\rho) e^{i(\mathbf{k}_p z - \omega_p t)} \tag{A.7}$$

where $\rho = (\rho_x, \rho_y)$ are the coordinates in the $x - y$ plane, perpendicular to the propagation direction. Considering this reference system also $\mathbf{r}$ and $\mathbf{k}$ in Eq. A.6 can be written as the component parallel to the pump direction, $k_{j,z}$ and the transverse component $\mathbf{q}_j$, i.e. the component in the plane perpendicular to pump direction. This decomposition is exemplified in Fig. A.1. In this terms the interaction hamiltonian is:
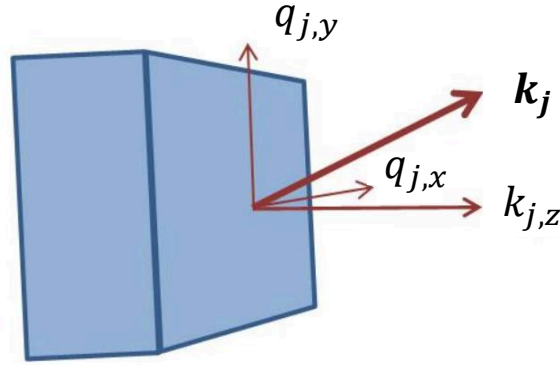

Figure A.1: Scheme for the reference system used in the decomposition of the position **r** and momentum **k** vectors.

$$\hat{H}_I(t) \propto \int \chi^{(2)} A_p(\rho) e^{i(k_p - k_{1,z} - k_{2,z})z} e^{i(\mathbf{q}_1 + \mathbf{q}_2)\rho} e^{-i(\omega_p - \omega_1 - \omega_2)t} \hat{a}_{\omega_1, \mathbf{q}_1} \hat{a}_{\omega_2, \mathbf{q}_2} \mathrm{d}\omega_1 \mathrm{d}\omega_2 \mathrm{d}\mathbf{q}_1 \mathbf{q}_2 \mathrm{d}\rho \mathrm{d}z \tag{A.8}$$

From the interaction hamiltonian, we can simply derive the system evolution. In particular, in the Schroedinger picture, the evolution of the down-converted modes $\hat{a}_1$ and $\hat{a}_2$, initially in the vacuum state, can be written as:

$$|twb\rangle = \hat{S}|00\rangle_{a_1, a_2} = \exp\left[-\frac{1}{i\hbar} \int_0^t \hat{H}_I(t') \mathrm{d}t'\right] |00\rangle_{a_1, a_2} \tag{A.9}$$

Let us now focus on the different contribution in the integral, and on the possible approximations in their evaluation, in order to arrive to the final twb expression in Eq. 1.99.

- dz: said L the length of the crystal it follows:

$$\int_0^L e^{i(k_p - k_{1,z} - k_{2,z})z} \mathrm{d}z = L e^{i\Delta kz/2} \operatorname{sinc}\left(\frac{\Delta kL}{2}\right), \tag{A.10}$$

with $\Delta k = k_p - k_1 - k_2$, representing the longitudinal phase mismatch. In the limit $L \to \infty$ the sinc function becomes a delta function. Under this condition the integral is different from zero only for $\Delta k = 0$, i.e. the perfect phase matching condition holds. In real experiments the finite crystal length L will lead to a certain spread around the perfect phase matching condition.

- dρ: this integral leads to the Fourier transform of the pump profile $A(\rho)$, extending over the transverse surface S. In the approximation of an incident plane wave it holds $A(\rho) = A_0$ thus following:

$$\int_S A(\rho) e^{i(\mathbf{q}_1 + \mathbf{q}_2)\rho} \mathrm{d}\rho = A_0 \delta(\mathbf{q}_1 + \mathbf{q}_2) \tag{A.11}$$

Therefore, in this approximation, the down-converted photons are perfectly correlated in transverse momentum. If the photon in the $\hat{a}_1$ mode has transverse momentum $\mathbf{q}$, the corresponding photon in the $\hat{a}_1$ has transverse momentum $-\mathbf{q}$.

- dt: having considered a monochromatic pump at frequency ω_p this integral over the interaction time simply leads to

$$\int e^{-i(\omega_p - \omega_1 - \omega_2)t} \mathrm{d}t = \delta(-\omega_p + \omega_1 + \omega_2) \tag{A.12}$$

As expected, the integral is therefore different from zero only if the energy of the down-converted photons respect the energy conversion law, i.e. $\omega_p = \omega_1 + \omega_2$. The two down-converted photons can have same frequency $\omega_1 = \omega_2 = \omega_p/2$, we refer to this frequency as degenerate frequency. Using the result presented in Eq. A.12, ω_1 and ω_2 can be written in terms of the degenerate frequency as $\omega_1 = \frac{\omega_p}{2} + \Omega$ and $\omega_2 = \frac{\omega_p}{2} - \Omega$ Note that in real situations the pump is not perfectly monochromatic, but a certain $\Delta\omega$ around ω_p is necessarily present.

According to all the considerations so far presented the time-evolution operator is:

$$\hat{S} = \exp\left[\int (f(\mathbf{q}, \Omega)\hat{a}_{\mathbf{q},\Omega}^\dagger \hat{a}_{-\mathbf{q},-\Omega} - H.C.)\mathrm{d}^2\mathbf{q}\mathrm{d}\Omega\right] \tag{A.13}$$

Finally, considering discrete values for $\mathbf{q}$ and Ω it is obtained:

$$\hat{S} = \exp\left[\sum_{\mathbf{q},\Omega} (f(\mathbf{q}, \Omega)\hat{a}_{\mathbf{q},\Omega}^\dagger \hat{a}_{-\mathbf{q},-\Omega} - H.C.)\right] \tag{A.14}$$

Being the explicit expression of $f(\mathbf{q}, \Omega)$:

$$f(\mathbf{q}, \Omega) = \chi^{(2)} A_0 L e^{i\Delta k z/2} \text{sinc}\left(\frac{\Delta k L}{2}\right) \tag{A.15}$$

Replacing Eq. 1.103 in Eq. A.9 we can write:

$$|\psi\rangle = \exp\left[\sum_{\mathbf{q},\Omega}(f(\mathbf{q},\Omega)\hat{a}_{\mathbf{q},\Omega}^\dagger \hat{a}_{-\mathbf{q},-\Omega} - H.C.)\right]|0\rangle = \tag{A.16}$$

$$= \otimes_{\mathbf{q},\Omega}\exp(f(\mathbf{q},\Omega)\hat{a}_{\mathbf{q},\Omega}^\dagger \hat{a}_{-\mathbf{q},-\Omega} - H.C.)|0\rangle \tag{A.17}$$

where the last equality follows from the independence between different modes, i.e.
$[\hat{a}_{\mathbf{q},\Omega}, \hat{a}_{\mathbf{q}',\Omega'}^\dagger] = \delta_{\mathbf{q},\mathbf{q}'}\delta_{\Omega,\Omega'}$ and the use of the Baker-Campbell-Hausdorff formula. Expanding the exponential and knowing the effects of the $\hat{a}$ and $\hat{a}^\dagger$ on the $|n\rangle$ state it is possible to write $|\psi\rangle$ in the Fock basis, finding exactly the expression in Eq. 1.100 [21]:

$$|\psi\rangle = \otimes_{\mathbf{q},\Omega}\sum_{n=0}^{\infty} c_{\mathbf{q},\Omega}(n)|n\rangle_{\mathbf{q},\Omega}|n\rangle_{-\mathbf{q},-\Omega} = \otimes_{\mathbf{q},\Omega}|twb\rangle_{\mathbf{q},\Omega} \tag{A.18}$$

with $c_{\mathbf{q},\Omega}(n)$ that can be regarded as constant respect to $\mathbf{q}$ and Ω. Its expression is $c_{\mathbf{q},\Omega}(n) \propto \sqrt{\mu/(\mu+1)^{n+1}}$, being $\mu = \sinh^2|f(\mathbf{q},\Omega)|$. The spontaneous parametric down-convertion process (SPDC) here described is therefore intrinsically multi-mode. In the plane wave pump approximation the SPDC state is a product of independent single-mode twb state defined in Eq. 1.99, each of them presenting two modes of correlated frequency and transverse momentum.

Appendix B

Functions for signal analysis in the frequency domain

B.1 Power Spectral Density

Most of this and the following sections are taken from [82]. The power spectral density describes how the power of a time series is distributed with frequency. Mathematically, it is defined as the Fourier transform of the autocorrelation sequence of the time series. The linear spectral density is simply the square root of the power spectral density.

Experimentally we always deal with finite length data, this implies the evaluation of the discrete Fourier transform (DFT). The practical implementation of the DFT on a computer nearly always uses the Fast Fourier Transform (FFT) algorithm.

The discrete Fourier transform in general takes a vector of N complex numbers $x_k, k = 0...N-1$, and transforms it into a vector of N complex numbers $y_m, m = 0...N-1$, being:

$$y_m^0 = \frac{1}{N} \sum_{k=0}^{N-1} x_k e^{-2\pi i \frac{mk}{N}} \tag{B.1}$$

If we simply take time series long N and we perform the DFT, we will probably find artifacts, which does not reproduce the physical system. The reason is that the DFT implicitly assumes that the signal is periodic, i.e. that the time series of length N repeats itself infinitely in a cyclic manner. The remedy is to multiply the time series with a 'window function' in the time domain before applying the DFT. One of the most commonly used window function is the Hanning function, defined as $w_j = 1/2[1 - \cos(\frac{2\pi j}{N})]$. To analyse the data we use this function, thus calculating the DFT as:

$$y_m = \frac{1}{N} \sum_{k=0}^{N-1} w_k x_k e^{-2\pi i \frac{mk}{N}} \tag{B.2}$$

We also define the following two normalizing factors:

$$S_1 = \sum_{j=0}^{N-1} w_j, \quad S_2 = \sum_{j=0}^{N-1} w_j^2,$$

(B.3)

We have now all the elements for defining the power-spectral densities of the initial time series x_k:

$$PSD = \frac{2|y_m|^2}{S_2 f_S}$$

(B.4)

where f_S is the sampling frequency.

If we compute one estimate of a spectrum with the methods described so far (i.e. multiplying one segment of the time series with a suitable window function, performing a DFT and scaling the results), we will find a noisy result. Note that it does not help the increase the length N of the DFT; that only reduces the width of one frequency bin without improving the variance. The remedy is to take the average of M estimates and hence reduce the standard deviation of the averaged result by a factor of $1/\sqrt{M}$. Note that the averaging must be done with the power spectrum (PS) or the power spectral density (PSD), not with their square roots LS or LSD.

If a long continuous data stream is simply split into several non-overlapping segments of length N, due to the fact that the window function is typically very small or zero near its boundaries, a significant portion of the data stream is effectively ignored in the analysis. This is clearly not optimal. The situation can be improved by letting the segments overlap by a factor that depends from the window used. For Hanning function the optimal overlap percentage is 50%.

Our data are analysed using Matlab 'pwelch' function, more details can be found in [69].

B.2 Linear Spectral Density

Having the PSD the linear spectral density can be obtained straight forward as:

$$LSD = \sqrt{PSD}$$

(B.5)

B.3 Cross Power Spectral Density

Given two time series $x1_k$ and $x2_k$, their cross-power spectral density is defined as the DFT of the correlation function, weighted using an opportune window function (we use Hanning window):

$$CPSD = S_{12}(m) = \frac{1}{S_2 f_s} \sum_{j=1}^{N} w_j R_{12}(j) e^{-2\pi i \frac{mj}{N}}$$

(B.6)

where $R_{12}(j) = \langle x1_k x2_{k+j} \rangle$ and N the number of elements in the sample. Similarly to what discussed for the PSD, the evaluation of the cpsd in this way would result too noisy. To solve this issue the Welch's method is applied: each of the time series are divided into $N_{spectra}$ bins, the CPSD is evaluated for each bin and then the average over the $N_spectra$ bins is performed. In this way the uncorrelated noise scales as $1/\sqrt{N_{spectra}}$. However unlike in the power spectral density evaluation there is no overlap taken between the several segments, additional correlations would be added due to overlapping, which would give us an error in the estimate of the CPSD. The estimation of CPSD was implemented by using a labview program.

B.4 Cross Linear Spectral Density

Having the CPSD, the CLSD can be evaluated straightforward considering the square root of the CPSD. Note that, differently from the PSD, the CPSD is a complex quantity, thus we consider its magnitude:

$$CLSD = \sqrt{|CPSD|} \qquad (B.7)$$

Appendix C

Locking techniques

The control of the interferometers degrees of freedom is essential. For each degree of freedom three elements are required:

- the monitoring of the current operating condition,

- the comparison of the current to the desired operating conditions,

- feedback to cancel the difference.

Aim of the locking is to fix each degree of freedom to the desired working point. There are different techniques for locking, however each of them is based on the production of an error signal, which must be anti-symmetric and proportional to the difference of the current and desired operating conditions. Finally the error signal is fed back to the system, trough a proportional-integral-derivative (PID) controller to correct for discrepancy between the current and desired operating conditions.

Common locking techniques are based on a phase modulation (PM) of the optical field. Experimentally a PM can be obtained using an electro-optic modulator (EOM), consisting in a crystal changing its refractive index with the applied voltage. Modulating the EOM at frequency Ω, the field, assumed as a coherent beam of frequency ω becomes:

$$\alpha = \alpha_0 e^{i(\omega t + A \sin(\Omega t))} \tag{C.1}$$

For small A, which is usually matched in real experiments, the Eq. C.1 can be approximated as:

$$\alpha \sim \alpha_0 e^{i\omega t}(1 + iA \sin(\Omega t)) \sim \alpha_0 e^{i\omega t}\left(1 + \frac{A}{2}e^{i\Omega t} - \frac{A}{2}e^{-i\Omega t}\right) \tag{C.2}$$

This means that imprintig a modulation at frequency Ω on the carrier field α produce two sidebands, at frequency $\omega \pm \Omega$.

The PM sidebands can be used as a reference while considering the interaction of the field with a cavity. This can be understood intuitively considering the following argument. Let us assume Ω much larger than the cavity linewidth and consider the carrier at

ω resonant with the cavity, long L. In this situation a small fraction of the incident light at ω is reflected and it receives no phase shift. On the contrary, the sidebands are well outside the linewidth of the cavity and therefore they are completely reflected and receive no phase shift. If L slighly increases, the reflected field at ω increases and receives a certain phase shift, ϕ. The sidebands, still well outside the cavity linewidth, remain unchanged. If L slighly decreases, the reflected field at ω increases and receives an opposit phase shift, $-\phi$. The sidebands, remain also in this case well outside the cavity linewidth, and are again reflected unchanged. It results that the interaction of the carrier and the PM sidebands with the cavity is different, thus allowing to develop locking techniques able to exploit this fact, extracting a proper error signal.

In the following we briefly report on the locking schemes used in the experiment described in Ch. 5. More details can be found in [69].

C.1 Pound-Drever-Hall locking technique

This technique is commonly used in optics to mantain cavities at the resonance (referring to a power reciclying interferometer it is used for locking the CARM). A detailed description of its working principle can be found in [83]. The experimental implementation of the technique is shown in Fig. C.1. The incoming light is phase modulated with
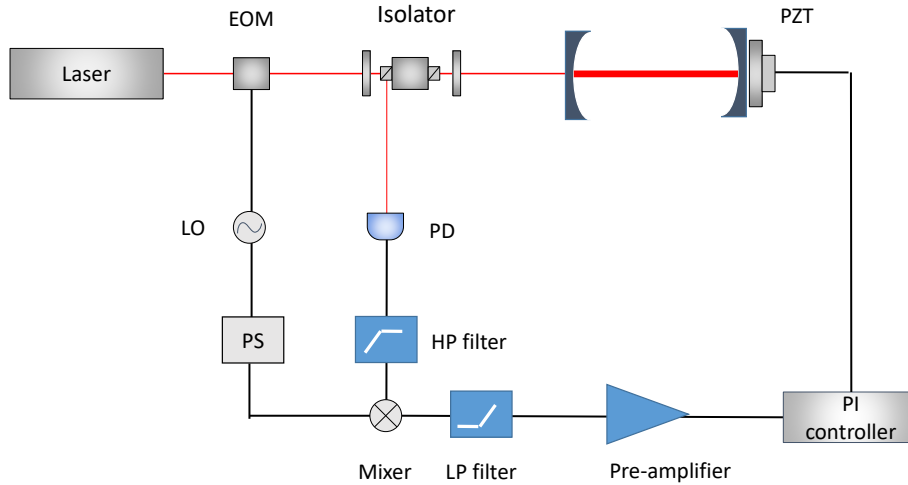

Figure C.1: Scheme of the Pound-Drever-Hall locking technique. EOM: electro-optic modulator. LO: local oscillator. PZT: piezo-electric transducer. PS: phase shifter. PD: photo-diode. PI controller: proportional integral controller.

a frequency, Ω well outside the linewidth of the cavity. The reflected light is measured on the photodetector. The detected signal at the modulation frequency is demodulated electronically. Demodulation transfers the measured signal at Ω down to DC, to be fed

back as an error signal. It also introduces a term at 2Ω which is removed by a low pass filter. The error signal is used lock the cavity length on resonance with the laser frequency using the PZT mounted on one of the two cavity end mirrors.

C.2   DC locking technique

This is a simple technique used to lock the DARM of a power reciclying interferometer at a certain working point. In this case the error signal is derived by subtracting a DC offset from the power transmitted to the output of the Michelson. For DC offset equal to zero the system should lock, ideally, exactly to the dark fringe. Introducing a small DC offset the position around the dark fringe can be tuned. Its experimental implementation is presented in Fig. C.2. One of the drawbacks of this locking technique is
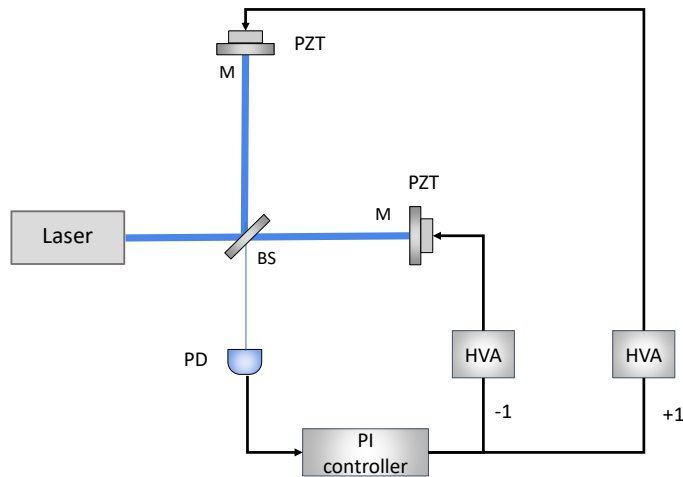

Figure C.2: Scheme of the DC locking technique. PZT: piezo-electric transducer. PD: photo-diode. PI controller: proportional integral controller. HVA: high voltage amplifier.

that, in particular for locking near to the dark fringe, it is not very stable and the system can easily go out of lock. This is due to the fact that the error signal is at its minimum in corresondence to our wished working point. To avoid this problems different locking techniques can be used, as for example the internal modulation technique.

C.3   Internal Modulation locking technique

This technique can be used to lock the DARM of an interferometer close to the dark fringe, with better stability respect the DC locking technique. Infact, in this case the error signal presents maximum slope in correspondence of the dark fringe, thus allowing

a better stability of the lock. Its experimental implementation is presented in Fig. C.3
In this case the EOM is placed inside the interferometer and generate sidebands at a
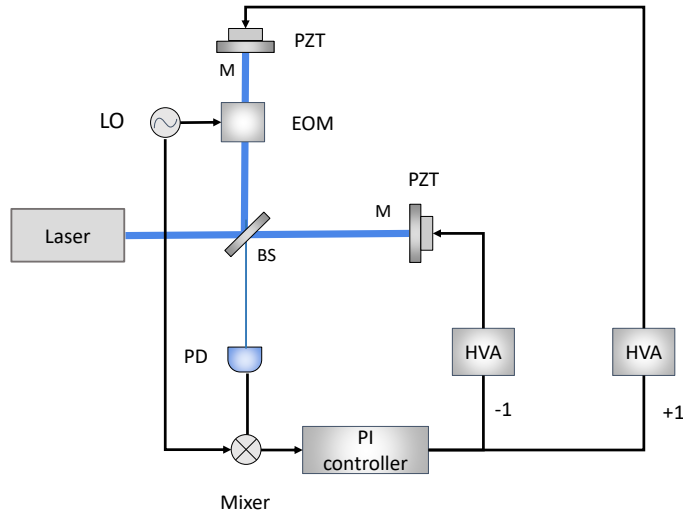

Figure C.3: Scheme of the internal modulation locking technique. EOM: electro-optic modulator. LO: local oscillator. PZT: piezo-electric transducer. PD: photo-diode. PI controller: proportional integral controller.

certain frequency Ω. The photodiode signal from the interferometer output is demodulated at Ω and the demodulated signal, opportunely filtered, represents the error signal to be sent to the PID module. The output of the PID is then sent to the end mirrors, in order to properly adjust the differential arm length. This method results particularly useful in our case since EOM used to produce the sidebands can be also used also to simulate signals with which testing our system performances. A possible drawback of this technique is that the EOM could introduce losses in the system, this can be highly mitigated taking care in the alignement procedure.

Bibliography

[1] Max F Riedel et al. "The European quantum technologies flagship programme". In: *Quantum Science and Technology* 2.3 (2017), p. 030501.

[2] Jonathan P Dowling and Gerard J Milburn. "Quantum technology: the second quantum revolution". In: *Phil. Trans. R. Soc. A* 361.1809 (2003), pp. 1655–1674.

[3] Nicolas Gisin and Rob Thew. "Quantum communication". In: *Nature photonics* 1.3 (2007), p. 165.

[4] Mohsen Razavi et al. "Quantum key distribution and beyond: introduction". In: *JOSA B* 36.3 (2019), QKD1–QKD2.

[5] T D Ladd et al. "Quantum computers". In: *Nature* 464.7285 (2010), p. 45.

[6] Valeria Cimini et al. "Quantum sensing for dynamical tracking of chemical processes". In: *Physical Review A* 99.5 (2019), p. 053817.

[7] Luca Pezzè et al. "Optimal measurements for simultaneous quantum estimation of multiple phases". In: *Physical review letters* 119.33 (2017), p. 130504.

[8] Michael A Taylor and Warwick P Bowen. "Quantum metrology and its application in biology". In: *Physics Reports* 615 (2016), pp. 1–59.

[9] Jonathan P Dowling and Seshadreesan Kaushik P. "Quantum optical technologies for metrology, sensing, and imaging". In: *Journal of Lightwave Technology* 33.12 (2015), pp. 2359–2370.

[10] Giorgio Brida et al. "Detection of multimode spatial correlation in PDC and application to the absolute calibration of a CCD camera". In: *Optics Express* 18.20 (2010), pp. 20572–20584.

[11] E D Lopaeva et al. "Experimental realization of quantum illumination". In: *Phys. Rev. Lett.* 110.15 (2013), p. 153603.

[12] Michael A Nielsen and Isaac L Chuang. "Quantum information and quantum computation". In: *Cambridge: Cambridge University Press* 2.8 (2000), p. 23.

[13] Vittorio Giovannetti, Seth Lloyd, and Lorenzo Maccone. "Quantum-enhanced measurements: beating the standard quantum limit". In: *Science* 306.5700 (2004), pp. 1330–1336.

[14] Vittorio Giovannetti, Seth Lloyd, and Lorenzo Maccone. "Advances in quantum metrology". In: *Nature photonics* 5.4 (2011), p. 222.

[15] M Genovese. "Real applications of quantum imaging". In: *Journal of Optics* 18.7 (2016), p. 073002.

[16] Junaid Aasi et al. "Enhanced sensitivity of the LIGO gravitational wave detector by using squeezed states of light". In: *Nature Photonics* 7.8 (2013), p. 613.

[17] Elena Losero et al. "Unbiased estimation of an optical loss at the ultimate quantum limit with twin-beams". In: *Scientific reports* 8.1 (2018), p. 7431.

[18] Elena Losero et al. "Quantum differential ghost microscopy". In: *arXiv preprint arXiv:1903.12630* (2019).

[19] Siva T Pradyumna et al. "Quantum-enhanced correlated interferometry for fundamental physics tests". In: *arXiv preprint arXiv:1810.13386* (2018).

[20] Cesare Rossetti. *Rudimenti di meccanica quantistica*. Levrotto & Bella, 2011.

[21] Leonard Mandel and Emil Wolf. *Optical coherence and quantum optics*. Cambridge university press, 1995.

[22] JM Palms, P Venugopala Rao, and RE Wood. "A Fano factor measurement for silicon using low energy photons". In: *Nuclear Instruments and Methods* 76.1 (1969), pp. 59–60.

[23] Henning Vahlbruch et al. "The GEO 600 squeezed light source". In: *Classical and Quantum Gravity* 27.8 (2010), p. 084027.

[24] Mette B Rasmussen, Lene Broeng Oddershede, and H Siegumfeldt. "Optical tweezers cause physiological damage to Escherichia coli and Listeria bacteria". In: *Appl. Environ. Microbiol.* 74.8 (2008), pp. 2441–2446.

[25] Richard Cole. "Live-cell imaging: The cell's perspective". In: *Cell adhesion & migration* 8.5 (2014), pp. 452–459.

[26] Alexander I Lvovsky. "Squeezed light". In: *Photonics: Scientific Foundations, Technology and Applications* 1 (2015), pp. 121–163.

[27] Meda A. et al. "Photon-number correlation for quantum enhanced imaging and sensing." In: *Jour. of Opt.* 19(9), 094002 (2017).

[28] A Meda et al. "Absolute calibration of a charge-coupled device camera with twin beams". In: *Applied Physics Letters* 105.10 (2014), p. 101113.

[29] DN Klyshko. "Use of two-photon light for absolute calibration of photoelectric detectors". In: *Soviet Journal of Quantum Electronics* 10.9 (1980), p. 1112.

[30] R_E Slusher et al. "Observation of squeezed states generated by four-wave mixing in an optical cavity". In: *Physical Review Letters* 55.22 (1985), p. 2409.

[31] Ling-An Wu et al. "Generation of squeezed states by parametric down conversion". In: *Physical review letters* 57.20 (1986), p. 2520.

[32] Henning Vahlbruch et al. "Observation of squeezed light with 10-dB quantum-noise reduction". In: *Physical review letters* 100.3 (2008), p. 033602.

[33] Henning Vahlbruch et al. "Detection of 15 dB squeezed states of light and their application for the absolute calibration of photoelectric quantum efficiency". In: *Physical review letters* 117.11 (2016), p. 110801.

[34] Moritz Mehmet et al. "Squeezed light at 1550 nm with a quantum noise reduction of 12.3 dB". In: *Optics express* 19.25 (2011), pp. 25763–25772.

[35] Ulrik L Andersen et al. "30 years of squeezed light generation". In: *Physica Scripta* 91.5 (2016), p. 053001.

[36] Christian Scheffmann Jacobsen, Ulrik Lund Andersen, and Kirstine Berg-Sørensen. "Quantum Information Protocols with Gaussian States of Light. Doctoral dissertation". In: (2016).

[37] Gerd Breitenbach, S Schiller, and J Mlynek. "Measurement of the quantum states of squeezed light". In: *Nature* 387.6632 (1997), p. 471.

[38] Daniel Braun et al. "Quantum-enhanced measurements without entanglement". In: *Reviews of Modern Physics* 90.3 (2018), p. 035006.

[39] Rafal Demkowicz-Dobrzański, Marcin Jarzyna, and Jan Kołodyński. "Quantum limits in optical interferometry". In: 60 (2015), pp. 345–435.

[40] Alex Monras and Matteo GA Paris. "Optimal quantum estimation of loss in bosonic channels". In: *Physical review letters* 98.16 (2007), p. 160401.

[41] Olivier Pinel et al. "Quantum parameter estimation using general single-mode Gaussian states". In: *Physical Review A* 88.4 (2013), p. 040102.

[42] G Adesso et al. "Optimal estimation of losses at the ultimate quantum limit with non-Gaussian states". In: *Physical Review A* 79.4 (2009), p. 040305.

[43] Alex Monras and Fabrizio Illuminati. "Measurement of damping and temperature: Precision bounds in Gaussian dissipative channels". In: *Physical Review A* 83.1 (2011), p. 012315.

[44] E Jakeman and JG Rarity. "The use of pair production processes to reduce quantum noise in transmission measurements". In: *Optics communications* 59.3 (1986), pp. 219–223.

[45] Paul-Antoine Moreau et al. "Demonstrating an absolute quantum advantage in direct absorption measurement". In: *Scientific reports* 7.1 (2017), p. 6256.

[46] Elena Brambilla et al. "High-sensitivity imaging with multi-mode twin beams". In: *Physical Review A* 77.5 (2008), p. 053807.

[47] Belinskii A and Klyshko D. "Two-photon optics: diffractlon, holography, and transformation of two-dimensional signals." In: *Sov. Phys. JETP* 78, 259 (1994).

[48] Pittman T. B. et al. "Optical imaging by means of two-photon quantum entanglement." In: *Phys. Rev. A* 52,R3429-32 (1995).

[49] Ryan S Bennink, Sean J Bentley, and Robert W Boyd. ""Two-photon" coincidence imaging with a classical source". In: *Physical review letters* 89.11 (2002), p. 113601.

[50] Fabio Ferri et al. "High-resolution ghost image and ghost diffraction experiments with thermal light". In: *Physical review letters* 94.18 (2005), p. 183602.

[51] Alejandra Valencia et al. "Two-photon imaging with thermal light". In: *Physical review letters* 94.6 (2005), p. 063601.

[52] Xi-Hao Chen et al. "High-visibility, high-order lensless ghost imaging with thermal light". In: *Optics letters* 35.8 (2010), pp. 1166–1168.

[53] Yan-Hua Zhai et al. "Two-photon interference with true thermal light". In: *Physical Review A* 72.4 (2005), p. 043805.

[54] Alessandra Gatti et al. "Ghost imaging with thermal light: comparing entanglement and classicalcorrelation". In: *Physical review letters* 93.9 (2004), p. 093602.

[55] Brida Giorgio et al. "Systematic analysis of signal-to-noise ratio in bipartite ghost imaging with classical and quantum light". In: *Physical Review A* 83.6 (2011), p. 063807.

[56] Jeffrey H Shapiro and Robert W Boyd. "The physics of ghost imaging". In: *Quantum Information Processing* 11.4 (2012), pp. 949–993.

[57] Emiliano Puddu et al. "Ghost imaging with intense fields from chaotically seeded parametric downconversion". In: *Optics letters* 32.9 (2007), pp. 1132–1134.

[58] Meda A. et al. "Magneto-optical imaging technique for hostile environments: The ghost imaging approach." In: *Appl. Phys. Lett.* 106, 262405 (2015).

[59] Ronald E Meyers et al. "Virtual ghost imaging through turbulence and obscurants using Bessel beam illumination". In: *Applied Physics Letters* 100.6 (2012), p. 061126.

[60] Wenlin Gong and Shensheng Han. "Correlated imaging in scattering media". In: *Optics letters* 36.3 (2011), pp. 394–396.

[61] Bina M. et al. "Backscattering differential ghost imaging in turbid media". In: *Physical Review letters* 110, 083901 (2013).

[62] Kam Wai Clifford Chan, Malcolm N O'Sullivan, and Robert W Boyd. "Two-color ghost imaging". In: *Physical Review A* 79.3 (2009), p. 033808.

[63] Reuben S Aspden et al. "Photon-sparse microscopy: visible light imaging using infrared illumination". In: *Optica* 2.12 (2015), pp. 1049–1052.

[64] Ferri F. et al. "Differential ghost imaging". In: *Phys. Rev. Lett.* 104(25), 253603 (2010).

[65] Carlton M Caves. "Quantum-mechanical noise in an interferometer". In: *Physical Review D* 23.8 (1981), p. 1693.

[66] Craig J Hogan. "Interferometers as probes of Planckian quantum geometry". In: *Physical Review D* 85.6 (2012), p. 064007.

[67] Ivano Ruo-Berchera et al. "Quantum light in coupled interferometers for quantum gravity tests". In: *Phys. Rev. Lett.* 110(21),213601 (2013).

[68] Ivano Ruo berchera et al. "io One and two mode squeezed light in correlated interferometry". In: *Physical Review A* 92,053821 (2015).

[69] Siva Pradyumna. "An application of quantum metrology: enhanced correlated interferometry". In: *Politecnico di Torino* Doctoral thesis Polito (2019).

[70] H Grote et al. "First long-term application of squeezed states of light in a gravitational-wave observatory". In: *Physical review letters* 110.18 (2013), p. 181101.

[71] KL Dooley et al. "GEO 600 and the GEO-HF upgrade program: successes and challenges". In: *Classical and Quantum Gravity* 33.7 (2016), p. 075009.

[72] Tomotada Akutsu et al. "Search for a stochastic background of 100-MHz gravitational waves with laser interferometers". In: *Physical review letters* 101.10 (2008), p. 101101.

[73] J Abadie et al. "Upper limits on a stochastic gravitational-wave background using LIGO and Virgo interferometers at 600−1000 Hz". In: *Physical Review D* 85.12 (2012), p. 122001.

[74] Aaron S Chou et al. "MHz gravitational wave constraints with decameter Michelson interferometers". In: *Physical Review D* 95.6 (2017), p. 063002.

[75] Aaron S Chou et al. "First measurements of high frequency cross-spectra from a pair of large Michelson interferometers". In: *Physical review letters* 117.11 (2016), p. 111102.

[76] Craig Hogan, Ohkyung Kwon, and Jonathan Richardson. "Statistical model of exotic rotational correlations in emergent space-time". In: *Classical and Quantum Gravity* 34.13 (2017), p. 135006.

[77] Craig Hogan. "Exotic rotational correlations in quantum geometry". In: *Physical Review D* 95.10 (2017), p. 104050.

[78] Sabine Hossenfelder. "Experimental search for quantum gravity". In: 1010 (2010).

[79] Craig J Hogan. "A model of macroscopic geometrical uncertainty". In: *arXiv preprint arXiv:1204.5948* (2012).

[80] Bahaa EA Saleh and Malvin Carl Teich. "Fundamentals of photonics". In: 18 (2019).

[81] A Chou, R Weiss, et al. "The Fermilab Holometer: A program to measure Planck scale indeterminacy". In: *Fermilab publication, Chicago* (2009).

[82] Gerhard Heinzel, Albrecht Rüdiger, and Roland Schilling. "Spectrum and spectral density estimation by the Discrete Fourier transform (DFT), including a comprehensive list of window functions and some new at-top windows". In: (2002).

[83] Eric D Black. "An introduction to Pound–Drever–Hall laser frequency stabilization". In: *American journal of physics* 69.1 (2001), pp. 79–87.